Inelastic background analysis from lab-based HAXPES spectra for critical interfaces in nano-electronics

Taylor Rose Bure

UNIVERSITÉ CLERMONT AUVERGNE

ÉCOLE DOCTORALE SCIENCES FONDAMENTALES (EDSF)

INSTITUT PASCAL, UMR 6602 - UCA/CNRS

LABORATOIRE D'ELECTRONIQUE DES TECHNOLOGIES DE L'INFORMATION (LETI)

COMMISSARIAT À L'ENERGIE ATOMIQUE ET AUX ENERGIES ALTERNATIVE (CEA)

INELASTIC BACKGROUND ANALYSIS FROM LAB-BASED HAXPES SPECTRA FOR CRITICAL INTERFACES IN NANO-ELECTRONICS

THÈSE DE DOCTORAT

Présentée par :

Taylor Rose BURE

Pour obtenir le grade de :

DOCTEUR D'UNIVERSITÉ

Spécialité : Milieux denses et matériaux

Soutenue publiquement le 20/12/2023 devant le jury composé de :

Rémi LAZZARI	Directeur de recherche CNRS, INSP	Rapporteur
Bruno DOMENICHINI	Professeur des Universités, ICB	Rapporteur
Mireille RICHARD-PLOUET	Directrice de Recherche CNRS, IMN	Présidente du Jury
Thierry CONARD	Directeur de recherche, IMEC	Invité
Nicolas PAULY	Professeur d'Université, ULB	Invité
Emmanuel NOLOT	Ingénieur-Chercheur, CEA-Leti	Co-encadrant de thèse
Olivier RENAULT	Directeur de Recherche du CEA, CEA-Leti	Co-directeur de thèse
Christine ROBERT-GOUMET	Maitre de Conférence-HDR, Institut Pascal	Co-directrice de thèse

Contents

Introduction

In the tirelessly advancing field of nanoelectronics, transistors are the crucial components that deliver the efficiency, power, reliability, and speed demanded of modern devices. This is achieved through miniaturizing components to the nanoscale, resulting in higher performance, lower power consumption, and smaller device sizes. Moore's law rules in the modern age of semiconductors, and the most advanced technology nodes (22 nm and beyond) enforce the industry standard for both materials design and device fabrication. The key factor of scaling-down in devices is indeed the materials used, especially, but not only, in gate dielectrics. High-k metal oxides have revolutionized the field of semiconductor technology by providing a solution to the limitations of traditional SiO_2 gate dielectrics in complementary metal oxide semiconductor (CMOS) devices. Now, multilayer structures with many active layers and critical interfaces occupy just a few microns of space. The proximity of the active layers to one another along with the complex interdiffusion phenomena brought on by several annealing steps make chemical and physical characterization an ongoing challenge.

Research and development (R&D) environments work with fab lines to meet the demand for high resolution and accurate characterization of new materials, driving innovation in lab-based instrumentation. The need for high throughput in turn requires innovation on the part of process fabrication. Hybrid solutions combine several analytical techniques with a common source in order to deliver a complete profile. Automation and artificial intelligence (AI) reduce user interaction, decreasing data processing times and also rendering the analysis user-friendly for non-specialists.

Laboratory and clean room environments are still challenged to nondestructively characterize buried interfaces, as many X-ray techniques remain surface sensitive or are unsuitable for analyzing rough surfaces or materials with similar densities. Hard X-ray photoelectron spectroscopy (HAXPES) increases the probing depth of the experiment to render the analysis depth-sensitive, at least at the sub-surface level, but due to poor X-ray fluxes was in the past limited to synchrotron radiation. With recent advances in instrumentation, lab-based X-ray source configurations with high flux and small spot sizes are soon to be commonplace in research environments and when integrated into process fabrication, can provide nondestructive depth-sensitive confirmation of the device structure and chemistry. XPS analysis, however, is still limited when it comes to nondestructive depth profiling and accurate determination of atomic concentration in real samples, often presenting non-homogeneous elemental compositions. Analysis of the inelastic background of an XPS spectrum provides information on the buried depth of the originating photoelectron and probes many times deeper into the sample than is reached by core-level analysis. The theory and practical implementation behind inelastic background analysis (IBA) has been in development since the late 1980s but has only in the last decade been

applied to HAXPES. This thesis develops upon previously existing developments combining synchrotron-based HAXPES and IBA in order to provide thickness measurements of technologically relevant materials for memory and power applications. Here, rather, the work uses lab-scale HAXPES in the perspective of IBA for applications in the metrology field, and we seek to meet the need for a method adapted for inline processes and routine analysis. The samples presented in this work were fabricated by pre-industrial processes and are representative of real device technology with concerns like complex interdiffusion properties and deeply buried active layers and interfaces

In this work, we investigate uncertainty in the HAXPES-IBA technique in regards to the free parameters and operator contributions. We present a self-contained analysis by accessing elements from each sample layer thanks to the expanded binding energy region of the XPS spectrum available with a novel lab-scale HAXPES technique. First, highly-controlled samples with relevant oxides were used to confirm the accuracy of the method through validation against highly-quantitative reference techniques and complimentary analyses found in established metrology. We go on to investigate two sample sets which employ these high-k oxides in order to test the previously developed method.

This thesis was a partnership between the Laboratory of Interfaces and Surfaces at Institut Pascal of University of Clermont-Auvergne and the Platform for NanoCharacterization (PFNC) of CEA-Minatec (Atomic and Alternative Energy Authority) in Grenoble. Thanks to the Tournesol N° 46254PL project, a collaboration with the Centre de Recherche en Métrologie Nucléaire at Université Libre Bruxelles was made possible.

The first chapter of this thesis introduces the state of the nanoelectronics industry and innovations in new materials, as well as the pressing demands for both R&D environments and metrology in the fab line. A special focus is placed on high-k semiconductor materials, and the critical buried interfaces which play an increasingly important role in device functionality. We present the physics behind the semiconductors studied in this work. We present the current state of inline fabrication processes, and go on to discuss advances in process control metrology and the existing needs which have yet to be met.

The second chapter discusses the experimental techniques used in this work. We discuss the atomic layer deposition (ALD) technique for sample fabrication, and provide a description of the destructive and nondestructive characterization methods for obtaining thickness measurements in the multilayer thin films. We present the quantitative destructive methods used in this work, as well as common nondestructive X-ray techniques employed in metrology steps along the process flow of the wafer. Among them, photoemission is widely used for its high surface sensitivity in the first nanometers; depth distribution can be obtained either with varying the photoelectron collection angle or by varying

the photon energy. We present lab-based HAXPES as an innovative solution to increasing the probing depth in device characterization, and suggest the IBA method for thickness measurements of deeply buried layers.

In the third chapter, we discuss the IBA method developed by Professor Sven Tougaard. We show how to obtain the depth distribution of elements through evaluation of the inelastic background and a provide practical approach to the software. We present previous developments in the combined HAXPES-IBA method, and achievements in increasing the probing depth and accuracy of the analysis. We give recent examples of how HAXPES-IBA can contribute to current understanding of materials physics. Finally, we discuss the impact of the energy of the X-ray source.

The fourth chapter is a comprehensive study of thickness determination in high-k dielectrics-based model stacks obtained by Atomic Layer Deposition (ALD). We begin with ultrathin Al_2O_3 from which we establish the quantitative capabilities of non-destructive X-ray techniques through validation by destructive but highly-calibrated Al-dose determination. We show how angle-resolved XPS (ARXPS) can track the linear growth mechanism of the ALD process, and discriminate between the Si substrate and native oxide formed at the interface. We develop the HAXPES-IBA method using bilayer systems of Al_2O_3 and HfO_2. In thick overlayer samples with a thin buried layer, we provide a complete analysis using both QUASES-Analysis and QUASES-Generate. Finally, we introduce HAXPES-IBA using a Ga Kα photon source and discuss the importance of adapting the energy of the X-ray source to the thickness class of the sample.

In chapter 5, we apply the method developed in chapter 4 to realistic technological samples. In the first study, we present a sample class of Al_2O_3 deposited over GaN by ALD representative of a recessed gate MOS channel High Electron Mobility Transistor (HEMT). Quantitative secondary ion mass spectrometry (SIMS) measurements compliment the IBA technique by confirming need for reference spectrum. In the second study, the HAXPES-IBA method is combined with ion sputtering to confirm the Ti/TiN overlayer thickness in a Ti/HfO_2-based structure used for oxide resistive random access memory (OxRRAM) technology.

In our general conclusion and perspectives, we review the method developed in this thesis and the results it provided. After, we provide a critical summary of advances necessary for a HAXPES-IBA method fully-integrated into the process control environment.

1 Technological and analytical context

Here we introduce the materials studied in this work, all of which are technologically relevant to state-of-the-art nanoelectronics development. We discuss their position in the industry, as well as the complex metrology used in the device fabrication process. It is evident that there is a need for non-destructive confirmation of thickness control which can be integrated into the inline metrology.

1.1 Overview of nanoelectronics and issues related to metrology and interface/thickness control

In this section, we briefly discuss progress in the semiconductor industry and the effect of scaling-down in the materials used in active components. We present the current state of film thickness metrology, and the growing needs of a fully-integrated device fabrication process.

1.1.1 Present context of nanoelectronics:

While the same principles have applied to nanodevice technology for the past decade (the patent for complementary metal oxide semiconductor (CMOS) was filed in 1963 [1]), the components and methods used in their production have been rapidly evolving. Thin film layers have shrunk from micrometers down to nanometer dimensions in advanced nodes. The nanometer-scale surface of a layer or the interface between layers may now make up a significant portion of the layer and affect the film properties. Advanced products may have up to nine interconnect levels, and the dielectric insulator between them is no longer SiO_2, but new organic/inorganic materials many of which have issues in homogeneity and stability in an uncontrolled environment. For example, sub-nm HfO_2-based films are used in gate dielectrics in some of the most advanced transistor technologies [2]. HfO_2 is highly reactive and unstable at the Si interface, so controlling the deposition conditions is paramount. Additionally, processing conditions may result in interdiffusion and a complex phase mixture. The affected interface may be buried under several layers, making it difficult to track changes in the overall thickness and interface position. This stresses the need for thickness control not only at the surface, but at the sub-surface level. Additionally, control is needed along a fabrication process which includes many steps and annealings, so confirmation of thickness control must be fast and easily integrated into existing and relevant metrology.

1.1.2 Film thickness metrology

In industry, metrology refers to measurement procedures of critical parameters with established tolerance limits that will produce a statistical process control (SPC) for device production. High

repeatability (low variation in measurements from a single process) and reproducibility (low variation in a measurement using different techniques) are required.

To keep up with the production line, a metrology step must be:

- Fast, with measurements within a few seconds or minutes,
- Robust, requiring minimal time down for maintenance,
- FAB compatible, as non-experts will be supervising the process.

Wafers are in the 200-300 mm range, the length of which must be mapped either completely or using a few evenly separated points. Inline metrology means the wafer must be transferred automatically between fabrication steps, with specially fitted outfits at each end. As mentioned above, a leading issue in film thickness metrology is the need for improved throughput in a high-volume manufacturing environment while retaining desired precision and accuracy in the measurement. These limits are constantly being tested and must be applicable to a large set of processes and technologies. Device technology is complexifying, and with these advances comes a need for advanced in-line control of the device fabrication. Lab-based procedures must be adapted for use with in-line tools. As an example, in-line X-ray Photoelectron Spectroscopy (XPS), a technique which is central in our work, provides high throughput for thickness control and composition analysis and can be paired with machine learning to hasten the procedure [3]. Yet, XPS is critically, too surface-sensitive and hampers thickness control of buried layers. Combined or hybrid solutions take data from several measurement sources and together can provide complete analysis of 3D architectures.

1.1.3 Critical buried interfaces

As stated above, the interface between the active layers has an increasing influence on the final device functionality as scaling-down results in thinner and thinner layers. The critical buried interfaces between heterostructures create band offsets that, along with electrostatic potentials already present in the device, act on the distribution and flow of mobile carriers. This makes the so-called hetero-interfaces an important design parameter in the functionality of the device. Kroemer[4] predicted in 1983 the incorporation of semiconductor hetero-interfaces into future high-performance semiconductor devices, as well as the scaling-down towards a device composed of many interfaces with minimal semiconductor thicknesses between them. Thus, we are to understand from his Nobel lecture in 2000, “The interface is the device [5].” In modern devices, insulators, conductors, and semiconductors occupy just a few nanometers of space, and controlling their impact on one another is paramount to the final device function. An example is shown below in Figure 1 where a scanning electron microscopy (SEM) cross section of a memory cell is depicted. The vertically integrated memory cell consists of one phase change memory (PCM) cell and one ovonic threshold switch (OTS) and is

abbreviated as a PCMS [6]. The OTS and PCM are linked by a middle electrode and sandwiched between a top and bottom electrode which are then connected to a column (write line) or row (bit line) metal, respectively. This complex structure is at the nanoscale, and it's easy to see how the interfaces make up a significant portion of the layers.

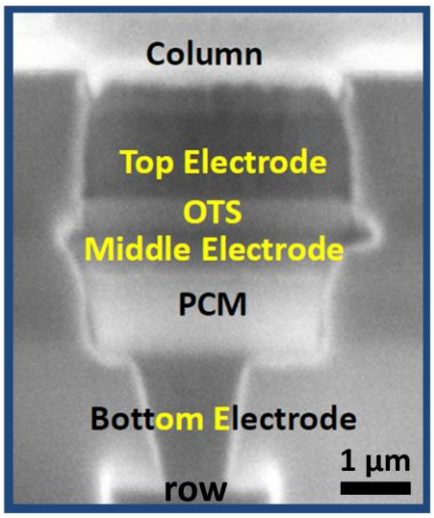

Figure 1. SEM cross section of a PCMS cell. The interfaces of the active middle electrode and OTS layers have similar thicknesses to the layers themselves. Taken from [6].

Another important way critical interfaces may affect the device is through the fabrication process. Device fabrication can consist of several steps of annealing, which may induce interdiffusion phenomena at the interface. AlGaN/GaN HEMT technology's fame comes from the 2-dimensional electron gas formed at the interface of the AlGaN channel and GaN substrate. In the fabrication of the HEMT devices, a series of annealing steps are performed to achieve the ohmic contact at the electrode/substrate interface in order to obtain good electrical properties. It was shown that the temperature of the process must be carefully controlled in order to avoid inhomogeneity at the interface and control nitrogen pumping [7,8]. These effects are difficult to characterize non-destructively, as the interface is deeply buried and sensitive.

1.1.4 High-k materials

One of the primary factors in attaining an efficient and compact transistor nanodevice is the gate dielectric. Properties to control include (a) permittivity, band gap, and band alignment to silicon, (b) thermodynamic stability, (c) film morphology, (d) interface quality, (e) compatibility with the current or expected materials to be used in processing for CMOS devices, (f) process compatibility, and (g) reliability. It must have high dielectric strength, permittivity, and tunability in a wide frequency range, as well as low dielectric loss [9,10]. Modern standards expect defect charge densities on the order of $10^{10}/cm^2$, midgap interface densities at ~$10^{10}/cm^2$ eV, and hard breakdown fields of 15 MV/cm [11]. These qualities are universally valued for nanoelectrics in energy storage, gate insulators, memory

devices, and high frequency devices [9,12]. The diverse applications call for a variety of dielectric materials and different layer thicknesses, in the sub-nm to tens of nm range, are needed depending on the final application.

Amorphous, thermally grown silicon dioxide (SiO_2) has taken the role of the dielectric for decades due to the stable bond formed at the Si-SiO_2 interface and excellent electrical isolation properties. In modern times, SiO_2 is unfit for the 90 nm process standardized by leading semiconductor companies due to capacitance limitations at this scale forcing the theoretical thickness to sub-10 Å, a dimension impossible to reliably achieve. This was confirmed by Muller et al.[13] when their transmission electron microscopy (TEM) electron energy loss spectroscopy (TEM/EELS) measurements of a processed gate stack of 12 Å nominal thickness confirmed that no bulk SiO_2 remained between the interfaces. In fact, increasing demands for improved performance find SiO_2 fundamentally limited in several material characteristics, namely its band offset, interfacial structure, and reliability [11].

Metal oxides with a high dielectric coefficient, κ, relative to SiO_2, so-called "high-k" gates, allow a substantially thicker dielectric for reduced leakage and reduced high capacitance densities. High-k materials have long-been integrated into high-performance CMOS applications [11,14]. Their success lies in the scaling of the equivalent oxide thickness (EOT) without increasing gate leakage. The EOT is the thickness of a silicon oxide film that provides the same electrical performance as that of the high-k material being used. Besides power applications, these dielectrics are also of great interest for application in mass storage memory devices like Dynamic Random Access Memory (DRAM). For memory applications, the most commonly studied material systems such as Ta_2O_2, Al_2O_3, $SrTiO_3$ have dielectric constants ranging from 10 to 80 [11]. While not adapted to logic Si-nanoelectronics due to low permittivity, Al_2O_3 is advantageous in power electronics due to its thermodynamic stability with Si. Hafnium-based high-k materials have increased in relevance, as they have short gate lengths [2].

1.1.5 MOSFET

Metal Oxide Semiconductor Field Effect Transistor (MOSFET) devices have been at the forefront of semiconductor technology since mid-last century [15]. Today they are a principal component of silicon chips, who's scaling down and increasing complexity in design have enforced the same requirement on the MOSFET device. Moore's law dictates that the number of transistors in an integrated circuit (IC) doubles every two years, meaning that in modern devices, billions of transistors are present on a single chip.

The MOSFET device operates by varying the width of a channel along which the charge carriers flow. It can be made as type P or type N (PMOS or NMOS) by the application of either a positive or negative gate voltage. The transistor can also be associated with another type of transistor in Complementary

MOS (CMOS). It works on the principle of field-effect modulation of charge density in a semiconductor channel by an imposed electric field. Charge carrier creation is ruled by the polarization V_g of the electrode (grid) through a dielectric. The carriers are transported through the channel from the source to the drain by the pulse of a differential potential V_d (Figure 2).

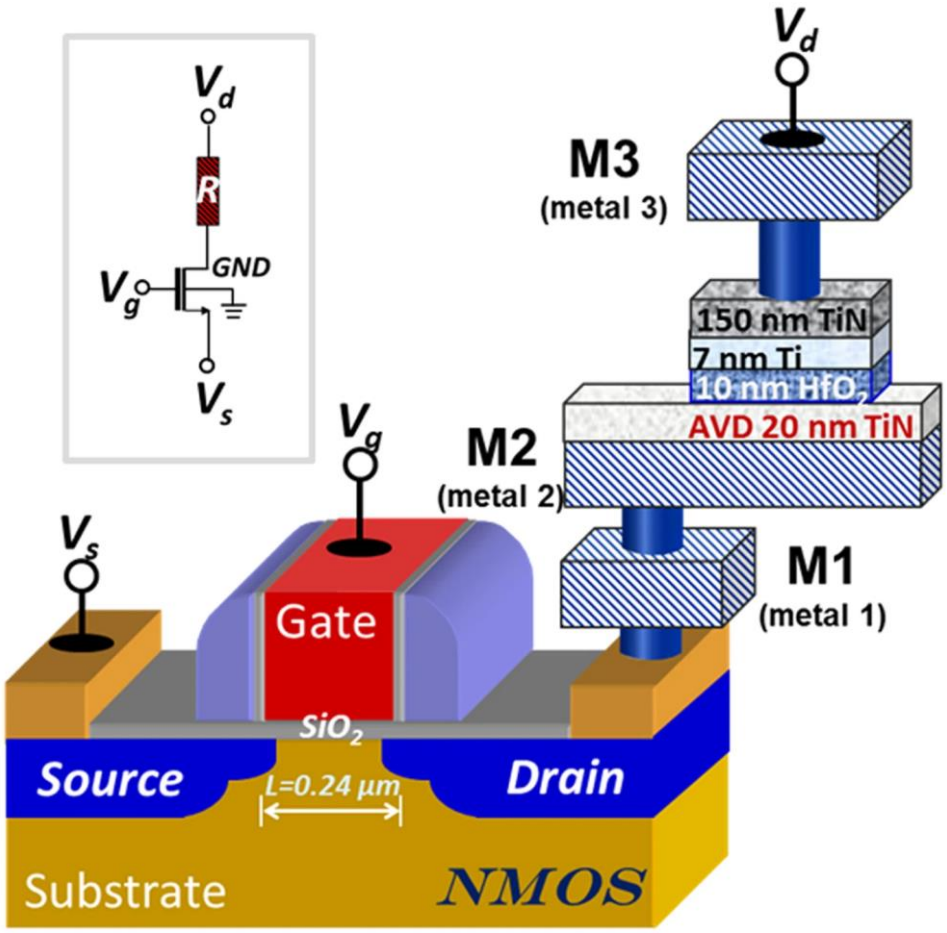

Figure 2. Sketch of a HfO_2-based MOSFET device structure, consisting of a TiN/HfO2/TiN structure and NMOS transistor. Inset shows the equivalent circuit. Taken from [16].

When operating, the transistor starts in a blocked state with no voltage across the gate terminal and V_g = 0 V. In this state, the channel has maximum conductance. The transistor then switches to an operating state where $V_g = V_d$. In order to achieve effective switching, V_g must be superior to the minimum threshold voltage V_{th} of the device. V_s is the source line voltage. Modern MOSFET devices circumvent the use of SiO_2 with new material compounds and device configurations. Hf and La oxides are promising dielectic materials that offer a high oxide capacity and reduced leakage currents [10,11]. The transistor is used to limit the pulse current in order to avoid the hard breakdown (HBD) in the

resistor, which consists of a metal-insulator-metal (MIM) structure for resistive switching (RS). In the device shown in Figure 2, HfO_2 is used as the insulator. HfO_2 deposition by ALD ensures the precise control of atomically specified film thickness and the high film quality. Titanium nitride (TiN) is a suitable metal gate, as it has high thermal stability, low resistivity and high-CMOS-process compatibility [17]. The 20 nm TiN layer was deposited by physical vapor deposition (PVD).

1.1.6 HEMT

High Electron Mobility Transistor (HEMT) devices offer up to millimeter wave frequencies and are essential to radio and microwave technologies. In order to compete with modern advancement and safety protocols, HEMT devices are required to have a high breakdown voltage, normally-OFF operation, and a low ON state resistance (R_{ON}) [18,19].

Gallium nitride (GaN) is a III-V wide band gap semiconductor of ~3.43 eV with a large breakdown voltage of 3.4 $MV.cm^{-1}$ [20]. This targeted breakdown voltage is possible with thinner drift layers, allowing for more compact devices and thus lower static and dynamic losses. As a result of an intrinsic carrier concentration n_i several orders of magnitude lower than Si, GaN obtains lower leakage currents and greater thermal stability [21].

HEMT devices achieve high frequency operation through the creation of a two-dimensional electron gas (2DEG) formed at the AlGaN/GaN heterojunction (See Figure 4). The two materials have differing band gaps, resulting in band discontinuities at their interface. The resulting potential well confines the electrons to a two-dimensional plane parallel to the hetero-interface with mobility values exceeding 100 $cm^2 \cdot V^{-1} \cdot s^{-1}$ [22].

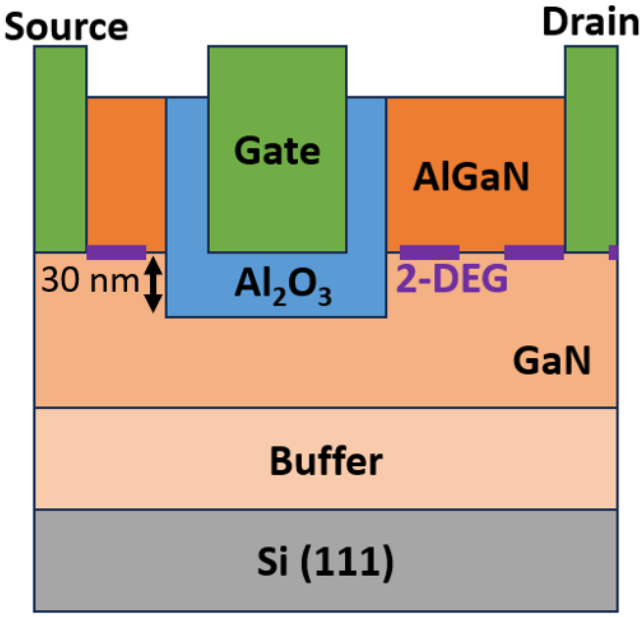

Figure 3. Scheme of a Normally-off MOSc-HEMT structure. A metal-oxide dielectric (blue) reduces the leakage current.

The principle of the 2DEG implies the existence of the device in a normally-on state, as the current will flow between the source and drain electrodes even at zero bias to the gate ($V_g = 0$). Failsafe operation condition for high power electronics, however, require a naturally-off device [23].

For a normally-off device, the electron flow must be enabled only when needed and at will. A fully recessed gate layout is one technological solution and sees the GaN substrate etched at the surface where the gate will be deposited. This forces the Fermi Level at the interface below the AlGaN conduction band minimum, thus depleting the 2DEG and inducing a positive threshold V_{th} [18]. The inclusion of an additional dielectric reduces the leakage current. Metal oxide semiconductor (MOSc) HEMT devices employ a metal oxide such as Al_2O_3 as the dielectric. Varying the thickness of the dielectric (generally from 10-30 nm) permits control of V_{th} [24]. This control must be maintained throughout the deposition process, calling for nondestructive thickness measurements during the many fabrication steps.

1.2 State of the art of metrology for thickness measurements

As explained above, high performance metrology is challenged to not only adapt lab-based techniques to the fab line, but also combine techniques for a complete analysis of the 3D devices being produced.

X-ray techniques are popular due to their non-destructive nature and versatility. The early days of the semiconductor industry favored Auger electron spectroscopy (AES), as it had higher lateral resolution and could perform elemental depth profiling quickly [25]. Over the last 15 years, however, X-ray

photoelectron spectroscopy (XPS) has become an integral part of device fabrication at early stages of the process flow (so-called Front-End Of the Line, or FEOL). This is in part due to the increasingly reactive species being used [26], pressing a need for chemical characterization. The main draw of XPS, however, is the scale at which device technology is produced. The probing depth of XPS is ideal for nanometer-scale surface and even in-depth characterization to some extent [15]. Fully automated XPS instrumentation is now capable of analyzing whole 200 mm and 300 mm wafers without exposing the sample to air in order to maintain the in-line environment. Angle-resolved XPS (ARXPS) is especially useful in determining individual layer thicknesses as it relies on the Beer-Lambert Law, in which the intensity of the photoelectrons emitted at depth d below the surface is directly related to the collection angle of the analyzer. In order to adapt to fab line needs for high throughput, the instrument provider Thermo Scientific has developed ARXPS instruments which, rather than tilting the sample, simultaneously collect angle resolved XPS data through the use of a wide angle input lens system and a 2-dimensional detector (Parallel-ARXPS or pARXPS) [27]. The ARXPS method, however, is limited in that the probing depth of traditional XPS is at the 1 – 10 nm scale, leaving ARXPS a surface-sensitive technique unfit for deeply buried layers.

Another important X-ray technique is one of the earliest, X-ray reflectivity (XRR) is long-standing technique for thickness determination in both crystalline and amorphous materials. In modern metrology, it is frequently combined with X-ray diffraction (XRD) and X-ray fluorescence (XRF) techniques. It was found that XRR combined with grazing incidence XRF (GIXRF) on the same experimental setup in a recursive method allowed for the estimation of uncertainties, paving the way for a quantitative hybrid technique [28]. Ellipsometry is monolayer sensitive, and so is useful for monitoring linear growth mechanisms like in atomic layer deposition (ALD). It can be integrated into the deposition reactor for *in situ* analysis and works well with thin films at the nm scale [29].

Full-mapping with X-ray techniques is, however, limited to the micron-scale. Single device thickness determinations require transmission electron microscopy (TEM) metrology or focus ion beam-assisted scanning electron microscopy (FIB-SEM). These techniques, however, are destructive and interrupt the device fabrication process. A fit cut is required in order to analyze the sample, which is time-consuming, further detracting from the objective of high throughputs in for in-line processes. Still, high throughput methods for in line microscopy are being developed such as the automation procedures developed by Thermo Scientific which greatly reduced preparation time and eliminated manual steps [30].

These are only some examples of demand in metrology driving innovation in lab-based thickness characterization. It is in the lab that the precise benefits and limitations of these techniques are determined.

1.3 State of the art of characterization for thickness measurements

Much like in metrology, information on the layer thicknesses can be obtained in many ways, and the best approach is often combining complementary methods.

1.3.1 Overview of lab-based thickness measurement techniques

Tables summarizing thickness measurement techniques are found in Annex A [31].

X-ray methods, especially XRR and XRF, are fast and accurate methods for characterizing the thickness of sample layers non-destructively and tracking the growth cycle in ALD [32]. XRR especially has a lateral resolution of 10 µm and has a probing depth as low as 3 nm [33]. Studies using reference-free X-ray fluorescence analysis include information pertaining to semiconductor surface contamination and nanolayered systems [34]. Grazing-incidence XRF employing synchrotron radiation can reveal elemental depth profiles and characteristics of buried nanolayers [35]. Both methods, however, are indiscriminate to the stacking order of layers.

ARXPS works well for thin layers with very flat surfaces like SiO_2 on Si and has excellent absolute depth resolution. Shadowing effects, however, render the analysis invalid in cases with rough surfaces or nano-structures, although it could be applied when distinguishing between or confirming the presence of non-smooth distributions. Replicate layers within the stack confuse the analysis, as a clear distinction between the layers is hardly possible. ARXPS is also a slow analysis, taking several hours to complete because it relies on the analysis of core-level spectra (see Chap. 2). Given known thicknesses, the method can determine the effective attenuation length λ of photoelectrons in the material. The max probed depth is 3λ [36,37]. This rends ARXPS a surface sensitive technique which is unfit for developing thickness characterization for stacks with increasing complexity, as there is an emerging need for increased sampling depths. For the most accurate and precise results and to confirm the nondestructive methods, complimentary analyses by destructive techniques are useful in a research and development environment.

TEM is an excellent method for determining the thickness of conductor layers and allows a maximum specimen thickness of 100 nm. It is a destructive technique, but provides lateral and in-depth resolutions in the sub-A range, making it a technique highly sensitive to crystalline imperfections. The measurement can also provide imaging of the sample, the crystalline structure, geometry, and

composition contrast between layers depending on the elemental composition. TEM has been used in studying the critical interfaces in III-V compound semiconductors for decades, and remains one of the most versatile methods available [38].

Another popular destructive technique is time of flight secondary ion mass spectrometry (TOF-SIMS). The technique is sufficient for all element types and provides an in-depth resolution of 0.5 nm and detection limits of $1\times10^{12\text{-}16}$ at/cm^3. TOF-SIMS can provide 3D distribution mapping, in-depth concentration profiles, composition and doping information, and identify elemental diffusion. The TOF-SIMS method has already been developed for analysis of thick AlGaN barrier layers in HEMT device technology [39]. A recent study combined TOF-SIMS and AFM to determine the absence of a stoichiometric gallium oxide layer at a Al_2O_3/GaN interface in a sample representative of a real recessed gate MOSc-HEMT architecture [40]. The same method was able to detect an approximately 4 nm gallium oxide layer intentionally grown using plasma-enhanced atomic layer deposition (PE-ALD) at with an O_2 plasma on the GaN surface before Al_2O_3 deposition. This is important because the presence of an oxide has been shown to have a great impact on the electrical properties of the transistor [18].

As devices become more complex, with many active layers and critical buried interfaces in a single stack, non-destructive techniques are required to probe deeper and deeper into the sample. In the next section, we discuss a technique for analyzing the inelastic background losses following an XPS or hard X-ray photoelectron spectroscopy (HAXPES) photoelectron peak in order to determine the thickness of buried layers. Formerly only available with synchrotron sources, HAXPES is now available at the lab-scale with high resolution and small area sensitivity [15,41–44]. Cr Kα and Ga Kα sources increase the probing depth to over tens of nanometers but remain limited in reaching deeply buried layers and interfaces.

1.3.2 HAXPES and Inelastic Background Analysis

An original work, developed by S. Tougaard [45–47] is a protocol for the analysis of the inelastic background contained in the X-ray photoemission spectrum rather than the core-level photoelectron peak. In this work, the inelastic background is used to determine the location and thickness of buried layers by quantifying the inelastic losses occurring as buried photoelectrons lose energy while exiting the material. Inelastic background analysis (IBA) can reach a probing depth of 8×IMFP [8,48–50]. Combining the method with HAXPES spectra has been shown to reach even higher [51,52]. This equates to over 100 nm for many elements. As a nondestructive method, it is capable of tracking the structural evolution in between fabrication steps like annealing or introduction of a capping layer. Since the surface morphology is described by the analysis, growth mechanisms can be followed as well.

The XPS acquisition supplying the spectra does not need to be long or highly resolved, allowing for fast results with only routine measurements. This makes a combined HAXPES-IBA method applied to lab-based HAXPES very useful in the process control of buried layer thicknesses as several depositions and annealings leave the exact thickness determination and interface location uncertain. With the complex interdiffusion phenomena of semiconductor materials being an ongoing field of research and key to device functionality, depth-sensitive nondestructive characterization is paramount to progress in nanodevice technology.

1.4 Conclusion and general objectives

The semiconductor industry is challenged to meet ever-increasing requirements in order to keep up with demand. As devices continue to shrink and incorporate new, reactive materials with complex interdiffusion properties, it is imperative that fab lines carefully control the fabrication process at each step. Clean room environments are adapting in order to produce fast results with high precision and accuracy. Repeatability and reproducibility are only achievable with reliable instrumentation and minimal interference that may be caused by additional measurements and instrumentation. More than ever, there is an overlap between lab-based techniques with high resolution and fab line control processes that guarantee high precision.

This work aims to investigate wether or not it would be possible to shift the lab-based IBA method to an in-line, metrological solution through the use of lab-based HAXPES. Lab-based HAXPES will soon be commonplace in research centers and is already contributing new information in major fields of research [15,53]. XPS is integral to process fabrication and industrial environments as a nondestructive verification of layer thicknesses and interface positions.

This work proposes a generic method for analyzing buried interfaces non-destructively and applies it to technologically relevant materials with diverse characteristics. We present stand-alone IBA-HAXPES at the lab-scale as an integrated step for process fabrication. Metrological techniques are used to evaluate the accuracy of the method. Additionally, a comprehensive analysis of all elements in the sample ensures the internal consistency of the method. Atomically-precise deposition delivered well-controlled, clean-room fabricated layers against which the method was evaluated.

We evaluate accuracy of the inelastic background method when using bulk spectra vs the universal inelastic scattering cross-section. This is in the interest of minimizing the dependence on outside measurements, which would take the analysis procedure “offline.”

[1] R. Puers, L. Baldi, M. Voorde, S.E. Nooten, Nanoelectronics: Materials, Devices, Applications, 2017. https://doi.org/10.1002/9783527800728.

[2] J.H. Choi, Y. Mao, J.P. Chang, Development of hafnium based high-k materials—A review, Mater. Sci. Eng. R Rep. 72 (2011) 97–136. https://doi.org/10.1016/j.mser.2010.12.001.
[3] Front Matter: Volume 10959, in: 2019: p. 1095901. https://doi.org/10.1117/12.2532423.
[4] H. Kroemer, Heterostructure devices: a device physicist looks at interfaces, Surf. Sci. 132 (1983) 543–576. https://doi.org/10.1016/0039-6028(83)90561-7.
[5] H. Kroemer, Quasi-Electric Fields and Band Offsets: Teaching Electrons New Tricks (Nobel Lecture), ChemPhysChem. 2 (2001) 490–499.
[6] DerChang Kau, S. Tang, I.V. Karpov, R. Dodge, B. Klehn, J.A. Kalb, J. Strand, A. Diaz, N. Leung, J. Wu, Sean Lee, T. Langtry, Kuo-wei Chang, C. Papagianni, Jinwook Lee, J. Hirst, S. Erra, E. Flores, N. Righos, H. Castro, G. Spadini, A stackable cross point Phase Change Memory, in: 2009 IEEE Int. Electron Devices Meet. IEDM, IEEE, Baltimore, MD, USA, 2009: pp. 1–4. https://doi.org/10.1109/IEDM.2009.5424263.
[7] D. Bertrand, M. Fayolle, A. Torres, E. Blanquet, F. Volpi, Study of Ti-Rich and Al-Rich Contact Metallization for AlGaN/GaN HEMT Power Devices, ECS Trans. 64 (2014) 263. https://doi.org/10.1149/06407.0263ecst.
[8] C. Zborowski, O. Renault, A. Torres, C. Guedj, Y. Yamashita, S. Ueda, G. Grenet, S. Tougaard, Quantitative determination of elemental diffusion from deeply buried layers by photoelectron spectroscopy, J. Appl. Phys. 124 (2018) 085115. https://doi.org/10.1063/1.5033453.
[9] J. Lutz, H. Schlangenotto, U. Scheuermann, R. De Doncker, Semiconductor Power Devices, Springer International Publishing, Cham, 2018. https://doi.org/10.1007/978-3-319-70917-8.
[10] J. Azadmanjiri, C.C. Berndt, J. Wang, A. Kapoor, V.K. Srivastava, C. Wen, A review on hybrid nanolaminate materials synthesized by deposition techniques for energy storage applications, J Mater Chem A. 2 (2014) 3695–3708. https://doi.org/10.1039/C3TA14034B.
[11] G.D. Wilk, R.M. Wallace, J.M. Anthony, High-κ gate dielectrics: Current status and materials properties considerations, J. Appl. Phys. 89 (2001) 5243–5275. https://doi.org/10.1063/1.1361065.
[12] T. Hori, Gate Dielectrics and MOS ULSIs: Principles, Technologies and Applications, Springer Berlin Heidelberg, Berlin, Heidelberg, 1997. https://doi.org/10.1007/978-3-642-60856-8.
[13] D.A. Muller, T. Sorsch, S. Moccio, F.H. Baumann, K. Evans-Lutterodt, G. Timp, The electronic structure at the atomic scale of ultrathin gate oxides, Nature. 399 (1999) 758–761. https://doi.org/10.1038/21602.
[14] J.A. Kittl, K. Opsomer, M. Popovici, N. Menou, B. Kaczer, X.P. Wang, C. Adelmann, M.A. Pawlak, K. Tomida, A. Rothschild, B. Govoreanu, R. Degraeve, M. Schaekers, M. Zahid, A. Delabie, J. Meersschaut, W. Polspoel, S. Clima, G. Pourtois, W. Knaepen, C. Detavernier, V.V. Afanas'ev, T. Blomberg, D. Pierreux, J. Swerts, P. Fischer, J.W. Maes, D. Manger, W. Vandervorst, T. Conard, A. Franquet, P. Favia, H. Bender, B. Brijs, S. Van Elshocht, M. Jurczak, J. Van Houdt, D.J. Wouters, High-k dielectrics for future generation memory devices (Invited Paper), Microelectron. Eng. 86 (2009) 1789–1795. https://doi.org/10.1016/j.mee.2009.03.045.
[15] O. Renault, P.-M. Deleuze, J. Courtin, T.R. Bure, N. Gauthier, E. Nolot, C. Robert-Goumet, N. Pauly, E. Martinez, K. Artyushkova, New directions in the analysis of buried interfaces for device technology by hard X-ray photoemission, Faraday Discuss. 236 (2022) 288–310. https://doi.org/10.1039/D1FD00110H.
[16] G. Niu, H.-D. Kim, R. Roelofs, E. Perez, M.A. Schubert, P. Zaumseil, I. Costina, C. Wenger, Material insights of HfO2-based integrated 1-transistor-1-resistor resistive random access memory devices processed by batch atomic layer deposition, Sci. Rep. 6 (2016) 28155. https://doi.org/10.1038/srep28155.
[17] J. Widiez, M. Vinet, T. Poiroux, P. Holliger, B. Previtali, P. Grosgeorges, S. Deleonibus, M. Mouis, TiN metal gate thickness influence on Fully Depleted SOI MOSFETs physical and electrical properties, in: 2005 IEEE Int. SOI Conf. Proc., IEEE, Honolulu, HI, USA, 2005: pp. 30–31. https://doi.org/10.1109/SOI.2005.1563523.
[18] C. Le Royer, B. Mohamad, J. Biscarrat, L. Vauche, R. Escoffier, J. Buckley, S. Bécu, R. Riat, C. Gillot, M. Charles, S. Ruel, P. Pimenta-Barros, N. Posseme, P. Besson, F. Boudaa, C. Vannuffel, W.

Vandendaele, A.G. Viey, A. Krakovinsky, M.-A. Jaud, R. Modica, F. Iucolano, R.L. Tiec, S. Levi, M. Orsatelli, R. Gwoziecki, V. Sousa, Normally-OFF 650V GaN-on-Si MOSc-HEMT Transistor: Benefits of the Fully Recessed Gate Architecture, in: 2022 IEEE 34th Int. Symp. Power Semicond. Devices ICs ISPSD, 2022: pp. 49–52. https://doi.org/10.1109/ISPSD49238.2022.9813672.
[19] J. He, W. Cheng, Q. Wang, K. Cheng, H. Yu, Y. Chai, Recent Advances in GaN-Based Power HEMT Devices, Adv. Electron. Mater. 7 (2021) 2001045. https://doi.org/10.1002/aelm.202001045.
[20] I. Vurgaftman, J.R. Meyer, L.R. Ram-Mohan, Band parameters for III–V compound semiconductors and their alloys, J. Appl. Phys. 89 (2001) 5815–5875. https://doi.org/10.1063/1.1368156.
[21] F. Roccaforte, G. Greco, P. Fiorenza, F. Iucolano, An Overview of Normally-Off GaN-Based High Electron Mobility Transistors, Materials. 12 (2019) 1599. https://doi.org/10.3390/ma12101599.
[22] O. Ambacher, J. Smart, J.R. Shealy, N.G. Weimann, K. Chu, M. Murphy, W.J. Schaff, L.F. Eastman, R. Dimitrov, L. Wittmer, M. Stutzmann, W. Rieger, J. Hilsenbeck, Two-dimensional electron gases induced by spontaneous and piezoelectric polarization charges in N- and Ga-face AlGaN/GaN heterostructures, J. Appl. Phys. 85 (1999) 3222–3233. https://doi.org/10.1063/1.369664.
[23] M. Su, C. Chen, S. Rajan, Prospects for the application of GaN power devices in hybrid electric vehicle drive systems, Semicond. Sci. Technol. 28 (2013) 074012. https://doi.org/10.1088/0268-1242/28/7/074012.
[24] Y. Zhang, M. Sun, S.J. Joglekar, T. Fujishima, T. Palacios, Threshold voltage control by gate oxide thickness in fluorinated GaN metal-oxide-semiconductor high-electron-mobility transistors, Appl. Phys. Lett. 103 (2013) 033524. https://doi.org/10.1063/1.4815923.
[25] S. Hofmann, Auger- and X-Ray Photoelectron Spectroscopy in Materials Science, Springer Berlin Heidelberg, Berlin, Heidelberg, 2013. https://doi.org/10.1007/978-3-642-27381-0.
[26] C.R. Brundle, G. Conti, P. Mack, XPS and angle resolved XPS, in the semiconductor industry: Characterization and metrology control of ultra-thin films, J. Electron Spectrosc. Relat. Phenom. 178–179 (2010) 433–448. https://doi.org/10.1016/j.elspec.2010.03.008.
[27] Angular Linearity and Resolution on Theta Probe, (n.d.).
[28] S. Melhem, Y. Ménesguen, E. Nolot, M. Lépy, A step toward calculating the uncertainties in combined GIXRF-XRR, X-Ray Spectrom. (2023) xrs.3377. https://doi.org/10.1002/xrs.3377.
[29] V. Drozd, Progress in device from Molecular Layering to atomic layer deposition worldwide technology, in: 2016 14th Int. Balt. Conf. At. Layer Depos. BALD, 2016: pp. 2–4. https://doi.org/10.1109/BALD.2016.7886521.
[30] M. Kuhn, Y. Zhou, K. Johnson, Opportunities and Challenges for Lab-based Hybrid Metrology for Emerging Technologies, Frontiers of Characterization and Metrology for Nanoelectronics, (2017).
[31] C. Zborowski, Characterization of deeply buried interfaces by Hard X-ray Photoelectron Spectroscopy, University of Southern Denmark, 2018.
[32] P.Y. Hung, C. Gondran, A. Ghatak-Roy, S. Terada, B. Bunday, H. Yeung, A. Diebold, X-ray reflectometry and x-ray fluorescence monitoring of the atomic layer deposition process for high-k gate dielectrics, J. Vac. Sci. Technol. B Microelectron. Nanometer Struct. 23 (2005) 2244. https://doi.org/10.1116/1.2009774.
[33] J. Wernecke, A.G. Shard, M. Krumrey, Traceable thickness determination of organic nanolayers by X-ray reflectometry: Traceable thickness determination of organic nanolayers by XRR, Surf. Interface Anal. 46 (2014) 911–914. https://doi.org/10.1002/sia.5371.
[34] P. Hoenicke, B. Beckhoff, M. Kolbe, D. Giubertoni, J. Van den Berg, G. Pepponi, Depth profile characterization of ultra shallow junction implants, Anal. Bioanal. Chem. 396 (2009) 2825–32. https://doi.org/10.1007/s00216-009-3266-y.
[35] P. Colombi, D.K. Agnihotri, V.E. Asadchikov, E. Bontempi, D.K. Bowen, C.H. Chang, L.E. Depero, M. Farnworth, T. Fujimoto, A. Gibaud, M. Jergel, M. Krumrey, T.A. Lafford, A. Lamperti, T. Ma, R.J. Matyi, M. Meduna, S. Milita, K. Sakurai, L. Shabel'nikov, A. Ulyanenkov, A. Van der Lee, C. Wiemer, Reproducibility in X-ray reflectometry: results from the first world-wide round-robin

experiment, J. Appl. Crystallogr. 41 (2008) 143–152. https://doi.org/10.1107/S0021889807051904.
[36] B.S. Semak, C. van der Marel, S. Tougaard, Comparison of the Tougaard, ARXPS, RBS and ellipsometry methods to determine the thickness of thin SiO2 layers, Surf. Interface Anal. 33 (2002) 238–244. https://doi.org/10.1002/sia.1206.
[37] S. Hüfner, Photoelectron Spectroscopy, Springer Berlin Heidelberg, Berlin, Heidelberg, 2003. https://doi.org/10.1007/978-3-662-09280-4.
[38] P.M. Petroff, Transmission electron microscopy of interfaces in III–V compound semiconductors, J. Vac. Sci. Technol. 14 (1977) 973–978. https://doi.org/10.1116/1.569406.
[39] P.A. Yunin, Yu.N. Drozdov, M.N. Drozdov, O.I. Khrykin, V.I. Shashkin, Surf. Interface Anal. 49 (2017) 117–121. https://doi.org/10.1002/sia.6068.
[40] T. Spelta, M. Veillerot, E. Martinez, N. Chevalier, D. Mariolle, R. Templier, B. Salem, P.F. Paes Pinto Rocha, L. Vauche, S. Boubenia, B. Hyot, Characterization of GaN structures for power electronics by secondary ion mass spectrometry and atomic force microscope approach, J. Vac. Sci. Technol. B. 41 (2023) 034003. https://doi.org/10.1116/6.0002573.
[41] B.F. Spencer, S.A. Church, P. Thompson, D.J.H. Cant, S. Maniyarasu, A. Theodosiou, A.N. Jones, M.J. Kappers, D.J. Binks, R.A. Oliver, J. Higgins, A.G. Thomas, T. Thomson, A.G. Shard, W.R. Flavell, Characterization of buried interfaces using Ga Kα hard X-ray photoelectron spectroscopy (HAXPES), Faraday Discuss. 236 (2022) 311–337. https://doi.org/10.1039/D2FD00021K.
[42] T. Spelta, M. Veillerot, E. Martinez, D. Mariolle, R. Templier, N. Chevalier, P. Fernandes Paes Pinto Rocha, B. Salem, L. Vauche, B. Hyot, Impact of etching process on Al2O3/GaN interface for MOSc-HEMT devices combining ToF-SIMS, HAXPES and AFM, Solid-State Electron. 208 (2023) 108743. https://doi.org/10.1016/j.sse.2023.108743.
[43] C. Zborowski, I. Hoflijk, I. Vaesen, A. Vanleenhove, K. Artyushkova, T. Conard, High energy x-ray photoelectron spectroscopy (HAXPES) Cr Kα measurement of bulk bismuth, Surf. Sci. Spectra. 30 (2023). https://doi.org/10.1116/6.0002703.
[44] P.-M. Deleuze, K. Artyushkova, E. Martinez, O. Renault, High-energy photoelectron spectroscopy of Al with Cr K *α* excitation, Surf. Sci. Spectra. 29 (2022) 014002. https://doi.org/10.1116/6.0001508.
[45] S. Tougaard, Background removal in x-ray photoelectron spectroscopy: Relative importance of intrinsic and extrinsic processes, Phys. Rev. B. 34 (1986) 6779–6783. https://doi.org/10.1103/PhysRevB.34.6779.
[46] S. Tougaard, Practical guide to the use of backgrounds in quantitative XPS, J. Vac. Sci. Technol. A. 39 (2021) 011201. https://doi.org/10.1116/6.0000661.
[47] S. Tougaard, Energy loss in XPS: Fundamental processes and applications for quantification, non-destructive depth profiling and 3D imaging, J. Electron Spectrosc. Relat. Phenom. 178–179 (2010) 128–153. https://doi.org/10.1016/j.elspec.2009.08.005.
[48] P. Risterucci, O. Renault, E. Martinez, B. Detlefs, J. Zegenhagen, G. Grenet, S. Tougaard, Inelastic background analysis of HAXPES spectra: towards enhanced bulk sensitivity in photoemission: Inelastic background analysis of HAXPES spectra, Surf. Interface Anal. 46 (2014) 906–910. https://doi.org/10.1002/sia.5484.
[49] P. Risterucci, O. Renault, E. Martinez, B. Detlefs, V. Delaye, J. Zegenhagen, C. Gaumer, G. Grenet, S. Tougaard, Probing deeper by hard x-ray photoelectron spectroscopy, Appl. Phys. Lett. 104 (2014) 051608. https://doi.org/10.1063/1.4864488.
[50] C. Zborowski, A. Vanleenhove, T. Conard, Comparison and complementarity of QUASES-Tougaard and SESSA software, Appl. Surf. Sci. 585 (2022) 152758. https://doi.org/10.1016/j.apsusc.2022.152758.
[51] Y.-T. Cui, S. Tougaard, H. Oji, J.-Y. Son, Y. Sakamoto, T. Matsumoto, A. Yang, O. Sakata, H. Song, I. Hirosawa, Thickness and structure of thin films determined by background analysis in hard X-ray photoelectron spectroscopy, J. Appl. Phys. 121 (2017) 225307. https://doi.org/10.1063/1.4985176.

[52] B.F. Spencer, S. Maniyarasu, B.P. Reed, D.J.H. Cant, R. Ahumada-Lazo, A.G. Thomas, C.A. Muryn, M. Maschek, S.K. Eriksson, T. Wiell, T.-L. Lee, S. Tougaard, A.G. Shard, W.R. Flavell, Inelastic background modelling applied to hard X-ray photoelectron spectroscopy of deeply buried layers: A comparison of synchrotron and lab-based (9.25 keV) measurements, Appl. Surf. Sci. 541 (2021) 148635. https://doi.org/10.1016/j.apsusc.2020.148635.
[53] O. Renault, E. Martinez, C. Zborowski, J. Mann, R. Inoue, J. Newman, K. Watanabe, Analysis of buried interfaces in multilayer device structures with hard XPS (HAXPES) using a CrKα source, Surf. Interface Anal. 50 (2018) 1158–1162. https://doi.org/10.1002/sia.6451.

2 Experimental methods

This chapter introduces the experimental methods used in this work. The description starts with the deposition process used to obtain the high-k nanolaminate structures from which we have developed the lab-based HAXPES-IBA method described in Chapter 3. We then go on to discuss the reference analytical techniques applied, as well as the photoemission theory at the base of the XPS and HAXPES method. Finally, we introduce the state-of-the-art lab-based HAXPES instrumentation available with the PHI Quantes and present the Scienta Omicron HAXPES-Lab.

2.1 Atomic Layer Deposition

ALD [1,2] produces nanolaminate structures comprised of alternating layers of binary oxides. It has a self-terminating growth mechanism which allows for atomic layer control and ensures perfect conformity in the deposition. ALD is a technique for growing thin films for a wide range of applications. ALD is a special variant of the chemical vapor deposition (CVD) technique where gaseous reactants (precursors) are introduced all together into the reaction chamber for forming the desired material via chemical surface reactions on a substrate kept at a certain temperature. A characteristic feature of ALD is that the precursors are pulsed alternately, one at a time, and separated by inert gas purging in order to avoid gas phase reactions (Figure 4). Thermal ALD at 300°C was used for the films in this work. The temperature of thermal annealing can range from room temperature (~20°C) to 350°C for ligand exchange or combustion type surface reactions [3]. In the synthesis of Al_2O_3 (Figure 4), trimethylaluminum (TMA) and water are employed as precursors. During the TMA exposure, TMA dissociatively chemisorbs on the substrate surface and any remaining TMA is pumped out of the chamber, leaving a surface of $AlCH_3$. The surface is then exposed to H_2O vapors, which reacts with the CH_3 bonds, forming a CH_4 byproduct and leaving behind a hydroxylated Al_2O_3 surface [2].

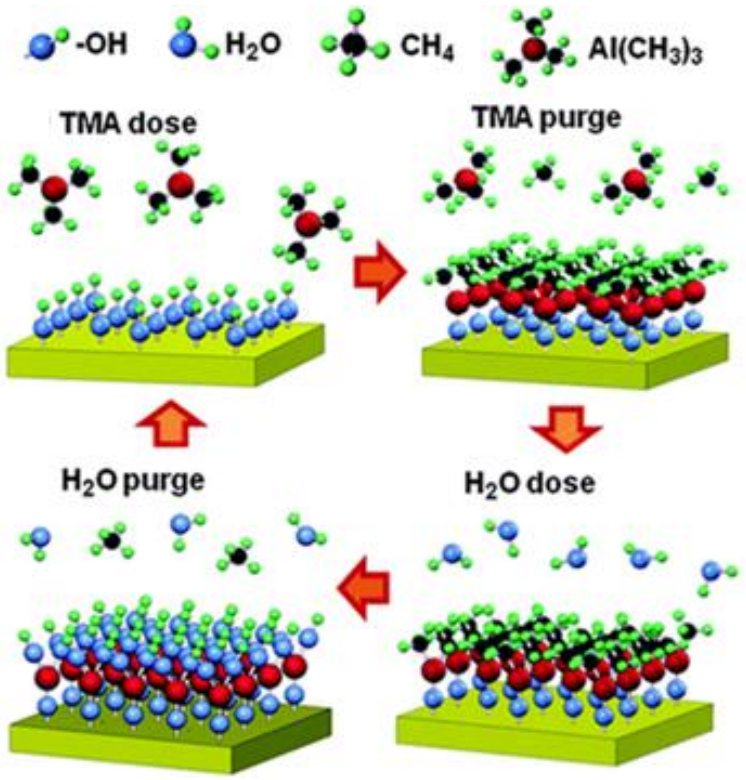

Figure 4. The ALD process for Al_2O_3 nanolaminate structures. TMA is used for the Al precursor, while H_2O is used for the oxide growth. Taken from [4].

The successive, self-terminated surface reactions of the reactants enable controlled growth of the desired material. The self-limiting growth mechanism results in perfect conformity and thickness uniformity of the film even on complicated 3D structures. Thanks to its superior conformality, uniformity, and atomic level control, ALD has made a breakthrough in various applications in modern technology [5,6]. ALD is a mainstream method of sample preparation in the nanoelectronics industry and has aided in the shrinking of semiconductor devices and adoption of increasingly demanding high-aspect-ratio structures. The limiting factor of the ALD process is the time required to complete the film. The time to reach saturation of a layer depends on the precursor pressure and the sticking probability. This is

Equation 1

$$R_{abs} = S \times F$$

Where R_{abs} is the rate of adsorption, S is the sticking probability, and F is the incident molar flux. Over time, more molecules will have reacted with the surface, decreasing S until reaching a value of zero once saturation is reached.

A key issue in successful application of ALD is continuous development of the precursor chemistry. The process also produces high material and energy waste. ALD technology is also strongly dependent on the reactor design. In summary, ALD is a thin film deposition technique for obtaining layers of well controlled thickness and minimal surface rugosity. This is the reason why it was considered in our work in which the development of the IBA method from lab-based HAXPES spectra requires flat samples of variable and accurate thicknesses.

2.2 Reference techniques

The following reference techniques provided reference values for the HAXPES-IBA technique briefly introduced in Chapter 1. Most of the techniques selected are in-line methods employed in metrology steps along the process flow of a wafer.

2.2.1 XRR

X-ray reflectivity (XRR) [7] is a non-destructive technique used to determine thin film structural parameters such as thickness, density and surface or interface roughness. The principle of this technique is based on the analysis of X-ray reflection intensity curves from a grazing incident monochromatic X-ray beam. The tool used in this thesis used a Cu Kα X-ray source. The X-ray reflects from the film surface and the interface forms interference fringes which gives information on the film thickness, roughness, and density. Figure 5 shows reflectivity profiles from HfO_2 films after 65 ALD cycles (top) and 20 ALD cycles (bottom). The critical angle is proportional to the electron density, while the number of fringes in the reflectometry profile is proportional to the thickness of the sample. The larger critical angle and denser interference fringes from the 65-cycle film indicate increased density and film thickness. Surface roughness is indicated by a lower reflectivity, while smearing or broadening in the fringes indicates interface roughness. The quantitative model to retrieve these parameters from an XRR spectrum can be complex and requires data fitting.

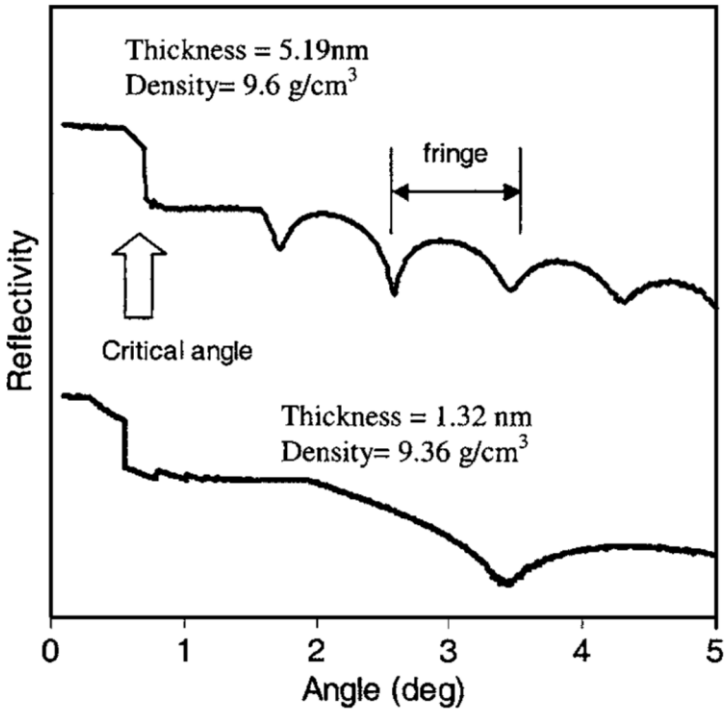

Figure 5. Sample XRR data for HfO_2 films produced by ALD after 65-cycles (top) and 20-cycles (bottom). The y scale is the reflectivity intensity in logarithmic scale and the x axis is the angle between the sample and X-ray. The critical angle and density of fringes indicate the density and thickness of the layer. Taken from [8].

The reflected intensity is collected as a function of reflected angle. The generated X-rays are reflected on a surface in a specular direction, i.e. the incident angle is equal to the reflected angle. In X-ray optics, the refractive index of a material is slightly less than 1. Total reflection occurs at, or below a critical angle (θ_c), which means that below this angle, the X-rays are fully reflected from the film and the incident X-rays do not penetrate. This angle varies depending on the electronic density of the material. When the incident angle (θ) is bigger than the critical angle, the incident X-rays penetrate the material and are both reflected and refracted.

In-line XRR does not require sample preparation. Integration of the measurement into the deposition set up minimizes exposure to a non-production grade environment. The measurement is fast, requiring only a few minutes and thus shortening the learning cycle. Itis a well-established technique, with studies dating back to the 90's having already illustrated the application of XRR in monitoring thin film growth [9–11] with thickness accuracy in the sub-nm atomic regime [11,12]. As stated above, data analysis requires modeling and curve fitting, which can be complex. A fast Fourrier transform (FFT) method delivers quick layer thickness estimations, while detailed analyses use a sample-model based fitting using dynamical scattering theory and requires input parameters for thickness, roughness, and density. Additionally, knowledge of the basic layer structure is necessary, as the technique does not distinguish between layer stacking order.

2.2.2 WDXRF

Wavelength dispersive X-ray fluorescence (WDXRF) [13] is one of two general types of X-ray fluorescence technique used for elemental analysis, the other being energy dispersive X-ray fluorescence spectroscopy (EDXRF). In WDXRF spectrometers, all of the elements in the sample are excited simultaneously. The different energies of the characteristic radiation emitted from the sample are diffracted into different directions by an analyzing crystal or monochromator. WDXRF systems are based on Bragg's law, which states that crystals will reflect x-rays of specific wavelengths and incident angles when the wavelengths of the scattered x-rays interfere constructively. With a fixed sample position, the angles of the crystal and detector are changed in compliance with Bragg's law so that a particular wavelength can be measured. Only x-rays that satisfy Bragg's law are reflected.

Sequential spectrometers have a moving detector on a goniometer that moves it through an angular range to measure the intensities of many different wavelengths, improving resolution and precision. The principle advantages of WDXRF systems are high resolution (typically 5 – 20 eV) and minimal spectral overlaps. Collimators further improve resolution by providing different angular divergences to restrict unwanted secondary x-rays from reaching the detector. Increasing the size of the collimators increases intensity but lowers resolution.

WDXRF instrumentation has been adapted for inline characterization of thin films. It is a complimentary technique often combined with other XRF methods like grazing incidence X-ray fluorescence spectroscopy (GIXRF) [14,15]. In addition to elemental composition, WDXRF analysis can provide information such as the mass deposition of the elements of interest per deposition cycle. WDXRF-XRR with dedicated mapping is used to control the quality of wafer deposition processes and ensure its conformity [15]. The established role WDXRF plays in metrology of thin films makes it an excellent reference technique for the method developed in our work.

2.2.3 LPD-ICPMS

Inductively Coupled Plasma Mass Spectrometry (ICP-MS) is a technique routinely used to analyze trace levels of a wide range of inorganic elements. The ICP-MS allows for the detection and quantification of elements with atomic mass ranges 7 to 250. This covers Lithium to Uranium. The typical detection limits are in the parts per billion (ppb) range and even parts per trillion (ppt) in some cases. Certified standards are available, allowing for direct quantification. In the experiment, argon plasma converts the sample into ions which are measured directly by mass spectrometry.

Coupling ICP-MS with liquid phase deposition (LPD) allows for the analysis of nanolaminates. LPD-ICPMS was developed for InP substrates and presented a CE higher than 85% for usual metallic contaminants except for Cu & noble metals, and very sensitive detection thresholds were reached (10^8

to 10^{11} at/cm²) [16]. This highly-quantitative technique provides accurate dose determinations which can be used to evaluate the nondestructive WDXRF method.

2.2.4 TOF-SIMS

Time of flight secondary ions mass spectroscopy (TOF-SIMS) [17] allows the obtention of elemental and molecular composition of a sample by analyzing secondary ions emitted upon bombardment with a primary ion beam. As a depth profiling technique, TOF-SIMS employs a secondary ion beam for sputtering the surface and the changes in chemical composition is tracked. Since secondary ions come from a single short primary ion pulse, free flight time through a drift tube can be directly measured. The mass spectrum is therefore an extrapolation of a secondary intensity ion diagram which is plotted as a function of time. The time of flight, t_{flight}, is proportional to the square root of the mass/charge of the secondary ion. This relationship, as well as the related parameters, is shown in Equation 2. This equation converts the spectrum to set the masses (m/z) in abscissa, delivering the traditional mass spectrum.

Equation 2

$$t_{flight} = L\sqrt{\frac{m/_z}{2e^{-}(E_0 + U)}}$$

Here, the flight chamber length (L), the acceleration potential (U) and the electron charge ($e-$) are known parameters, while E_0 corresponds to the initial energy of the ion before acceleration. The principle of the generation of secondary ions by primary ion bombardment and resulting mass spectra are shown in Figure 6.

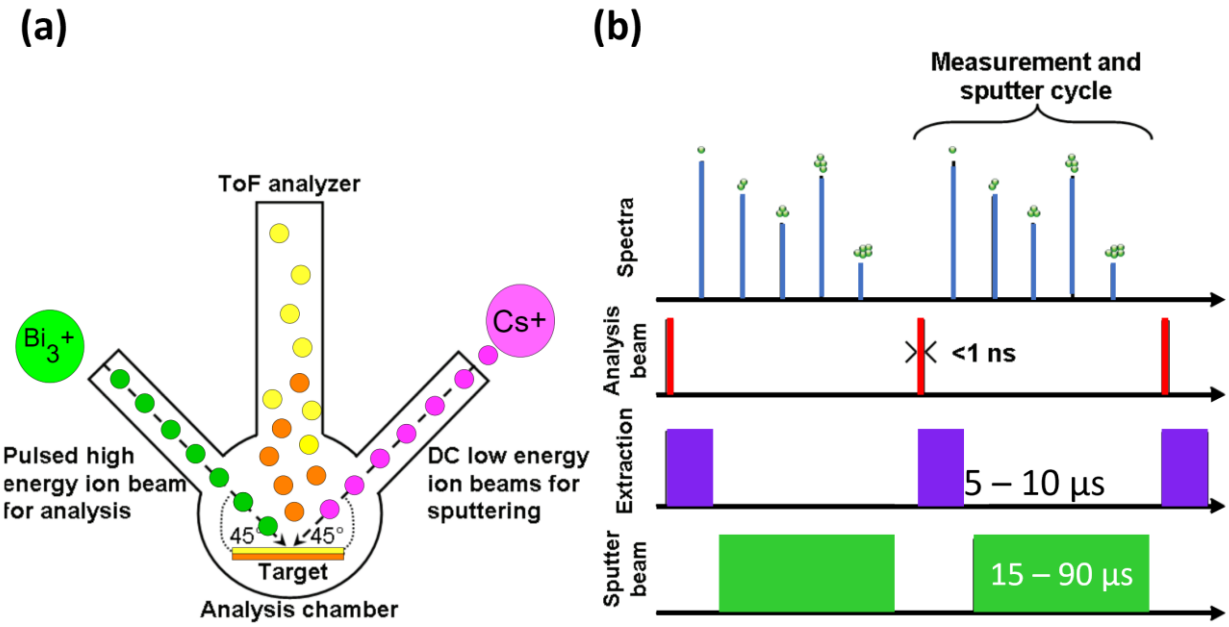

Figure 6. (a) On the left the pink ions are the sputtering ion beam, whereas the green are the analysis ion beam. (b) The right panel shows successive sequences of sputtering (green), extracting (purple) and analysis (red). The resulting spectrum (in black) is obtained.

The spot size is typically around a few μm^2. The energy of primary ion beam ranges from a few hundred eV to a few keV (typically 25 keV for analysis beam) and can be made of various ions, the most usual being Bi_n^+, Cs^+, O_2^+, Au^+ and C_{60}^+. The primary ion beam has a pulse of a few ns, allowing precise measurements of the time of fight of the ions. Reference samples of well-known elemental composition are needed for obtaining accurate quantification.

A TOF-SIMS method has been developed for determining quantitatively the overlayer thickness of Al_2O_3 in HEMT structures [18] similar to those found in our work.

2.3 Classical photoemission techniques

In this section, we discuss the theory and instrumentation used in classical XPS, specifically using Al Kα radiation.

2.3.1 Overview of X-ray photoelectron spectroscopy

X-ray photoemission spectroscopy (XPS) is favored for the breadth of information provided in a single acquisition which includes chemical and valence states, depth profiling, depth-resolved information at the nanometer scale, energy-level alignments at interfaces, and more [19]. XPS analyses require minimal to no sample preparation and can, given the proper equipment, be analyzed even in a dynamic state to reflect changes in chemical composition and electrical properties (*operando* XPS*)*.

In an XPS experiment, an X-ray beam impinges on the sample at some angle to the surface, exciting the core shell electron within the material. Should the radiation energy be great enough to overcome the electron's binding energy, the electron is liberated. The so-called photoelectron escapes though the material and into the vacuum, at the end of which it is analyzed. This is the photoelectric effect, a phenomena discovered by Hertz in 1887 [20].

We can see in Figure 7 a schematic of the electron shells in lead, where photoelectrons escaping from the irradiated material present a continuous signal. Each orbital creates discrete peaks of varied widths and intensities that characterize the sample. The continuous background formed by photoelectrons undergoing energy loss provides information on the location and distribution of elements [21].

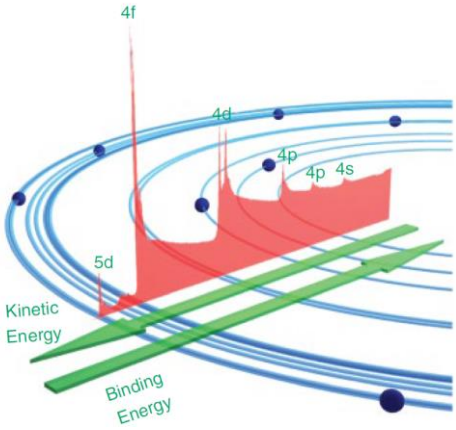

Figure 7. Figure: photoelectron spectrum of lead showing the region of the shallow core-level peaks. Each peak is discrete within its electron orbital (blue), and a continuous background is delineated by inelastic losses. [22]

2.3.2 The basis of X-ray photoelectron spectroscopy

In XPS, the data is represented as the intensity of the photoelectron signal versus the photoelectron binding energy E_B. From the knowledge of the excitation energy, hv, and work function of the sample ϕ_{sa}, the experiment permits the binding energy of the electron E_B, to be deduced from the measured photoelectron kinetic energy E_K. (Equation 3).

Equation 3

$$h\nu = E_K + E_B + \phi_{sa}$$

Where v is the photon's frequency and h is Plank's constant. The binding energies are referred to the Fermi level E_F, of the material. For solids, the two spectra meet at E_{Fermi} = 0. The value 0 is representative of the vacuum level for free atoms and molecules. E_B is measured because E_{Fermi} is

assumed to be the same as that of the spectrometer, E_{Fermi} = 0, (Figure 8) in case of perfect electrical contact between the sample and the spectrometer. However, the measured kinetic energy E_K' is dependent on the work function of the spectrometer ϕ_{sp}. Then, E_K can then be written as:

Equation 4

$$E_k = E_K' + (\phi_{sp} - \phi_{sa})$$

where ϕ_{sp} can be determined experimentally by measuring the value of the Fermi level on a reference sample such as clean silver. The electrical contact between sample and spectrometer can be insufficient for insulator samples, so holes stay at the sample surface and the entire XPS spectrum shifts towards higher binding energies. This can be overcome by providing electrons to the sample surface with a flood gun. Figure 8 illustrates the photoelectric phenomenon and Equation 4 and Equation 5.

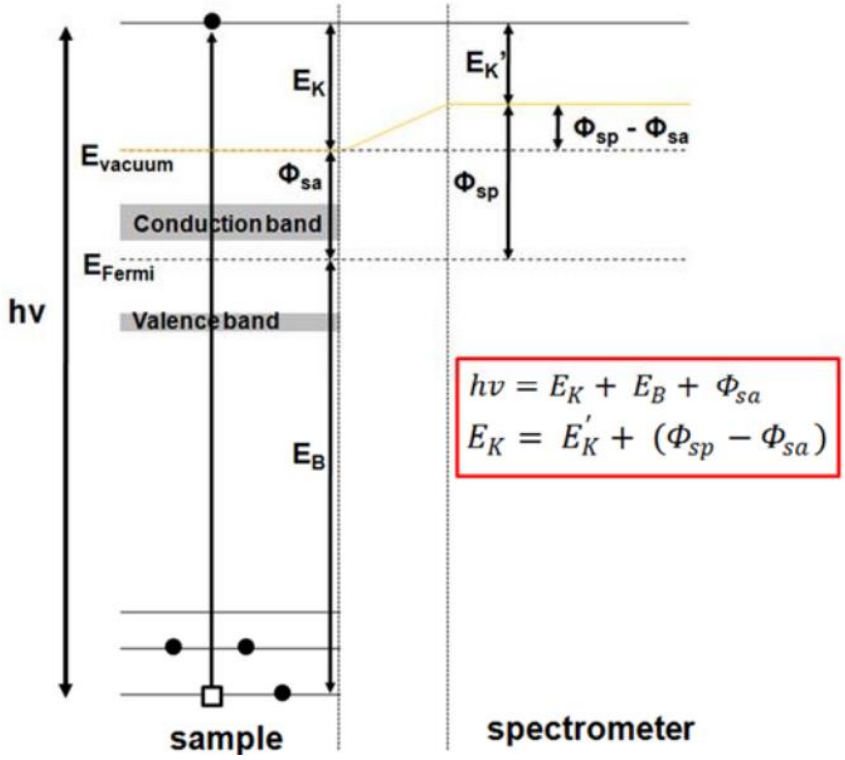

Figure 8. Illustration of the principles an XPS experiment with the relevant energy levels in the sample [23].

The method based on this principle was developed by Kai Siegbahn throughout the 1960's [24]. Each element (Figure 9) contains specific binding energies according to its electronic structure, and the resulting spectrum is unique. A compound material will give what is essentially a sum of the unique spectra for each element in the material. The relative peak areas are indicative of the elemental abundance, while the chemical state can be derived from the peak energy positions. A study of the

valence levels provides information about chemical binding and the density of states, as valence electrons will be delocalized amongst the elements.

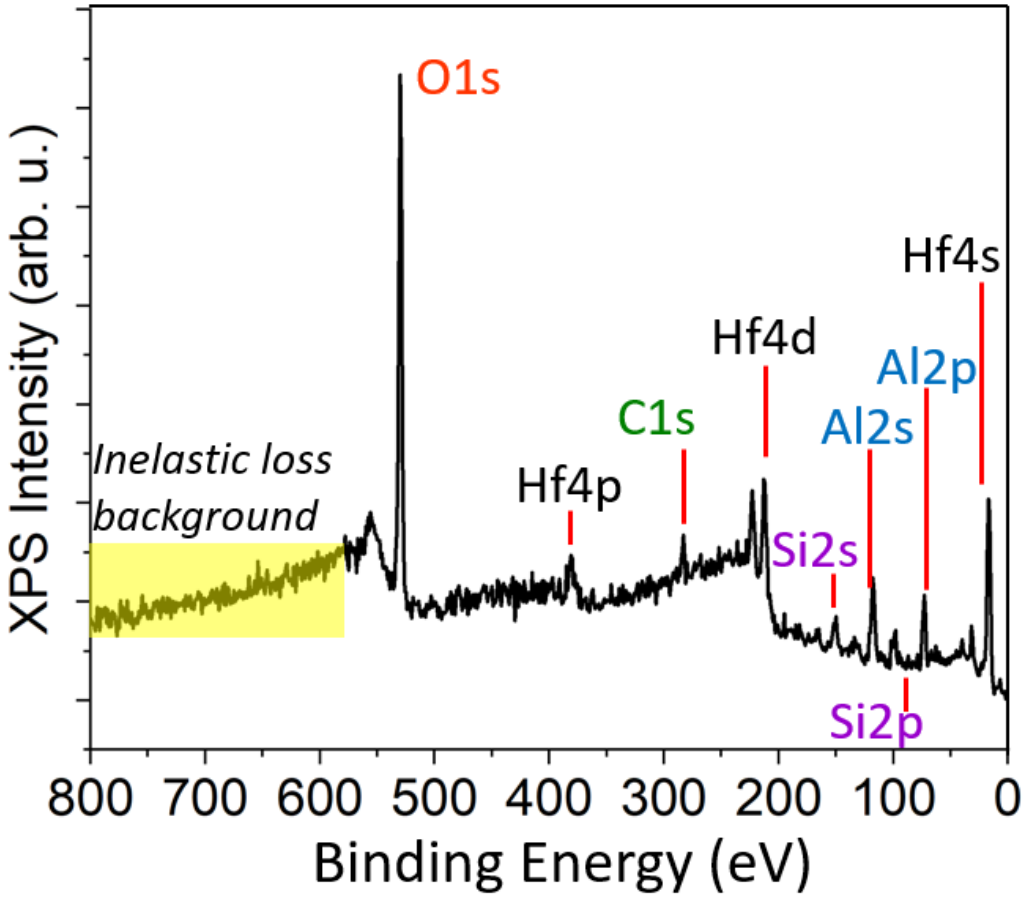

Figure 9. The XPS spectrum of a bilayer sample composed of 2 nm Al_2O_3 deposited over 1.5 nm of HfO_2.

2.3.3 The three step model

One of several ways to describe the photoemission process is through a three step model. It considers the events in terms of excitations and energy loss: photoexcitation of the photoelectron, intrinsic excitations arising from the sudden creation of the core-hole, and extrinsic excitations occurring due to photoelectron transport through the medium, out of the surface, and into the vacuum. These factors can be completely decoupled when explaining the process in a phenomenological way. The events are regrouped into three independent processes. The three step model, described by Berglund and Spicer in 1964 [25], is as follows:

(1) Photoexcitation of core electrons

In the inciting event, photon absorption by the occupied electronic state prompts the expulsion of a photoelectron. The probability of the excitation event is specific to the electronic state at the atomic subshell nl and incident beam energy and is called the photoionization cross-section σ [26].

(2) Transport to the surface

As the photoelectron travels through the material, inelastic scattering events dampen the electron intensity, and the corresponding signal forms the inelastic background of the XPS spectrum. The elastic peak is comprised of unscattered phtotoelectrons and its attenuation with increasing depths is quantified with the inelastic mean free path (IMFP) λ, defined as the average distance that an electron with a given energy travels between successive inelastic collisions [27]. This step is at the heart of the inelastic background method considered in this work.

(3) Photoelectron emission and analysis

The photoelectron has reached the surface and will leave the crystal. Before escaping, it has to pass through the surface potential barrier, described by the work function. Excitations in this step are especially complex and do not contribute significantly to the peak intensity. Just beneath the surface, σ decreases and the probability of surface excitations increases. Additionally, the probability of interactions with valence electrons in the surface region must be accounted for. Band bending may occur, in which surface atoms are ionized and a compensating space charge appears [28]. Surface photovoltage occurs when irradiation of the sample increases the surface potential. The electric field generated will bring diffusion into the bulk in the case of majority carriers the inverse for minority carriers which will be trapped on the surface [29].The three step model is presented in Figure 10.

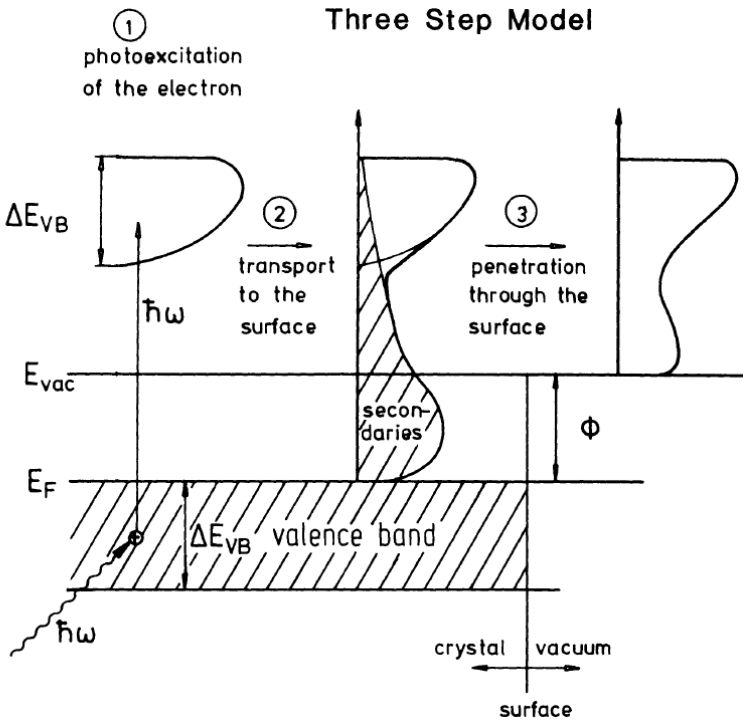

Figure 10. Photoemission can be explained in three steps: (1) photoexcitation of electrons; (2) travel through the bulk with accompanying secondary losses (shaded); (3) passage through the surface barrier and escape into the vacuum. Taken from [19].

This thesis is concerned with the second step, and the background signal which arises from the inelastic losses experienced by the photoelectron. The intensity of the inelastic background following the elastic loss peak (see Figure 9) can provide information on deeply buried layers which cannot be probed through traditional peak analysis.

2.3.4 Photoionization cross section

As stated above, the photoionization cross section is the probability for an electron in an atomic subshell *nl* to be excited to an energy level in the continuum by absorption of the photon energy. The value is atom-dependent and also changes with the considered electronic energy level. In XPS experiments, it is evaluated within the electrical dipole approximation. The dipolar approximation simplifies the formalism for describing the transition probability in photoemission by neglecting the spatial variations of the vector potential of the photon yield over the characteristic length of the electron states. However, non-dipolar contributions to the angular distribution become significant for photon energies higher than a few keV (HAXPES energies) [30].

In the case of an unpolarized photoelectron source (such as Cr K_α or Al K_α sources used in this work), the subshell differential photoionization cross section can be approximated for the solid angle Ω, and the atomic subshell nl by Equation 5.

Equation 5

$$\frac{d\sigma_{nl}}{d\Omega} = \frac{\sigma_{nl}}{4\pi}\left(1 - \frac{\beta_{nl}}{2}(3\cos^2\alpha - 1)\right)$$

β_{nl} is the energy dependent asymmetry parameter of the atomic subshell nl while α is the angle between the propagation directions of photons and photoelectrons. The photoionization cross-section decreases with increasing photon energy [31,32].

2.3.5 The inelastic scattering cross section

Electron-electron scattering is the dominating mechanism hindering electron transport through the bulk. The effects of these extrinsic excitations are described by the differential inelastic electron scattering cross-section $K(E_0, T)dRdT$ which is the probability that an electron of energy E_0 will lose energy in the interval $T, T - T + dT$ after having traveled a path length dR in the solid. The equation is as follows:

Equation 6

$$K(E_0, \hbar\omega) = \frac{1}{\pi a_0 E_0}\int \frac{dk}{k} lm\left\{\frac{1}{\epsilon(k, \hbar\omega)}\right\}$$

Energy, $\hbar\omega = T$, and E_0 is the initial energy of the electron, $a_0$is the Bohr radius, and k is the wave vector transferred from the electron. We will provide more details on the inelastic scattering cross-section later in Chapter 3.

2.4 Interpretation of XPS core-level spectra

High resolution XPS (ΔE < 0.5 eV) allows close inspection of the core level peak. As stated in the introduction, the shape, intensity, and energy position of the peak carry much information to non-destructive surface characterization.

2.4.1 Line shape analysis

While other descriptions exist, the total lineshape of a core level spectrum is commonly modeled by the Voigt function, or a Lorentzian convoluted with a Gaussian. The Lorentzian part is defined by the FWHM width and the lifetime of the core ionized state, which ends with the core hole being filled by another electron. The Gaussian part considers experimental broadening due to the limited photon

energy and spectrometer resolutions, or monochromaticity of the photons. In Figure 11 are shown several XPS spectra of the Al 2p transition in aluminum. The Al $2p_{1/2}$ and Al $2p_{3/2}$ transitions are very close, with a spin orbit splitting of only 0.42 eV. The bottom most spectrum is representative of a pure aluminum metal. Here, we see an asymmetry with broadening towards a higher binding energy. Electron-hole pairs in the vicinity of the Fermi level are excited, causing inelastic collisions with the photoelectron, and contributing to the background. The asymmetric contributions can be modelled with Doniach-Sunjic functions [19],[33].

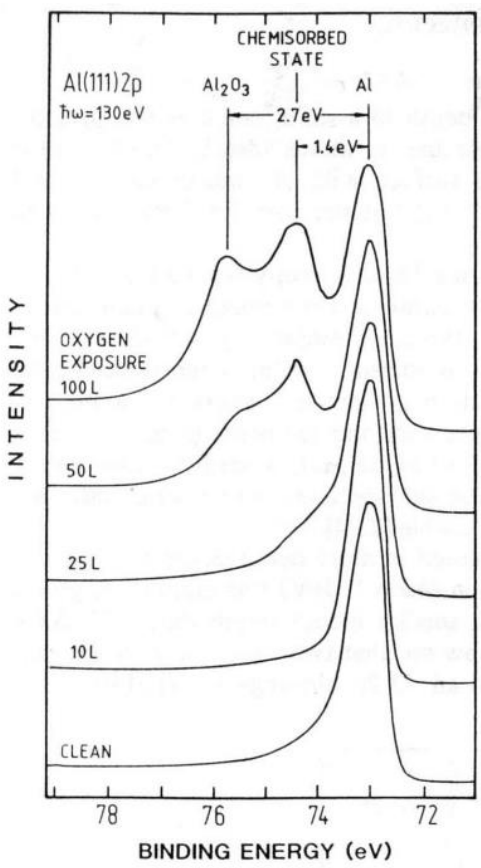

*Figure 11. Al2p1/2-3/2 Core level XPS spectra of Aluminum (111). Oxygen exposure (measured in Langmuir, 1L = 10^{-6} mbar*s) reacts at the surface, causing chemical shifts to a higher binding energy. From [19].*

2.4.2 Chemical Shift

The energy position of the core level photoemission peak provides information on chemical states in the material. The energy of the peak is characteristic of the elemental core level, but is also influenced by chemical bonding with other elements. Bonding to an atom with greater electronegativity will leach valence electrons to the other atom, forcing the remaining electrons to tighten and thus decreasing the kinetic energy of the ejected photoelectrons from the primary atom (increasing binding energy).

The inverse is true in which valence electrons are transferred from the bonded atom to the more-electronegative primary atom. This chemical shift, or $\Delta\varepsilon$ [19],[34] can be expressed as:

Equation 7

$$\Delta\varepsilon = Ce + qV$$

where C is a constant, e is the charge of the atom, and V is the potential of neighboring atoms. The chemical shifts of common compounds are catalogued in the NIST X-ray database [35].

Figure 11 demonstrates chemical shifts of the Al 2p core peak as the sample is flushed with increasing amounts of oxygen. The energy loss shift is due to chemisorbed oxygen binding. The metallic peak is seen at E_B = 73 eV. As more oxygen is added, weak spectral features take form at greater binding energies. The first signature to appear, after 50 L oxygen, can be attributed to Al surface atoms which have chemisorbed oxygen. At E_B = 74.4 eV, it has shifted 1.4 eV from the metal peak. After 100 L of oxygen exposure, the third peak appears at E_B = 75.7 eV. This peak can be attributed to Al surface atoms bonded within an Al_2O_3 environment. Thus, the chemical shift of the Al 2p core level by 2.7 eV indicates the oxidation of metallic aluminum to alumina [19].

2.5 Photoelectron transport

Photoelectron transport and the production of a photoelectric peak at the characteristic binding energy is governed by inelastic scattering events. The inelastic losses will deliver a signal at a higher binding energy in the spectrum, thus forming the inelastic background.

2.5.1 Inelastic scattering events

The likelihood of inelastic scattering events increases with the distance the photoelectron is traveling through the medium. This phenomenon is described by λ the inelastic mean free path (IMFP) of an electron. As previously mentioned, the IMFP is defined in ISO 18115 to be the average distance that an electron with a given energy travels between successive inelastic collisions in a material [27].

The IMFP λ, is determined by electron-electron and electron-photon collisions. While other methods of determining the IMFP exist, Tanuma, Penn and Powell provide a straightforward formula for predicting λ [36–38]:

Equation 8

$$\lambda = \frac{E}{E_p^2[\beta \ln(\gamma E) - (C/E) + (D/E^2)]}$$

with

Equation 9

$$\beta = -0.10 + 0.944\left(E_p^2 + E_g^2\right)^{-\frac{1}{2}} + 0.069\rho^{0.1}$$

Equation 10

$$\gamma = 0.191\rho^{-\frac{1}{2}}$$

Equation 11

$$C = 1.97 - 0.91U$$

Equation 12

$$D = 53.4 - 20.8U$$

Equation 13

$$U = N_v\rho/M = E_p^2/829.4$$

where

Equation 14

$$E = 28.8\left(\frac{N_v\rho}{M}\right)^{1/2}$$

E is the free electron plasmon energy (in eV), N_v is the number of valence electrons per atom or molecule, ρ is the density (in g.cm^{-3}), M is the atomic or molecular weight and E_g is the bandgap energy (in eV). This calculation is applied in the QUASES-IMFP software [39], or by accessing the NIST Electron Inelastic-Mean-Free-Path Database [35].

The IMFP of different materials displays a similar curve shape along increasing energy. The position of the curve along the energy axis, however, depends on the electronic structure of the material. This effect is shown in Figure 12.

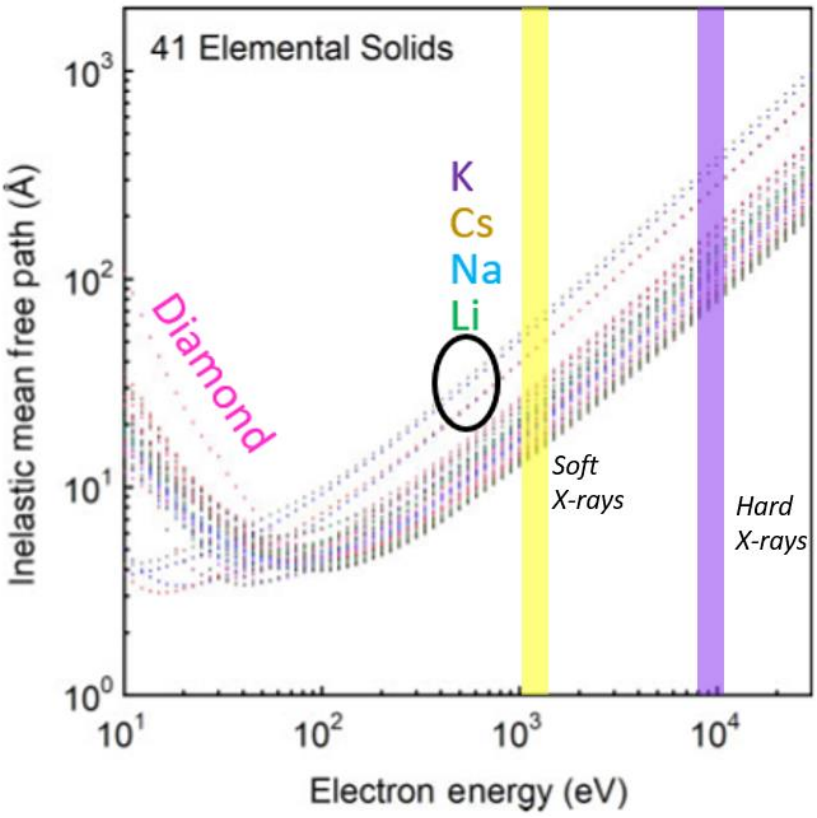

Figure 12. IMFP values for 41 elements: Li, Be, three forms of carbon (graphite, diamond, glassy C), Na, Mg, Al, Si, K, Sc, Ti, V, Cr, Fe, Co, Ne, Cu, Ge, Y, Nb, Mo, Ru, Rh, Pd, Ag, In, Sn, Cs, Gd, Tb, Dy, Hf, Ta, W, Re, Os, Ir, Pt, Au, and Bi. The alkali metals and diamond demonstrate the influence of the electronic structure characteristics. From [40].

The IMFP increases with the kinetic energy of the photoelectron, therefore low KE photoelectrons are representative of the surface and high KE of the bulk. This also means that increasing the energy of the source will increase the IMFP. In soft XPS (Al Kα hv = 1486.7 eV et Mg Kα hv = 1254.6 eV) sources, the IMFP is of the order of several Angstroms.

The maximum probing depth of an XPS experiment when $\theta = 0$ is 3λ. Given that this value is around 3 nm for many core peaks used for analysis with soft X-ray sources, contamination of the surface is a serious concern. Using Cr Kα (hv = 5414.7) and Ga Kα (hv = 9251.7 eV) sources, Hard X-ray photoelectron spectroscopy (HAXPES) increases the IMFP to several tens of nanometers. This opens up non-destructive characterization by XPS to increasingly thick and complex samples.

2.5.2 Photoemission peak intensity

Monte-Carlo simulations [41] show that the intensity of elastically scattered photoelectrons (contributing to the core-level peak) follow an exponential decay law [42]. The intensity of the core-level peak as a function of depth can be expressed as a Beer-Lambert law [43]:

Equation 15

$$I(d) = I_0 e^{-\frac{d}{\lambda sin\theta}}$$

where I_0 is the intensity from an infinitely thick layer, d is the probing depth, λ is the IMFP, and θ the detection angle from the surface. This relationship is skteched in Figure 13, where exponential decay in the peak intensity is shown for three layers of thickness $\lambda sin\theta$ at increasing depths.

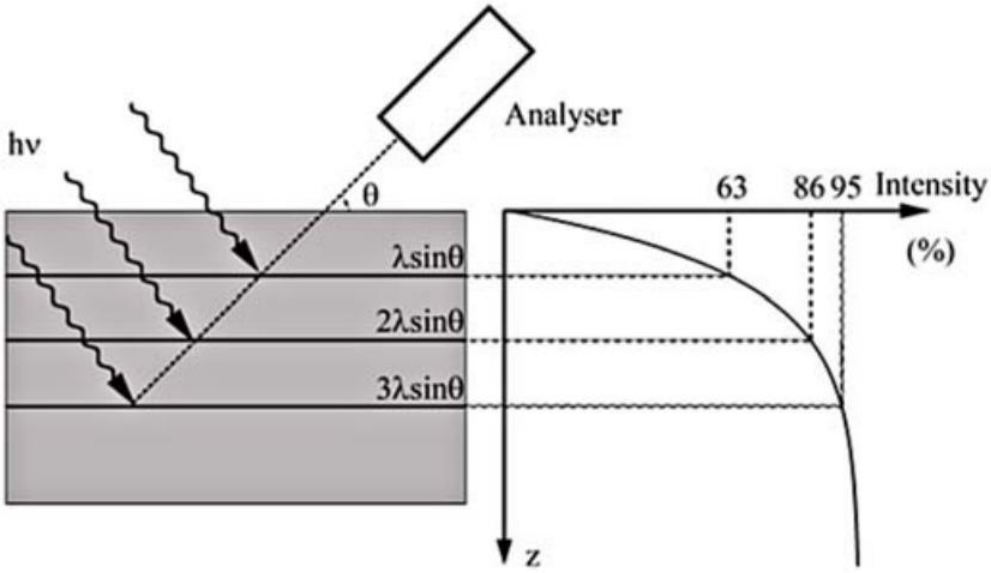

Figure 13. The relative intensity contribution from layers at increasing depths. [19]

From Figure 13 and Equation 15 we can predict how manipulating the angle of detection might deliver information on the depth distribution of elements in a multilayer sample. This angular dependence is applied in Angle Resolved X-ray Photoelectron Spectroscopy (ARXPS) and will be discussed further in Section 2.6.3 of this chapter.

2.5.3 Elastic scattering effect

Photoelectrons may also scatter elastically, meaning the energy loss to the sample is less than the experimental resolution limit. Elastic collisions change the direction of the photoelectrons, thereby modifying the photoionization cross-section as:

Equation 16

$$\frac{d\sigma_{nl}}{d\Omega} = \frac{\sigma_{nl}}{4\pi} Q_{nl} \left(1 - \frac{B_{eff}}{4}(3\cos^2\alpha - 1)\right)$$

Where Q_{nl} is the parameter describing the decrease of intensity due to elastic scattering and B_{eff} is the effective asymmetry parameter describing the decrease of anisotropy due to elastic scattering to correct Equation 5 for these elastic losses.

2.5.4 Effective attenuation length

To take into account the elastic scattering effect, the effective attenuation length (EAL) may be introduced into XPS and AES equations in the place of the IMFP [27]. The EAL describes the rate at which the XPS signal intensities from a substrate material or an overlayer film change as a function of the film thickness. It takes into account, unlike the I:FP, elastic scattering effects. It can be expressed as [44]:

Equation 17

$$EAL = \lambda(1 - 0.735\omega)$$

2.5.5 Effect of elastic scattering on the measured spectrum

In cases where angular deflection by electron scattering modifies the XPS spectra intensity to a significant degree, a correction factor $CFA(z, \theta)$ [45] can be applied in the intensity equation:

Equation 18

$$I(z) = C \times e^{\frac{-z}{\lambda cos\theta}} \times CF(z, \theta)$$

where C is a constant, z the depth, and θ is the angle of emission with respect to the surface normal.

$CF(z, \theta)$ can provide a small correction to the TPP-2M IMFP value, between, 0.9 and 1.1, but it can be substantial for depths $z > 2\lambda$. The effect increases with greater take off angles ($\theta > 35°$). In homogenous materials, $CF \sim 1$. For $\theta > 30°$, $CF(z, \theta)$ is expressed as [46]:

Equation 19

$$CF(z) = \exp(-0.157764\tau - 1.25132) + \exp(-0.0562417\tau^2 + 0.00698849\tau - 0.201962)$$

With

Equation 20

$$\tau = \frac{z(\lambda + \lambda_{tr})}{\lambda\lambda_{tr}}$$

2.5.6 Intrinsic and extrinsic losses

Energy loss in the photoemission process can be categorized into two types: **intrinsic** losses resulting from interactions with the core hole, and **extrinsic** losses experienced in photoelectron transport through the medium and into the vacuum. These mechanisms seldom act independently, as **interferences** frequently occur amongst the intrinsic and extrinsic loss events. All of these events decrease the photoelectron energy, and contribute to the continuous inelastic background.

Intrinsic excitations

A simplistic execution of the photoelectric effect sees the atom ionized in the ground state, and with no interaction with its electronic environment. Intrinsic excitations, however, may occur as a result of the creation of the core-hole and the potential between it and the photoelectron. These may result in plasmons (quasi-particles), or Duniach-Sunjic lineshapes (discussed in section 2.4.1.) Valence band electrons excited in a "shake-up" process are promoted to a higher orbital in the valence band, producing a well-defined satellite peak a few eV over from the main line at higher binding energy [47]. If the valence electron draws sufficient energy to pass into the conduction band in a "shake-off" effect, the resulting energy loss in the photoelectron will contribute to the inelastic background following the main peak. In the quantification of XPS spectra, it was found that the relative contribution from intrinsic excitations is roughly equivalent in all ofthe photoelectron peaks in a given sample and therefore can be canceled out when comparing peak area ratios [48].

Extrinsic contributions

As the photoelectron travels through the bulk, it creates an electric field which excites its environment. The collective excitations of electrons are referred to as plasmons, and their interactions are the main extrinsic losses experienced by the photoelectron during transport. The plasmon energy s dependent on the energy of the photoelectron and the density of free electrons. The plasmon resonances are of several amplitudes, and their intensity is positively correlated to the photoelectron's energy. The plasmons may originate in the bulk or at the surface, and their characteristic energy is of 10-20 eV. Plasmon features in the spectrum are separated by a quantized energy, as they are harmonics of a resonance mode.

2.5.7 Correlated Effects

The core hole left by photoemission may be filled with an electron from an outer energy level, producing an Auger electron or a photon. In the Auger process, an electron is double charged and ejected. The kinetic energy of the Auger electron is the energy difference between the initial ion and the double charged ion. This means that when changing the X-ray energy, an Auger emission peak will have a constant kinetic energy value, while the photoelectron will have a constant binding energy [22].

Auger electron spectroscopy (AES) uses the shape and energy of Auger features to acquire quantitative elemental and chemical state information in solid surfaces [49]. Figure 14 visualizes the different emission processes occurring after x-ray excitation of a surface.

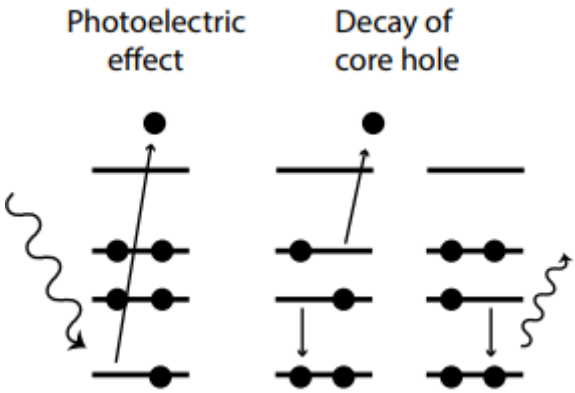

Figure 14. The photoelectric effect producing photoemission and Auger emission process. The creation of a photoelectron and core-hole (left), the Auger emission process resulting from the ejection of the photoelectron (center), and a photon (right).

2.6 XPS instrumental aspects

Kai Siegbahn received the Nobel Prize in 1981 for the development of the actual method named Electrons Spectroscopy for Chemical Analysis (ESCA) [24], nowadays currently named PES (Photoelectron spectroscopy) or XPS.

2.6.1 XPS X-ray laboratory sources

A current passes through a tungsten wire which is heated by it and emits electrons by thermo-ionization. These electrons are accelerated by a potential (~ 10-20 keV) to a metallic anode. Generally, the anode is made of aluminum or magnesium-covered bulk copper and these present a better photoemission intensity compared to the first source used by K. Siegbahn which was copper. Then high energy electrons are emitted from deep core-levels and when these are filled by outer electrons, the energy released is emitted as X-rays with an energy which is particular to the metal of the target. Aluminum and Magnesium emit Kα1 rays at 1486.6 eV and 1253.6 eV, respectively. A metallic foil separates the X-ray chamber from the analysis chamber, it permits to absorb the secondary and diffused electrons and ensure a protective separation of the different vacuum chambers. Al Kα X-ray sources are may also be fitted with a monochromator which allows to select the Kα1 radiation based on Bragg diffraction of photons and eliminates rays coming from contaminations on the electrode..

2.6.2 Electron energy analyzer

Most modern XPS instruments employ an electrostatic hemispherical analyzer (HSA). In this system, the photoelectrons are retarded at the entrance with electrostatic lenses, then selected in energy inside two half spheres (Figure 15). The spheres (generally out of graphite) have radii of R1 and R2, and

are covered with gold. Potentials –V1 and –V2 are applied to the external and internal sphere, respectively, thereby yielding an electric field which separates the electron trajectories depending on their kinetic energy at the entrance compared to the analyzer pass energy, E_p.

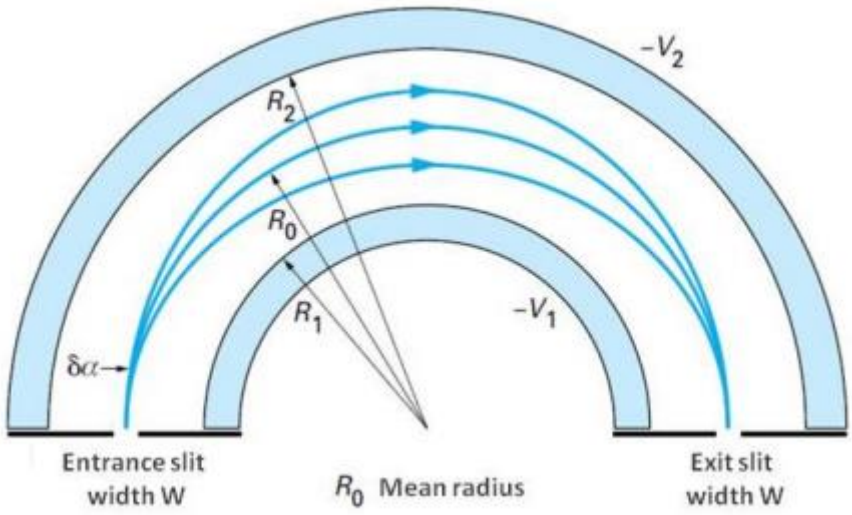

Figure 15. 180° hemispherical analyzer description of an ESCA instrument, from ref [23].

The energy window for passage through the hemispherical electrodes is selected for by electrostatic lenses at the entrance of the analyzer. This allows the experiment to scan over all possible ranges, and provide the number of electrons hitting the detector at each particular energy. The resolution of the spectrometer ΔE is determined by the pass energy, entrance slit width S, and radius of the analyzer R_0. This relationship is shown in Equation 21.

Equation 21

$$\Delta E = E_p \frac{S}{2R_0}$$

The detector is typically a system with a multichannel plate or channel photomultiplier coupled to a Charge Couple Device (CCD) camera. The multichannel plate amplifies the signal of photoelectrons along glass capillaries. Then, they are localized by resistive anodes over a phosphorescent screen. Here,

they emit light detectable by the CDD camera. This configuration achieves high speed recording and very high spatial resolution.

2.6.3 ARXPS

In Angle Resolved X-ray Photoelectron Spectroscopy (ARXPS) [19] the Beer-Lambert equation is manipulated to exploit the angular dependence of the peak intensity on the in-depth concentration profile. Increasing the photoelectron emission angle θ makes the analysis more surface sensitive.

Equation 22

$$I(d) = I_0 e^{-\frac{d}{\lambda sin\theta}}$$

In the equation, I is the intensity of electrons, I_0 is the intensity from an infinitely thick, uniform substrate, and d is the depth of the originating atom. Figure 16 illustrates the ARXPS principle: the sample consists of a top overlayer on a substrate with a broad interface between them. If photoelectrons are collected at low take-off angle (TOA) (in red), the measured spectrum is representative of the surface overlayer. If the TOA increases (in blue), the experiment becomes more bulk sensitive and the measured spectrum is representative of the overlayer, the substrate and the interface. With measurements at various angles, the depth profile can be reconstructed. It must be kept in mind that, depending on the analyzer acceptance angle, the signal may integrate a more or less wide range of angle (and therefore, depth) values about the nominal take-off angle.

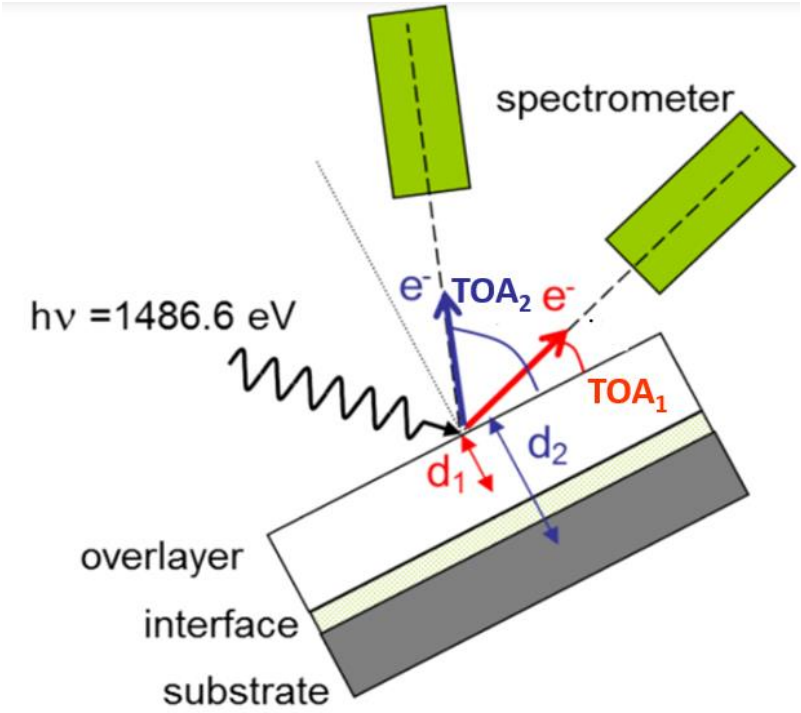

Figure 16. Scheme of the principle of ARXPS.

The experiment can tilt the sample and fix the analyzer, or, with Parallel Acquisition ARXPS (p-ARXPS) [50], it can fix the sample and choose the angle from which the analyzer accepts the signal. This is achieved using an angle resolving lens at the analyzer exit and a 2-dimensional detector.

The method achieves excellent absolute depth resolution. Without prior information on the sample, however, atomic resolution cannot be achieved. ARXPS works well for thin layers with very flat surfaces like SiO_2 on Si. Shadowing effects, however, complicate the analysis in cases with rough surfaces or nano-structures, requiring a modeling procedure [51]. Since core-level excitations contribute to the no-loss peak, the max probed depth is 3λ [52]. Replicate layers within the stack confuse the analysis, as a clear distinction between the layers is hardly possible. ARXPS is also a slow, sequential analysis, taking several hours to complete. Given known thicknesses, the method can determine the effective attenuation length of a material.

The key point is that a variety of surface morphologies can present the same intensity of the photoelectron core level peak corresponding to elastically scattered photoelectrons [46]. So the study of the intensity variation of the different stacks can not give exploitable results.

2.7 Laboratory HAXPES

A hard X-ray source was used in the first XPS experiments by K. Siegbahn et al. in the 1960's [24]. The Mo $K\alpha_1$ and Mo $K\alpha_2$ (1745 eV and 1737 eV, respectively) and later Cu $K\alpha$ and Cu $K\beta$ (8040 eV). These X-ray sources produced a low photoemission intensity, and were quickly abandoned. Softer X-rays (such as Al $K\alpha$ or Mg Kα) remained the principle sources for lab-based XPS from the 1970's until now, while synchrotron facilities eventually developed Hard X-ray Photoelectron Spectroscopy (HAXPES) beamlines with improved energy resolution and signal intensity. In 2003, the ESRF in Grenoble, France held the "1st International Workshop on HAXPES," bringing high-resolution HAXPES to the forefront of non-destructive depth-sensitive materials characterization.

The principle drawback of HAXPES is the rapid decrease in the photoionization cross-section σ due to high energy excitation [31,32,53]. High-energy and high-brilliance undulator X-rays in third generation synchrotron radiation facilities like the Spring-8 and ESRF helped circumvent this limitation, but left users with narrow timeframes for experiments and potentially long wait-lists to access the beamlines. Lab-based HAXPES is quickly being adopted in research centers across the globe, paving the way for routine analyses of burgeoning device technologies and methodologies, as well as a potential for integration into process fabrication for in-line control metrology.

2.7.1 Photoionization in HAXPES

The lab-based HAXPES experiments in this work were performed with two X-ray sources, Cr Kα (hv = 5414.72 eV), and Ga Kα (hv = 9251.74 eV). The primary method used to measure all samples employed Cr $K\alpha$radiation with the Quantes dual X-ray microprobe from Physical Electronics at the Platform for Nanocharacterization (PFNC) at the Minatech campus of CEA-LETI. HAXPES with Cr Kα radiation delivers a photon energy which is low enough to retain photoionization cross-section values while accessing several times further into the material than traditional XPS. Additional experiments were performed with the help of the Interuniversity Microelectronics Centre (IMEC) in Leuvan, Belgium on the Scienta Omicron HAXPES Lab system with a Ga Kα source located at Hasselt University.

The photoelectron spectrum obtained by hard X-rays also contains additional spectroscopic information not available with general XPS. Photoelectrons from deeper core levels can be excited by hard X-rays compared to soft X-rays, extending the spectrum to much higher binding energies. These high energy transitions possess greater photoionization cross-sections and may be measured in the place of core-level peaks for which the cross-section has diminished. Cross-sections for several elements studied in this work can be seen in Figure 17. The energy of Cr $K\alpha$ radiation is in proximity to core transitions whose photoionization cross-sections are comparable or superior to those at the Al $K\alpha$ radiation line. The energy of the Ga $K\alpha$ HAXPES experiment also provided acceptable cross-sections.

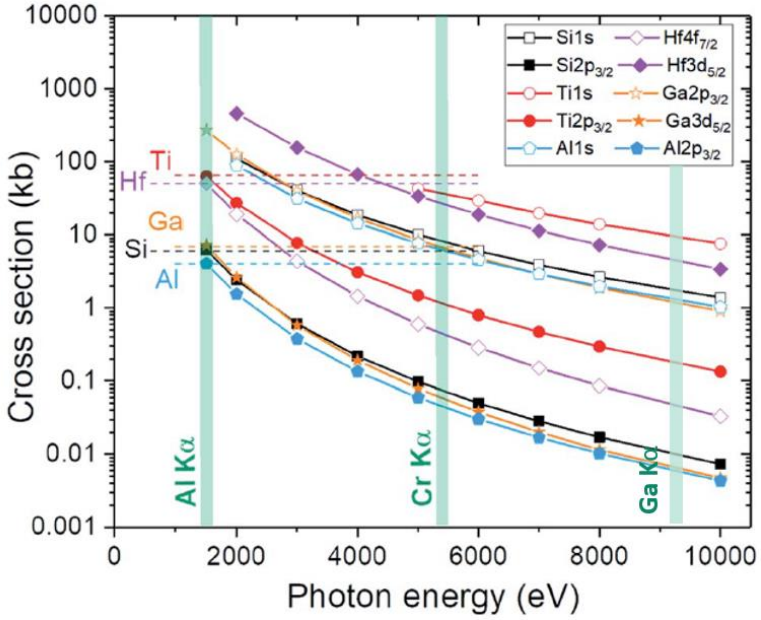

Figure 17. Photoionization cross-sections for the elements, Al, Si, Ti, Ga, and Hf for photon energies from 1.4 to 10 keV. Access to higher energy transitions with HAXPES radiation delivers comparable cross-section values to those used in traditional XPS. Taken from [54] which uses the tables of [31,32].

An added benefit of changing the energy of the source moves the photoelectron peaks in relation to the Auger electrons, which are associated with the kinetic energy of the transition, and with HAXPES will thus appear in a lower kinetic energy region of the spectrum far from the binding energy region of principle peaks of analysis for soft X-ray XPS. An example shown in the survey spectra in Figure 18, which were obtained from a stainless steel sample with Al Kα X-rays and Cr Kα X-rays. The O KLL and Fe LMM Auger transitions are shifted away from the Fe 2p spectral region of interest for studying these materials, allowing the reliable analysis of Fe 2p and Fe 2s peaks.

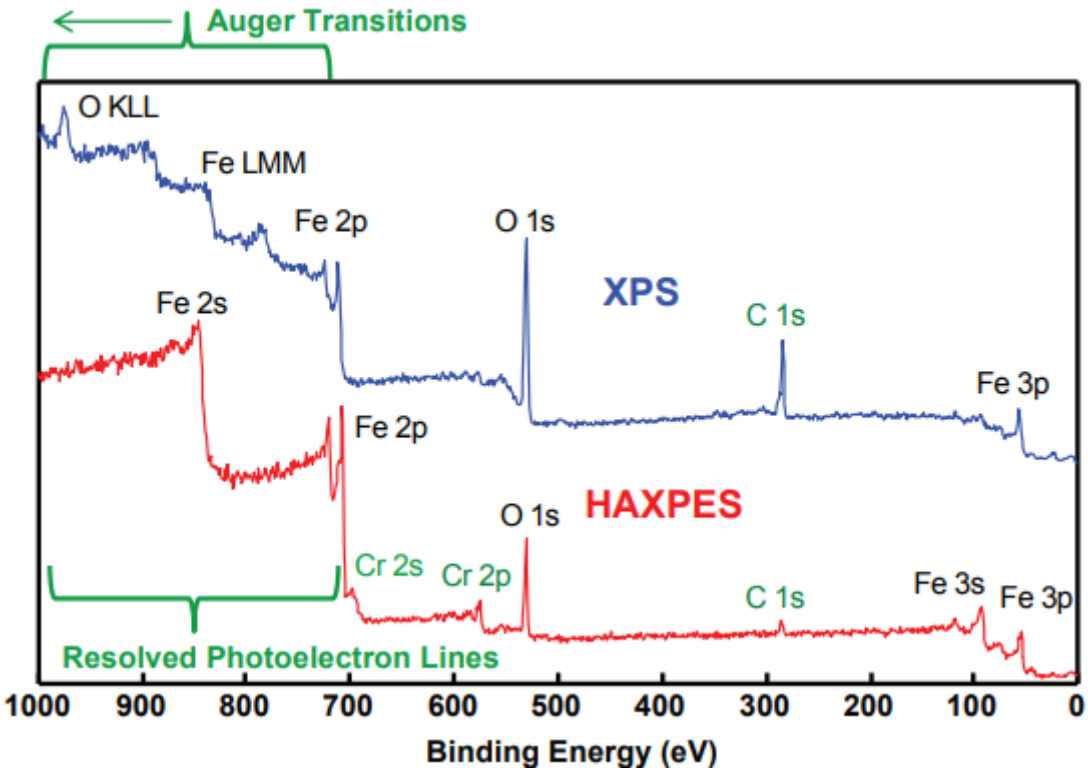

Figure 18. In the survey spectrum obtained from a stainless-steel sample with Al X-rays (blue trace), the Fe and O Auger transitions overlap with photoelectron lines. Using the Cr X-ray source (red trace) the Auger peaks are shifted, and the photoelectron lines can be resolved. Of note: Because of the larger analysis volume of HAXPES, the C 1s peak is much smaller in the HAXPES spectrum, compared to the XPS spectrum. (source PHI Electronics)

2.7.2 Quantes system

The PHI Quantes system used in this work is equipped with a dual scanning X-ray source composed of a hard X-ray source (Cr Kα) and a conventional soft X-ray source (Al Kα), both micro-focused. This state-of-the-art XPS instrument can therefore analyze the very small areas where the user is interested in as well as a large area of the uniform sample surface. The two different types of X-ray sources can be switched automatically, allowing users to analyze the same area and/or points of a sample. A schematic diagram of the instrument design is shown in Figure 19. The automated dual anode switches between the Al Kα and Cr Kα sources. An LaB_6 electron source is used for thermal emission to achieve a high signal-to-noise ratio and higher resolution. The X-ray spots are tunable from sub-7.5 µm to 200

µm for Al Kα and from 7 µm to 100 µm for Cr Kαwith the spatial coincidence of both spots within 7 µm. The angle between the Cr source and the analyzer is 46.05, while for the Al source this angle is 45. The best overall energy resolutions available from this instrument are 0.55 eV and 0.77 eV with Al $K\alpha$ and Cr $K\alpha$ excitation, respectively. Detection efficiency is maximized and the X-ray dose for analysis is minimized with a proven high voltage analyzer and high transmission input lens. The high voltage proof 32-channel multi-channel detector allows snapshot acquisition up to 128 channels in interlaced mode.

Both X-ray sources are aligned to the same focal point of the electron energy analyzer, enabling same area analysis using either XPS or HAXPES, thus providing chemical information from small or large areas at different sample depths.

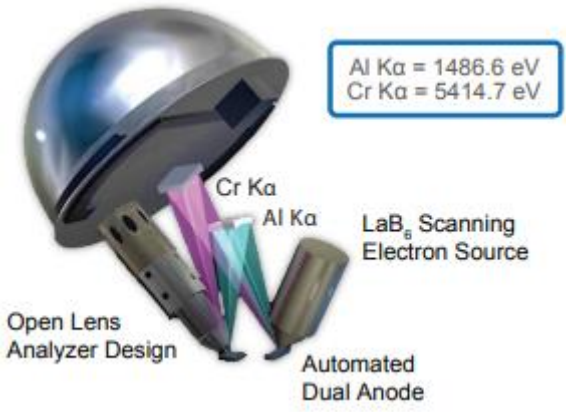

Figure 19. A schematic diagram of the dual scanning X-ray. (Figure by PHI Electronics)

PHI's patented turnkey charge neutralization allows automatic charge compensation of the charged sample surface. In this configuration (Figure 20) a low-energy electron beam and an ion beam irradiate the sample simultaneously. Several Cr $K\alpha$ HAXPES reference spectra of elemental solids and compounds obtained from the Quantes

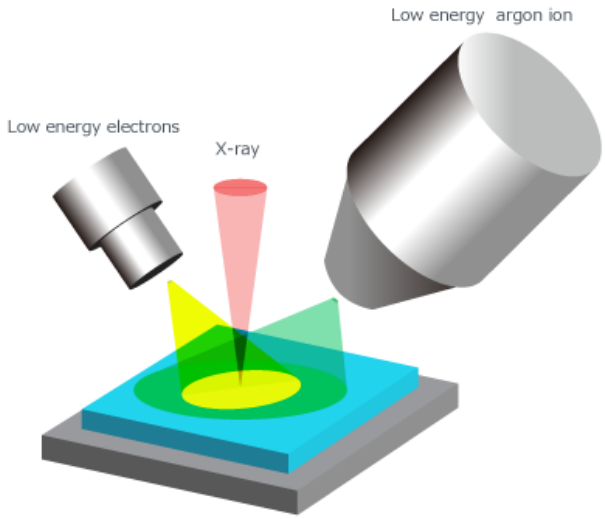

Figure 20. Schematic diagram of turkey charge neutralization. (Figure by PHI Electronics)

2.7.3 HAXPES-Lab system

The HAXPES Lab system by Scienta Omicron offers a dual beam analysis set up using a high flux Ga liquid jet Ga Kα source (*hv* = 9251.74 eV). This photon energy nearly doubles the IMFP value from that from Cr Kα (IMFP O 1s = 8.20 nm with the Cr Kα source vs 13.36 nm using Ga Kα). The HAXPES-Lab was first installed at the Henry Royce Institute at the University of Manchester, who went on to provide the necessary standardisation, calibration and library of relative sensitivity factors (RSFs) for every accessible core level up to 9250 eV that are required from a new X-ray source for spectroscopy, as well as a thorough comparison to synchrotron sources [55].

A thorough investigation of the Ga K∝ system behind the HAXPES Lab determined the basic characteristics of the spectrometer [56]. An energy resolution of 485 meV (16/84% width of E_{Fermi}) was reached for Au $4f_{7/2}$ with a pass energy of 100 eV, step size of 50, and a slit dimension of 100 mV at a grazing angle of 2.4° [56]. Increasing the pass energy to 200 eV and increasing the step size to 100 meV for faster analysis still reached a resolution of 16/84% width of E_{Fermi} of 560 meV. The X-ray power delivered by the Excillum MetalJet-D2+ 70 kV X-ray tube was tested from 50 to 250 W and provided a consistent energy position of 2206.7 eV and a FWHM of 2.2 ± 0.1 eV for Au $3d_{5/2}$. High quality data was collected from technologically relevant samples from bulk and heterostructures.

2.8 Conclusion: needs for a new approach

Current nanofilm deposition techniques allow for atomic control of film thicknesses, but the mechanisms behind the procedures are still being studied. In order to achieve reproducibility of complex nanostructure semiconductor materials, the exact layer thicknesses must be known.

Destructive methods are needed for quantitative analysis in developing technology, but are not fit for process control during the fabrication process. The X-ray reflectivity and fluorescence techniques currently integrated into inline fabrication provide accurate and repeatable results but require reference measurements and/or complicated modeling procedures. X-ray photoemission gives much information on the chemical nature of a sample, and, in the case of ARXPS, nondestructive depth profiling and layer thickness determinations. Traditional XPS, however, is limited to surface sensitivity, and repeating layers require a complex regularization model which is uncertain. Increasing the photon source energy with HAXPES radiation takes the technique to a depth-sensitive technique capable of probing many nm into a sample, but the angle-resolved procedure is still being developed. There is a need for accurate thickness measurements of deeply buried layers using combined techniques using high energy photon sources and advanced HAXPES spectra interpretation.

[1] P.K. Park, E.-S. Cha, S.-W. Kang, Interface effect on dielectric constant of HfO2⁄Al2O3 nanolaminate films deposited by plasma-enhanced atomic layer deposition, Appl. Phys. Lett. 90 (2007) 232906. https://doi.org/10.1063/1.2746416.

[2] R.L. Puurunen, Surface chemistry of atomic layer deposition: A case study for the trimethylaluminum/water process, Journal of Applied Physics. 97 (2005) 121301. https://doi.org/10.1063/1.1940727.

[3] F. Güder, M. Zacharias, Atomic Layer Deposition Assisted Nanostructural Transformations: Atomlagenabscheidung Unterstützt Nanostrukturelle Transformationen, Universität, 2012. https://books.google.fr/books?id=j53bswEACAAJ.

[4] K. Deng, L. Li, Advances in the Application of Atomic Layer Deposition for Organometal Halide Perovskite Solar Cells, Advanced Materials Interfaces. 3 (2016) 1600505. https://doi.org/10.1002/admi.201600505.

[5] V. Drozd, Progress in device from Molecular Layering to atomic layer deposition worldwide technology, in: 2016 14th International Baltic Conference on Atomic Layer Deposition (BALD), 2016: pp. 2–4. https://doi.org/10.1109/BALD.2016.7886521.

[6] E. Ghiraldelli, C. Pelosi, E. Gombia, G. Chiavarotti, L. Vanzetti, ALD growth, thermal treatments and characterisation of Al2O3 layers, Thin Solid Films. 517 (2008) 434–436. https://doi.org/10.1016/j.tsf.2008.08.052.

[7] E. Chason, T.M. Mayer, Thin film and surface characterization by specular X-ray reflectivity, Critical Reviews in Solid State and Materials Sciences. 22 (1997) 1–67. https://doi.org/10.1080/10408439708241258.

[8] P.Y. Hung, C. Gondran, A. Ghatak-Roy, S. Terada, B. Bunday, H. Yeung, A. Diebold, X-ray reflectometry and x-ray fluorescence monitoring of the atomic layer deposition process for high-k gate dielectrics, J. Vac. Sci. Technol. B. 23 (2005) 2244. https://doi.org/10.1116/1.2009774.

[9] J. -M. Baribeau, X-ray reflectometry study of interdiffusion in Si/Ge heterostructures, Journal of Applied Physics. 74 (1993) 3805–3810. https://doi.org/10.1063/1.355290.

[10] J. -M. Baribeau, D.J. Lockwood, R.W.G. Syme, Interfaces in Si/Ge atomic layer superlattices on (001)Si: Effect of growth temperature and wafer misorientation, Journal of Applied Physics. 80 (1996) 1450–1459. https://doi.org/10.1063/1.363013.

[11] J. -M. Baribeau, Low angle x-ray reflection study of ultrathin Ge films on (100) Si, Applied Physics Letters. 57 (1990) 1748–1750. https://doi.org/10.1063/1.104055.

[12] E. Chason, D.T. Warwick, X-Ray Reflectivity Measurements of Surface Roughness Using Energy Dispersive Detection, MRS Online Proceedings Library. 208 (1990) 351–356. https://doi.org/10.1557/PROC-208-351.

[13] T. Arai, N. Langhoff, A. Simionovici, V. Arkadiev, W. Kn¨upfer, T. Cech´ak, J. Leonhardt, J. Chavanne, A. Erko, A. Bjeoumikhov, A. Alexander, B. Beckhoff, I. Grigorieva, B. Kanngießer, B. Vidal, F. Scholze, A. Longoni, C. Fiorini, L. Str¨uder, W. Malzer, Handbook of Practical X-Ray Fluorescence Analysis, 2006.
[14] E. Nolot, S. Cadot, F. Martin, P. Hoenicke, C. Zech, B. Beckhoff, In-line characterization of ultrathin transition metal dichalcogenides using X-ray fluorescence and X-ray photoelectron spectroscopy, Spectrochimica Acta Part B Atomic Spectroscopy. 166 (2020). https://doi.org/10.1016/j.sab.2020.105788.
[15] E. Nolot, W. Pessoa, S. Torrengo, Y. Mazel, M. Bernard, P. Gergaud, Y. Ménesguen, M.C. Lépy, D. Eichert, Grazing-incidence X-ray fluorescence analysis of thin chalcogenide materials deposited on Bragg mirrors, Spectrochimica Acta Part B: Atomic Spectroscopy. 168 (2020) 105864. https://doi.org/10.1016/j.sab.2020.105864.
[16] H. Fontaine, T. Lardin, Quantitative Analysis of the Metallic Contamination On GaAs and InP Wafers by TXRF and ICPMS Techniques, ECS Transactions. 58 (2013) 327. https://doi.org/10.1149/05806.0327ecst.
[17] B. Garrison, J. Vickerman, D. Briggs, ToF-SIMS: Surface analysis by mass spectrometry, Surface Spectra/IM Publications. (2001).
[18] P.A. Yunin, Yu.N. Drozdov, M.N. Drozdov, O.I. Khrykin, V.I. Shashkin, Quantitative SIMS depth profiling of Al in AlGaN/AlN/GaN HEMT structures with nanometer-thin layers, Surf. Interface Anal. 49 (2017) 117–121. https://doi.org/10.1002/sia.6068.
[19] S. Hüfner, Photoelectron Spectroscopy, Springer Berlin Heidelberg, Berlin, Heidelberg, 2003. https://doi.org/10.1007/978-3-662-09280-4.
[20] H. Hertz, Ueber einen Einfluss des ultravioletten Lichtes auf die electrische Entladung, Annalen Der Physik. 287 (1887) 983–1000.
[21] S. Tougaard, H.S. Hansen, Non-destructive depth profiling through quantitative analysis of surface electron spectra, Surf. Interface Anal. 14 (1989) 730–738. https://doi.org/10.1002/sia.740141109.
[22] J.F. Watts, J. Wolstenholme, An introduction to surface analysis by XPS and AES, Second edition, Wiley, Hoboken, 2019.
[23] C. Zborowski, Characterization of deeply buried interfaces by Hard X-ray Photoelectron Spectroscopy, University of Southern Denmark, 2018.
[24] K. Siegbahn, ESCA: atomic, molecular and solid state structure studies by means of electron spectroscopy, Almqvist and Wiksell, Uppsala, 1967.
[25] C.N. Berglund, W.E. Spicer, Photoemission studies of copper and silver, theory, Physical Review. 136 (1964) A1030–A1044.
[26] J. Cooper, R.N. Zare, Angular Distribution of Photoelectrons, (n.d.) 3.
[27] ISO 18115-1, Surface Chemical Analysis—Vocabulary, Part 1—General Terms and Terms Used in Spectroscopy, International Organization for Standardization Geneva, 2013.
[28] M.A. Reshchikov, M. Foussekis, A.A. Baski, Surface photovoltage in undoped n-type GaN, J. Appl. Phys. 107 (2010) 113535. https://doi.org/10.1063/1.3430979.
[29] L. Kronik, Surface photovoltage phenomena: theory, experiment, and applicationsSurf. Sci. Rep. 37 (1999) 1–206. https://doi.org/10.1016/S0167-5729(99)00002-3.
[30] M. Novák, N. Pauly, A. Dubus, Polarization and dipole effects in hard X-ray photoelectron spectroscopyJ. Electron Spectrosc. Relat. Phenom. 185 (2012) 4–12. https://doi.org/10.1016/j.elspec.2011.12.002.
[31] M.B. Trzhaskovskaya, V.I. Nefedov, V.G. Yarzhemsky, Photoelectron angular distribution parameters for elements z=1 to z=54 in the photoelectron energy range 100–5000 ev, Atomic Data and Nuclear Data Tables. 77 (2001) 97–159. https://doi.org/10.1006/adnd.2000.0849.
[32] M.B. Trzhaskovskaya, V.I. Nefedov, V.G. Yarzhemsky, Photoelectron angular distribution parameters for elements z=55 to z=100 in the photoelectron energy range 100–5000 ev, Atomic Data And Nuclear Data Tables. 82 (2002) 257–311. https://doi.org/10.1006/adnd.2002.0886.

[33] S. Doniach, M. Sunjic, Many-electron singularity in X-ray photoemission and X-ray line spectra from metals, J. Phys. C: Solid State Phys. 3 (1970) 285–291. https://doi.org/10.1088/0022-3719/3/2/010.
[34] C.S. Fadley, S.B.M. Hagström, J.M. Hollander, M.P. Klein, D.A. Shirley, Chemical Bonding Information from Photoelectron Spectroscopy, Science. 157 (1967) 1571–1573. https://doi.org/10.1126/science.157.3796.1571.
[35] NIST X-ray Photoelecron Spectroscopy Database, NIST Standard Reference Database Number 20, National Institute of Standards and Technology, Gaithersburg MD, 20899, (2000), doi: 10.18434/T4T88K (retrieved 2022), (n.d.).
[36] S. Tanuma, C.J. Powell, D.R. Penn, Calculation of electron inelastic mean free paths (IMFPs) VII. Reliability of the TPP-2M IMFP predictive equation, Surf. Interface Anal. 35 (2003) 268–275. https://doi.org/10.1002/sia.1526.
[37] S. Tanuma, C.J. Powell, D.R. Penn, Calculations of electron inelastic mean free paths. IX. Data for 41 elemental solids over the 50 eV to 30 keV range, Surf. Interface Anal. 43 (2011) 689–713. https://doi.org/10.1002/sia.3522.
[38] S. Tanuma, C.J. Powell, D.R. Penn, Calculations of electron inelastic mean free paths. V. Data for 14 organic compounds over the 50-2000 eV range, Surf. Interface Anal. 21 (1994) 165–176. https://doi.org/10.1002/sia.740210302.
[39] S. Tougaard, Software Packages to Characterize Surface Nano-Structures by Analysis of Electron Spectra, (2021). http://www.quases.com/.
[40] S. Tanuma, C.J. Powell, D.R. Penn, Calculations of electron inelastic mean free paths. IX. Data for 41 elemental solids over the 50 eV to 30 keV range, Surf. Interface Anal. 43 (2011) 689–713. https://doi.org/10.1002/sia.3522.
[41] C.J. Powell, A. Jablonski, S. Tanuma, D.R. Penn, Effects of elastic and inelastic electron scattering on quantitative surface analyses by AES and XPS, J. Electron Spectrosc. Relat. Phenom. 68 (1994) 605–616. https://doi.org/10.1016/0368-2048(94)80023-5.
[42] C.J. Powell, A. Jablonski, Progress in quantitative surface analysis by X-ray photoelectron spectroscopy: Current status and perspectives, J. Electron Spectrosc. Relat. Phenom. 178–179 (2010) 331–346. https://doi.org/10.1016/j.elspec.2009.05.004.
[43] M. Pijolat, G. Hollinger, New depth-profiling method by angular-dependent x-ray photoelectron spectroscopy, Surf. Sci. 105 (1981) 114–128.
[44] A. Jablonski, Photoelectron transport in the surface region of solids: Universal analytical formalism for quantitative applications of electron spectroscopies, Journal of Physics D: Applied Physics. 48 (2015) 075301. https://doi.org/10.1088/0022-3727/48/7/075301.
[45] T. Jablonski, Evaluation of validity of the depth-dependent correction formula (CF) for elastic electron scattering effects in AES and XPS, Sur, Interface Anal. 26 (1998) 11.
[46] S. Tougaard, Energy loss in XPS: Fundamental processes and applications for quantification, non-destructive depth profiling and 3D imaging, J. Electron Spectrosc. Relat. Phenom. 178–179 (2010) 128–153. https://doi.org/10.1016/j.elspec.2009.08.005.
[47] A.G. Shard, Practical guides for x-ray photoelectron spectroscopy: Quantitative XPS, J. Vac. Sci. Technol. A: Vac. Surf. Films. 38 (2020) 041201. https://doi.org/10.1116/1.5141395.
[48] E. Gnacadja, N. Pauly, H.J. Kang, S. Tougaard, XPS quantification with universal inelastic electron scattering cross section including intrinsic excitations, Surf. Interface Anal. 2022; 54(12): 1186-1191. doi:10.1002/sia.7142.
[49] L. Davis, N. MacDonald, P. Palmberg, G. Riach, R. Weber, Handbook of Auger electron spectroscopy, 2nd ed., Physical Electronics Division, Eden Prairie, Minnesota 55343, 1976.
[50] Angle Resolved XPS, (n.d.) 10.
[51] G. Tsamo, G. Monier, P. Hoggan, C. Robert-Goumet, M. Petit, A. Ranguis, L. Bideux, XPS modeling of GaN/GaAs nanostructure grown by the droplet epitaxy technique, J. Electron Spectrosc. Relat. Phenom. 261 (2022) 147257. https://doi.org/10.1016/j.elspec.2022.147257.

[52] B.S. Semak, C. van der Marel, S. Tougaard, Comparison of the Tougaard, ARXPS, RBS and ellipsometry methods to determine the thickness of thin SiO2 layers, Surf. Interface Anal. 33 (2002) 238–244. https://doi.org/10.1002/sia.1206.
[53] J.J. Yeh, I. Lindau, Atomic subshell photoionization cross sections and asymmetry parameters: 1 ⩽ Z ⩽ 103, Atomic Data and Nuclear Data Tables. 32 (1985) 1–155.
[54] O. Renault, P.-M. Deleuze, J. Courtin, T.R. Bure, N. Gauthier, E. Nolot, C. Robert-Goumet, N. Pauly, E. Martinez, K. Artyushkova, New directions in the analysis of buried interfaces for device technology by hard X-ray photoemission, Faraday Discuss. 236 (2022) 288–310. https://doi.org/10.1039/D1FD00110H.
[55] B.F. Spencer, S. Maniyarasu, B.P. Reed, D.J.H. Cant, R. Ahumada-Lazo, A.G. Thomas, C.A. Muryn, M. Maschek, S.K. Eriksson, T. Wiell, T.-L. Lee, S. Tougaard, A.G. Shard, W.R. Flavell, Inelastic background modelling applied to hard X-ray photoelectron spectroscopy of deeply buried layers: A comparison of synchrotron and lab-based (9.25 keV) measurements, App. Surf. Sci. 541 (2021) 148635. https://doi.org/10.1016/j.apsusc.2020.148635.
[56] A. Regoutz, M. Mascheck, T. Wiell, S.K. Eriksson, C. Liljenberg, K. Tetzner, B.A.D. Williamson, D.O. Scanlon, P. Palmgren, A novel laboratory-based hard X-ray photoelectron spectroscopy system, Review of Scientific Instruments. 89 (2018) 073105. https://doi.org/10.1063/1.5039829.

3 Inelastic background analysis

3.1 "Classical" IBA as implemented in XPS: basic principles

An original work, developed by S. Tougaard [1,2], provides a theoretical and experimental framework for the analysis of the inelastic background contained in the X-ray photoemission spectrum. In this semi-classical model, the photoexcitation process is modeled within the dielectric theory describing how a charge is moving through a dielectric medium. With this approach, calculations for general materials are straightforward provided the dielectric function is known.

The inelastic background is associated with the originating location of the photoelectron signal, and thus provides information on the depth distribution of the layer in the sample. Additionally, removal of the inelastic losses allows increased accuracy in the elemental concentration quantification from the determination of the core-level spectrum.

Inelastic background analysis (IBA) can reach a probing depth of 8×IMFP [3] and, more recently, up to 20×IMFP [4,5] enabled by a particular excitation energy and a sample suitable for background analysis over such depths. As a non-destructive method, it can track the structural evolution in between fabrication steps like annealing or the introduction of a capping layer. Since the surface morphology is described by the analysis, growth mechanisms can be followed as well. The XPS acquisition supplying the spectra does not need to be long or highly resolved, allowing for swift results.

An example is displayed in Figure 21, which depicts simulated photoemission spectra obtained using QUASES-Generate of copper in a gold matrix. Copper is distributed with varied atomic concentrations and distribution profiles. The corresponding Cu 2p core level peak corresponding to elastically scattered photoelectrons exhibits the same intensity of the photoelectron peak in each case. However, the inelastic background has a strongly different shape. Note that the copper located 25 Å below the surface (case d) possesses a background many magnitudes greater than the distributions containing copper closer to the surface and in decreased quantity.

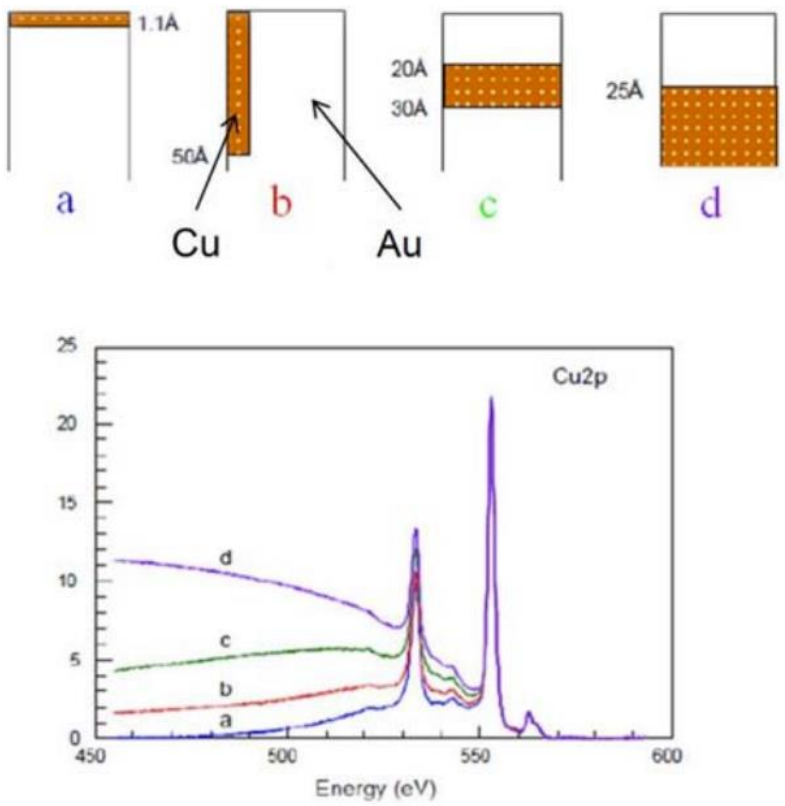

Figure 21. XPS spectra of Cu 2p for various depth distributions of cupper (orange) inside a gold matrix (white). Thicker, more deeply buried layers have a greater inelastic background signal (d), while a thin layer at the surface has very little signal after the core peak (a). Taken from [1].

Indeed, the inelastic losses responsible for the attenuation are attributed in part to morphology, and they delineate a characteristic pattern in the background at low kinetic energies away from the photoelectron core peak. If the element is deeply buried, more photoelectrons will lose energy before they reach the surface and will collectively produce a wider distribution of the signal into the decreasing kinetic energy range.

Tougaard's method associates the experimental measured spectrum *J(E)* and its inelastic background to the energy loss distribution generated by the photoelectron transport through the material. The method is implemented through the QUASES software framework. Subtraction of the computed background using the QUASES software reveals the final, intrinsic, spectrum *F(E)* from which quantitative core-level analysis can be made with increased accuracy. To be more specific to QUASES-Analyze and QUASES-Generate, Tougaard's universal function calculates bulk extrinsic losses, not intrinsic losses. Figure 22 below explains the contributions of extrinsic and intrinsic losses to the XPS spectrum. Extrinsic losses (Figure 22 (a)) occur from inelastic scattering of the photoelectron during transport. Intrinsic losses (Figure 22 (b)) occur from interactions between the photoelectron and the core-hole and valence electrons. In QUASES-Analyze, the bulk extrinsic losses are modeled with an

inelastic scattering cross-section, while QUASES-Generate models the losses using a reference spectrum. The inelastic scattering cross-section is applied to the reference spectrum for the selected depth distribution model, resulting in a model spectrum which is used to evaluate the experimental spectrum. $F(E)$ contains the primary function as well as intrinsic losses and surface extrinsic losses [1,6].

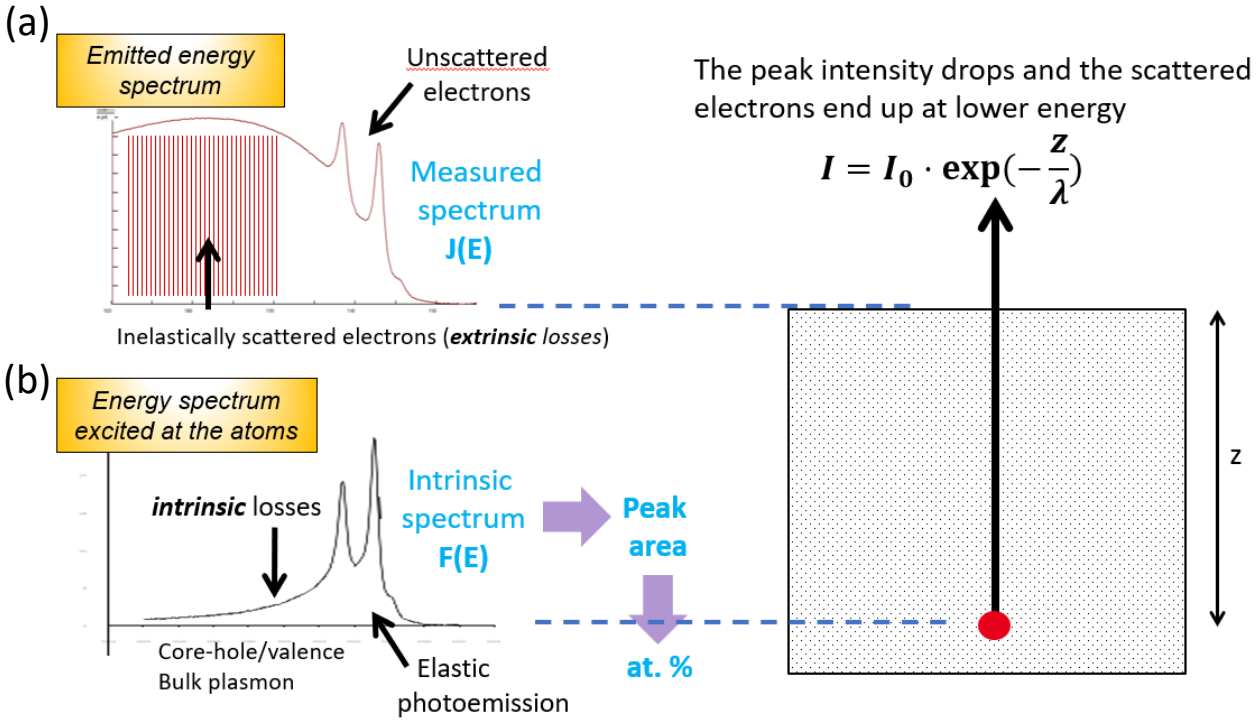

Figure 22. (a) The measured XPS spectrum J(E) containing the core peak resulting from unscattered electrons, and the inelastic scattering background in the energy loss region after the peak resulting from extrinsic losses. (b) The intrinsic spectrum F(E) containing only the elastic photoemission and intrinsic losses associated with interactions between the photoelectron and the the core-hole and valence electrons. F(E) peak area analysis will give an accurate atomic percentage determination.

The power of this method lies in evaluating the background itself, and in bringing information on the in-depth concentration profile *f(z)* of the element as well as surface morphology. The computation of *J(E)* as a function of *f(z)* requires the following known quantities:

- The inelastic mean free path (IMFP) λ_i of the photoelectron as it passes through the overlayers,
- The inelastic scattering cross-section *K(T)* of the material,
- The emission angle to the surface normal, θ.

The user must therefore provide *priori* information on the in-depth concentration profile. The QUASES software proposes five possible depth concentration profiles: buried layer, islands on active or passive substrate, exponential profile, and several buried layers.

Two hypotheses are tested using the QUASES software, one using QUASES-Analyze and the next in QUASES-Generate. The basis of each technique lies in using formulae that depend on the in-depth

concentration profile *f(z).* In QUASES-Analyze, the primary atomic spectrum *F(E)* is calculated from the measured spectrum *J(E)*. The in-depth concentration profile *f(z)* is varied until the background signal is equal to zero over a large energy region (~100 eV) below the plasmon loss peaks located next to the main core-level peak. A reference spectrum may be used, in which case the in-depth concentration profile is changed until a good match is obtained for the shape *and* intensity of the reference. In QUASES-Generate, a model spectrum of *J(E)* is calculated starting from a bulk reference spectrum from a pure elemental solid. The in-depth concentration profile *f(z)* is then varied until a good agreement with the measured spectrum is obtained. In this way, *f(z)* is obtained.

3.1.1 How the background spectrum is evaluated

The first action of the Tougaard formalism is to simplify the classical model describing the photoemission process. The three step model is comprised of (1) photoionization, (2) travel of the photoelecton through the material, and (3) emission from the material and subsequent analysis. In the formalism, this process is abridged into a two step system in which the excitations in the third step are ignored. Indeed, the third process was shown to have little impact on the resulting calculation of depth distribution and atomic concentration, and ignoring this latter allows for a more robust approach to the method [7].

3.1.1.1 The Two Step Model

The spectrum described in step 1 is the primary exitation spectrum $F(E,\Omega)$ and is governed principally by the photoionization cross-section σ. σ is calculated using the atomic subshell of the electron nl and the solid angle of the analyzer Ω [8]. The excitations in step 1 are predominantly intrinsic and are due to core-hole interactions (see section 2.1.2).

3.1.1.2 The inelastic scattering cross-section

Step 2 events are the main contributers to the inelastic background. During transport through the material, a potential is created between the moving photoelectron and other electrons in the medium. When using the universal function, the complex dielectric function of the medium $\epsilon(k,\omega)$ describes the variation in time and space of the induced potential at a given depth inside an infinite medium where surface excitations are neglected. From the potential arises interactions with valence and core-shell electrons in the medium which take energy $\hbar\omega$ and momentum $\hbar k$ from the photoelectron. Their effects are described by the differential inelastic electron scattering cross-section $K(E_0,T)dRdT$ which is the probability that an electron of energy E_0 will lose energy in the interval T $(T = E_0 - E)$, $T + dT$ after having traveled a path length dR in the solid. The equation was developed by Lindhard [9], is given by [10] and is as follows:

Equation 23

$$K(E_0, \hbar\omega) = \frac{1}{\pi a_0 E_0} \int \frac{dk}{k} lm\left\{\frac{1}{\epsilon(k, \hbar\omega)}\right\}$$

Here, $\hbar\omega = T$, E_0 is the kinetic energy of the photoelectron, a_0 is the Bohr radius, and k is the wave vector transferred from the electron. $k_{\pm} = \left(\frac{2m}{\hbar^2}\right)^{1/2} [E_0^{1/2} \pm (E_0 - \hbar\epsilon)^{1/2}]$ are the limits of integration over *k*, imposed by energy and momentum conservation in the inelastic scattering process.

The probability that an electron with initial energy E_0 has energy in the interval $E, E + dE$ after having traveled the path length R will be referred to as $G(E_0, R; E)dE$. $G(E_0, R; E)$ was expressed by Landau [11] as:

Equation 24

$$G(E_0, R; E) = \frac{1}{2\pi} \int_{-\infty}^{\infty} e^{is(E_0 - E)} e^{-R\Sigma(s)} ds$$

With

Equation 25

$$\Sigma(s) = \frac{1}{\lambda_i} - \int_0^{\infty} K(T) e^{-isT} dT$$

For energy spectra where the total energy loss is small in comparison with the primary electron energy, $K(E, T) \cong K(T)$ independent of E. s is an integration variable and has no physical significance.

3.1.1.3 The measured spectrum

The measured spectrum is evaluated using the inelastic scattering cross-section of the material, the IMFP λ_i of the photoelectron, and the solid angle of the detector.

In the two step model, the number of electrons detected per second, per unit energy and solid angle Ω is given by [7]:

Equation 26

$$J(E, \Omega) = \int dE_0 \, F(E_0, \Omega) \int f(z) \, G\left(E_0, \frac{z}{cos\theta}; E\right) dz$$

Where $F(E_0, \Omega)d^2\Omega dE_0$ is the flux of electrons excited from an atom in an energy interval dE_0 at E_0 into the solid angle element $d\Omega$. θ is the angle to surface normal, $f(z)$ is the number of atoms per unit volume at depth z.

3.1.1.4 The intrinsic spectrum

The relationship between the measured spectrum, the intrinsic spectrum, and the inelastic background is shown in Figure 23. The Ta $3p_{3/2}$ peak (black) from pure tantalum was recorded with synchrotron excitation at a photon energy of 8 keV. Having selected the Universal cross-section to model the inelastic background (red), the *F(E)* intrinsic spectrum (green) is left with an intensity equal to zero over a large range of the energy-loss region of the spectrum.

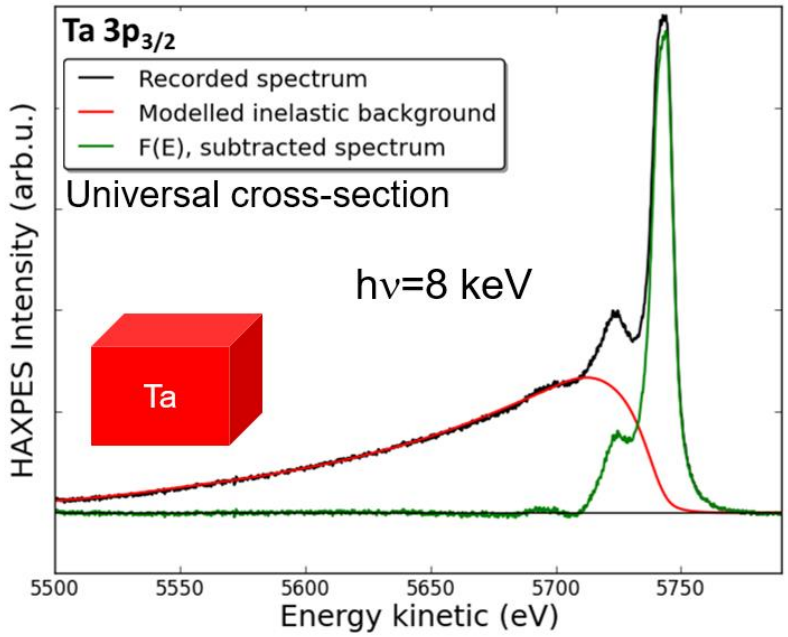

Figure 23. Measured HAXPES spectrum of Ta $3p_{3/2}$ (black) with modeled inelastic background (red) and subtracted intrinsic spectrum F(E) (green). A synchrotron radiation source at energy of 8 keV was used for excitation, and the Universal cross-section was used to model the inelastic background, which is perfectly fitted without the need of any adjustable parameter.

The expression of the XPS intensity $F(E, \Omega)$, or intrinsic spectrum, is defined in terms of the experimental spectrum $J(E, \Omega)$ [12]

Equation 27

$$F(E,\Omega) = \frac{1}{P_1}\left[J(E,\Omega) - \frac{1}{2\pi}\int dE' J(E',\Omega)\int ds e^{-is(E-E')}\left(1 - \frac{P_1}{P(s)}\right)\right]$$

with

Equation 28

$$P(s) = \int f(z) e^{\left(-\frac{z}{cos\theta}\right)\Sigma(s)} dz$$

and

Equation 29

$$P_1 = \int_0^\infty f(z) e^{-z/\lambda_i cos\theta} dz$$

which can be evaluated using a discrete Fourier transformation. *P(s)* is a Fourier transform of the energy distribution function. It is introduced solely for mathematical convenience and has no direct physical significance. Concerning P_1 and E', $P_1 = lim_{s \to \pm \infty} P(s)$ and $E' - E = \hbar\omega$.

Equation 27 is applicable to cases in which the intrinsic spectrum is known via a homogenous reference sample and f(z) is the unknown in the experiment or the converse.

3.1.2 The path of the photoelectron

Equation 26 demonstrates the importance of *K(T), the inelastic scattering cross-section,* and λ in defining *J(E,Ω)* and therefore *F(E,Ω)* and *f(z)*.

3.1.2.1 The Universal cross-section

The inelastic scattering cross-section characterizes the energy losses as the photoelectron travels through the material. Tougaard asserts in [10] that the product $\lambda(E)K(E,T)$ depends strongly on the energy loss T, moderately on the specific solid, and is largely invariant with the energy of the photoelectron E. Without the contribution of E, the equation for the applied cross-section can be simplified into a Universal cross-section $\lambda(E)K(E,T)$. It is sufficiently accurate in most cases and will be discussed in Chapter 4.

For most metals, their oxides, and alloys, the two-parameter Universal cross-section can be applied [10]. It is as follows:

Equation 30

$$\lambda(E)K(E,T) = \frac{BT}{(C + T^2)^2}$$

With $B \cong 3000$ eV^2 and $C = 1643$ eV^2. B is normalized to $2C$, while C was determined via a dielectric-response calculation.

In solids containing a narrow plasmon structure, the function is better described with an additional parameter D:

Equation 31

$$\lambda(E)K(E,T) = \frac{BT}{(C - T^{2)^2} + DT^2}$$

B, C and D have been defined for different classes of materials (e.g. polymers, semiconductors, and free-electron-like solids). The various cross sections are shown in Figure 24.

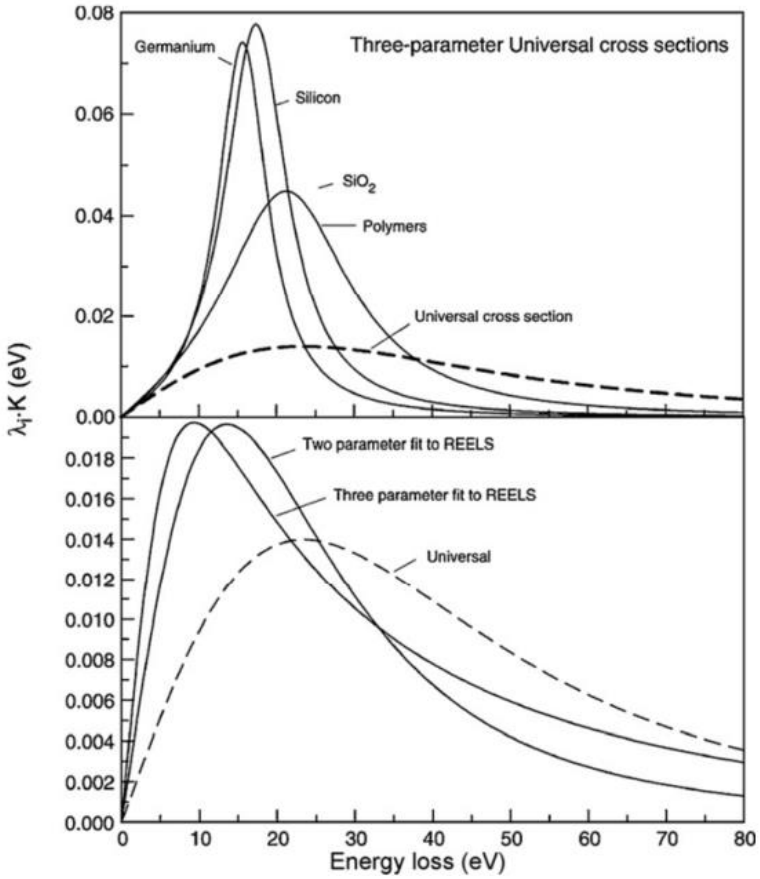

Figure 24. Cross-sections for different classes of materials. The two-parameter Universal cross-section can be applied to most metals, their oxides, and alloys. Taken from [13].

Determination of $K(E)$ by REELS analysis includes some overestimation of surface effects to be accounted for, and the dielectric calculation is time-consuming. REELS analysis and dielectric calculations may be circumvented in many circumstances if one accepts the generality of the distribution in the energy range of interest following the elastic peak. Figure 25 demonstrates this

tendency, where $\lambda(E)K(E,T)$ for various elements determined by REELS analysis are superimposed over one another. The distributions in the 30 eV following the elastic peak follow a similar trend.

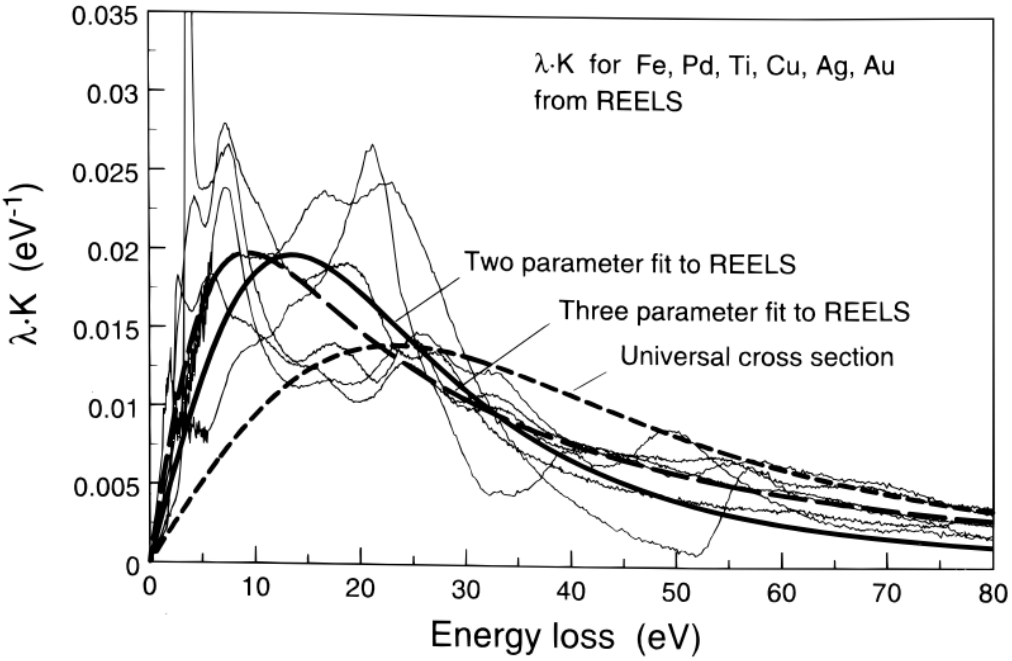

Figure 25. Cross-sections for Fe, Pd, Ti, Cu, Ag, and Au determined from REELS analysis and the best least-square fits of the Two- and Three-parameter universal cross-sections of Equation 8 and Equation 9. The cross-sections follow a similar path once energy loss > 55 eV. Taken from [13].

3.1.2.2 An effective IMFP and inelastic scattering cross-section

Previous studies have shown that the IMFP and $K(E)$ parameters should take into account all of the sample layers through which the photoelectron travels in the form of an effective IMFP or effective cross-section $K(E)$ [14–17]. They also assume that the proportions of each individual IMFP and $K(E)$ used in the calculation are expected to be related to the thicknesses of the material layers involved in the stack [16,17]. The most-recent work by Zborowski et al. [14] used spectra calculated with the QUASES-Generate software for spectra recorded both with synchrotron radiation and laboratory Al Kα sources for a wide range of material combinations in the overlayer and buried layer. They found that an effective IMFP and effective inelastic scattering cross-section with relative weights being half the thickness of the buried layer and the full thickness of the overlayer provided the most accurate depth distribution solution. This is supported by the assumption that the electrons from atoms in the buried layer will not all come from the deeper interface. By this consideration, the electrons collected come from the middle of the layer. The new effective calculations are shown below:

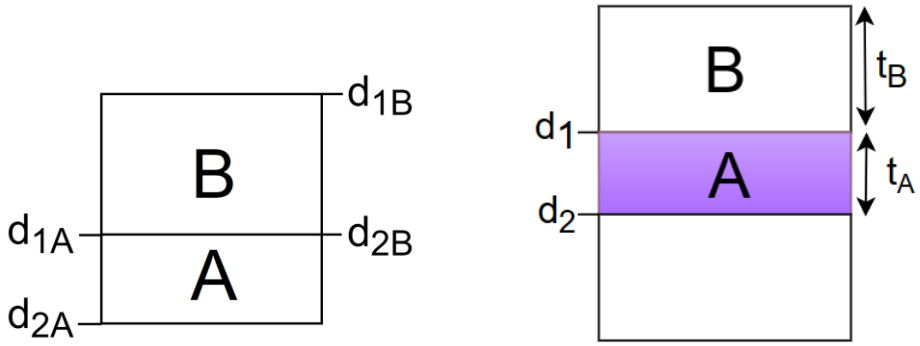

Figure 26. d_1 is the start depth in either layer A or B. d_2 is the respective end depth. In this diagram, we see that the elements originating in atoms from the buried layer A of thickness t_A are unlikely to originate from the interface d_2. This approximation gives good results in practice [14,17,18]. This supports an effective IMFP and effective K(E) calculation which only accounts for a half-contribution from the buried layer.

Equation 32

$$IMFP_{eff_{-1/2}} = \frac{\frac{1}{2}t_A}{\frac{1}{2}t_A + t_B} \times IMFP_A + \frac{t_B}{\frac{1}{2}t_A + t_B} \times IMFP_B$$

Equation 33

$$K_{eff_{-1/2}} = \frac{\frac{1}{2}t_A}{\frac{1}{2}t_A + t_B} \times K_A + \frac{t_B}{\frac{1}{2}t_A + t_B} \times K_B$$

As shown in Figure 26, t_A is the thickness of the buried layer of material A, t_B is the overlayer thickness (material B), K_A and $IMFP_A$ are the cross section and IMFP of material A, and K_B and $IMFP_B$ are the cross section and IMFP of material B, respectively. The selection of the cross-section is dependent on the material, and K_{eff} may be composed of a combination of cross-sections either available in the software like the Universal cross-section, or cross-sections specific to the material such as those aquired through REELS measurements.

It will be seen in Chapter 4 that the d_1 and d_2 parameters for individual layers will not always agree. This means that the start depth of layer A coincidies with the end depth of layer B. For this reason, we define layer dependent depth parameters as in Figure 26 (b).

3.1.2.3 Parameter dependency in the $IMFP_{eff}$ determination

Here we discuss the impact of the overlayer thickness on the $IMFP_{eff}$ of elements in the buried layer. We also point out the

Error in the nominal thickness determination has little impact on the $IMFP_{eff}$. This is clear from Equation 32, but is demonstrated in Figure 27. The $IMFP_{eff}$ was calculated for Hf 3d in 2.4 nm HfO_2 buried under 9.9 nm Al_2O_3. The Al_2O_3 overlayer thickness was varied by 20% in either direction, but the $IMFP_{eff}$ calculation varied only 1 Angstrom from one extreme to the other.

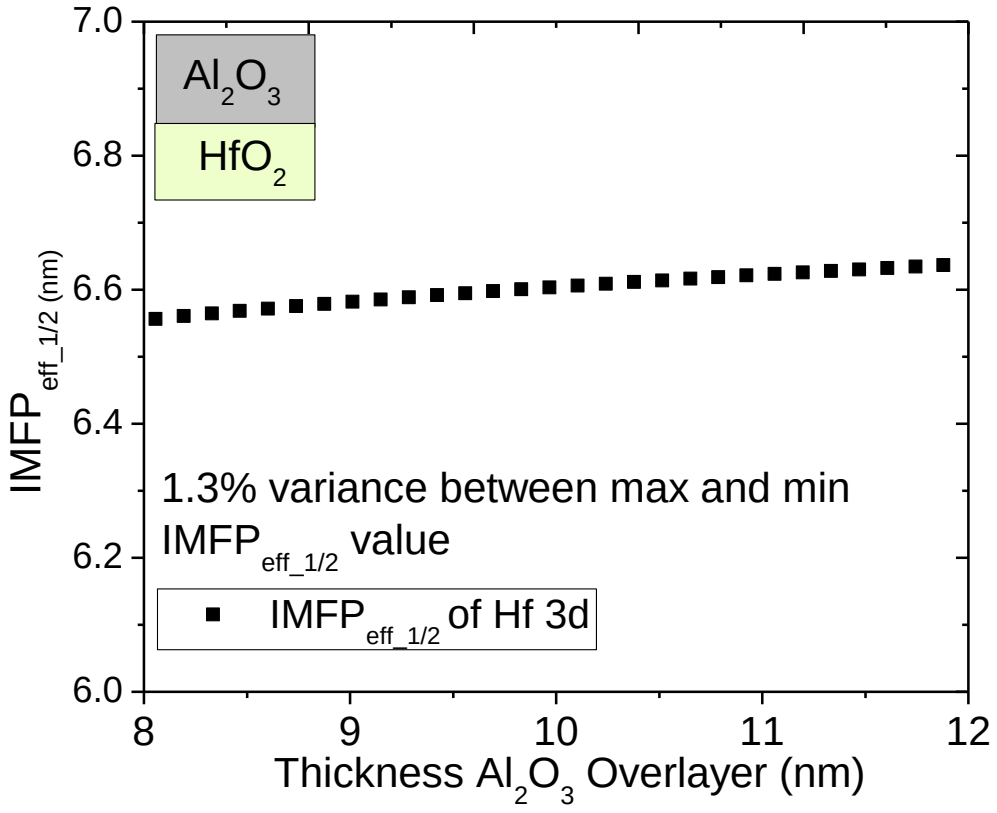

Figure 27. $IMFP_{eff}$ calculations for Hf3d in 2.4 nm HfO_2 buried under 9.9 nm Al_2O_3. The Al_2O_3 overlayer thickness was varied by 20% in either direction, but the $IMFP_{eff}$ calculation varied only 1 Angstrom from one extreme to the other.

Error in the TPP2M values, however, has a significant impact on the $IMFP_{eff}$ result. Figure 28 demonstrates the impact of uncertainty in the IMFP value for the overlayer in the same Al_2O_3/HfO_2 stack. Although the 20% variance in the TPP2M IMFP value is reasonable by the standards for the TPP2M calculation, the resulting $IMFP_{eff}$ is very imprecise and delivers IBA solutions different by several nanometers.

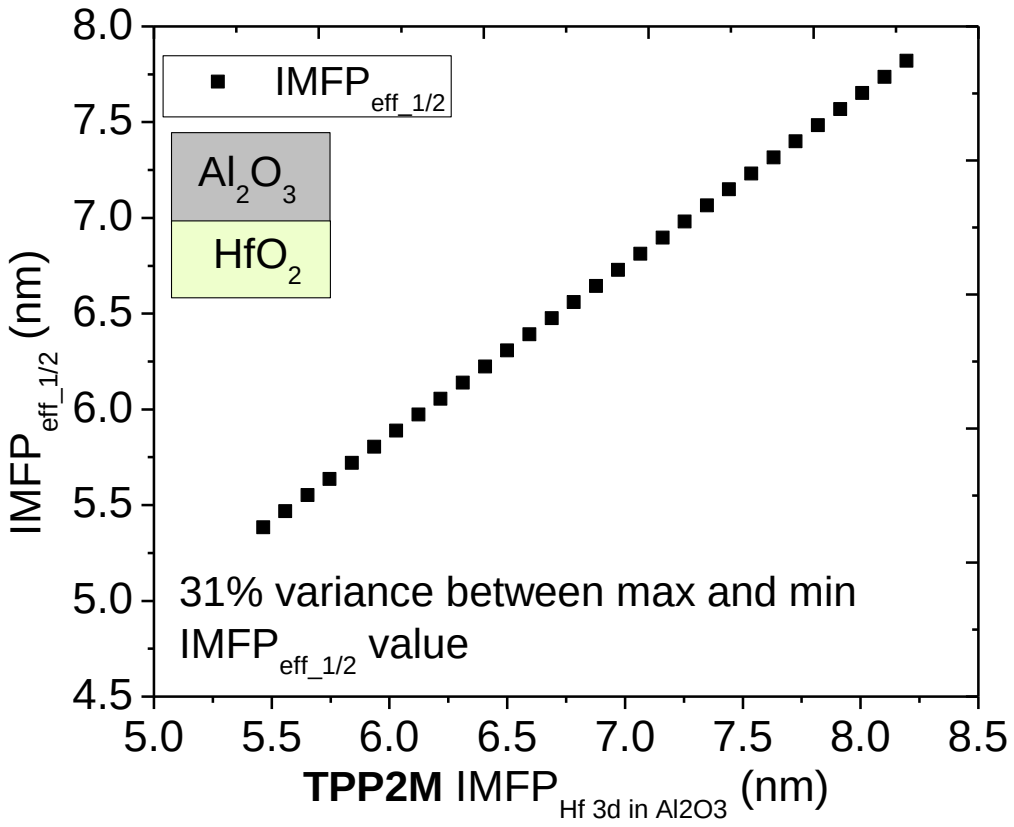

Figure 28. $IMFP_{eff}$ calculations for Hf3d in 2.4 nm HfO_2 buried under 9.9 nm Al_2O_3. The IMFP of Hf 3d (IMFPa) was varied 10% in either direction, resulting in a 35% change in the $IMFP_{eff}$ from one extreme to the other.

From this data, we conclude that uncertainty in the layer thickness does not increase uncertainty in the IBA result, while the TPP2M calculation does. It was shown that the TPP2M IMFP calculation may deviate more from experimental data as the energy of the source increases. In the first study [19], elastic peak electron spectroscopy (EPES) were used to determine the IMFP in GaAs in an energy range of 0 – 5000 eV. At 5000 eV, the experimental IMFP was estimated to be 8.5 nm, while the TPP2M calculated it to be 12.5 nm. A follow up study [20] on InSb using the same procedure showed a difference of 2 nm for InSb at 5000 eV, from 12.0 nm with the TPP2M calculation to 10.0 nm through experimental means.

3.1.3 Practical approach to QUASES-Analyze

Inelastic background analysis using the QUASES-Analyze and QUASES-Generate software interfaces requires only a handful of steps. In addition to the measured spectrum, the user must provide the IMFP of the photoelectron as it passes through the sample and select the suitable inelastic scattering cross-section. The measured spectrum must be corrected for the transmission function of the spectrometer,

even if in reality this has little effect on the results. For the hemispherical analyzers used in this work, $m = e^{-0.7}$ is a good approximation [21].

A low signal-to-noise ratio in the spectrum may hinder the assessment of the IBA solution. The user may smooth the spectrum with a Savitsky-Golay filter found in the Tools option. The recommended polynomial fit is of the order 2-6, but, in some spectra, significant distortion of the spectrum occurs before the noise is sufficiently reduced and so the user must use caution.

The next step in preparing the spectrum for analysis sets the signal before the peak to zero, effectively removing any influence of the continuous background before the core peak. In drawing the baseline, the user is expected to project a line as though the signal of the continuous background before the peak did not exist. For some spectra, this line may not be wholly evident, and the incline or decline of the baseline may have an impact on the resulting analysis. This concept is discussed further in Chapter 6. The scale factor parameter in the analysis window scales the calculated and measured backgrounds to 1:1 and is a correction for the inelastic scattering cross-section. The recommended value of X-scale = 0.95 should be maintained unless the user has additional information on the value of the cross-section.

As explained in section 3.1.2.1, the two-parameters Universal cross-section is acceptable for most metals, their oxides, and alloys while the three-parameter cross-section is best for solids with a narrow plasmon structure. This work largely focuses on the default two-parameter cross-section setting, as we sought to develop a generalized and simple method applicable to a wide range of semiconductor materials. In cases of a sharp plasmon structure, however, the three-parameter cross-section is necessary, and the width and position of the cross-section at the plasmon must be modified to achieve a good fit [22–25]. This is done in the External Cross-section window accessible from the cross-section selection menu. Changing C shifts the plasmon fit position, while D varies the width. This is allowed because the fitting of the cross-section is done in the short energy range while the background is fitted by the structure in a much wider energy range.

Quantitative analysis of the material composition can be achieved in two ways. The first method uses QUASES-Analysis. The software interface is shown in Figure 29. One starts with the experimental spectrum $J(E,\Omega)$ (shown in black). After choosing the morphology class, the computed inelastic background (purple) is obtained by varying the Start and End Depth parameters until the computed background is well-fitted to the experimental. The computed inelastic background is subtracted from $J(E,\Omega)$, leaving the intrinsic-losses-only spectrum $F(E,\Omega)$ (green). Elemental concentration quantification will be more accurate by using $F(E,\Omega)$ for peak area determination.

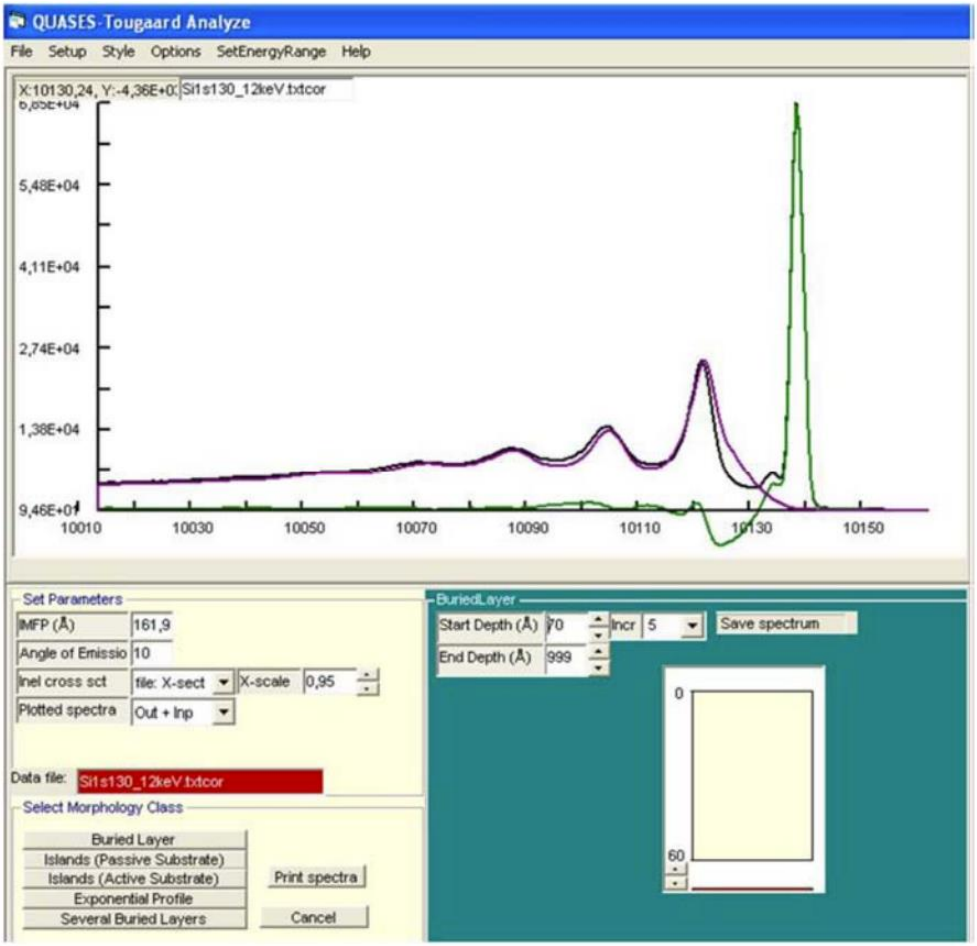

Figure 29. QUASES-Analyze software interface demonstrating background subtraction of a Si 1s spectrum. Taken from [26]. The intrinsic spectrum F(E) (green) is equal to zero in the energy range > 50 eV after the peak. The fit in the 0 - 50 eV range after the peak is not concerned, as the model does not account for intrinsic losses.

The second method of IBA is executed with QUASES-Generate. In this software, the user manipulates a theoretical spectrum $J_{calc}(E,\Omega)$ obtained by modifying the spectrum of a well-defined pure homogeneous sample $J_h(E,\Omega)$. $J_{calc}(E,\Omega)$ is super-imposed over $J(E,\Omega)$ so that the absolute intensity and peak shape may be compared.

In the QUASES software, XPS spectra are not evaluated using Equation 26, but rather by expressions specific to the class of the depth profile. QUASES supports depth profile classes *f(z)* described by homogenous, exponential, and island-like depositions of elements. Several homogenous layer-simulations are available as well. The depth profile classes considered in this thesis are displayed in Figure 30.

Buried Layer Profile

The work of this thesis is concentrated on developing and evaluating an IBA method adapted to lab-based HAXPES. As such, we studied sample stacks which were fabricated by epitaxial growth methods

expected to deliver distinct and even layers. The inelastic background for these samples is evaluated using the buried layer and several buried layer profiles.

Also called the sandwich profile, the simplest case is shown in (a) on Figure 30. If the element in red has $z_0 < z < z_0 + \Delta z$. We can consider that for our stacks, each layer owns a constant concentration profile, so the depth distribution can be written as:

Equation 34

$$f(z) = c$$

$f(z)$ is represented by c in order to simplify the equations.

then [12],

Equation 35

$$P_1 = c \cdot \lambda \cdot cos\theta \cdot \exp\left(-\frac{z_0}{\lambda cos\theta}\right) \times \left[1 - \exp\left(-\frac{\Delta z}{\lambda cos\theta}\right]\right.$$

and

Equation 36

$$P(s) = c \cdot \frac{cos\theta}{\Sigma(\mathrm{s})} \cdot \exp\left(-z_0 \cdot \frac{\Sigma(\mathrm{s})}{cos\theta}\right) \times \left[1 - \exp\left(-\Delta z \frac{\Sigma(\mathrm{s})}{cos\theta}\right)\right]$$

Several Buried Layer Profile

This profile is represented by (b) in Figure 30. For N atoms localized at depth z_0, the depth distribution function can be written as:

Equation 37

$$f(z) = N\delta(z - z_0)$$

Then [12],

Equation 38

$$P_1 = Ne^{\left(\frac{-z_0}{\lambda \cos\theta}\right)}$$

And

Equation 39

$$P(s) = Ne^{\left(\frac{-z_0\Sigma(s)}{\cos\theta}\right)}$$

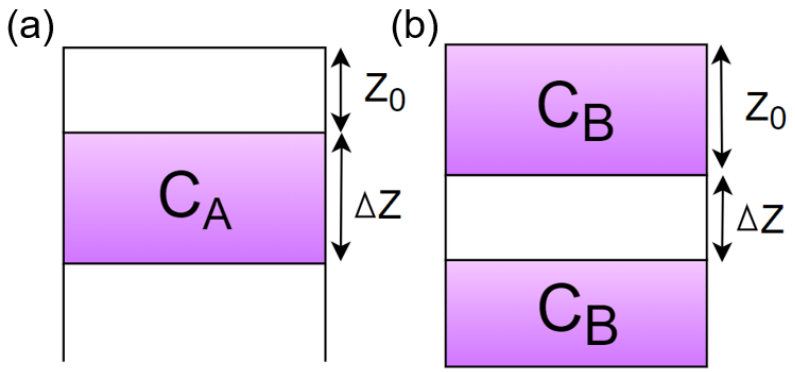

Figure 30. Elemental morphologies that can be analyzed in QUASES software. (a) single layer, (b) several buried layers. Taken from [27].

The simplicity and speed of the QUASES method had led to its use in some XPS studies just by merit of requiring no information aside from that needed for classical XPS analysis.

3.2 Applications of IBA with HAXPES

Here we will discuss the foundational contributions to HAXPES combined with IBA using a synchrotron source, as well as recent developments using lab-based HAXPES instrumentation.

3.2.1 Previous work in HAXPES-IBA

Previous work in inelastic background analysis was implemented with synchrotron HAXPES spectra to increase the probing depth of the XPS-based IBA method, permitting the characterization of deeply buried interfaces in semi-conductor materials.

Risterucci et al. [28] used a very high energy synchrotron source for the first study of HAXPES-IBA. The study reached a probing depth of 35 nm using hard X-rays ($h\nu$ = 12 keV) in the study of lanthanum monolayers buried under electrodes of varied thicknesses [29,30]. The work confirmed the accuracy of HAXPES-IBA when compared to destructive techniques TEM and atom probe tomography (APT) as well as a destructive technique such as Auger depth profiling. A final study on HEMT samples presented the complementarity of high-resolution spectra of core-levels and IBA, finding that a chemical analysis which indicates the best cross-section allows an accurate IBA depth distribution to be applied in the sample component analysis [15].

Zborowski et al. [26] reached a probing depth of up to 70 nm in determining the thicknesses of Al and Ta layers with an accuracy of 95% with the use of a reference spectrum. It was also confirmed that, while accuracy is high in the analysis of deeply buried elements, uncertainty is also increased to over 10% [31]. The work also used HAXPES-IBA with a synchrotron source (*hv* = 7935.7 eV) to show the formation of an inhomogeneous structure made up of a blend of Al, Ga and Ta during annealing. The HAXPES-IBA method was found to achieve greater accuracy to TEM (< 5%) than EDX and XPS (< 15%) [16].

A study [4] at the Japan Synchrotron Radiation Institute with an energy of 7939 eV reached a probing depth of 20 times IMFP in the inelastic background analysis of Ru films deposited over Si(111). The surface topography of the Ru films was correctly modeled using the islands depth profile class in the QUASES-Tougaard software package, and a 5-12% deviation was achieved for thicknesses greater than 12 nm.

More recently, Spencer *et al.* developed a routine for lab-based HAXPES-IBA with a Ga Kα source. The method was demonstrated through the analysis of metal-organic complexes buried underneath calibrated overlayer thicknesses up to 200 nm thick [5]. In the study of Ru 3d photoelectrons, a comparison of a synchrotron source and the lab-based monochromated *hv* = 9251.74 eV source showed probing depths of up to 18.5 times IMFP and 15 times IMFP, respectively. The routine also implemented the angle-resolved mode in the lab-based system to reduce the sampling depth of the measured photoelectrons, enabling profiling from the surface into the bulk of a material.

This recent work demonstrates the potential for a fully-developed HAXPES-IBA method to play an important role in the characterization of deeply buried interfaces as more lab-based HAXPES instruments are introduced to routine analysis.

3.2.2 Advantages of using HAXPES in IBA

The previous examples of HAXPES-IBA indicate the power of combining hard x-rays and analysis of the inelastic background for an accurate and precise characterization of the elemental depth distribution many tens of nanometers into a sample. The dramatic increase in depth sensitivity is owed not only to an increased IMFP, but also the expanse of information gained by following large ranges of energy loss and reaching inner core shell electrons with no peak overlap as one would encounter in XPS. The low binding energy region of the XPS spectrum may be in some cases crowded with photoelectron signals. HAXPES spectra acquired with Ga Kα and Cr Kα sources (*hv* = 9251.74 eV and 5414.72 eV, respectively) of 9.9 nm Al_2O_3 deposited over 2.4 nm HfO_2 are displayed in Figure 31. The photoelectron signals in both spectra are well-distributed, with hundreds of eV between the high energy loss Hf peaks acquired with the Ga Kα source. The hard x-ray sources reach core level electrons from Al 1s and Si 1s which are

unavailable from softer x-ray excitation. Consistent with a higher energy source, and thus increased IMFP, the Si 1s photoelectron peak originating in the substrate is more intense in the Ga Kα spectrum. Accordingly, the ratio between the Si 1s elastic peak and inelastic background intensities is high since more photoelectrons are able to reach the detector without undergoing inelastic collisions. In contrast, the inelastic background signal from Si 1s in the Cr Kα is higher than the elastic peak since the lower energy radiation reaches less far into the substrate.

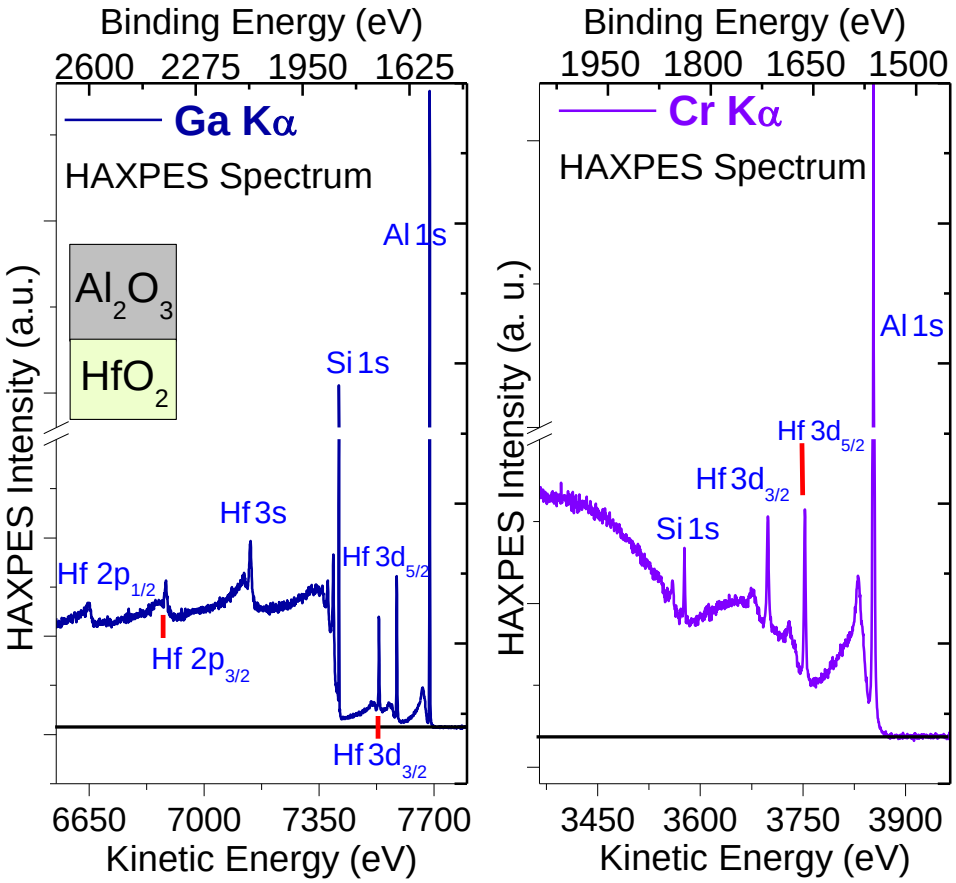

Figure 31. HAXPES spectrum from Ga Kα (9.25 keV) and Cr Kα (5.41 keV) x-ray sources of 9.9 nm Al_2O_3 deposited over 2.4 nm HfO_2. Si 1s and Al 1s signals with a high photoionization cross section σ are available. In the Ga Kα-recorded spectrum, Hf signals in the high energy loss region are spaced over 100 eV apart.

Comparing the spectrum in Figure 31 to a similar sample scaled down for use with XPS makes evident that the benefit of HAXPES goes beyond increasing the probing depth. Figure 32 shows the Al Kα (1.49 eV) spectrum of a sample case in which 3 nm of Al_2O_3 was deposited of over 1.5 nm HfO_2. Peak crowding and overlapping signals prevent analysis of the Al and Si backgrounds, and Hf4p is unavailable due to carbon contamination 50 eV from the peak.

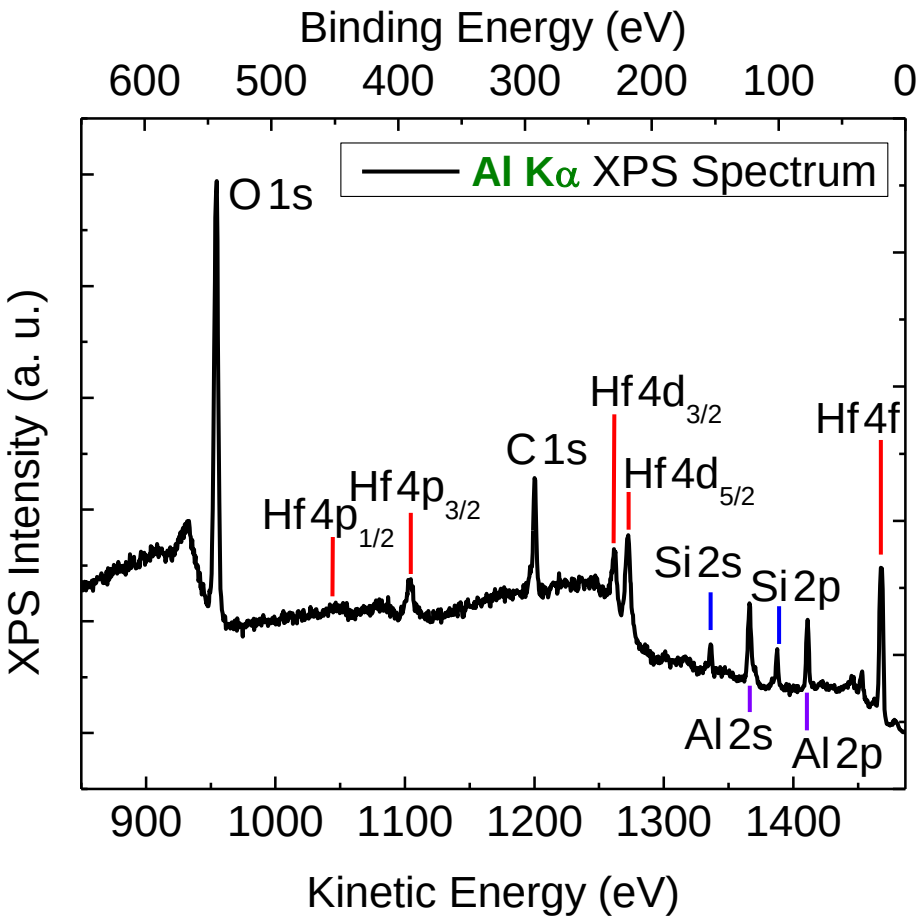

Figure 32. XPS spectrum from an Al Kα (E = 1486.6 eV) source of 3 nm Al_2O_3 deposited over 1.5 nm HfO_2. The Al and Si regions overlap, preventing IBA. C 1s contamination prevents Hf 4p analysis.

Another benefit of switching to higher photon energies lies in the companion signal found in XPS spectra, Auger X-ray excited electrons. Since Auger electrons are the result of intra-atomic processes, they have constant kinetic energies but variable apparent binding energies. Therefore, changing the excitation energy will shift the Auger peak position in the binding energy scale. While this is true for soft X-rays as well, increasing the photon energy with hard X-rays shifts the Auger electrons much farther from the principal peaks of interest at lower binding energies. An example is shown below in Figure 33 (a) of an Al Kα XPS spectrum of a sample stack of 10 nm Al_2O_3 deposited by ALD over GaN. Buried Ga LMM Auger lines produce a large background signal that interferes with and prevents analysis of O 1s, while O KLL and C KLL Auger signals block IBA of Ga 2p. C 1s and F 1s surface contamination is present, but a sharp drop after the peak and very little background shows that it does not go into the layer.

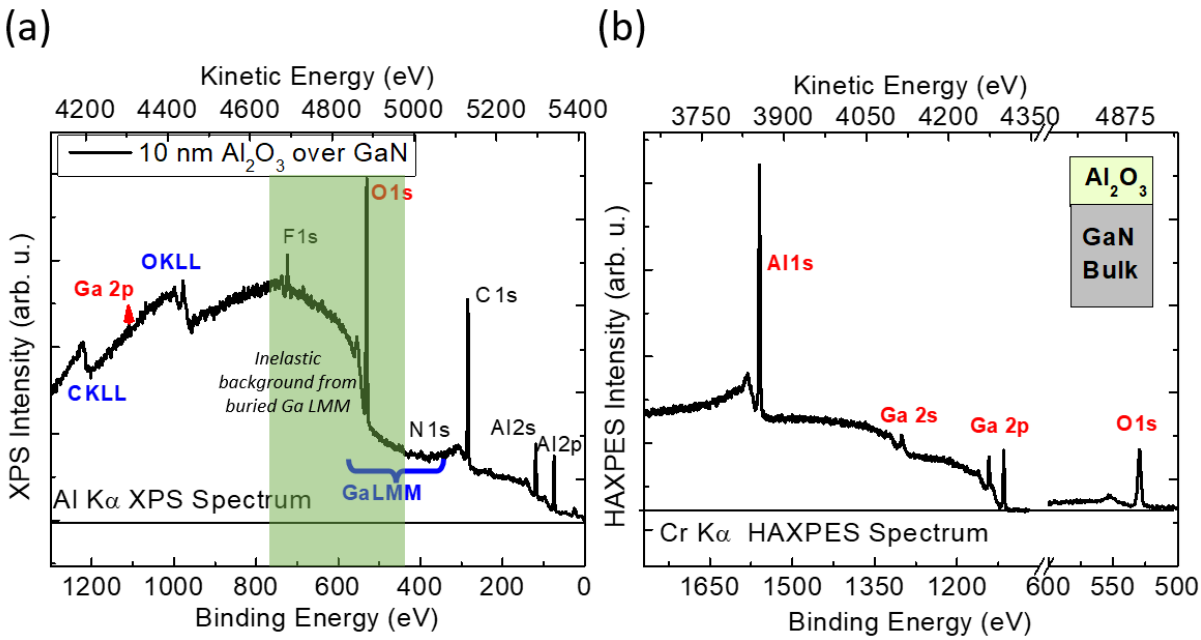

Figure 33. (a) Al Kα XPS spectrum of 10 nm Al_2O_3 over GaN. Ga LMM energy losses from deeply buried Ga contribute to the continuous background, preventing analysis of O1s. On the other hand, prominent O KLL and C KLL signals from the surface block IBA of Ga 2p. (b) The continuous background after O 1s contains only O 1s energy loss signals. The Ga 2p region is free of other peaks, allowing IBA over an energy range of over 300 eV since the Ga 2s signal is included in the analysis.

The complete IBA of this sample and the others in the series is presented in Chapter 5. These samples were important in assessing the dependence of the HAXPES-IBA method on the $IMFP_{eff}$ and comparing the two softwares QUASES-Analyze and QUASES-Generate.

3.3 Conclusion

Lab-based HAXPES will soon be commonplace in research centers, and is already contributing new information in major fields of research [32]. XPS is integral in process fabrication systems as a non-destructive characterization tool. There is no doubt of HAXPES and dual HAXPES/XPS instrumentation's integration into process fabrication in the near future.

This work proposes a generic method for analyzing buried interfaces non-destructively and applies it to technologically relevant materials with diverse characteristics. We tentatively present stand-alone HAXPES-IBA at the lab-scale as an integrated characterization step for helping process optimization. Metrological techniques are used to evaluate the accuracy of the method. Additionally, a comprehensive analysis of all elements in the sample ensures the internal consistency of the method. Atomically precise deposition delivered well-controlled, clean-room fabricated layers against which the method was evaluated.

We evaluate accuracy of the inelastic background method when using bulk spectra vs the universal inelastic scattering cross-section. This is in the interest of minimizing the dependence on outside instrumentation like REELS, which would take the analysis procedure "offline." A semi-automated J(E) spectrum creation procedure is introduced, which circumvents the transmission function correction and handset baseline interfaces. This minimizes user interaction with the software, and the need to switch between multiple windows before performing the background-fitting. Previous work and upgrades to the QUASES-Analyze and QUASES-Generate software searched to eliminate the need for a visual inspection of the fit of the simulated and recorded backgrounds by implementing an error calculation [14,26,31]. The proposed method was a simple area error calculation which spanned the entire background of the spectrum. In a small study, we discuss the impact of the selection of the range over which the error calculation is performed, and which ranges provide an error value which is lowest for the "true" solution in a model spectrum. Through this study, we provide insight on the relative sensitivity of the QUASES background fitting to various portions of the spectrum. We also provide conditions for an accurate visual inspection, and discuss the precision introduced by an error calculation vs the ensured precision of a material deposition.

[1] S. Tougaard, Energy loss in XPS: Fundamental processes and applications for quantification, non-destructive depth profiling and 3D imaging, J. Electron Spectrosc. Relat. Phenom. 178–179 (2010) 128–153. https://doi.org/10.1016/j.elspec.2009.08.005.

[2] S. Tougaard, Practical guide to the use of backgrounds in quantitative XPS, J. Vac. Sci. Technol. A. 39 (2021) 011201. https://doi.org/10.1116/6.0000661.

[3] S. Tougaard, Accuracy of the Non-destructive Surface Nanostructure Quantification Technique Based on Analysis of the XPS or AES Peak Shape, Surf. Interface Anal. 26 (1998) 249–269. https://doi.org/10.1002/(SICI)1096-9918(199804)26:4<249::AID-SIA368>3.0.CO;2-A.

[4] Y.-T. Cui, S. Tougaard, H. Oji, J.-Y. Son, Y. Sakamoto, T. Matsumoto, A. Yang, O. Sakata, H. Song, I. Hirosawa, Thickness and structure of thin films determined by background analysis in hard X-ray photoelectron spectroscopy, J. Appl. Phys. 121 (2017) 225307. https://doi.org/10.1063/1.4985176.

[5] B.F. Spencer, S. Maniyarasu, B.P. Reed, D.J.H. Cant, R. Ahumada-Lazo, A.G. Thomas, C.A. Muryn, M. Maschek, S.K. Eriksson, T. Wiell, T.-L. Lee, S. Tougaard, A.G. Shard, W.R. Flavell, Inelastic background modelling applied to hard X-ray photoelectron spectroscopy of deeply buried layers: A comparison of synchrotron and lab-based (9.25 keV) measurements, Appl. Surf. Sci. 541 (2021) 148635. https://doi.org/10.1016/j.apsusc.2020.148635.

[6] F. Yubero, S. Tougaard, Quantification of plasmon excitations in core-level photoemission, Phys. Rev. B. 71 (2005) 045414. https://doi.org/10.1103/PhysRevB.71.045414.

[7] S. Tougaard, P. Sigmund, Influence of elastic and inelastic scattering on energy spectra of electrons emitted from solids, Phys. Rev. B. 25 (1982) 4452–4466. https://doi.org/10.1103/PhysRevB.25.4452.

[8] J. Cooper, R.N. Zare, Angular Distribution of Photoelectrons, (n.d.) 3.

[9] J. Lindhard, On the Properties of a Gas of Charged Particles, Høst & Søn, 1954. https://books.google.fr/books?id=hhtzMQAACAAJ.

[10] S. Tougaard, Universality Classes of Inelastic Electron Scattering Cross-sections, Surf. INTERFACE Anal. 25 (1997) 18.

[11] L.D. Landau, On the energy loss of fast particles by ionization, J Phys. 8 (n.d.) 201–205.

[12] S. Tougaard, H.S. Hansen, Non-destructive depth profiling through quantitative analysis of surface electron spectra, Surf. Interface Anal. 14 (1989) 730–738. https://doi.org/10.1002/sia.740141109.
[13] S. Tougaard, Universality Classes of Inelastic Electron Scattering Cross-sections, Surf. Interface Anal. 25 (1997) 137–154. https://doi.org/10.1002/(SICI)1096-9918(199703)25:3<137::AID-SIA230>3.0.CO;2-L.
[14] C. Zborowski, S. Tougaard, Theoretical study toward rationalizing inelastic background analysis of buried layers in XPS and HAXPES, Surf. Interface Anal. 51 (2019) 857–873. https://doi.org/10.1002/sia.6660.
[15] P. Risterucci, O. Renault, C. Zborowski, D. Bertrand, A. Torres, J.-P. Rueff, D. Ceolin, G. Grenet, S. Tougaard, Effective inelastic scattering cross-sections for background analysis in HAXPES of deeply buried layers, Appl. Surf. Sci. 402 (2017) 78–85. https://doi.org/10.1016/j.apsusc.2017.01.046.
[16] C. Zborowski, O. Renault, A. Torres, C. Guedj, Y. Yamashita, S. Ueda, G. Grenet, S. Tougaard, Quantitative determination of elemental diffusion from deeply buried layers by photoelectron spectroscopy, J. Appl. Phys. 124 (2018) 085115. https://doi.org/10.1063/1.5033453.
[17] C. Zborowski, O. Renault, A. Torres, Y. Yamashita, G. Grenet, S. Tougaard, Determination of the input parameters for inelastic background analysis combined with HAXPES using a reference sample, Appl. Surf. Sci. 432 (2018) 60–70. https://doi.org/10.1016/j.apsusc.2017.06.081.
[18] C. Zborowski, A. Vanleenhove, T. Conard, Comparison and complementarity of QUASES-Tougaard and SESSA software, Appl. Surf. Sci. 585 (2022) 152758. https://doi.org/10.1016/j.apsusc.2022.152758.
[19] M. Krawczyk, A. Jablonski, S. Tougaard, J. Toth, D. Varga, G. Gergely, The inelastic mean free path and the inelastic scattering cross-section of electrons in GaAs determined from highly resolved electron energy spectra, Surf. Sci. 402–404 (1998) 491–495. https://doi.org/10.1016/S0039-6028(97)00939-4.
[20] G. Gergely, A. Sulyok, M. Menyhard, J. Toth, D. Varga, A. Jablonski, M. Krawczyk, B. Gruzza, L. Bideux, C. Robert, Experimental determination of the inelastic mean free path of electrons in GaSb and InSb, Appl. Surf. Sci. 144–145 (1999) 173–177. https://doi.org/10.1016/S0169-4332(98)00793-4.
[21] S. Tougaard, QUASES-Tougaard Quantitative Analysis of Surfaces by Electron Spectroscopy, (2011).
[22] S. Tougaard, Guide to the posted videos, (2021). http://www.quases.com/data/documents/Videos/Guide%20to%20the%2014%20posted%20videos.pdf (accessed September 20, 2023).
[23] 10. Using 1 the external cross section facility, 2021. http://www.quases.com/data/documents/Videos/Using_1%20the%20external%20cross%20section%20facility.mp4 (accessed September 20, 2023).
[24] A. Müller, K. Sparnacci, W.E.S. Unger, S. Tougaard, Determining nonuniformities of core-shell nanoparticle coatings by analysis of the inelastic background of X-ray photoelectron spectroscopy survey spectra, Surf. Interface Anal. 52 (2020) 770–777. https://doi.org/10.1002/sia.6865.
[25] S. Tougaard, M. Greiner, Method to correct ambient pressure XPS for the distortion caused by the gas, Appl. Surf. Sci. 530 (2020) 147243. https://doi.org/10.1016/j.apsusc.2020.147243.
[26] C. Zborowski, Characterization of deeply buried interfaces by Hard X-ray Photoelectron Spectroscopy, University of Southern Denmark, 2018.
[27] S. Tougaard, Energy loss in XPS: Fundamental processes and applications for quantification, non-destructive depth profiling and 3D imaging, J. Electron Spectrosc. Relat. Phenom. 178–179 (2010) 128–153. https://doi.org/10.1016/j.elspec.2009.08.005.
[28] P. Risterucci, Coupling of electron spectroscopies for high resolution elemental depth profiles in complex architectures of functional materials, University of Lyon, 2015.

[29] P. Risterucci, O. Renault, E. Martinez, B. Detlefs, V. Delaye, J. Zegenhagen, C. Gaumer, G. Grenet, S. Tougaard, Probing deeper by hard x-ray photoelectron spectroscopy, Appl. Phys. Lett. 104 (2014) 051608. https://doi.org/10.1063/1.4864488.
[30] P. Risterucci, O. Renault, E. Martinez, B. Detlefs, J. Zegenhagen, G. Grenet, S. Tougaard, Inelastic background analysis of HAXPES spectra: towards enhanced bulk sensitivity in photoemission: Inelastic background analysis of HAXPES spectra, Surf. Interface Anal. 46 (2014) 906–910. https://doi.org/10.1002/sia.5484.
[31] C. Zborowski, O. Renault, A. Torres, Y. Yamashita, G. Grenet, S. Tougaard, Determination of the input parameters for inelastic background analysis combined with HAXPES using a reference sample, Appl. Surf. Sci. 432 (2018) 60–70. https://doi.org/10.1016/j.apsusc.2017.06.081.
[32] O. Renault, P.-M. Deleuze, J. Courtin, T.R. Bure, N. Gauthier, E. Nolot, C. Robert-Goumet, N. Pauly, E. Martinez, K. Artyushkova, New directions in the analysis of buried interfaces for device technology by hard X-ray photoemission, Faraday Discuss. 236 (2022) 288–310. https://doi.org/10.1039/D1FD00110H.

4 Application of HAXPES-IBA method to high-k ALD bilayer samples

This chapter presents a study of high-k metal-oxide materials prepared by atomic layer deposition (ALD). From ultrathin Al_2O_3 to bilayer Al_2O_3/HfO_2 systems of several nanometers, we discuss the evolving needs for an effective thickness determination, and the advanced XPS methods suitable for each sample case. Part of this work was published in Applied Surface Science in early 2023:

T. R. Bure, O. Renault, E. Nolot, T. Lardin, C. Robert-Goumet, N. Pauly. Assessing advanced methods in XPS and HAXPES for determining the thicknesses of high-k oxide materials: from ultra-thin layers to deeply buried interfaces. *Appl. Surf. Sci.* 609 (2023) 155317.

4.1 Experimental methods

Here we present the fabrication processes and characterization methods used on the metal oxide samples.

4.1.1 Sample preparation

Layers of Al_2O_3 and HfO_2 with individual thicknesses in the sub-nanometer to 25 nm range were deposited on 300 mm silicon (001) wafers by ALD. The layer thickness is determined by the number of ALD cycles. Water vapor was used as the oxygen source for both metal-oxides, while Trimethylaluminum and $HfCl_4$ were used as precursors. The deposition temperature was 300 °C. Three classes of ALD samples are examined in this work and are presented in Figure 34.

a) Ultrathin samples of Al_2O_3 with sub-nanometer thicknesses. The samples from the first class were deposited either over the native oxide, or after so-called HF-last surface preparation. HF-last preparation removes the native oxide, saturating the surface with silicon-hydrogen bonds. In one sample featuring the native SiO_2 oxide, a layer of carbon contamination is present.

b) An intermediate stack of SiO_2, HfO_2, and Al_2O_3 layers of 1-2 nm. The sample in the second class was prepared according to the experimental specifications found in Hönicke's work [1]. A 1 nm chemical oxide was formed prior to the HfO_2 ALD layer deposition.

c) Thin buried Al_2O_3 or HfO_2 layers underneath a thick layer (9 – 25 nm) of HfO_2 or Al_2O_3, respectively. The third class of ALD samples used HF surface preparation and features two sets of three bilayer samples in which a HfO_2 or Al_2O_3 overlayer of approximately 10, 15, and 25 nm was deposited over an approximately 2.5 nm layer of either Al_2O_3 or HfO_2, respectively.

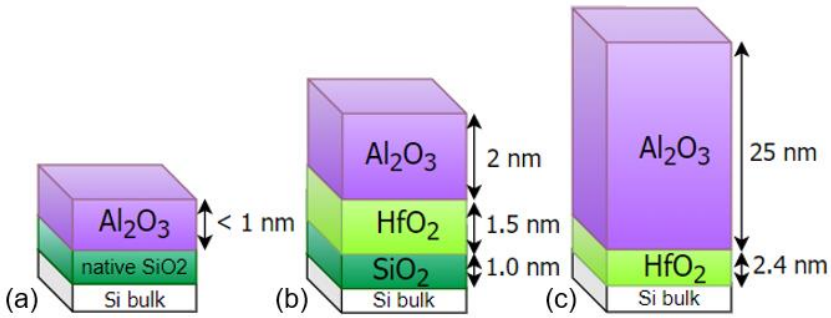

Figure 34. The schematic representation of the structure of (a) the sub-nanometer ultrathin class of samples (with or without native oxide); (b) tri-layer of thin metal oxide layers and (c) bilayers with deeply buried layer of HfO_2 or Al_2O_3 and overlayer of approximately 10, 15, and 25 nm composed of the opposing metal-oxide.

The individual samples in the third class will be denoted by A (Al_2O_3 on top) or H (HfO_2 on top) followed by 1 – 3 with 1 indicating the thinnest overlayer in the series and 3 the thickest. The complete sample descriptions are available in Table 1. The target layer thicknesses are obtained by varying the number of ALD cycles. The XRR thickness measurement is correct to a tenth of a nanometer.

Table 1. Sample descriptions for the thick overlayer series. Thickness values were given by XRR measurements.

Overlayer	Sample name	t_B Surface Layer (nm)	t_A Buried Layer (nm)
Al_2O_3	A1	9.9	2.4
Al_2O_3	A2	14.8	2.4
Al_2O_3	A3	24.4	2.4
HfO_2	H1	9.2	2.7
HfO_2	H2	13.6	2.8
HfO_2	H3	18.2	2.8

The experimental parameters for the reference techniques used in determining the sample thicknesses in these samples are presented below. We will discuss in the results section how the different sample classes are best characterized by the selected reference techniques.

4.1.2 Reference techniques

The ultrathin samples from sample class (a) and (b) were measured using complimentary methods in order to establish the validity of the IBA method. The IBA method was then tested against X-ray reflectivity (XRR) thickness determinations.

4.1.2.1 Ultrathin sample characterization

LPD-ICPMS (Liquid Phase Decomposition coupled to Inductively Coupled Plasma Mass Spectrometry) was used as a destructive, whole surface and reference technique since it is calibrated with certified standards for the quantification of Al dose. LPD is very sensitive, condensing the metal impurities in even ultra-trace amounts. ICP-MS is an elemental analysis technique that uses argon plasma to convert the sample into ions which are measured directly by mass spectrometry. For chemical collection, a

home-made LPD system and VPD reactor were used. Droplet collection was carried out manually. A diluted HF solution was selected as collection solution for LPD. Analysis was performed with an Agilent ICPMS7500cs. LPD-ICPMS delivers an uncertainty of 10% and typical detection limits of the ICP-MS method are in the parts per billion (ppb) range and even parts per trillion (ppt) in some cases.

Equation 40

$$Al_2O_3 + 6\ HF \rightarrow 2\ Al^{3+} + 6\ F^- + 3\ H_2O$$

p-ARXPS analyses were carried out with a Thermo Scientific Theta 300 spectrometer using a monochromatic Al Kα source (1486.6 eV). The two-dimensional detector at the output plane has photoelectron energy dispersed in one direction and the angular distribution dispersed in the other direction. Such setup provides an angular range of ~ 60° (from 20° to 78° emission angle) with a resolution close to 1°. High-resolution spectra were collected using an analysis area of ~ (400 µm²) and a 40 eV pass energy. The energy resolution was 0.45 eV as determined from the Fermi cutoff of a gold reference sample.

p-ARXPS data were analyzed using Thermo Avantage software (version 5.9902), more specifically using the sharp interfaces multi-overlayer model. A 20-60° emission angular range was used in order to get rid of the contributions of elastic interactions.

Wavelength-dispersive X-ray fluorescence (WDXRF) analysis was performed on the Rigaku AZX400 tool operated with Rhodium anode. The spectrometer is ideal for multilayer film metrology, as it was specifically designed to handle very large and/or heavy samples up to 400 mm diameter, 50 mm thick and 30 kg mass. Sequential WDXRF uses a goniometer to feed one wavelength from the spectrum at a time into the detector for high resolution and precision.

We used Al-Kα and Hf-Mα lines and fundamental parameter method calibrated against Al and Hf pure targets to evaluate the deposited mass of Al and Hf. This technique has already demonstrated 1 % accuracy for ultrathin films [20]. The layer thickness was then determined based on assumptions on the material stoichiometry (HfO_2, Al_2O_3) and mass density (9.6 and 3.9 g/cc resp.).

XPS measurements (PHI 5000 VersaProbe II) used monochromated Al-Kα radiation with a takeoff angle of 45° for a pass energy of 117 eV. The FWHM for Ag $3d_{7/2}$ is 1.5 eV for this pass energy. The analyses were done with and without surface preparation by argon gas-cluster ion beam (GCIB) with a cluster size of 2500 atoms at 10 keV for 4 eV per atom of argon and a dose of 1.25 nA per mm².

4.1.2.2 Thick Overlayer Sample Characterization

The thick overlayer samples were characterized by two techniques: X-ray reflectometry for reference thickness values and HAXPES for thickness determination using IBA.

X-ray reflectometry (XRR) was performed on the Bruker D8 Fabline tool operated with monochromatic Cu-Kα radiation. The thickness, mass density and roughness of the layers were evaluated with Bruker Leptos 7 software.

The experimental specifications for the HAXPES experiments are shown in the tables below. In the first experiment, an X-ray monochromated Cr Kα source (hv = 5414.72 eV) and an analyzer pass energy of 280 eV provided a FWHM for Ag $3d_{7/2}$ as 2.3 eV (see Table 2). The photoelectron emission angle (sample-analyzer angle) varied between 45° - 65°. A comparative analysis used monochromated X-ray Ga Kα source (hv = 9251.74 eV) and an analyzer pass energy of 200 eV to achieve a FWHM equivalent to 0.9 eV for Au $4f_{7/2}$ with an Al Kα source. The photoelectron signal was collected normal to the sample surface.

The spectra were recorded over an extended energy range suitable for inelastic background analysis (IBA). The spectra included Al 1s at 1559.6 eV BE, Hf 3d at 1662 eV BE, and Si 1s at 1839 eV BE in the high binding energy region, and O 1s at 531 eV BE in the low binding energy region. The analysis regions are available in Table 2. Additional scans were taken in the 518 eV kinetic energy region in order to record the O KLL Auger signal for IBA.

Reduced step sizes and increased sweeps for more time per step in the measurement improved the signal-to-noise ratio in the spectra while maintaining a reasonable analysis time of approximately three hours for the full range of background signals. The experiment parameters are found in Table 2.

Table 2. Experiment parameters for Cr Kα HAXPES experiments. Small step sizes and increased time per step improved signal-to-noise ratio and subsequent analysis of the background spectra

	Source Energy (eV)	Pass Energy (eV)	Take-Off Angle θ	Step Size (eV)	Time Per Step (s)
Cr Kα	5414.72	280	45°	0.5	3
Ga Kα	9251.74	200	90°	0.5	3

The HAXPES spectral regions over which the data was collected are shown in Table 3. Wide scans in the low binding energy region were used in the experiments to observe potential carbon contamination and changes in the Hf 4f – 4s and Al and Si 2p – 2s transition intensities in addition to O 1s for IBA.

Table 3. Spectral regions of the Cr Kα and Ga Kα HAXPES experiments. A wide scan of the low binding energy range confirmed a lack of carbon contamination. A single wide scan of the high binding energy range recorded the signals of all metal elements in the analysis.

		Cr Kα Source	Ga Kα Source
Line photoelectron Background Region	**Binding energy Range (eV)**	**Kinetic Energy Range (eV)**	**Kinetic Energy Range (eV)**
Hf 4f – O 1s	0 - 750	5414 - 3835	8500 - 9250
Al 1s – Hf3d – Si 1s – Hf3s	1450 - 2700	3965 - 2385	6550 - 7800

The wide energy ranges allowed for ample space over which to calculate the inelastic background. Increased distance between element transitions in HAXPES spectra allows profoundly buried elements to be analyzed [2,3]. In our case, the high BE element signals of primary interest lie in the 1450 – 2000 eV BE range.

4.1.3 Implementation of HAXPES-IBA method

HAXPES-IBA was implemented from HAXPES spectra recorded using two different photoelectron spectrometers described in Chap. 2: one delivering monochromated Cr Kα excitation, the other one working with monochromated Ga Kα radiation.

Two parameters are selected that are specific to the sample and the photoelectron signal. The effective inelastic mean free path ($IMFP_{eff\_1/2}$) considers the full medium through which the photoelectron travels with a weighted calculation based on layer thicknesses and where the photoelectron originates [4,5]. More information can be found in Chapter 3 section 3.1.2.2. $IMFP_{eff\_1/2}$ for the thick overlayer sample series are listed below in Table 4. As is expected practically doubling the Kα radiation energy (5414.72 to 9251.74 eV) has a similar effect on the TPP-2M calculation.

Table 4. $IMFP_{eff\_1/2}$ values for the thick overlayer samples.

	$IMFP_{eff\ 1/2}$			$IMFP_{eff\ 1/2}$			$IMFP_{eff\ 1/2}$		
Sample	**Signal**	**Cr Kα**	**Ga Kα**		**Cr Kα**	**Ga Kα**	**Signal**	**Cr Kα**	**Ga Kα**
A1	**Hf 3d**	6.6	11.79	**O 1s**	8.20	13.36	**Si 1s**	6.34	11.65
A2	**Hf 3d**	6.67	11.92	**O 1s**	8.29	13.50	**Si 1s**	6.41	11.77
A3	**Hf 3d**	6.73	12.02	**O 1s**	8.36	13.62	**Si 1s**	6.47	11.88
H1	**Al 1s**	5.09	8.97	**O 1s**	6.18	10.02	**Si 1s**	4.79	8.75
H2	**Al 1s**	5.02	8.85	**O 1s**	6.09	9.87	**Si 1s**	4.72	8.62
H3	**Al 1s**	4.97	8.76	**O 1s**	6.03	9.78	**Si 1s**	4.68	8.53

The universal inelastic scattering cross-section, $K(T)_{Universal}$, is appropriate for most metal-oxides and transition elements [4,5]. In the case of analyzing the Si (100) substrate, an effective inelastic scattering cross-section $K(T)_{eff\_1/2}$ considering $K(T)_{Universal}$ and a half-contribution of the Si cross-section, $K(T)_{Si}$ available in the QUASES software was tested and compared against $K(T)_{Universal}$ alone.

4.2 Results for thin bilayer samples with native SiO_2 oxide or HF-last surface preparation

Tracking the ALD process in its early stages is important for both metrology and for the knowledge of the sample composition but presents a challenge when following the increasing thickness of the layer. Highly accurate physical characterization techniques could nevertheless result in high error for an ultrathin deposition of only several angstroms. Determining the dose of an element in the material is accurate and precise, but at the cost of destroying the sample. In this section, we discuss the first class of ALD samples (Fig. 1(a)). In the study of ultrathin Al_2O_3 with a native silicon oxide layer, we first confirm the sensitivity and accuracy of nondestructive WDXRF against the destructive reference technique LPD-ICPMS in determining the Al dose. Now validated, WDXRF serves as a complimentary technique to pARXPS for thickness determinations in Al_2O_3 ALD samples with and without a HF-last surface preparation. The resulting pARXPS analyses demonstrate the capability of the method to resolve the thickness of not only a layer of carbon contamination, but also the thickness of the buried SiO_2 layer present in the sample in the case of an untreated surface.

4.2.1 Quantification of Al dose

In Figure 35, we present the quantitative dose of Al in Al_2O_3 ALD samples as determined by LPD-ICPMS and WDXRF. LPD-ICPMS was used as a whole surface reference technique by destructive elemental analysis of Al. It is calibrated with certified standards and delivers an estimated uncertainty of 10% in the Al dose. The non-destructive WDXRF technique is confirmed by agreement with LPD-ICPMS to provide a quantitative determination of the dose of Al in an Al_2O_3 ALD process with low uncertainty. Al surface concentration was measured in atoms per cm^2 of the sample. WDXRF layer thickness determination was converted to Al dose using the stoichiometric relationship between the thickness (calculated), density (3.99 g/cm^3), and atomic weight of the material (101.96 g/mol). The WDXRF values have a linear dependence and agreement within LPD-ICPMS uncertainties, with a scaling factor of 0.94

and a R^2 of 0.99. This confirms WDXRF as an accurate complimentary reference technique for the following pARXPS methods.

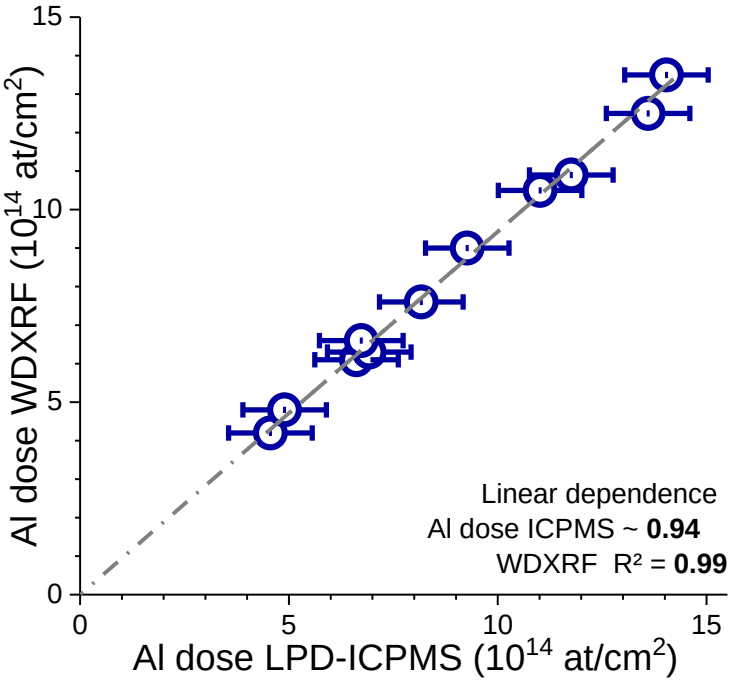

Figure 35. Al Dose in Al2O3 as Determined by LPD-ICPMS and WDXRF. LPD-ICPMS has a 10 % uncertainty margin. Error was determined by the Al dose calculation from WDXRF-determined thickness and the dose quantification by ICPMS.

4.2.2 pARXPS results for ultrathin Al_2O_3 with a native SiO_2 layer or HF-last preparation

pARXPS was first used as a non-destructive technique for the determination of the thicknesses of layers in an ALD process of ultrathin Al_2O_3 (ref. Figure 34 (a)) grown on SiO_2 with surface contamination in the form of adventitious carbon. Later, the same technique was used on ultrathin Al_2O_3 whose silicon substrate was first treated with HF surface preparation. The so-called HF-last preparation prevents the formation of the native oxide by covering the surface with silicon-hydrogen bonds.

The principle of ARXPS is to consider the relationship between the intensity of the XPS signal as a function of angle and the depth distribution of the element in the material at the nm-scale. A discussion of it's mechanics is available in Chapter 2 section 2.6.3. In pARXPS, spectra are collected over a wide angular range in parallel and without tilting the sample, permitting fast parallel acquisition and constant transmission. The experimental configuration of ARXPS permits analysis of every layer in the sample, including surface contamination and the oxide formed at the bulk-sample interface, which is impossible in solely chemical techniques like mass spectrometry (which would not discern the presence of the metal Si in two unique layers), nor solely physical techniques like WDXRF (which would be indiscriminate in layer ordering).

Figure 36 demonstrates the angular dependence of the Si-O signal from the native oxide layer and the Si-Si signal from the silicon substrate. The high-resolution spectra belonging to glancing angles have stronger signals in the region 4 eV after the Si peak where the SiO_2 signal lies. Conversely, bulk contributions have the greatest intensity for smaller angles of emission. The Al 2p peak which is attributed to the Al_2O_3 layer demonstrates the angular dependence of the core peak intensity.

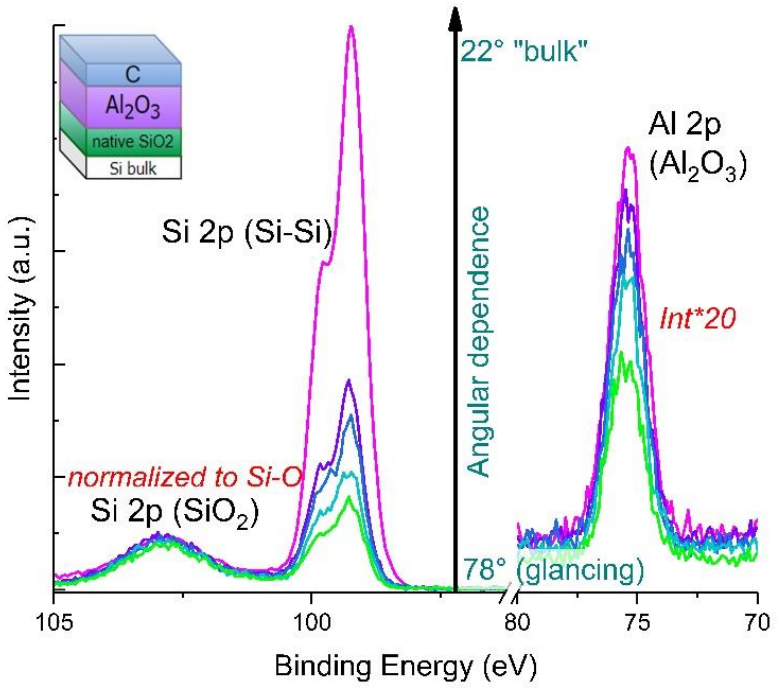

Figure 36. pARXPS data of an ultrathin Al_2O_3 sample with carbon contamination for Si 2p (left panel) and Al 2p (right panel). The violet line is from spectra recorded at the glancing emission angle, while the green and blue are spectra recorded from smaller angles which probe the bulk of the sample. The Al 2p spectrum has been increased by a factor of 20 for visual purposes.

The angular data in Figure 36 can be accurately described by a 3-layer model with sharp interfaces as demonstrated in Figure 37, which tends to confirm that interdiffusion is negligible in the stack. The sharp interfaces model relies on the difference between two materials at the interface and is specific to the ordering and thickness of the multilayer stack [6,7]. The carbon contamination in these samples is not studied.

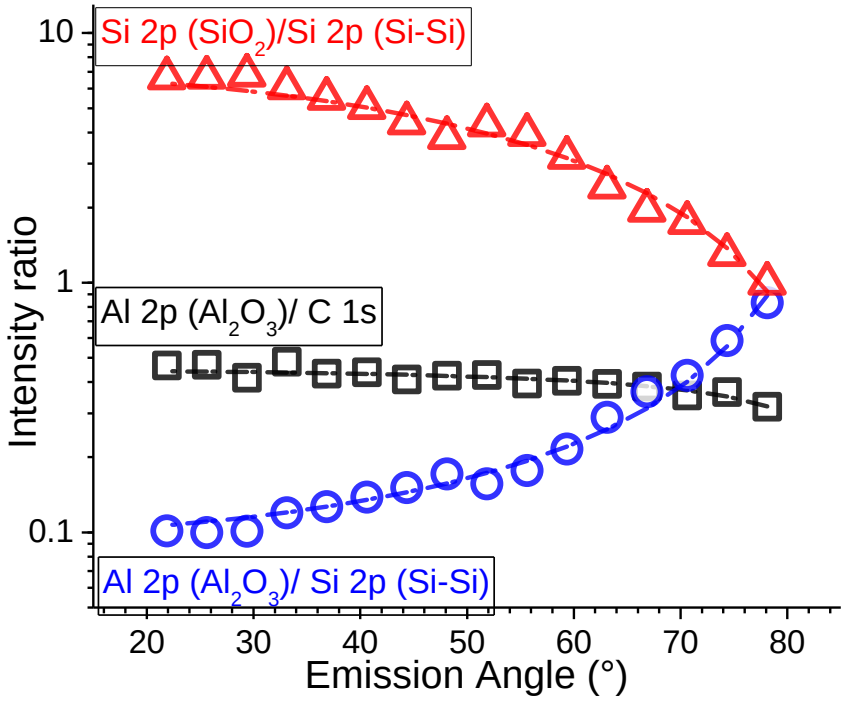

Figure 37. Non-destructive depth profile of the ultrathin Al_2O_3 sample with carbon contamination and SiO_2 layer.

Angular dependence in the pARXPS method can differentiate between the Si substrate and native oxide when no substrate surface treatment is applied prior to the deposition. The following results show that the method is also accurate enough to track the linear growth with increasing cycles of the ALD technique when a HF-last surface preparation is applied in order to prevent the oxide.

In Figure 38, pARXPS is confirmed to be effective in following the growth of ALD cycles from the starting phases up through the linear growth period. The pARXPS technique evidences the nucleation delay induced by HF surface preparation, followed by the expected linear growth once the surface is covered with Al_2O_3.

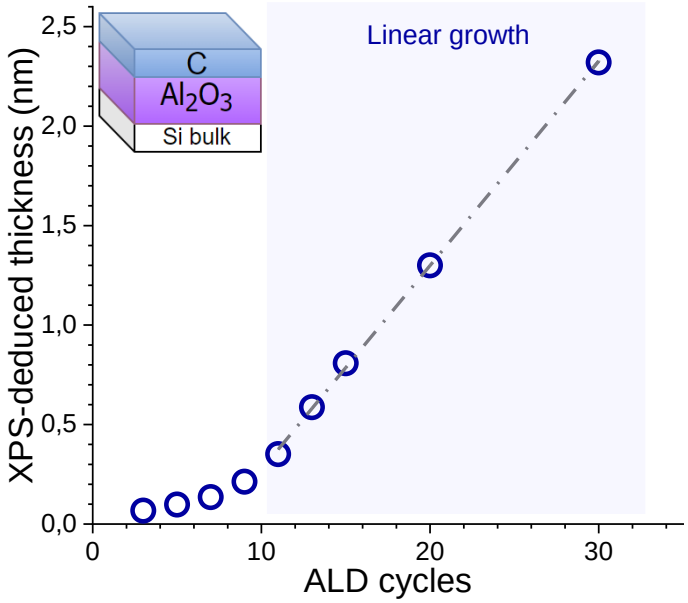

Figure 38. pARXPS thickness determinations as a function of ALD cycle for an ultrathin Al_2O_3 sample with a HF-last surface preparation.

pARXPS is useful tool to study the growth mechanisms of the ALD process. Combining it with complimentary non-destructive methods can deliver a comprehensive analysis of the structure.

4.2.3 pARXPS and WDXRF

Here we study ALD stacks of ultrathin Al_2O_3 when deposited over the native oxide as in the samples above, or after HF-last surface preparation.

In Figure 39, the thickness of the Al_2O_3 layer as determined by WDXRF and pARXPS is tracked with increasing ALD cycle repetitions. The two methods are well-correlated in the case of a chemical SiO_2 surface condition, with a less than one-percent difference between pARXPS and WDXRF determination. The thickness determinations by WDXRF and pARXPS are still correlated in the case of HF surface preparation but differ at the ALD cycle number extremities where pARXPS analysis shows greater thicknesses in earlier cycles, while WDXRF demonstrates greater layer thickness starting from 7 ALD cycles.

WDXRF, while non-destructive, is indiscriminate to the layer stacking order and position of the individual element. It is a physical analysis that provides the thickness of the layer without distinguishing between the silicon content in the bulk and its presence in the native oxide layer formed at the beginning of the deposition process. pARXPS allows the discrimination between the buried SiO_2 layer and the Si bulk. This permits unique characterizations for depositions with a HF prepared surface,

where the SiO_2 layer is negligible, and unprepared surfaces, where the buried layer is distinguishable by the technique.

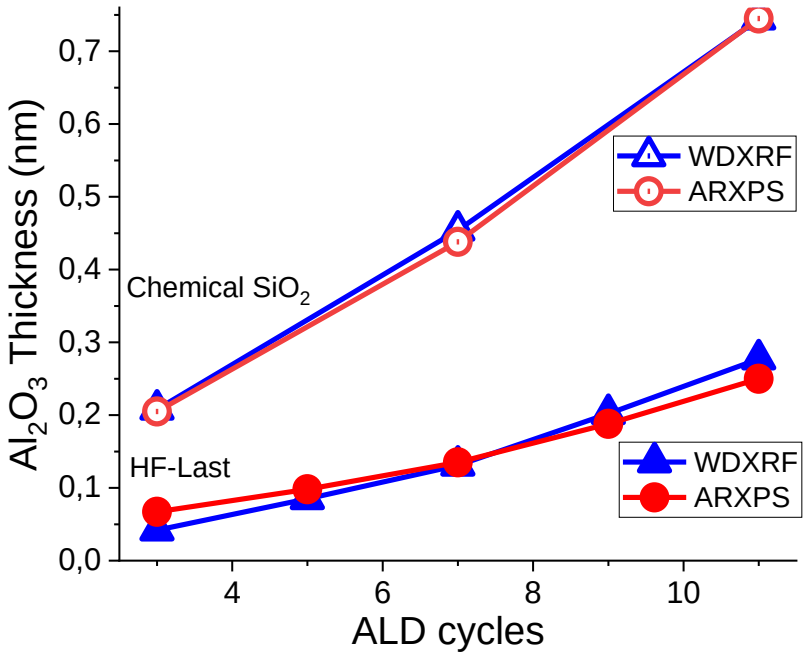

Figure 39. Al_2O_3 thickness as a function of the number of ALD cycles for chemical SiO_2 and HF-last sample preparation as determined by pARXPS and WDXRF.

The results from the two methods are shown in Table 5. The thickness determinations are largely in agreement for both methods (within 0.03 nm). Both pARXPS and WDXRF are slow techniques, taking a single measurement at a time which, in order to achieve a good signal-to-noise ratio, requires considerable time to record.

Table 5. Al_2O_3 thickness for increasing number of ALD cycles as determined by WDXRF and pARXPS.

Surface preparation		ALD	Al_2O_3 Thickness (nm)		Error
Chemical SiO_2	HF Last	ALD cycles	WDXRF	pARXPS	% Difference between methods
X		3	0.21	0.21	0 %
X		7	0.45	0.44	2 %
X		11	0.74	0.75	1 %
	X	3	0.04	0.07	54 %
	X	5	0.09	0.10	11 %
	X	7	0.13	0.14	7 %
	X	9	0.20	0.19	5 %
	X	11	0.28	0.25	11 %

Here we have presented a progressive study with three complimentary methods: LPD-ICPMS, WDXRF, and pARXPS. We showed how WDXRF can accurately and non-destructively determine the dose of Al within the uncertainty provided by LPD-ICPMS. We then showed the angular dependence of pARXPS and its capability to discern between the Si substrate and the SiO_2 layer formed before the ALD deposition process. Finally, we showed how pARXPS is uniquely sensitive to the nucleation process that occurs when a HF-last preparation is applied to the Si substrate.

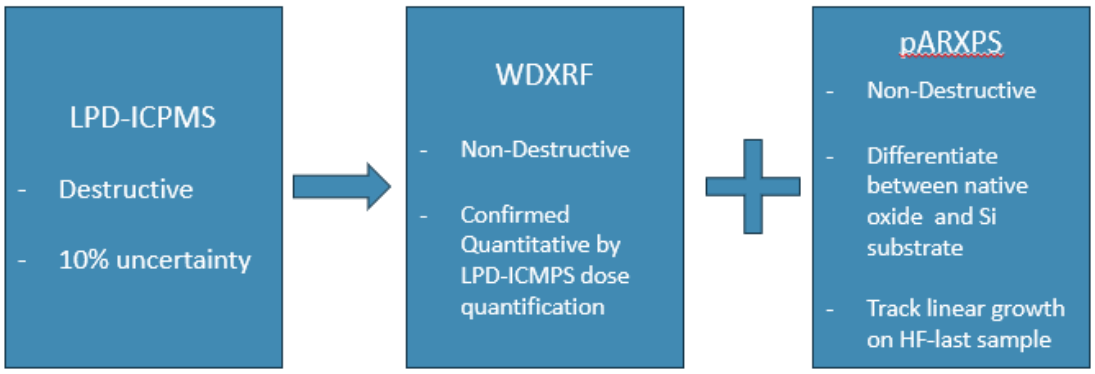

Figure 40. Al_2O_3 quantification by three powerful methods.

4.2.4 Results for thin Al_2O_3/HfO_2 bilayer with a chemical oxide

The IBA method discussed in Section 3 was applied to a thin bilayer sample of Al_2O_3 deposited over HfO_2 on native SiO_2 (1 nm)/Si substrate (Figure 34 (b)). In the previous section, we established the reliability of the ALD process to produce highly calibrated samples. By respecting the thicknesses

delivered by the deposition technique, we add a constraint to the possible depth distribution models. Additionally, we search for internal consistency amongst the elements in the sample in order to produce a sample model for which the layers lie directly one on top of the other, as we are confident of no interdiffusion between the layers. The precision of the technique is determined by the range of start and end depths which together deliver a good fit between the experimental and simulated inelastic background, as well as a reasonable thickness determination within a nanometer or so of the nominal thicknesses.

This sample appears in a previous work by Hönicke [1] in which it is evaluated with a reference-free GIXRF technique for quantifying the mass deposition of each layer. Hönicke's work demonstrates that the XRR technique suffers from uncertainties when dealing with ultrathin multilayered stacks. XRF at grazing incidence led to improved uncertainty in the mass deposition that is guaranteed by PTB National Metrology Institute (Germany). This sample was chosen as a test sample to assess IBA and pARXPS [8]. First, we discuss the result from the GIXRF reference technique in determining the mass deposition of Hf and Al in the sample as compared to determinations through the sharp-interfaces model of ARXPS. In order to compare the quantifications, the thickness obtained from ARXPS analysis (nm) is related to the density of the material (g/cm^3), delivering the mass deposition (ng/mm²) of each element in the sample. The results are available in Table 6. GIXRF gives a value of 3.14 ± 0.24 ng/mm² for the mass deposition of Al, while the ARXPS calculation yields 2.90 ng/mm². Hf mass deposition is 7.4 ± 0.6 ng/mm² according to GIXRF, and 9.0 ng/mm² by ARXPS. The proximity in these values further supports ARXPS as a quantitative method for depth profiling in high-*k* ALD samples.

Table 6. Mass deposition calculations for the thin Al_2O_3 and HfO_2 bilayer sample as determined by GIXRF and ARXPS.

	GIXRF Mass deposition (ng/mm²)	**pARXPS Thickness (nm)**	**pARXPS Mass deposition (ng/mm²)**
Al	3.14 ± 0.24	2.00	2.90
Hf	7.4 ± 0.6	1.5	9.0

The bilayer sample was subjected to additional analyses by IBA of the Al K*α* XPS spectrum. Here, IBA is proposed as a fast and non-destructive depth profiling method which, unlike ARXPS, is sensitive several nanometers deep into the material. In contrast to ARXPS, which requires high-resolution core-level spectra of each element for several angles, IBA utilizes a single survey scan from which to extract depth distribution information. For metrological purposes it is desirable to implement IBA with optimal

accuracy and ease of implementation enabled by spectrum analysis with minimal signal noise. Here, we investigate how gentle surface in-situ cleaning can improve the IBA analysis.

Figure 41 presents a complete depth profiling by IBA of a bilayer SiO_2 / HfO_2 / Al_2O_3 stack. The analysis was done before and after surface treatment using Gas Cluster Ion Beam (GCIB) for removing adventitious carbon contamination. The depth distribution, d, of oxygen is taken to represent the overall thickness, t, of the stack comprised of HfO_2, Al_2O_3, and SiO_2. The depth distribution of Hf, from Hf $4p_{3/2}$, can then be taken to indicate the HfO_2 layer, the subtraction of which enables inferring Al_2O_3 and SiO_2 overall thickness. Al 2p peak lies in the low binding energy region where peak overlap with Si 2p and Si 2s prevent IBA for either species. IBA requires that the background spectra be approximately 100 eV long and free of peaks from other elements. This is to prevent interference in the background signal.

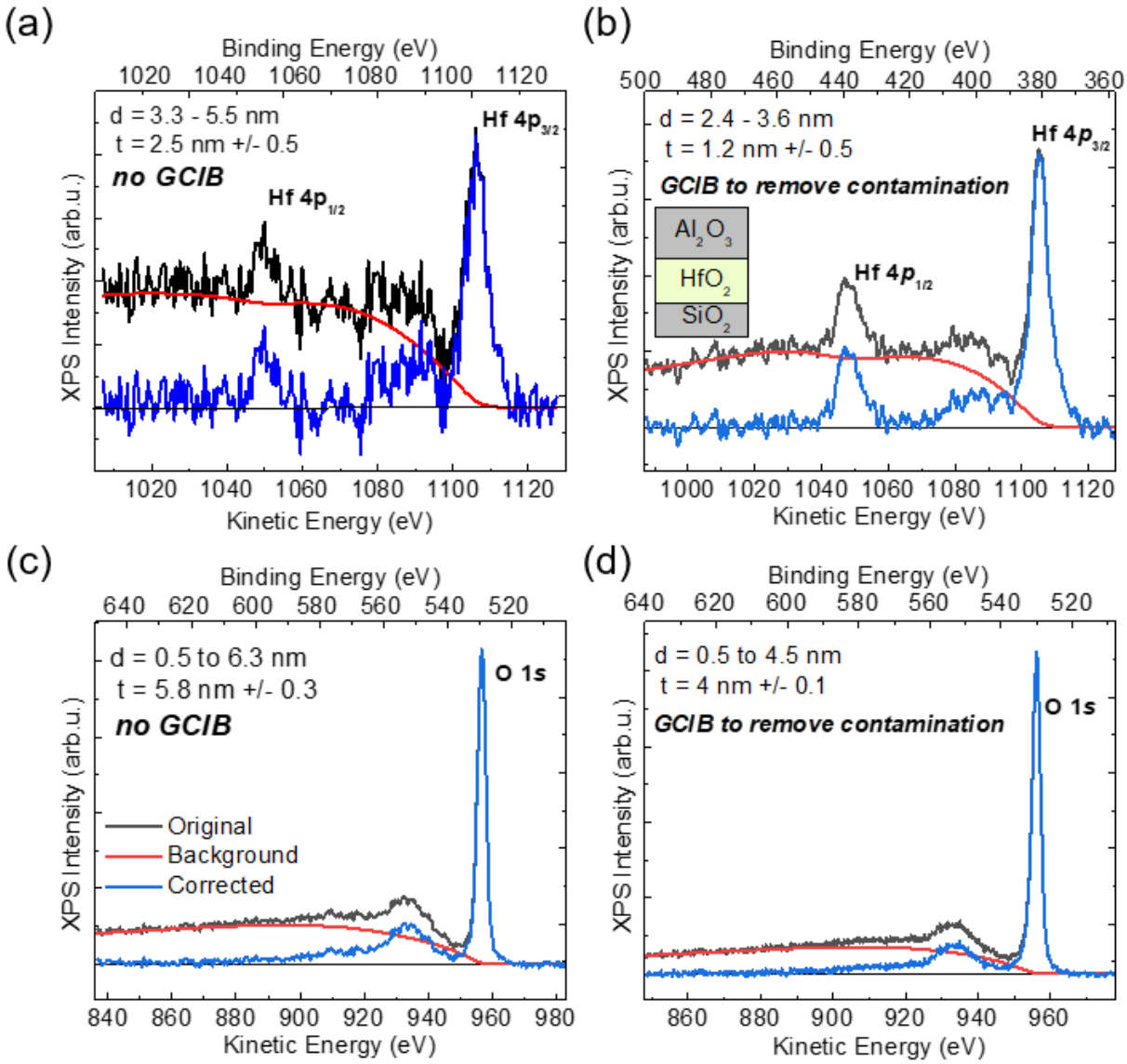

Figure 41. QUASES-Analyze IBA for the ALD bilayer stack: HfO_2 (1.5 nm) buried under Al_2O_3 (2 nm) before and after GCIB treatment. The black line is the original spectrum, the red line is the calculated inelastic background, and the blue line is the spectrum corrected for inelastic losses by subtracting the red line. The depth distribution, d, in (a) and (c) indicates a contamination layer on the sample which was removed by GCIB surface treatment. The HfO_2 and total sample thickness, t, is also closer to GIXRF and pARXPS determinations in (b) and (d).

The Hf 4p spectra in Figure 41 (a) and (b) contain the Hf $4p_{3/2}$ and Hf $4p_{1/2}$ doublet. The Hf $4p_{1/2}$ peak at 1050 eV KE is ignored in the evaluation of the fit since it originates from the same element. The inelastic background originates from this peak as well and is included in the calculation. The XPS spectra from the untreated sample in Figure 41 (a) and (c) reflect large and well-defined Hf 4p and O 1s peaks with pronounced backgrounds indicative of a wide elemental distribution in the sample. The resulting depth distribution for oxygen is from the surface of the material to 6.3 nm deep. The fit remains constant along the kinetic energy range. A resulting depth distribution of 3.0 to 5.5 nm for a thickness of 2.5 nm is not aligned with the expected 1.5 nm thickness of HfO_2 in the sample nor the modeled depth distribution of oxygen minus 1 nm SiO_2 and 2 nm of Al_2O_3. The start depth of 3.0 nm is

also not consistent with the anticipated 2 nm thickness of the Al_2O_3 overlayer. A significant photoelectron signal from C 1s was evident in the spectra and suggests a surface contamination layer (see Figure 42).

After surface treatment by GCIB, the signal noise in both spectra is somewhat diminished. The resulting depth distribution of oxygen is from 0.5 nm below the surface to 4.5 nm deep. The carbon signal was eliminated after surface treatment, so the displacement of O 1s is unlikely to be from contamination. Rather, the oxygen content is different across the three metal oxide layers, and so the photoelectron transport is unlikely to be perfectly reproducible. While elastic effects are not considered in the software modeling, they do have a small influence on the transport process which could come into play for this error in the analysis [9,10]. In Figure 41 (b), the fit between the modeled and experimental background has improved, and the noise reduced. In alignment with oxygen modeling after removal of surface contamination, hafnium is shown modeled at a depth from 2.4 to 3.6 nm. Thus, the XPS-IBA results are well-aligned to the nominal values predicted by the number of cycles in the ALD process.

Figure 42 shows that IBA with GCIB is accurate to nominal deposition data within 6% and provides information on the location of interfaces within a tenth of a nanometer. In addition to being a faster method than pARXPS, less information on the sample is needed for IBA. pARXPS can provide a more precise measurement, with a precision down to a tenth of an angstrom. The visual fitting uncertainty in the IBA procedure is variable and depends on the signal-to-noise ratio and general sensitivity of the model to changes in the Start and End Depth parameters. As material layers get too thick for pARXPS ($3\times$IMFP = 5.5 nm for Hf $4p_{3/2}$), IBA becomes the more relevant depth profiling technique for depth profiling. This is demonstrated in the following section.

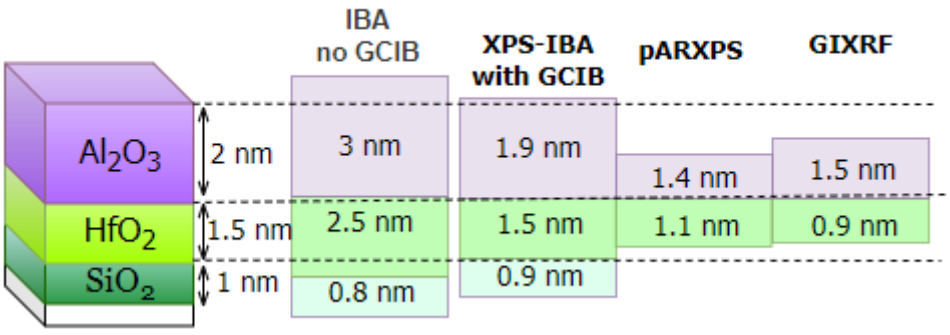

Figure 42. Comparison of thickness determinations by IBA, pARXPS, and GIXRF. IBA distributions are shown for before and after a GCIB surface treatment in order to remove contamination.

4.3 Results for thick bilayer samples with Cr Kα

In comparison to logic applications, some technologies such as power nanoelectronics require greater thicknesses of the dielectric layers. The thickness reaches a range for which traditional XPS using soft

X-rays are limited by the IMFP of the element. As discussed in Chapter 2, the IMFP is directly related to the kinetic energy of the photoelectrons and so to the energy of the X-ray source. It is therefore necessary to investigate lab-based analytical methods for determining depth distributions over 3×IMFP below the surface. ARXPS especially is relegated to a purely surface-sensitive technique, for which the typically 1 nm-IMFP does not allow probing more than 10 nm. For truly buried layers lying under a top electrode, capping layer, or dielectric, a higher energy source is necessary for non-destructive depth profiling of the critical interfaces. Lab-based HAXPES using a Cr Kα source was evaluated on six samples of Al_2O_3 and HfO_2 stacks with increasingly thick overlayers up to 24.4 nm (Figure 34 (c), Table 1) to give a maximum IMFP of 8.4 nm for O 1s (8×IMFP = 67.2 nm). The layers were thick enough to use an XRR technique as a reference to assess IBA thickness results. The IBA thicknesses obtained from QUASES-Analyze using $K(T)_{Universal}$ were compared with QUASES-Generate using bulk reference spectra. The impact of an even higher photon energy was investigated by recording the spectra using a Ga Kα source (9.25 keV). Finally, an AR-HAXPES routine was introduced as a complimentary analysis to improve the IBA method.

Following the guidelines of Risterucci [11], we aim for a very good fit at the lower kinetic energy region of the spectrum for deeply buried or thick layers. The goal of this section is to evaluate the precision and accuracy of the method for various sample configurations and elements in the metal-oxide stacks.

4.3.1 The Cr Kα HAXPES spectrum of buried HfO_2 with an Al_2O_3 overlayer

Figure 43. Cr Kα HAXPES spectrum of both Al2O3 and HfO2 layer combinations. The left side of the spectrum contains high energy transitions which are not available with an Al Kα X-ray source. The right side of the spectrum depicts the low binding energy signals (i.e. high kinetic energy region) which are accessible through traditional XPS, and where overlapping peaks and background signals make IBA not applicable.

Whatever the stacking samples (buried HfO_2 with Al_2O_3 overlayer (samples A) or buried Al_2O_3 with HfO_2 overlayer (samples H)), in the low kinetic energy region (i.e. high binding energy), the deeper Si 1s, Hf 3d, and Al 1s core levels are well suited for analysis because the peaks do not overlap, unlike the soft-XPS case using Al and Mg Kα sources. These transitions are necessary for a complete depth profiling of the samples incorporating each element present in the material.

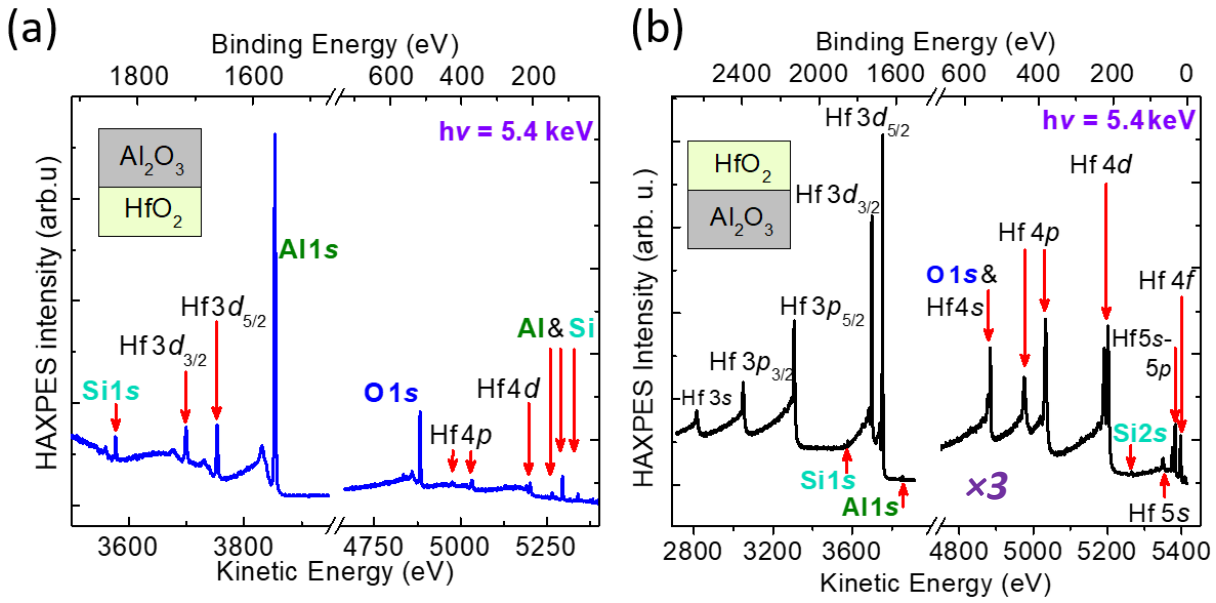

Figure 43. Cr Kα HAXPES spectrum of both Al_2O_3 and HfO_2 layer combinations. The left side of the spectrum contains high energy transitions which are not available with an Al Kα X-ray source.

4.3.2 Overlayer depth distribution

The IBA results for the Al_2O_3 overlayers are presented in Figure 44 for A1, A2 and A3 samples. The Al 1s inelastic background was well-modeled by $K(T)_{Universal}$, with 100% accuracy to the XRR values and a fitting uncertainty in the visual inspection of 0.2 nm for all three analyses. A significant plasmon peak forced the IBA fit to be assessed 50 – 90 eV after the peak. As shown in Figure 43, the full range of the inelastic background was not available for analysis due to the emergence of the Hf $3d_{5/2}$ peak starting at around 3755 eV. The start depth for the 9.9 nm and 14.8 nm (Figure 44 (a), (b)) was shifted 0.5 and 0.2 nm, respectively. This indicates some contamination on the samples and, considering the samples had no surface treatment, is plausible.

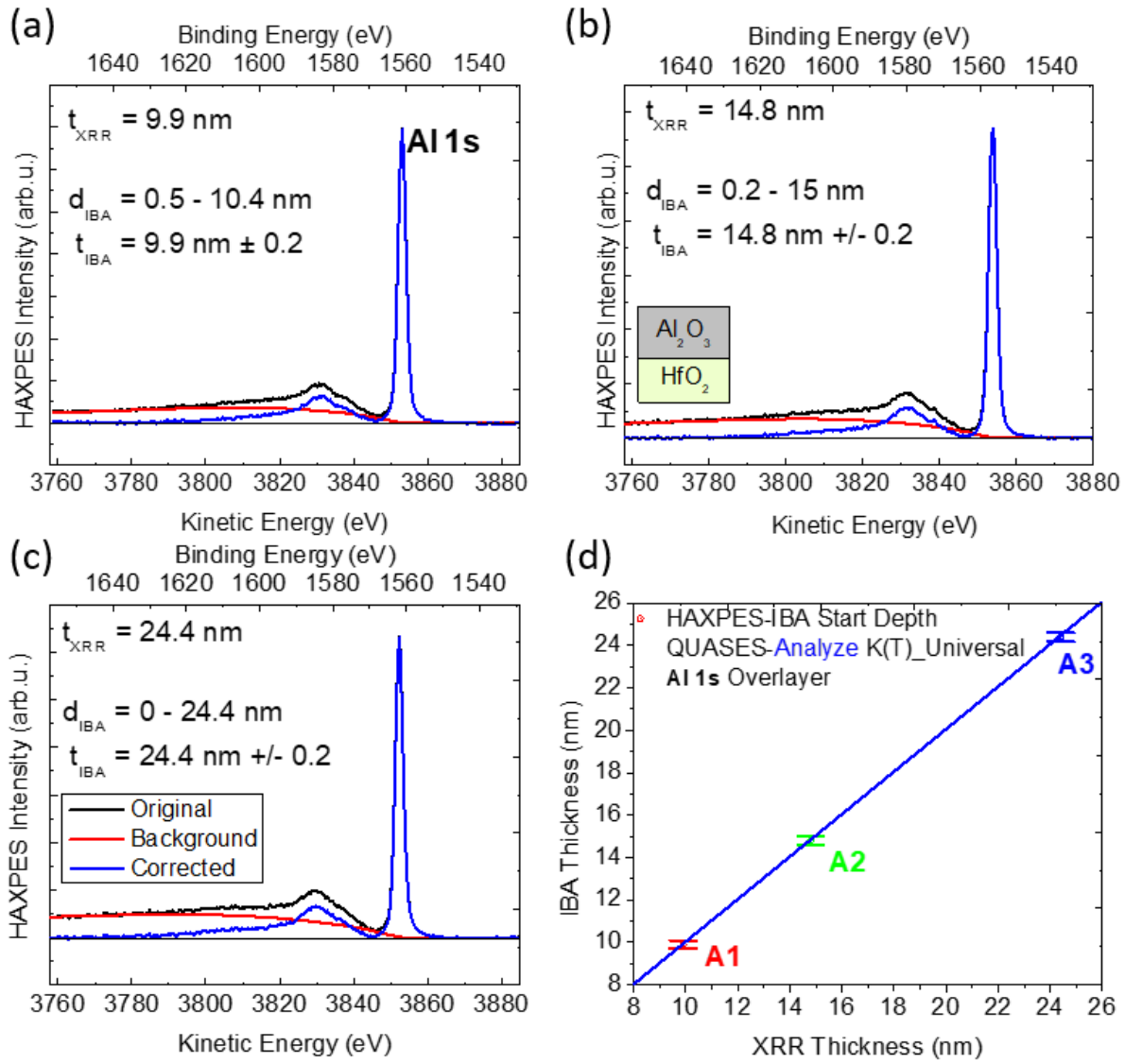

Figure 44. (a-c) QUASES-Analyze HAXPES-IBA results for Al 1s in Al_2O_3 overlayers for 3 samples. The inelastic background 50 – 90 eV after the core peak is well-modeled by $K(T)_{Universal}$. (d) Shows the linear dependence between the IBA and XRR-estimated thicknesses.

The HAXPES-IBA results for Hf 3d in the HfO_2 overlayer samples H1, H2, and H3 are presented in Figure 45. The start depth for the 13.6 and 18.2 nm thick HfO_2 layers (Figure 45 (b), (c)) was 0.7 nm, suggesting surface contamination. The fitting uncertainty in the visual inspection increased to +/- 0.7 nm in the thickest sample (Figure 45 (c)). Figure 45 (d) shows a good accuracy between the layer thicknesses obtained by IBA and XRR methods.

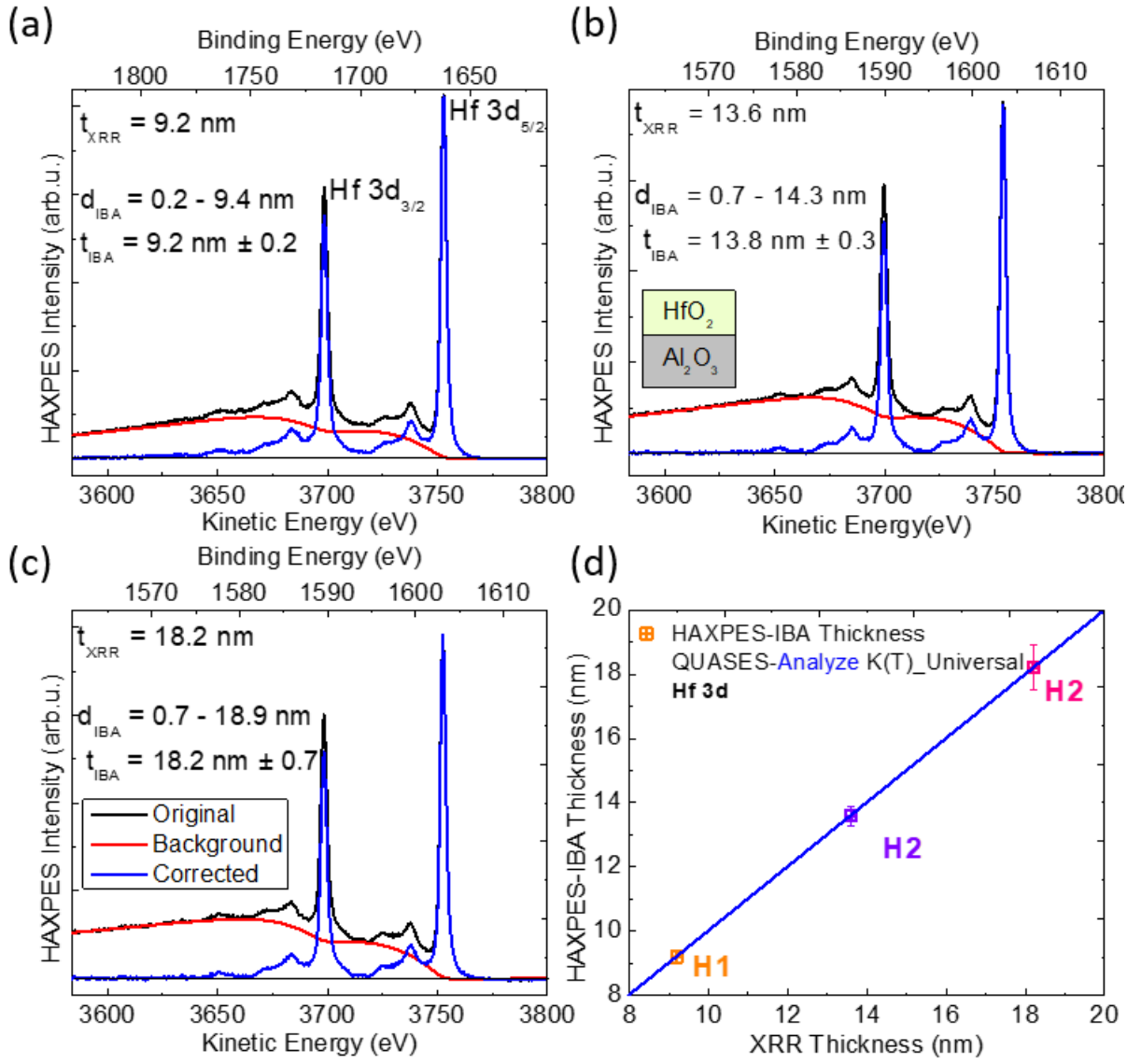

Figure 45. QUASES-Analyze HAXPES-IBA results for Hf 3d in HfO_2 overlayers. The inelastic background fit is evaluated starting at 3650 eV, but the short region between the doublet peaks is calculated as well.

Both sample sets had depth distribution solutions within the ranges provided by XRR, with minimal surface contamination and end depth values at the anticipated interfaces. The IBA solutions had low fitting uncertainty, meaning the model was sensitive to changes in the start and end depth parameters.

4.3.3 Buried layer depth distribution

Here we present the results from the Al 1s or Hf 3d signal in the buried layer. The layer thickness, t, is evaluated as well as a depth distribution, d, which should agree with the thickness of the overlayer. This interface position indicated in Figure 46 as d_1 (start depth of layer A) should be at or around the total thickness (or end depth) of the overlayer.

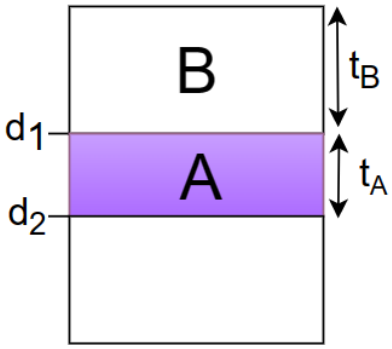

Figure 46. A bilayer model consisting of the otherlayer B and buried layer A. t_B and t_A are the individual layer thicknesses. d_1 to d_2 is the depth distribution (denoted d in IBA figures) of A. d_1 also represents the interface position between B and A according to A.

In contrast to the overlayers, IBA in the buried layers of the two samples yielded different results. Below we will discuss IBA of the buried Al_2O_3 layer in the H series, where t and d_1 were consistent with IBA of Hf 3d but imprecise. After, we discuss the results from buried HfO_2 in the A sample set which do not agree with IBA of Al 1s in the overlayers.

The IBA results for Al 1s in 2.7 – 2.8 nm Al_2O_3 buried under HfO_2 are shown in Figure 47. Despite the implementation of an increased takeoff angle, the Al 1s signal could not be meaningfully resolved in H3 in order to facilitate analysis of the inelastic background. This is due in part to the weak signal of Al 1s photoelectrons traveling through the dense HfO_2 layer, but also as a result of the especially strong Hf $3d_{5/2}$ signal which follows just 100 eV behind. Sensitivity of the technique is lower in the HfO_2 overlayer series due to the density of HfO_2 and its contribution to the reduced inelastic mean free path of the buried species. Further experiments increasing the takeoff angle of the experiment did not improve resolution of Al 1s in H3.

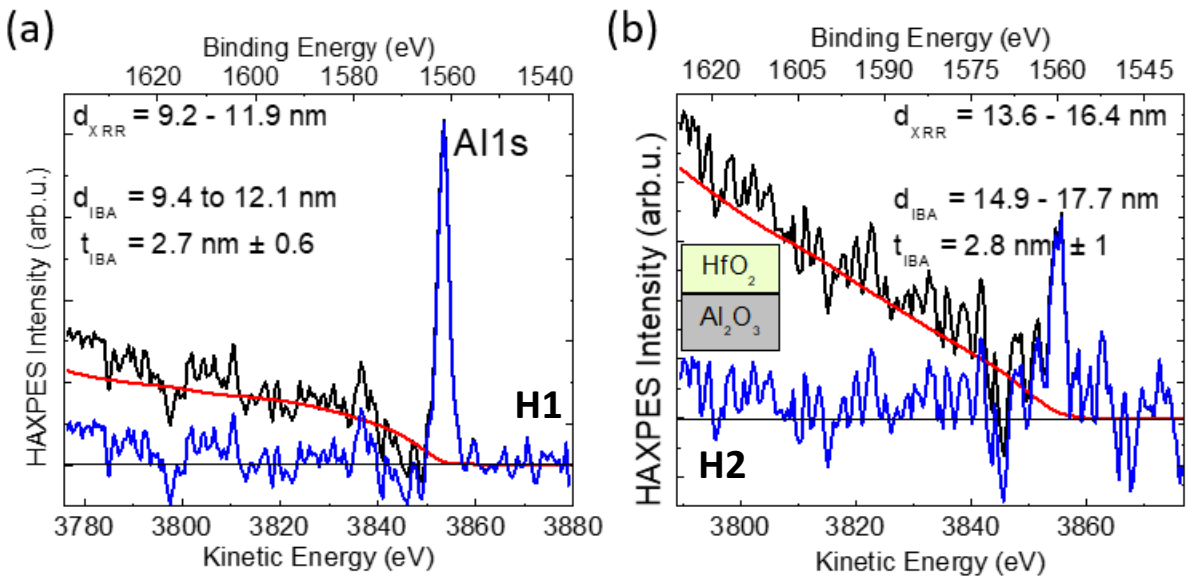

Figure 47. QUASES-Analyze HAXPES-IBA results for Al 1s buried under HfO_2. The background signal of Al 1s in H3 was not available for analysis due to lack of intensity.

A qualitative IBA result is seen in Figure 48. This figure depicts several long scans in the Hf 3d range for samples with a thin HfO_2 layer buried under Al_2O_3 layers of increasing thicknesses (Figure 48 (a), (b), (c)), as well as a spectrum of pure HfO_2 (Figure 48 (d)). An increasing inelastic background is seen in respect to a decreasing elastic peak signal with increasingly buried layers.

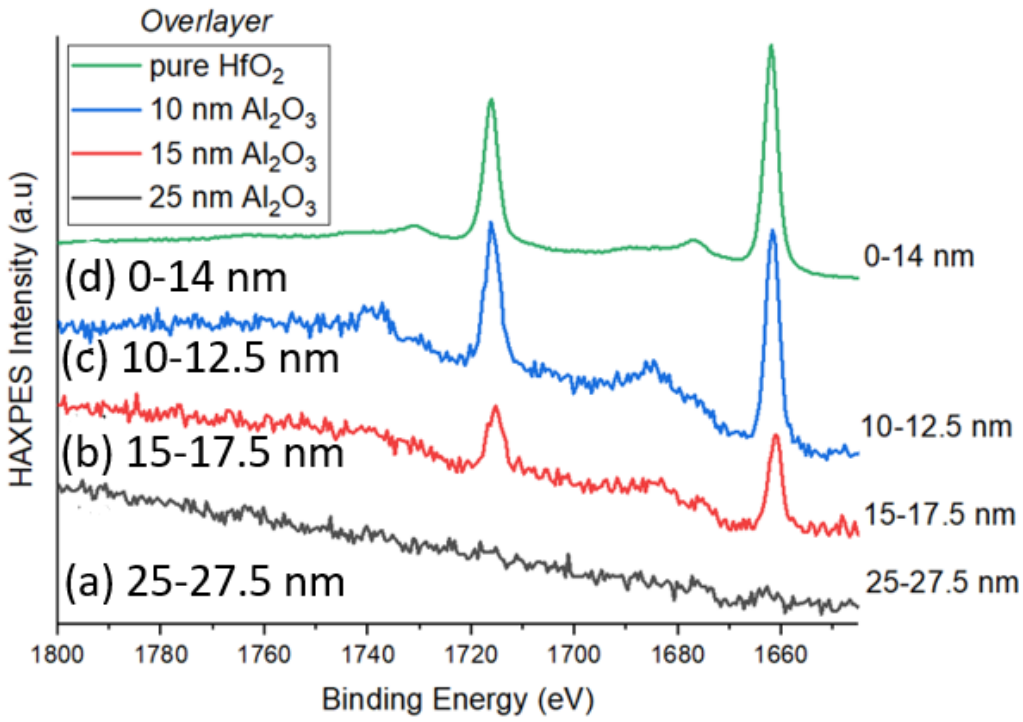

Figure 48. Long scans over the Hf 3d range for (a) deeply buried HfO_2, (b) HfO_2 buried approximately 15 nm below the surface, (c) HfO_2 approximately 10 nm below the surface, and finally, (d) bulk HfO_2. The increasing background in respect to a decreasing elastic peak signal is demonstrated with increasingly buried layers [12].

The IBA results for Hf 3d buried under Al_2O_3 are shown in Figure 49. The Hf 3d signal from the 2.4 nm buried HfO_2 layer does not demonstrate the anticipated spatial depth distribution. The optimal start and end depth obtained from the inelastic background fitting procedure reflects a two-nanometer shift deeper into the bulk and away from the Al_2O_3 interface. The buried HfO_2 layer in A2 is similarly shifted as in A1. Hf 3d in A3 showed an opposite effect, presenting a median IBA solution which placed the start depth of the layer at 23 nm in the place of the anticipated 24.4 nm. Uncertainty in the IBA result, however, increased to +/- 2 nm in this analysis, thus allowing the 24.4 nm solution. Overlap or empty space between the layers does not make physical sense and shows that the present model does not properly describe the interfaces. The layer thicknesses, however, agreed with XRR and were accurate.

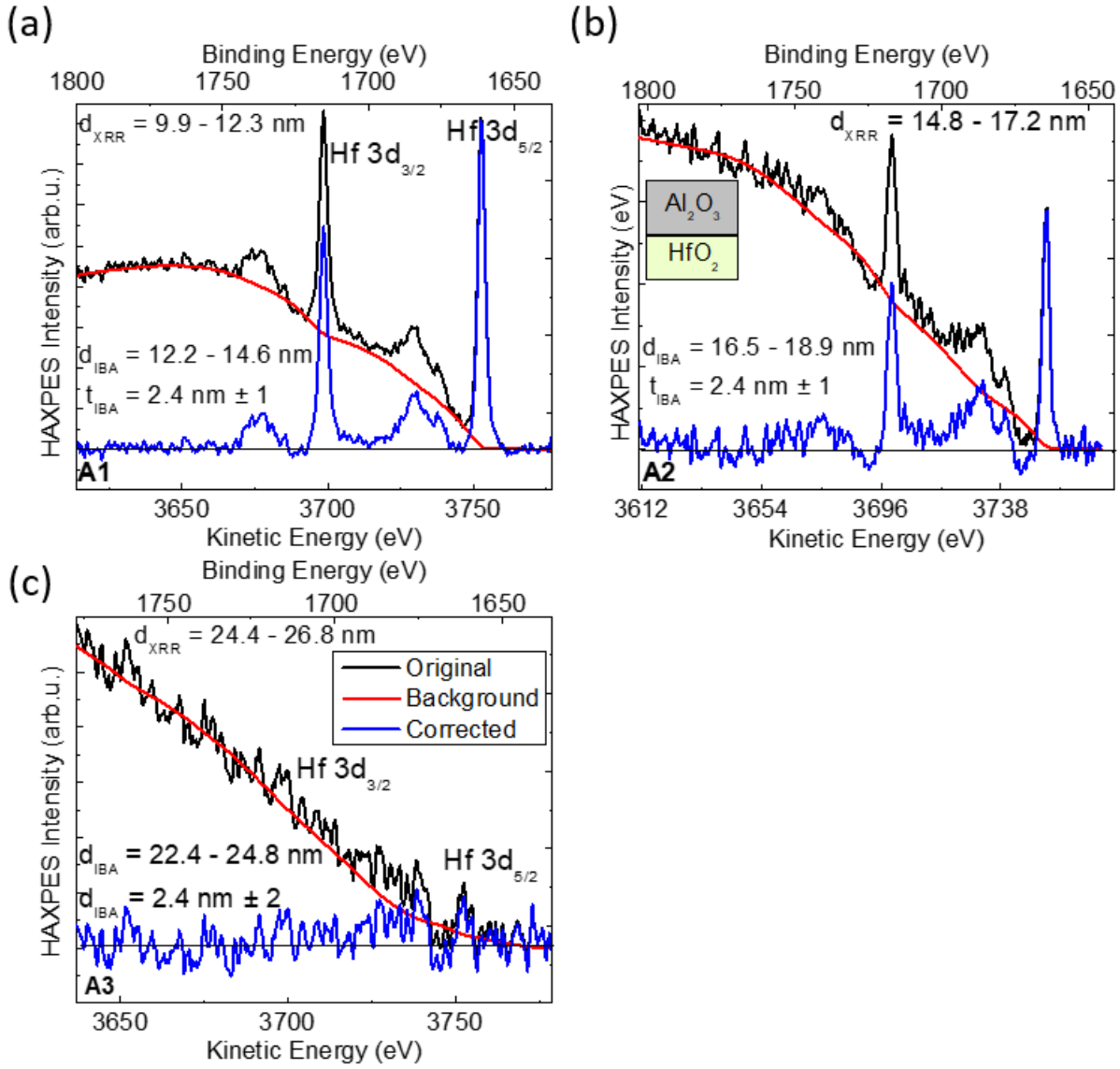

Figure 49. QUASES-Analyze HAXPES-IBA results for Hf 3d in the Al_2O_3 over layer samples.

These results show that the metal peaks from the oxide layers alone do not provide enough information for a conclusive depth distribution model. IBA of oxygen and silicon may help determine the total thickness and the location of the interface with the Si substrate.

4.3.4 Obtention of total bilayer thickness

The Si 1s signal originating from the silicon substrate provided additional information of the depth distribution of the bilayers. The start depth of Si 1s was taken to represent the total thickness of the metal-oxide bilayer and compared against the XRR total thickness. An example of the Si 1s IBA is shown below in Figure 50. The background fit is evaluated starting at 3510 eV KE. SiO_2 and Si-O contributions may be seen in the spectrum.

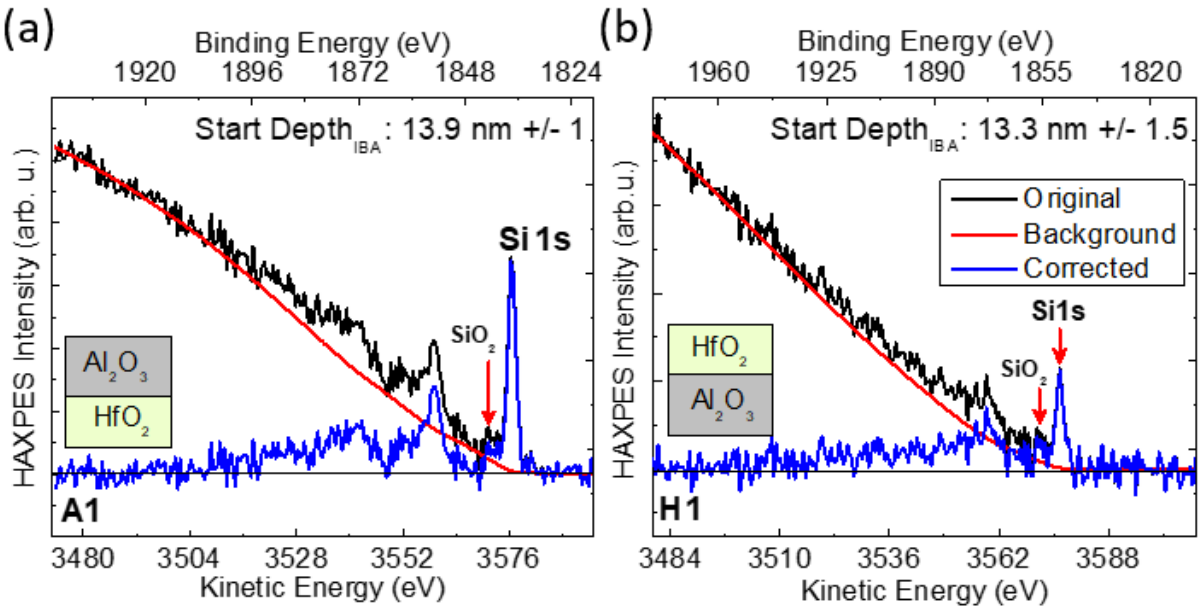

Figure 50. HAXPES-IBA of Si 1s with a Cr Kα source and K_Universal for sample (a) A1 and (b) H1.

The Si 1s analysis had high uncertainty in the visual fitting procedure, ranging from +/- 1 – 4 nm. Fitting uncertainty in the analysis increased with overlayer thickness. The results are shown in Table 7.

Table 7. QUASES-Analyze HAXPES-IBA results for Si 1s for all bilayer samples using K(T)_Universal.

Cr Kα QUASES-Analyze K(T)_Universal Si 1s				
Sample	**XRR Thickness (nm)**	**Cr Kα IBA Thickness (nm)**	**Fitting Uncertainty (nm)**	**% Error against XRR**
A1	12.3	13.9	1	13 %
A2	17.2	17.5	1.5	1.7 %
A3	26.8	23.0	4	14 %
H1	11.9	13.3	1.5	-11.7 %
H2	16.4	16.4	2	0 %
H3	21	23.5	2.5	-11.9 %

Aside from the metal transitions, O 1s was accessible in the low BE region of the Al_2O_3 overlayer series.

In the spectra of the HfO_2 overlayer samples, the continuous background before the O 1s signal was blocked by preceding Hf signals and the overlapping Hf 4s signal, preventing its analysis. This obstacle was circumvented by accessing the O KLL peak at 4.9 keV and increasing the TOA to 65°. Example spectra from A1 and H1 are shown in Figure 51.

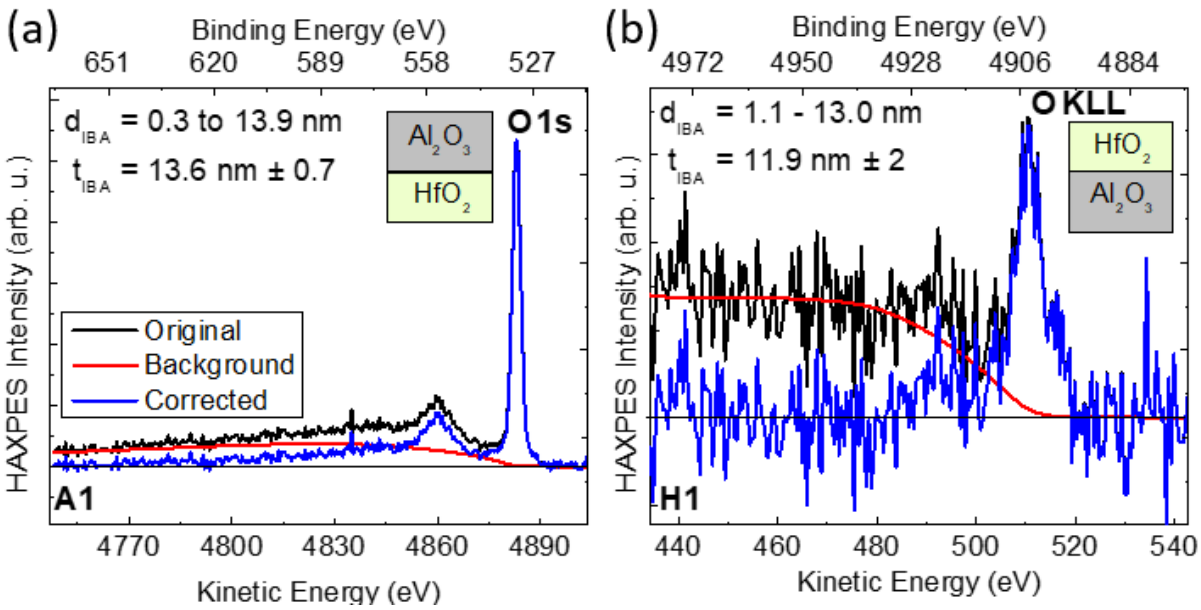

Figure 51. HAXPES-IBA of O 1s in QUASES-Analyze. The O 1s depth distribution can be taken as the total thickness of the bilayers

IBA of the O KLL spectrum could only provide the start depth and confirm that the layer was thicker than 10 nm, as the model was not sensitive to increasing the end depth even to several hundred nm.

Table 8. Cr Kα HAXPES-IBA results of O 1s in both layers modeled with $K_{\_Ujniversal}$.

Sample	XRR Thickness (nm)	Cr Kα IBA Thickness (nm)	Fitting Uncertainty (nm)	% Error against XRR
A1	12.3	13.6	0.7	13.0 %
A2	17.2	17.2	1.0	-1.7 %
A3	26.8	26.0	1.0	14.2 %

4.3.5 Discussion regarding internal consistency

The analysis of every element in the sample permitted the cross-verification of interface positions and layer thicknesses. The interface position d_{1A} or d_{2B} depending on the layer (Figure 52) is determined by IBA of both the buried layer A and overlayer B. Agreement between the d_{1A} and d_{2B} is important to control for internal consistency and to provide a realistic IBA model. An interface position d_{1A} which is greater than d_{2B} (Figure 52 (a)) would indicate the lack of contact between the layers. In this case, we can look at the TPP-2M IMFP and confirm if the error in the fitting procedure is equivalent to the error in the IMFP value needed to reach an adequate model. When d_{1A} is less than or equivalent to d_{2B}, we can assume that an interface is present which may be narrow or broad based on the individual uncertainties in the interface position.

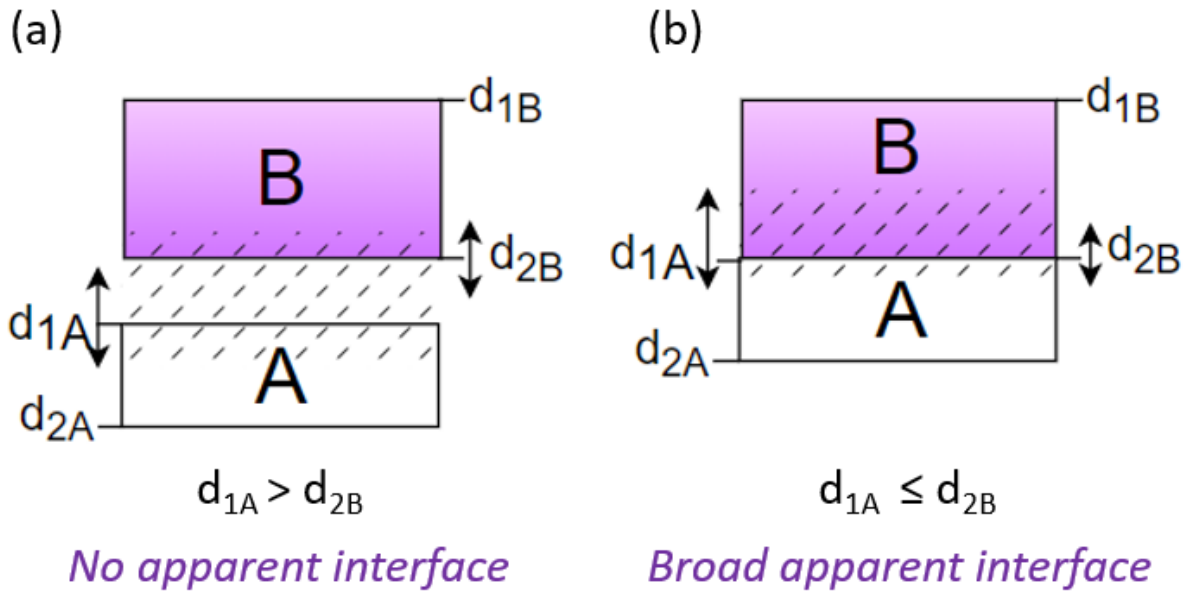

Figure 52. The interface positions d_1 and d_2 give the depth distribution of the layer. d_1 locations are given by the end depth of layer B (d_{2B}) and the start depth of layer A (d_{1A}). The dashed zone indicates the range of possible interfaces or gaps between the two layers according to the uncertainty of the fitting procedure.

Figure 53 shows the differences between d_{1A} and d_{2B} for all the samples (except for H3, where buried Al 1s is not resolved). $d_{1A} \sim d_{2B}$ for H1 and H2, but for none of the Al_2O_3 overlayer samples (A1, A2 and A3). It is important to note that, while the median start depth of Hf 3d in the A3 sample is inaccurate to the overlayer end depth, the uncertainty in the analysis allows for agreement in d_{1A}/d_{2B}. The disparity in the d_{1A}/d_{2B} position in A1 and A2 may be due to unaccounted for elastic effects in the spectrum, which has a greater effect on the higher energy-loss region of the spectrum [13]. Photoelectrons experiencing greater inelastic collisions are most likely originating from greater depths, and so are also more likely to experience elastic scattering losses. The calculated inelastic background dips slightly below the experimental background around 3625 eV in spectra (b) and (c) of Figure 49, supporting this theory.

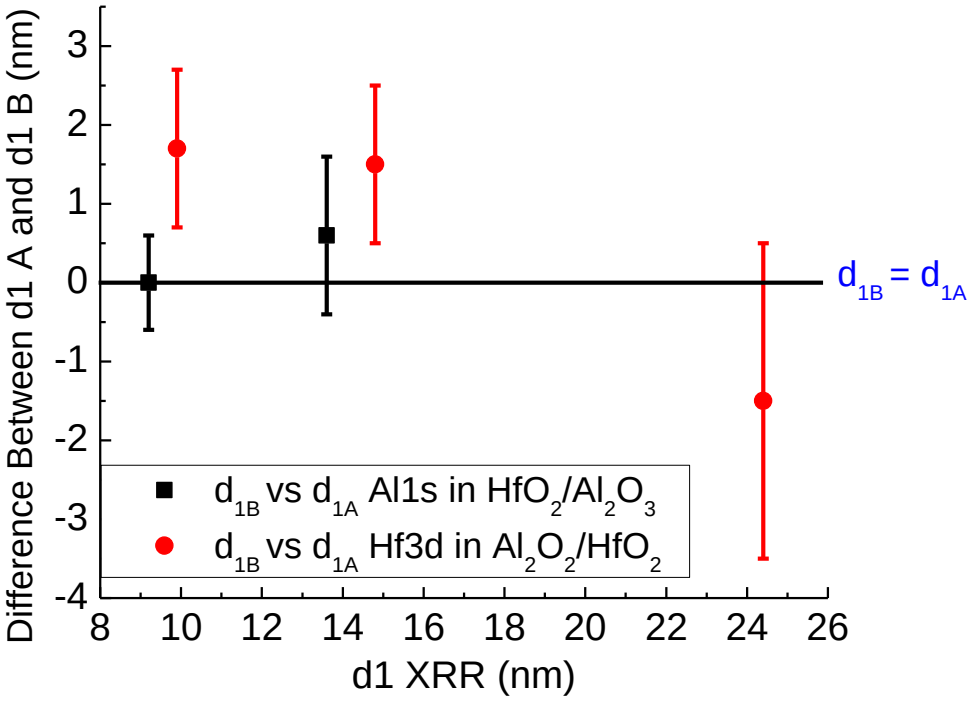

Figure 53. Disparity in the interface location d_1 between the buried layer A and overlayer B in the bilayer samples.

Uncertainties in the IMFP and K(E) parameters may explain the shift seen in the depth distribution of the buried HfO_2 layers. In this next section, we will discuss alternative methods that reduce the error in K(E). First, we present a method executed with the QUASES-Generate software that uses a reference spectrum in the place of $K(E)_{Universal}$. Second, we investigate the error in the Si 1s IBA by applying an effective K(E) which accounts for the Si metal K(E) as well as K_Universal.

4.3.6 Alternative methods to reduce error in the IBA results

An alternative method using QUASES-Generate and bulk reference spectra was investigated as a complementary analysis. The use of a reference spectrum allowed for the analysis of O 1s in the HfO_2 overlayer samples, introducing greater rigor to the analysis. The QUASES-Analyze spectrum of O 1s in H1 is shown below in Figure 54.

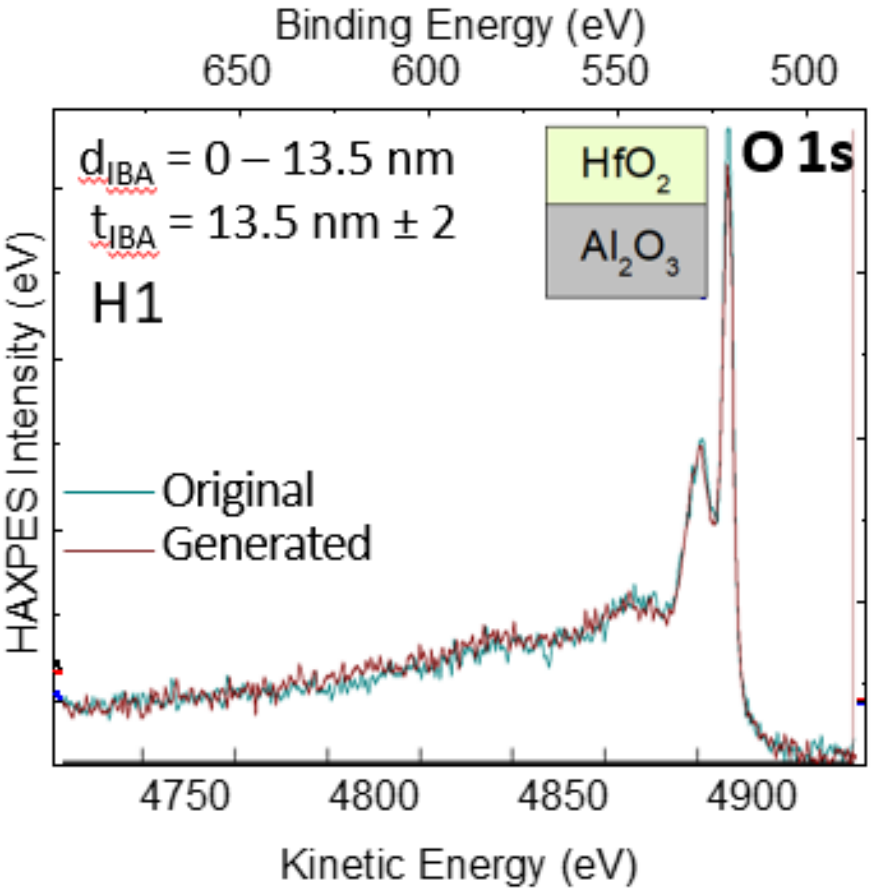

Figure 54. QUASES-Generate spectrum of O 1s in H1.

The thickness determinations with QUASES-Analyze and $K(T)_{Universal}$ are compared with QUASES-Generate and a reference spectrum in Table 9. The IBA thicknesses determined using the two-parameter Universal cross-section were accurate to XRR in all cases except for Si 1s in A1 and H2. This is unsurprising, as the Si 1s signal is weak, and $K(T)_{Universal}$ is does not best describe the Si inelastic scattering cross-section [14].

The use of a reference sample had little effect on the resulting layer thicknesses, except to increase the number of IBA solutions with error between the IBA result and the XRR thickness. It is also notable that the uncertainty increased when using a reference spectrum. IBA precision with $K(T)_{Universal}$ was to the order of 0.2 - 1 nm and increased to 0.5 – 4 nm for the buried layers. The reference and measured spectra were not perfectly aligned, making the assessment of the background fit more difficult. The bulk references are not identical to the individual layers, so small differences may occur which hinder the analysis. QUASES-Generate is also a more time-consuming method and requires homogeneous reference samples which may not be immediately available or easy to produce [15]. The ALD method specifically is not ideal for very thick Al_2O_3 samples since the amorphous structure is likely to become crystalline with so many cycles.

Table 9. QUASES-Analyze and QUASES-Generate IBA Thicknesses of all Bilayer Samples.

Sample	**Layer**	**XRR Thickness (nm)**	$K(T)_{Universal}$ **QUASES-Analyze Thickness (nm)**	Reference Spectra **QUASES-Generate Thickness (nm)**	**Accuracy of QUASES-Generate Thickness % Error to XRR**
A1	Al_2O_3	9.9	9.9 ± 0.2	9.9 ± 2	0.0%
	HfO_2	2.4	2.4 ± 1.1	2.4 ± 2.5	0.0%
	Surface to Si	12.3	13.9 ± 1 **(13% error to XRR)**	14.3 ± 0.5	16.2%
A2	Al_2O_3	14.8	14.8 ± 0.2	14.8 ± 2	0.0%
	HfO_2	2.4	2.4 ± 0.9	2.4 ± 0.9	0.0%
	Surface to Si	17.2	17.2 ± 0.4	17.2 ± 1	0.0%
A3	Al_2O_3	24.4	24.4 ± 0.5	23 ± 2	5.7%
	HfO_2	2.4	2.4 ± 1.8	2.4 ± 4	0.0%
	Surface to Si	26.8	26.8 ± 0.6	26.8 ± 3	0.0%
H1	HfO_2	9.2	9.2 ± 0.2	9.2 ± 1.5	0.0%
	Al_2O_3	2.7	2.8 ± 1	2.8 ± 3	0.0%
	Surface to Si	11.9	11.9 ± 0.6	15 ± 0.7	3.7%
H2	HfO_2	13.6	13.6 ± 0.8	13.6 ± 1	0.0%
	Al_2O_3	2.8	2.8 ± 1	2.8 ± 2.5	0.0%
	Surface to Si	16.4	17.1 ± 0.8 **(4% error to XRR)**	18 ± 0.5	9.7%
H3	HfO_2	18.2	18.2 ± 0.9	18.2 ± 1	0.0%
	Al_2O_3	2.8	-		
	Surface to Si	21	21 ± 1	21 ± 1	0.0%

The inelastic scattering cross-section for Si is different from that of metal-oxides [16], therefore a weighted inelastic scattering cross-section as discussed in Section 3 was considered which took into account $K(T)_{Universal}$ for the metal oxide bilayer and $K(T)_{Si}$ for the substrate.

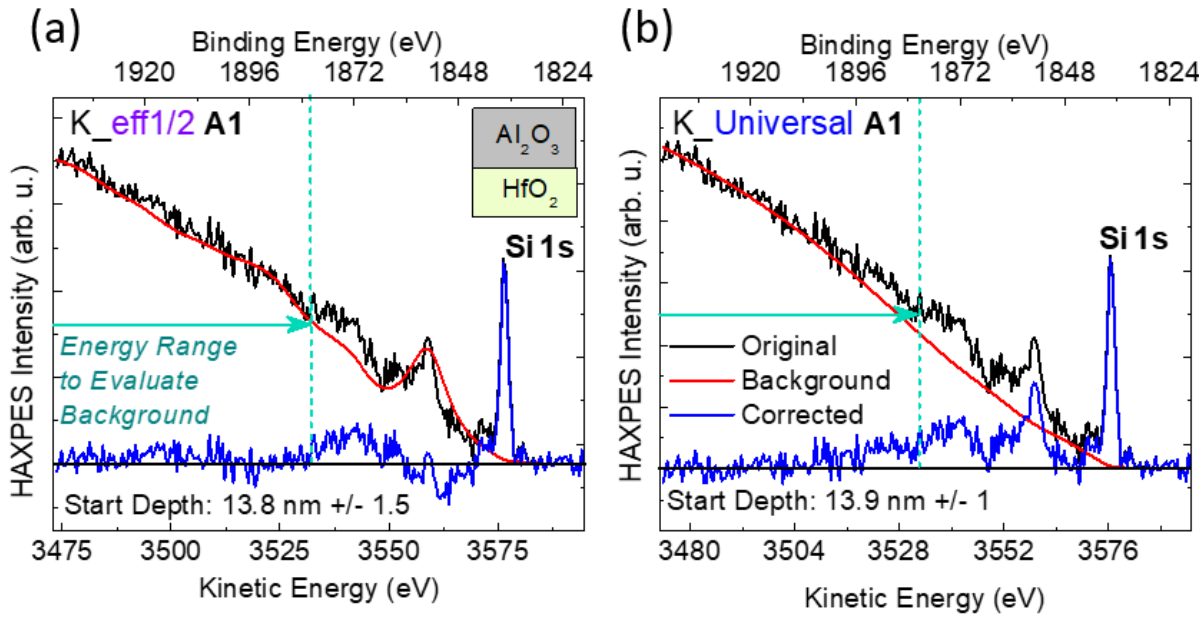

Figure 55 shows the QUASES-Analyze IBA spectra for Si 1s in sample A1 modeled with either $K(T)_{Universal}$ or $K(T)_{eff\_1/2\ 40\%\ Universal\ 60\%\ Si}$. In Figure 55 (a), for which the effective cross-section was applied, we see that the inelastic background fit may be assessed in the energy range of 3470 – 3530 eV KE. The range is reduced 10 eV in Figure 55 (b), where $K(T)_{Universal}$ does not account for the plasmon excitations characteristic to Si.

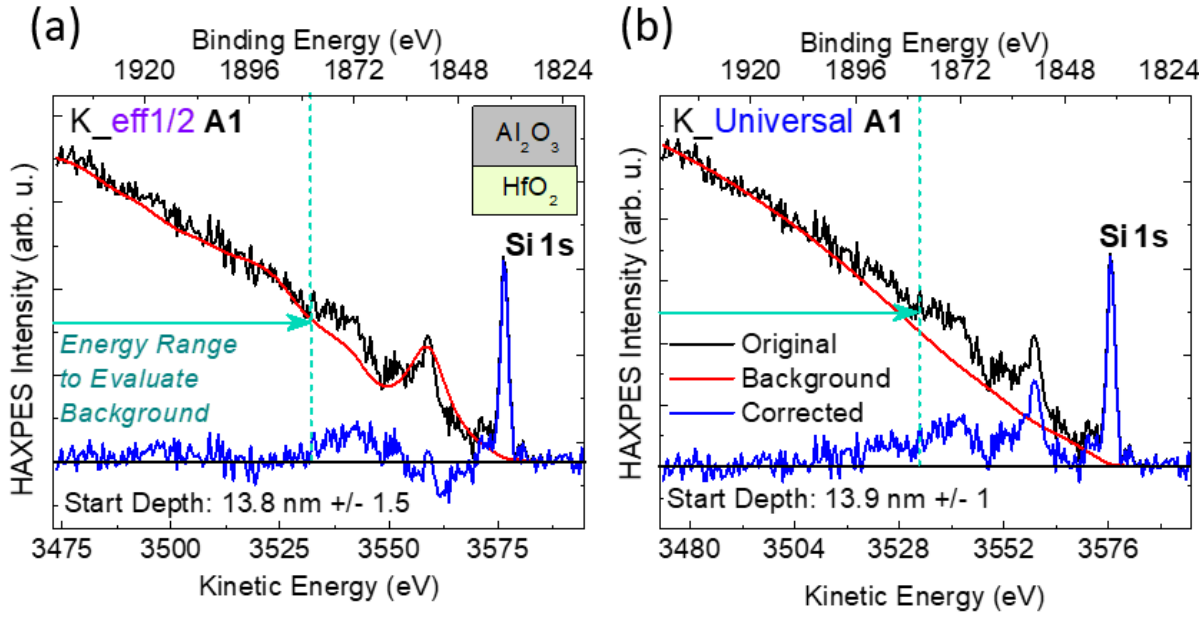

Figure 55. QUASES-Analyze spectra of Si 1s of sample A1 where an effective K(T) which takes into account the Si substrate is compared to $K(T)_{Universal}$.

The IBA procedure, however, was not improved with the effective cross-section. Table 10 presents the IBA results where the start depth of Si 1s is taken to represent the total IBA thickness of the bilayer. The effective cross-section was less sensitive than $K(T)_{Universal}$ to changes in the start depth parameter for all samples, increasing uncertainty in the analysis. Error in comparison to the XRR total bilayer thickness also increased for the median projected sample thickness. For this reason, we chose to remain with the default two-parameter Universal inelastic scattering cross-section.

Table 10. QUASES-Analyze HAXPES-IBA results for Si 1s for the determination of all bilayer thickness using $K(T)_{eff\_1/2}$.

Cr Kα HAXPES-IBA with $K(T)_{eff\_1/2}$				
Sample	XRR Thickness (nm)	Cr Kα IBA Thickness (nm)	IBA Fitting Uncertainty (nm)	% Error against XRR
A1	12.3	13.8	1.5	12 %
A2	17.2	17.2	2.5	0 %
A3	26.8	23	4	14 %
H1	11.9	13.6	1.7	14 %
H2	16.4	16.8	2.3	3 %
H3	21	24	4	14 %

4.4 Results for thick bilayer samples with Ga Kα

The ALD bilayer series was recorded with a Ga Kα source (9.25 keV) using a Scienta Omicron HAXPES Lab. The objective of the study was to evaluate the HAXPES-IBA method for higher photon energies and compare thickness determinations and spectra quality between a Cr Kα and Ga Kα source.

Figure 56 displays the QUASES-Analyze IBA spectra for A1. The core peaks are intense, and there is very little inelastic background compared to the spectra recorded with the Cr Kα source. This is due to the increased probing depth of the experiment at such very high excitation energies.

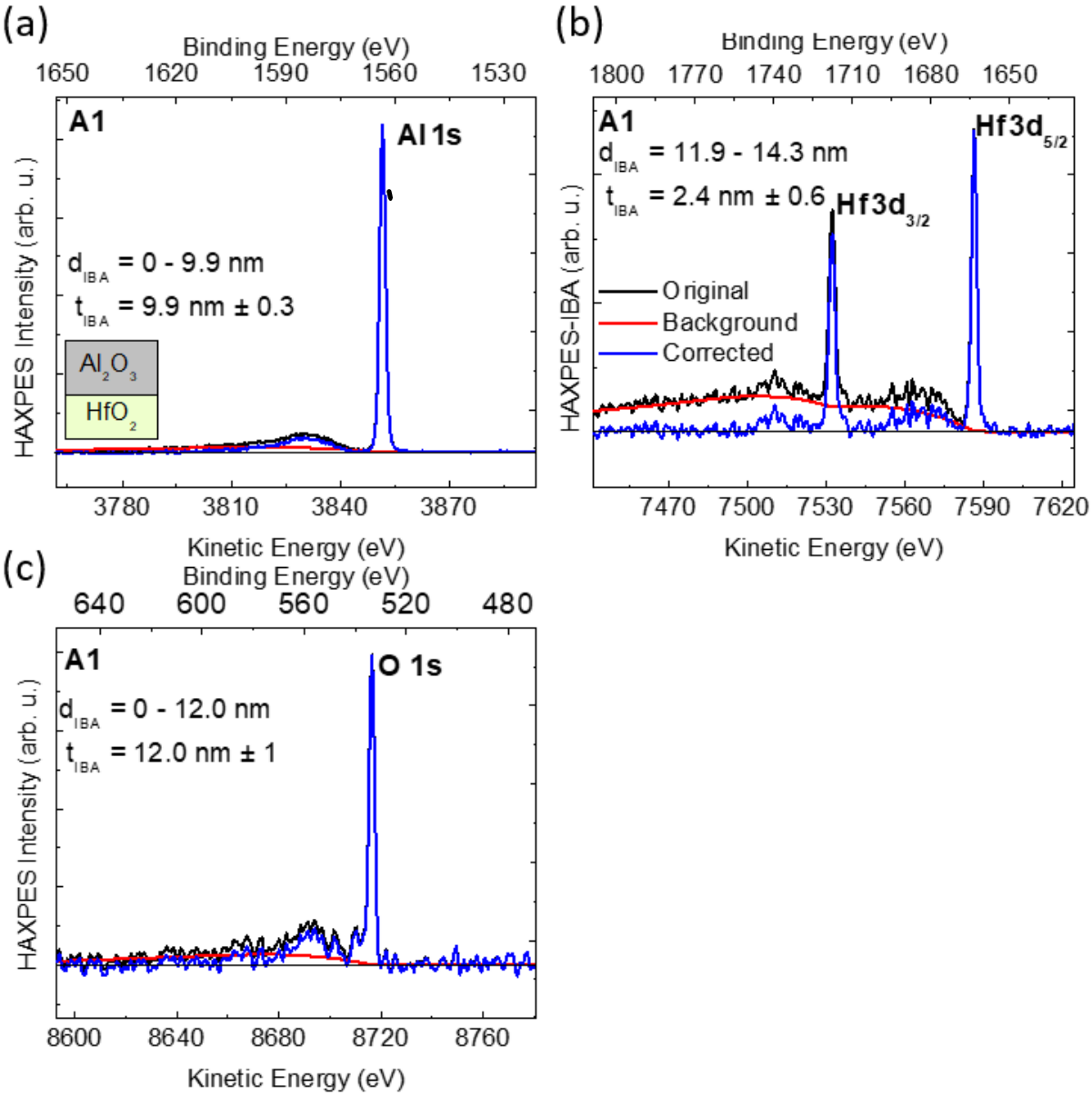

Figure 56. HAXPES-IBA for A1 using a Ga Kα source.

Another effect of the increased photon energy is shown in Figure 57. Recall that in Section 3, it was explained that an inelastic background range of 100 eV is needed for an accurate and precise inelastic background analysis. It can be seen in Figure 56 (a) that the inelastic background of the Al 1s signal is overlapped by the Hf 3d peak ~20 eV before the signal is expected to end. The large plasmon of Al 1s obliges the user to analyze the background fit at lower energies, so the 20 eV that is not accounted for may increase error in the analysis.

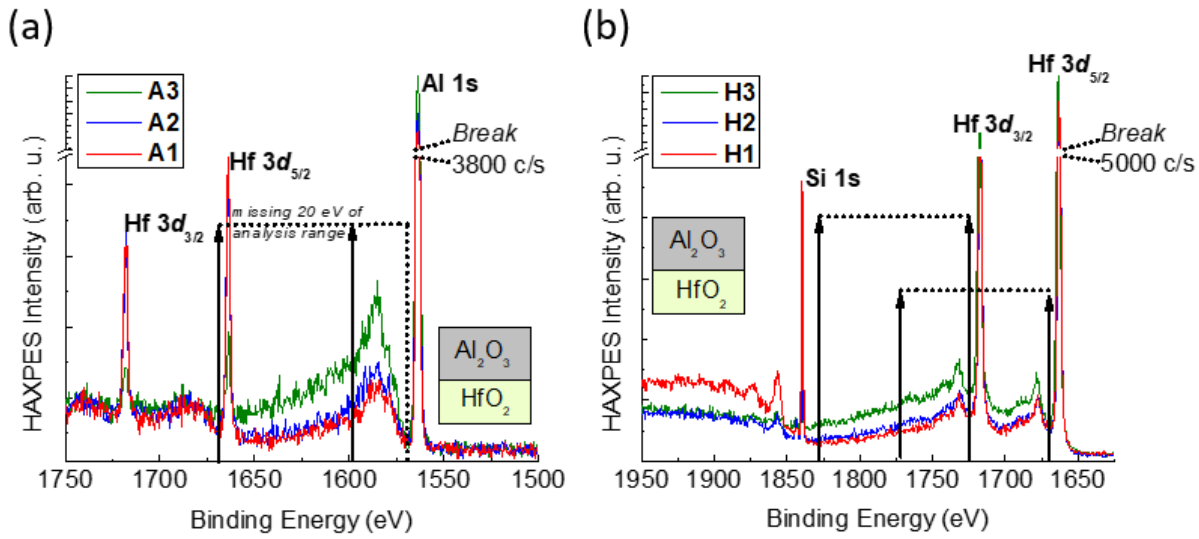

Figure 57. Ga Kα HAXPES spectra of all six samples.

4.4.1 Overlayer depth distribution

As shown in Figure 57 (c), the Al 1s background has very little signal. Nevertheless, an accurate and precise IBA thickness was reached. The full thickness determinations for the Al_2O_3 overlayers are shown in Figure 58. The depth distributions were accurate to XRR and modeled a start depth of 0 nm, indicating little to no contamination.

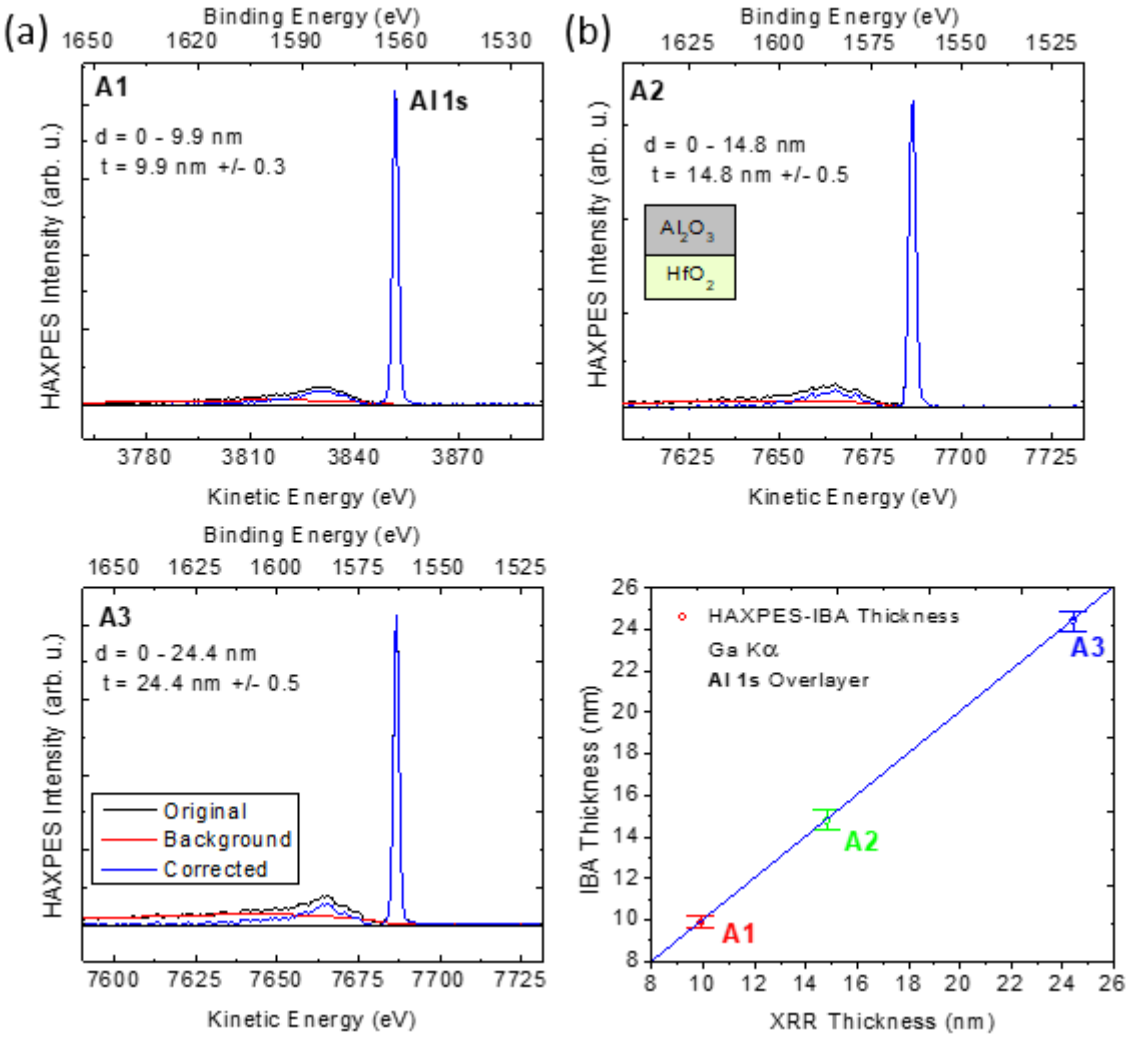

Figure 58. Ga Kα HAXPES-IBA for Al_2O_3 overlayers.

Ga Kα HAXPES-IBA for the Hf 3d signal in HfO_2 are shown in Figure 59. The XRR thickness is respected for each solution, but the overlayers do not appear to begin at 0 nm as expected. This may suggest contamination. The samples underwent no surface treatment, and a small C 1s peak was seen in the spectra. Increasing the energy of the source gives a more depth-sensitive method, so minor surface contamination may go unnoticed in the survey spectra.

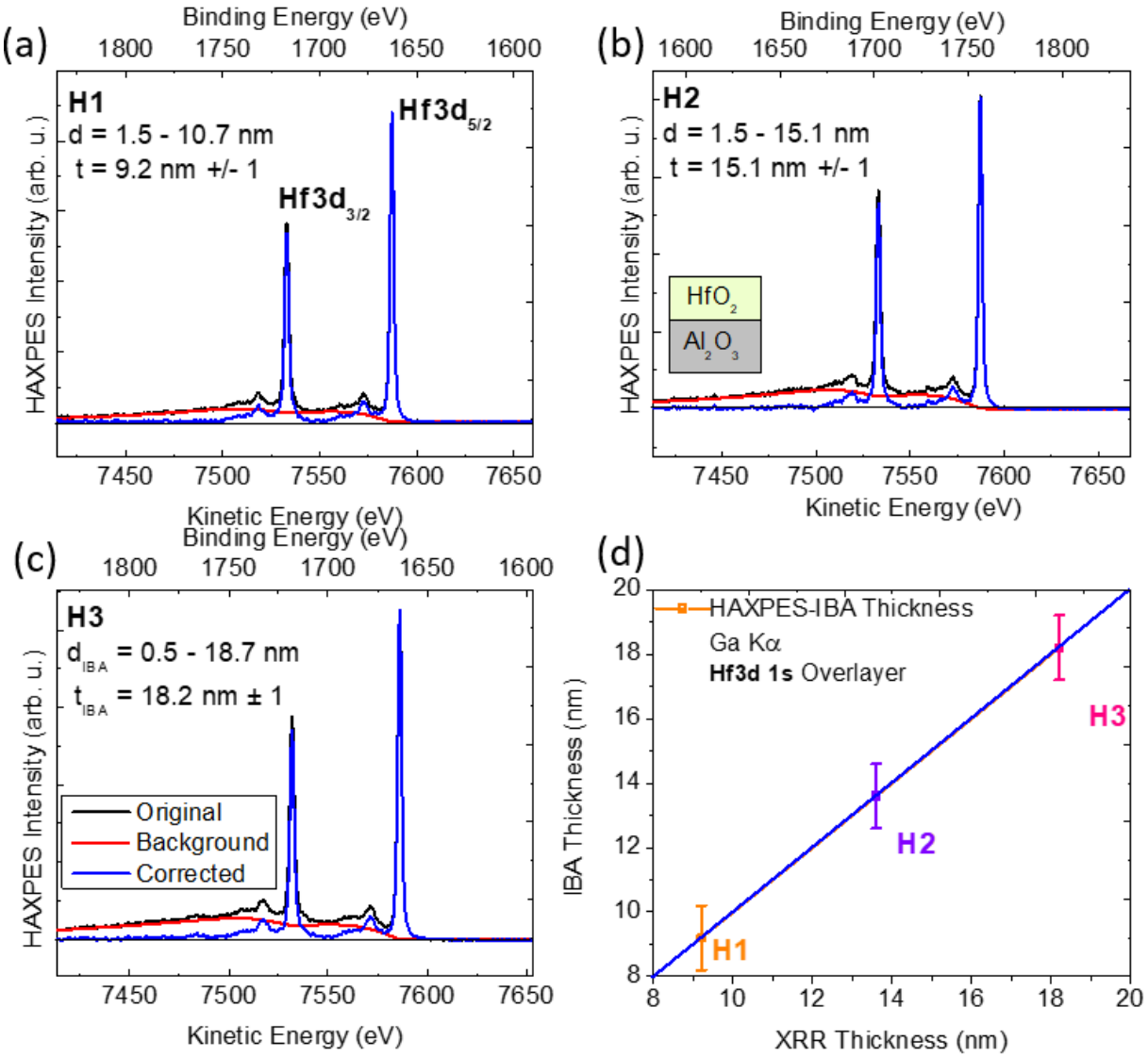

Figure 59. Ga Kα HAXPES-IBA for HfO_2 overlayers.

4.4.2 Buried layer depth distribution

The depth distributions in the buried layers are shown in Table 11. The XRR thicknesses were maintained for all samples. Al 1s had a much greater uncertainty than Hf 3d, but the median start depth values are more accurate to XRR. HAXPES-IBA with the Cr Kα source also presented the Hf 3d buried layer deeper or closer to the surface than the Al 1s distribution model (Figure 53).

Table 11. Buried layer depth distribution of buried Al_2O_3 and HfO_2 measured with Ga Kα radiation source. The depth distributions of

Sample	Signal	XRR Start Depth (nm)	XRR Thickness (nm)	QUASES-Analyze Thickness (nm)	QUASES-Analyze Depth Distribution (nm)
A1	Hf 3d	9.9	2.4	2.4 ± 0.6	11.9 ± 0.3 to 14.3 ± 0.3
A2	Hf 3d	14.8	2.4	2.4 ± 1.4	17.8 ± 0.7 to 20.2 ± 0.7
A3	Hf 3d	24.4	2.4	2.4 ± 2	32.4 ± 1 to 34.8 ± 1
H1	Al 1s	9.2	2.7	2.7 ± 2	9.4 ± 1 to 12.1 ± 1
H2	Al 1s	13.6	2.8	2.8 ± 2	15.1 ± 1 to 17.9 ± 1
H3	Al 1s	18.2	2.8	2.8 ± 2	18.7 ± 1 to 21.7 ± 1

Figure 60 shows the QUASES-Analyze IBA spectrum of Hf 3d in HfO_2 buried under 24.4 nm Al_2O_3. The calculated background shape does not follow the same course as the measured. As discussed in chapter 3, the QUASES-Analyze software does not account for elastic scattering. Since elastic scattering increases with photon energy and affects the higher-energy loss region of the spectrum, this may increase error and uncertainty in the IBA solution. The TPP-2M IMFP value may deviate from the EAL either measured or found theoretically.

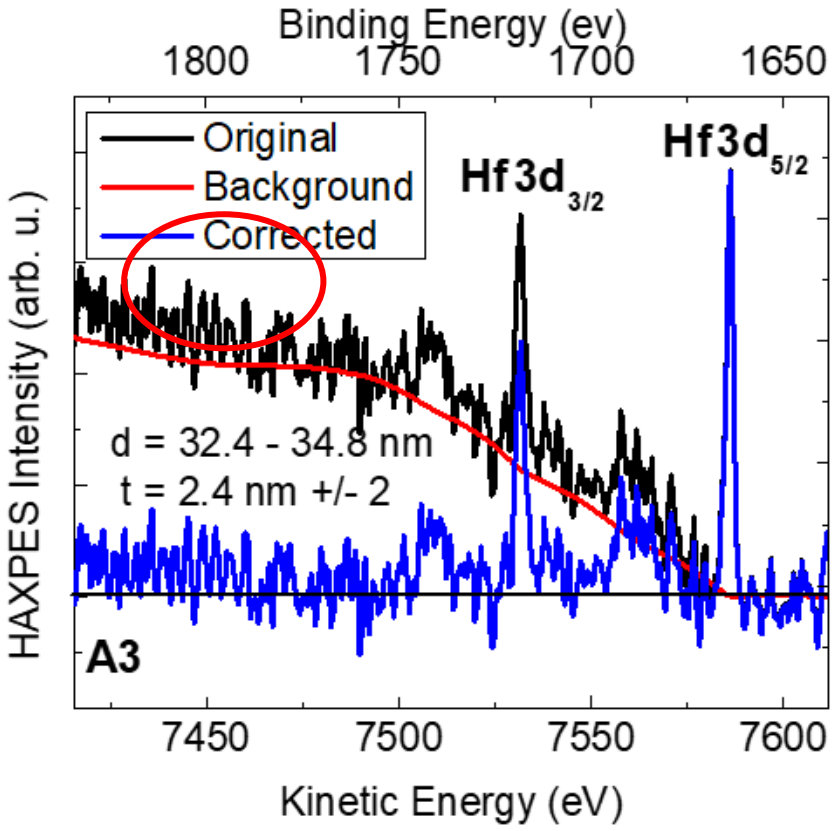

Figure 60. Ga Kα HAXPES-IBA for Hf 3d in A3. The calculated background shape does not follow the measured in the low kinetic energy region.

4.4.3 Discussion regarding internal consistency

The interface position d_1 (Figure 52) is determined by IBA of both the buried layer A and overlayer B. Agreement between the d_{1A} and d_{1B} is important to control for internal consistency and to provide a realistic IBA model. Figure 61 shows the differences between d_{1A} and d_{1B} for all the samples. d_{1A} ~d_{1B} for the HfO_2 over Al_2O_3 series. This is due in part to the large uncertainty in the Al 1s IBA solution, which allows for ± 2 nm variation in the depth distribution. d_{1B} and d_{1A} vary approximately 2 nm apart in the A1 and A2 models. O 1s is not precise enough to make a conclusion on the distribution of the HfO_2 layer, and Si 1s was not able to be modeled in this experiment.

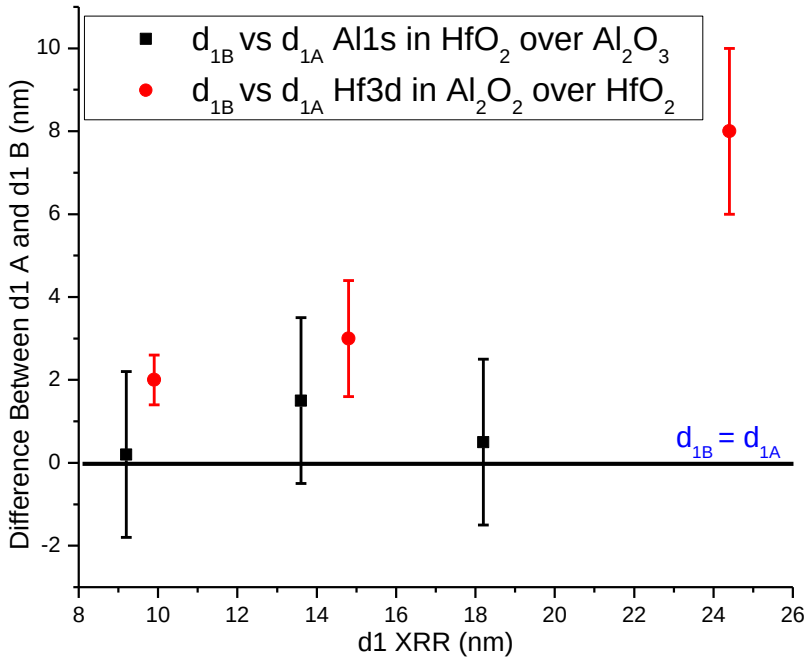

Figure 61. Disparity in the interface location d_1 between the buried layer A and overlayer B in the bilayer samples.

4.4.4 Comparison of Cr Kα and Ga Kα IBA analyses

Thickness determinations for Al 1s in the Al_2O_3 overlayers and Hf 3d in the HfO_2 overlayers are shown in Table 12. Both IBA determinations were accurate to XRR. Cr Kα was more precise, on the order of 0.2 – 0.9 nm. As shown in Figure 56, there is much less background signal in the Ga Kα spectra, which may account for increased error and uncertainty. Figure 57 demonstrates the interruption in the inelastic background of Al 1s. We also again point to increased elastic scattering as a potential source of uncertainty.

Table 12. Comparison of HAXPES-IBA thicknesses with Cr Kα vs Ga Kα photon sources.

	IBA Signal	XRR Thickness (nm)	Cr Kα IBA Thickness (nm)	Fitting Uncertainty (nm)	Ga Kα IBA Thickness (nm)	Fitting Uncertainty (nm)
A1	Al 1s	9.9	9.9	0.2	9.9	0.3
A2	Al 1s	14.8	14.8	0.2	14.8	0.7
A3	Al 1s	24.4	24.4	0.5	24.4	0.7
H1	Hf 3d	9.2	9.2	0.2	9.2	1
H2	Hf 3d	13.6	13.6	0.8	13.6	1
H3	Hf 3d	18.2	18.2	0.9	18.2	1

A comparison of the IBA depth distribution in the buried layers is shown below in Table 13. Since all of the results arrived at the expected thickness, the Start Depth is compared. The percent difference was calculated from the absolute difference and average of the two results as follows:

Equation 41

$$\frac{|V_{Cr\,K\alpha} - V_{Ga\,K\alpha}|}{(V_{Cr\,K\alpha} + V_{Ga\,K\alpha})/2} \times 100$$

Where V is the Start Depth value. The values for the thinnest overlayer samples A1 and H1 are very similar between the Cr Kα and Ga Kα sources. Increasing the overlayer thickness in samples A2 and H2 result in a greater difference, but with a similar increase to 8.8% in buried Hf 3d, and 11.3 % in buried Al 1s. Al 1s was only available when using the Ga Kα source, but the Start Depth value was similar to the XRR determination. In all cases except for Al 1s in H2, the HAXPES-IBA model using Ga Kα excitation overestimated the Start Depth position. These results indicate the importance of carefully selecting the source energy for the sample. Here, Ga Kα radiation was necessary to overcome the limited probing depth of Cr Kα and reach the buried Al_2O_3 layer in the thickest HfO_2 overlayer sample, but the Start Depth determination was less-accurate and less-precise in the other sample models.

Table 13. Comparison of HAXPES-IBA buried layer depth distributions using a Cr Kα and Ga Kα sources.

Sample	Signal	XRR Start Depth (nm)	Cr Kα IBA Start Depth (nm)	Ga Kα IBA Start Depth (nm)	% Difference Cr Kα and Ga Kα
A1	Hf 3d	9.9	11.6 ± 1	11.9 ± 0.6	2.6 %
A2	Hf 3d	14.8	16.3 ± 1	17.8 ± 1.4	8.8 %
A3	Hf 3d	24.4	22.4 ± 1.5	32.4 ± 2	36.4 %
H1	Al 1s	9.2	9.2 ± 0.6	9.4 ± 2	2.2 %
H2	Al 1s	13.6	16.9 ± 1	15.1 ± 2	11.3 %
H3	Al 1s	18.2	-	18.7 ± 2	-

The QUASES-Analyze and QUASES-Generate techniques were thoroughly studied for lab-based HAXPES in this study. By using well-controlled samples with opposing stacking configurations and varying thicknesses, the inelastic scattering cross-section parameter and source energy were evaluated for the accuracy and precision of the resulting IBA models.

4.5 Summary and conclusion

This work was performed in the technological context of stronger requirements for non-destructive characterization and metrology of ALD dielectric oxide layer stacks with increasing material thicknesses in the 1-30 nm range, for applications from logic to power transistor devices. We have presented highly-calibrated, destructive metrology techniques as references, and assessed the implementation of alternative, non-destructive X-ray photoelectron spectroscopic methods. In the study of ultrathin (≤ 2 nm) Al_2O_3 layers a linear dependence between LPD-ICPMS and WDXRF dose determinations of the amount of aluminum in a sample confirmed WDXRF to be a quantitative and precise technique. Thickness measurements using pARXPS and IBA-XPS were compared to the latter reference technique. IBA-XPS combined with GCIB cleaning before the measurement was shown to greatly improve the layer thickness determinations with less than a 10% error from the nominal values. IBA-XPS also provided information on the 1 nm SiO_2 layer at the Si substrate interface.

For dielectric layer thicknesses in the 10-25 nm range and < 3 nm-thick buried layers, Cr Kα-based lab-scale HAXPES combined with IBA was evaluated for the thickness determination and compared to an XRR metrology technique. The method afforded the analysis of each element in the oxide layers including oxygen by use of the O KLL Auger transition. Through this method, a complete depth profiling was achieved independent of a reference technique with resulting thickness values in excellent agreement with XRR for both the surface and buried layers. The thickness determination is accurate with an uncertainty below 6% for the surface layer with an expected increased uncertainty in the buried layer.

Bulk reference spectra were used in the place of the two-parameter Universal cross-section for use in QUASES-Generate. The resulting IBA thicknesses were found to be less-accurate and less-precise, introducing new error in the analysis and increasing uncertainty from the angstrom-scale to up to 4 nm in the buried layer. This conclusion may save the operator time and resources as it can be challenging to obtain a proper bulk reference sample, especially for ALD samples.

HAXPES-IBA was performed on the thick ALD samples using spectra recorded with a Ga Kα (9.25 keV) source. Increasing the photon source increased uncertainty in the IBA solution but did not impact the accuracy to XRR in the thickness determination. Ga Kα excitation increased the probing depth such buried Al_2O_3 was able to be analyzed in the thickest HfO_2 overlayer sample.

In summary, we explored the unique performance of XPS, which can reliably reveal depth-dependent elemental distributions in a wide range of sample thicknesses. From monolayers to layers tens of nanometers thick, pARXPS, HAXPES, and investigation of the inelastic background permitted non-

destructive depth profiling with < 50 nm spatial resolution. This aligns with industrial needs for inline process control by XPS analysis.

[1] P. Hönicke, B. Detlefs, E. Nolot, Y. Kayser, U. Mühle, B. Pollakowski, B. Beckhoff, Reference-free grazing incidence x-ray fluorescence and reflectometry as a methodology for independent validation of x-ray reflectometry on ultrathin layer stacks and a depth-dependent characterization, J. Vac. Sci. Technol. A. 37 (2019) 7. https://doi.org/10.1116/1.5094891.

[2] B.F. Spencer, S. Maniyarasu, B.P. Reed, D.J.H. Cant, R. Ahumada-Lazo, A.G. Thomas, C.A. Muryn, M. Maschek, S.K. Eriksson, T. Wiell, T.-L. Lee, S. Tougaard, A.G. Shard, W.R. Flavell, Inelastic background modelling applied to hard X-ray photoelectron spectroscopy of deeply buried layers: A comparison of synchrotron and lab-based (9.25 keV) measurements, Appl. Surf. Sci. 541 (2021) 148635. https://doi.org/10.1016/j.apsusc.2020.148635.

[3] Y.-T. Cui, S. Tougaard, H. Oji, J.-Y. Son, Y. Sakamoto, T. Matsumoto, A. Yang, O. Sakata, H. Song, I. Hirosawa, Thickness and structure of thin films determined by background analysis in hard X-ray photoelectron spectroscopy, J. Appl. Phys. 121 (2017) 225307. https://doi.org/10.1063/1.4985176.

[4] C. Zborowski, O. Renault, A. Torres, Y. Yamashita, G. Grenet, S. Tougaard, Determination of the input parameters for inelastic background analysis combined with HAXPES using a reference sample, Appl. Surf. Sci. 432 (2018) 60–70. https://doi.org/10.1016/j.apsusc.2017.06.081.

[5] C. Zborowski, S. Tougaard, Theoretical study toward rationalizing inelastic background analysis of buried layers in XPS and HAXPES, Surf. Interface Anal. 51 (2019) 857–873. https://doi.org/10.1002/sia.6660.

[6] A.K. Livesey, G.C. Smith, The determination of depth profiles from angle-dependent XPS using maximum entropy data analysis, J. Electron Spectrosc. Relat. Phenom. 67 (1994) 439–461. https://doi.org/10.1016/0368-2048(93)02035-K.

[7] M.A. Scorciapino, G. Navarra, B. Elsener, A. Rossi, Nondestructive Surface Depth Profiles from Angle-Resolved X-ray Photoelectron Spectroscopy Data Using the Maximum Entropy Method. I. A New Protocol, J. Phys. Chem. C. 113 (2009) 21328–21337. https://doi.org/10.1021/jp906326m.

[8] B.J. Tielsch, J.E. Fulghum, Application of Angle-resolved XPS Algorithms to Overlayers and Concentration Gradients, Surf. Interface Anal. 21 (1994) 621–630. https://doi.org/10.1002/sia.7142.

[9] E. Gnacadja, N. Pauly, H.J. Kang, S. Tougaard, XPS quantification with universal inelastic electron scattering cross section including intrinsic excitations, (n.d.) 6.

[10] T. Jablonski, Evaluation of validity of the depth-dependent correction formula (CF) for elastic electron scattering effects in AES and XPS, Surf. Interface Anal. 26 (1998) 11. https://doi.org/10.1002/(SICI)1096-9918(19980501)26:5<374::AID-SIA382>3.0.CO;2-U.

[11] P. Risterucci, Coupling of electron spectroscopies for high resolution elemental depth profiles in complex architectures of functional materials, University of Lyon, 2015.

[12] O. Renault, P.-M. Deleuze, J. Courtin, T.R. Bure, N. Gauthier, E. Nolot, C. Robert-Goumet, N. Pauly, E. Martinez, K. Artyushkova, New directions in the analysis of buried interfaces for device technology by hard X-ray photoemission, Faraday Discuss. 236 (2022) 288–310. https://doi.org/10.1039/D1FD00110H.

[13] N. Pauly, S. Tougaard, F. Yubero, Modeling of X-ray photoelectron spectra: surface and core hole effects: XPS: surface and core hole effects, Surf. Interface Anal. 46 (2014) 920–923. https://doi.org/10.1002/sia.5372.

[14] P. Risterucci, O. Renault, C. Zborowski, D. Bertrand, A. Torres, J.-P. Rueff, D. Ceolin, G. Grenet, S. Tougaard, Effective inelastic scattering cross-sections for background analysis in HAXPES of deeply buried layers, Appl. Surf. Sci. 402 (2017) 78–85. https://doi.org/10.1016/j.apsusc.2017.01.046.

[15] C. Zborowski, O. Renault, A. Torres, Y. Yamashita, G. Grenet, S. Tougaard, Determination of the input parameters for inelastic background analysis combined with HAXPES using a reference sample, Appl. Surf. Sci. 432 (2018) 60–70. https://doi.org/10.1016/j.apsusc.2017.06.081.
[16] S. Tougaard, Energy loss in XPS: Fundamental processes and applications for quantification, non-destructive depth profiling and 3D imaging, J. Electron Spectrosc. Relat. Phenom. 178–179 (2010) 128–153. https://doi.org/10.1016/j.elspec.2009.08.005.

5 Case studies of the IBA method from lab-scale HAXPES: technological applications

This chapter applies the IBA method explained in Chapter 3 and developed in Chapter 4 to technologically relevant materials. It is important to know precisely the layer thicknesses and interface positions in semiconductor devices. The case studies presented are related to two kinds of developments at the the forefront of technological research at CEA-Leti and worldwide: GaN-based power transistors (MOSc-HEMT) and ferroelectric HfO2-based field effect transistors (FE-FET). In the case of MOSc-HEMT devices containing Al_2O_3 and GaN layers, diffusion and the possibility of an oxide formed at the interface can influence the effectiveness of the device operation [1]. The thickness of the gate oxide requires HAXPES radiation to analyze the buried layers and interfaces, and combing the technique with IBA allows even greater probing depths.

The influence of the TiN metal gate thickness of MOSFETs has long been established, affecting leakage currents and channel mobility [2]. The buried interface between ferroelectric HfO_2 layers and TiN electrodes is determinant for the electric polarization characteristics of TiN/HfO_2/TiN capacitors, requiring non-destructive characterization past the limits of traditional XPS [3].

We show how HAXPES combined with IBA is capable of determining the thickness of the overlayer and interface position with the buried layer in two series of real MOSc-HEMT and MOSFET materials whose syntheses reflect industrial fabrication techniques.

5.1 Experimental methods

Here we present the fabrication methods and characterization techniques used for sample series of Al_2O_3/GaN and TiN/Ti/HfO_2.

5.1.1 Sample preparation

These samples were prepared with techniques used in the fabrication of real devices. In the case of AlGaN/GaN HEMT technology, wet cleaning and surface preparation techniques prevent damage during the GaN etching process and remove contamination through chemical or annealing treatments, as explained in Sec. 5.1.1.1. The TiN/HfO_2 interface is carefully controlled in MOSc-FET devices by varying the oxygen flow, as detailed in Sec. 5.1.1.2 [3].

5.1.1.1 Al2O3/GaN for HEMT devices

Five samples were prepared composed of a metal oxide layer of Al_2O_3 in the 3 – 30 nm range deposited on GaN by atomic layer deposition (ALD). The sample composition is shown in Figure 62.

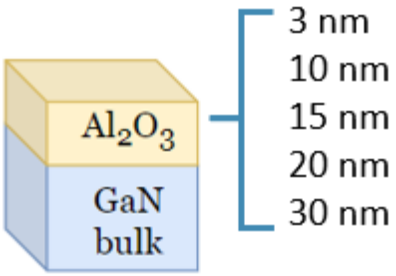

Figure 62. The schematic representation of the Al_2O_3/GaN samples. Five samples were studied, with Al_2O_3 overlayers with thicknesses from 3 nm up to 30 nm.

GaN was grown using metal organic vapor deposition (MOVCD) on top of several AlGaN/GaN buffer layers deposited on silicon. The GaN layer was then etched using inductively coupled plasma reactive ion etching (ICP-RIE) with chlorine. The GaN surface was then treated with hydrofluoric acid (HF) to remove the gallium oxide. These steps are representative of a real MOSc-HEMT device fabrication process. For the Al_2O_3 layers, ALD at 300°C was performed using trimethylaluminum (TMA) with H_2O and O_3 as oxidant precursors. The layer nominal thicknesses are determined by the number of ALD cycles and the thickness of the Al_2O_3 monolayer. The individual thicknesses and specific oxygen sources are shown in Table 14. In the 10 – 20 nm-thick layers, a 5 nm layer of Al_2O_3 using H_2O as the oxidant precursor is in contact with the etched GaN surface. To increase the thickness, Al_2O_3 using O_3 as the oxidant precursor was deposited in 5, 10, and 15 nm-thick layers. This method prevents the formation of carbon hydrogen impurities, thus preventing a higher oxidation of Ga with increasing thicknesses. The 10 nm overlayer sample was studied in the work of Spelta et al. [4].

Table 14. Individual thicknesses and precursor descriptions for the Al_2O_3/GaN series.

Al_2O_3 thickness (nm)	**Oxide precursor**
3	H_2O (3 nm)
10	H_2O (5 nm) + O_3 (5 nm)
15	H_2O (5 nm) + O_3 (10 nm)
20	H_2O (5 nm) + O_3 (15 nm)
30	H_2O (30 nm)

Bulk Al_2O_3 and GaN were used as reference materials in the HAXPES-IBA method carried out in QUASES-Generate. Al_2O_3 was deposited over silicon wafers (111) by ALD using TMA/H_2O for the first 10 nm of the sample, and then TMA/O_3 for 50 nm giving a 60 nm-thick sample. The bulk GaN sample was formed by epitaxial growth over a silicon wafer (111) for a 100 nm-thick sample.

This sample set is important for testing the HAXPES-IBA method on technologically relevant MOSc-HEMT structures whose fabrication steps are representative of real devices with real concerns in their functionality.

5.1.1.2 TiN/HfO2 for FE-FET applications

Three TiN/HfO_2 structures were studied (Figure 63) They consist of a TiN bottom and top electrodes deposited by Physical Vapor Deposition (PVD) at 350°C. The 10 nm-thick HfO_2 film between both electrodes is deposited by Atomic Layer Deposition (ALD) at 300°C and doped by Si through ion implantation. The pure Ti film between the HfO2 film and the top electrode is also deposited by PVD with no air break between Ti and TiN subsequent deposition. For electrical characterization purposes, the stacks were processed on a 200 mm BEOL platform, in a similar way as in the work by L. Grenouillet et al. [5].

The first (Figure 63 (a)) was a complete 20 nm thick TiN overlayer with a 10-nm thick HfO_2 buried layer deposited over 100 nm TiN and 150 nm SiO_2 on a Si substrate. The third (Figure 63(c)) and fourth (Figure 63(d)) structures were from the sample in Figure 63 (b), a 10 nm TiN overlayer deposited over 10 nm Ti with the same HfO_2/SiO_2/Si substrate configuration that underwent with Ar^+ sputtering at 1 kV in a spot size of 3x3 mm for 0.8 nm/min removed. Therefore, to remove 5 and 10 nm of the 10 nm TiN layer, sputter times of 6.25 and 12.5 min were used. The spectra from the original, unsputtered sample were unable to be analyzed due to a very low signal to noise ratio as they were not recorded with a step size and time per point conducive to IBA. Instead, spectra from the unsputtered sample in Figure 63(a) with a 20 nm TiN overlayer were used. Although the sample is composed of TiN only rather than the TiN/Ti structure, this is acceptable since the TPP2M values for Ti 1s in Ti and TiN are only 0.03 nm apart and do not impact the IBA result.

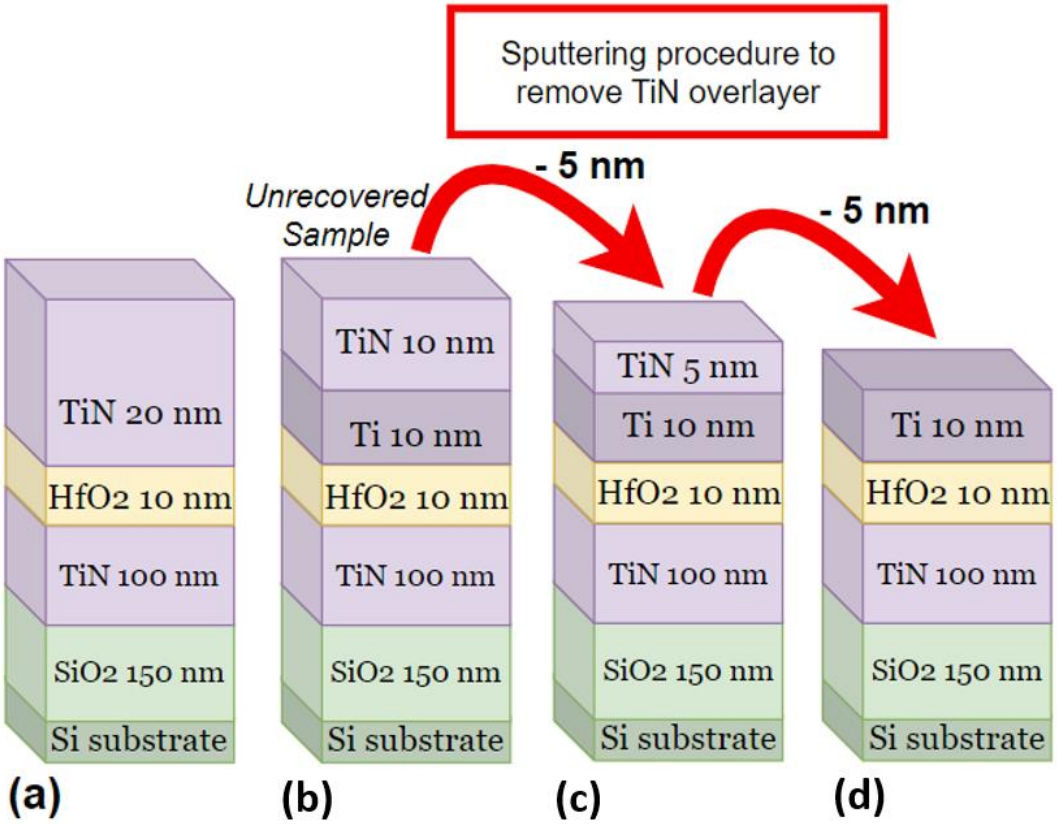

Figure 63. Sketch of the TiN/HfO_2 heterostructures studied. Models (c) and (d) are representative of (b), a TiN(10 nm)/Ti(10 nm) overlayer which was treated by in situ sputtering to remove 5 nm at the time of the overlayer. (a) is the sample from which spectra were recorded to represent (b).

Figure 64 shows a depth profile of sample (a) using an Ar^+ gun sputtering technique at 1 keV. We see there is 33% oxygen content in the Ti layer, suggesting there is actually a Ti_2O stoichiometry. This is expected, and in fact an important part of the functionality of the dielectric lies in the existence of oxygen vacancies in HfO_2 caused by Ti reduction. The O 1s transition was unable to be analyzed by IBA, so this complimentary analysis provides information on the interfacial oxide which would be otherwise unknown.

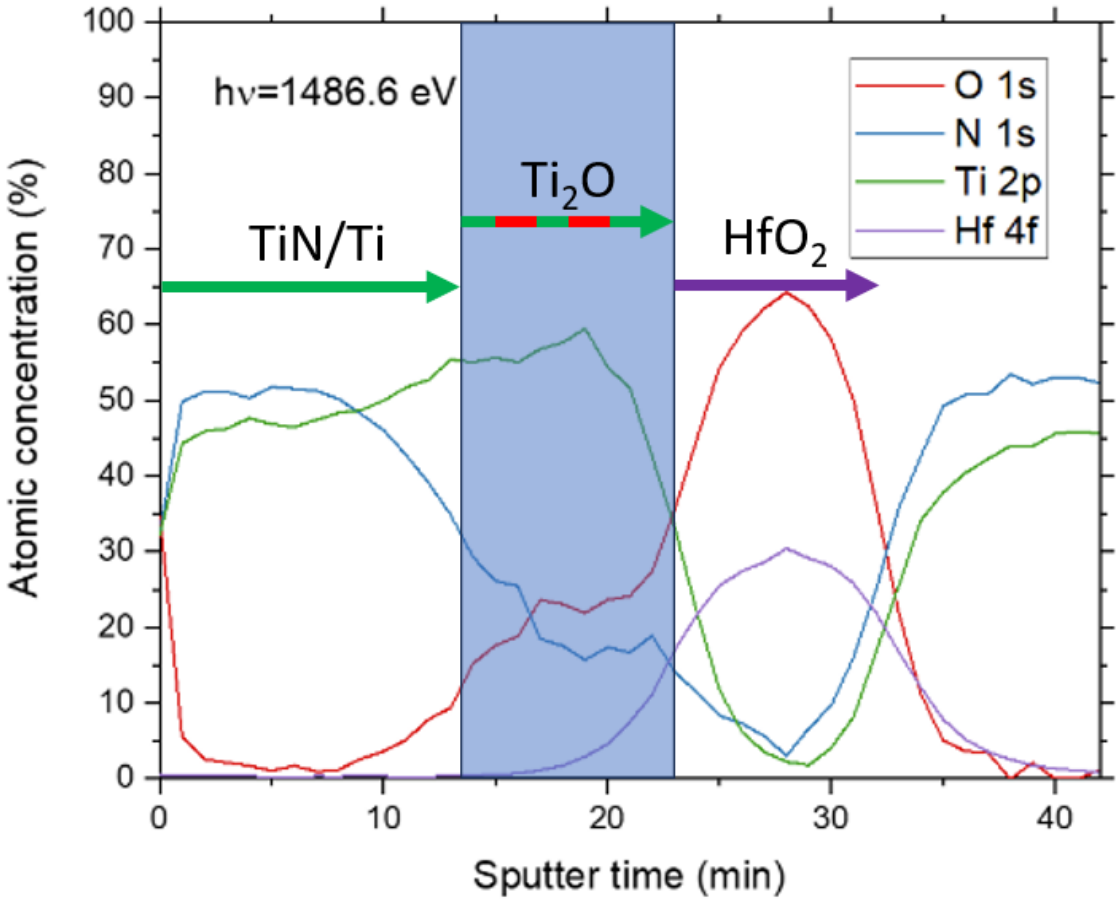

Figure 64. XPS depth profiling of (a) with Ar ion sputtering at 1 keV. The chemistry of the Ti interlayer was determined to be Ti_2O.

In order to study the samples nondestructively, HAXPES-IBA combined with sputter depth profiling was used to determine the total overlayer thickness and sputter rate. The analysis techniques are discussed in the following section.

5.1.2 Characterization of the samples

The samples described above were all analyzed by Cr Kα-based HAXPES only. The experimental specifications for the HAXPES experiment are available in Chapter 4. The analysis regions are shown below in Table 15. The analysis regions were selected over a wide range of energy to capture the continuous background before and after the photoelectron peak. The TiN/HfO_2 sample set was recorded at 75° TOA. The Al_2O_3/GaN spectra were recorded at 45° TOA with a supplementary measurement taken at 75° TOA for the 30 nm overlayer sample.

Table 15. Analysis regions in the HAXPES experiments.

Background region	Binding energy range (eV)	Kinetic energy range (eV)
O 1s	452 - 800	4963 – 4615
Ga 2p – Al 1s	1070 - 1800	4345 – 3615
Ti 1s	4900 – 5200	515 – 215
Hf 3d	1640 - 1875	3775 – 3540

The TOF-SIMS experiment parameters used with the Al_2O_3/GaN sample set can be found in [4]. ToF-SIMS measurements were carried out using a ToF-SIMS 5 (IonTof Gmbh) in the positive mode with Cs+ sputtering at 500 eV and a Bi3+ analyzing beam at 15 keV. It was determined that low energy cesium sputtering is an adequate path to depth profiling of III-N thin structures [6]. The angle of incidence of both guns is 45° with respect to the surface normal, the raster area was 300 µm2, and the analyzed area was 80 µm2. In order to ensure consistent experimental conditions, the primary current for both analyzing beams was checked for each measurement.

5.1.3 Implementation of the HAXPES-IBA method

The effective inelastic mean free path ($IMFP_{eff}$) was calculated using the TPP-2M formula and Equation 32 from Chapter 3. It takes into account the overlayer and the layer from which the buried photoelectron is generated. The values are shown below in Table 16.

Table 16. Effective IMFPs for the photoelectron signals from buried GaN and HfO_2 in the two sample series.

Sample	Signal	IMFP eff ½ (nm)	Max probing depth of core-level HAXPES 3×IMFP (nm)	Max probing depth of IBA-HAXPES 8×IMFP (nm)
3 nm Al_2O_3 over Ga	Ga $2p_{3/2}$	6.27	18.81	50.16
10 nm Al_2O_3 over GaN	Ga $2p_{3/2}$	6.60	19.80	52.80
15 nm Al_2O_3 over GaN	Ga $2p_{3/2}$	6.79	20.37	54.32
20 nm Al2O3 over GaN	Ga $2p_{3/2}$	6.96	20.88	55.68
30 nm Al_2O_3 over GaN	Ga $2p_{3/2}$	7.22	21.66	57.76
10 nm TiN/Ti over HfO_2	Hf $3d_{5/2}$	5.21	15.63	41.68
15 nm TiN/Ti over HfO_2	Hf $3d_{5/2}$	5.10	15.30	40.80
20 nm TiN over HfO_2	Hf $3d_{5/2}$	4.99	14.97	39.92

The IMFP of the transitions in the overlayers were calculated by the TPP-2M formula and are as follows: Ti 1s – 1.22 nm, Al 1s – 7.00 nm, O 1s – 8.50 nm.

The two-parameter Universal inelastic scattering cross section (Section 3.1.2.1 Equation 8) created by S. Tougaard was used for all analysis except for Ti 1s. Ti has a sharp plasmon structure so the three-parameter cross section was used (Section 3.1.2.1 Equation 9) [7,8]. In the external cross section window of the QUASES-Analyze software, the C and D parameters were adjusted until the position and width of the cross section matched to the plasmon [9,10]. The selection and modification of the cross section is discussed more thoroughly in section 3.1.3. The values used are displayed in Table 17 below.

Table 17. C and D values used in calculating the three-parameter Universal inelastic scattering cross section used to model the inelastic background and plasmon Ti 1s.

Sample	C	D
20 nm TiN	195	60
5 nm TiN / 10 nm Ti	190	175
10 nm Ti	185	245

As in Chapter 4, the Al_2O_3/GaN samples were analyzed in QUASES-Analyze with the two parameter cross section as well as QUASES-Generate with a reference spectrum. This provides additional understanding of IBA in Al 1s and O 1s, as well as on another doublet (Ga 2p).

5.2 Results of IBA on Al_2O_3/GaN samples

In this section, we apply the HAXPES-IBA method developed in Chapter 4 on model bilayer samples containing Al_2O_3 layers to real device samples of Al_2O_3/GaN with Al_2O_3 overlayer thicknesses from 3 to 30 nm. The nominal thicknesses are determined by the number of ALD cycles and knowledge of the thickness of one monolayer of Al_2O_3. AlGaN/GaN heterostructures are ideal for HEMTs due to the two-dimensional electron gas channel (2-DEG) generated by the contact between the two GaN and AlGaN semiconductors. The 2DEG increases the mobility of the charge carriers and, consequently, allows a greater current passage than silicon-based transistors. In order to achieve a normally-OFF structure, which is important in power, high-voltage applications, a fully recessed gate metal-oxide-semiconductor (MOS)-channel using Al_2O_3 is employed. As shown in Figure 65, the Al_2O_3 dielectric may be quite thick, surpassing the probing depth limits of traditional XPS, and even HAXPES. Table 16 shows the effective IMFPs for buried GaN, for which the values lie around approximately 7 nm. Considering

the general limit of XPS/HAXPES methods to be 3×IMFP, even an excitation with Cr Kα radiation is not sufficient. The HAXPES-IBA method, however, reaches upwards of 8×IMFP probing depths, and can provide valuable information on the overlayer thickness and Al_2O_3/GaN interface position.

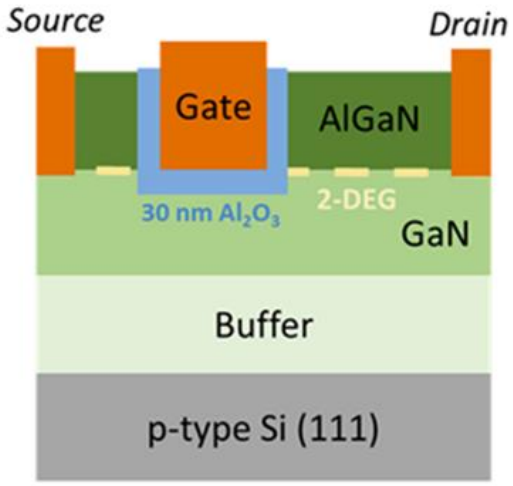

Figure 65. Scheme of the normally-OFF GaN MOSc-HEMT structure with a 30 nm-thick dielectric.

Here, we show how the HAXPES-IBA method executed in QUASES-Analyze using the two-parameter Universal inelastic cross section, and QUASES-Generate with reference spectra, can model the Al_2O_3/GaN bilayer samples.

5.2.1 Buried layer depth distribution

The buried GaN layer was studied using the Ga $2p_{1/2}$ and $2p_{3/2}$ transition at 1117 eV BE (4298 eV KE). As shown in Figure 66, this transition is not available for IBA with Al Kα radiation due to the O KLL (978 eV KE) and C KLL (1223 eV KE) Auger lines which interrupt the Ga 2p inelastic background signal. Additionally, buried Ga produces an inelastic scattering background following the LMM Auger lines from 419 – 514 eV. Since this background overlaps with the background from O 1s (531 eV BE), IBA is not possible. A prominent C 1s peak is seen at ~285 eV BE. This is expected, as there was no surface cleaning before the analysis. Fluorine contamination is present as well as evidenced by the F 1s peak at 686 eV BE but is only superficial and will not affect HAXPES analysis. The inelastic background after the peaks drops quickly and was unable to be analyzed in either case, supporting the position that it does not go into the sample layer

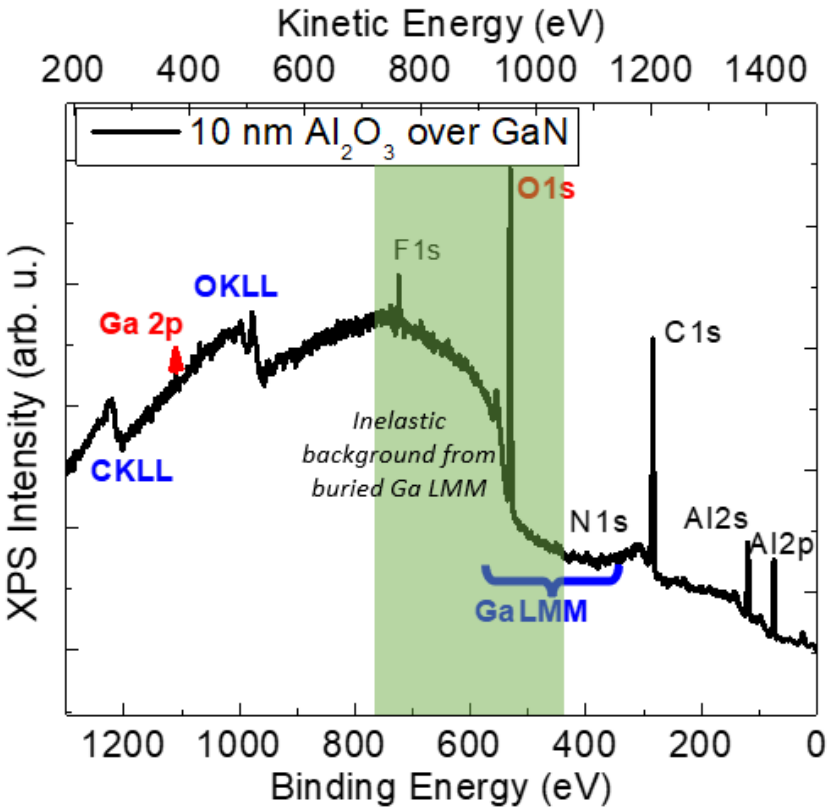

Figure 66. Al Kα XPS spectrum of 10 nm Al_2O_3 over GaN. Prominent Auger lines hinder IBA of the Ga 2p and O 1s transitions.

In Figure 67, we see how increasing the energy of the photon source allows for the analysis of Ga 2p buried under 10 nm of Al_2O_3. Previously practically invisible in the Al Kα spectrum, Ga 2p is now a prominent doublet with an intense background signal. We also see how shifting the analysis to a higher energy region using Cr Kα radiation removes the Auger lines around Ga 2p and O 1s and permits the analysis of Al 1s. It should be noted that Ga 2s is included in the IBA of the buried GaN layer, as it follows the Ga 2p signal without interruption by other element transitions. The ability to analyze the inelastic background over a large energy range is one of the reasons HAXPES-IBA may exceed the previously reported 8λ of XPS-IBA. The N 1s transition was not included in the analysis due to a lack of signal intensity as well as the encroaching O 1s peak at 531 eV BE.

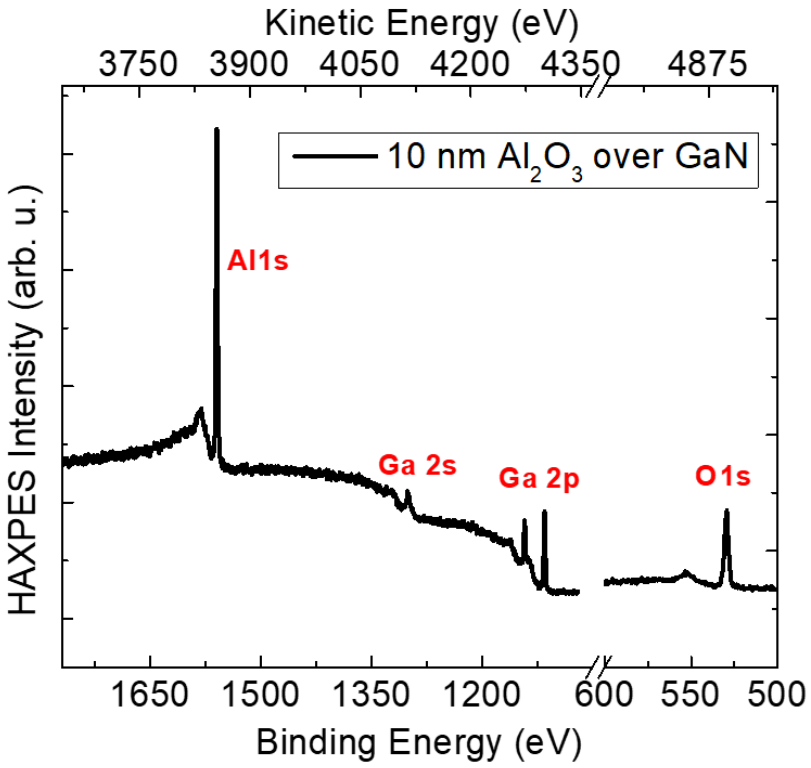

Figure 67. Cr Kα HAXPES spectra of 10 nm Al_2O_3 over GaN. The photoelectron peaks are well-spaced, permitting complete IBA of the peaks of interest.

After this qualitative assessment of the HAXPES spectra, we now move on to a quantitative determination of the depth distribution of the buried GaN layers.

5.2.1.1 Two-parameter Universal inelastic scattering cross section

In Chapter 4, we established that the two-parameter Universal inelastic scattering cross section allowed for the most accurate and precise IBA solution regarding Al_2O_3 and HfO_2layer thicknesses in model bilayer samples. It is also the simplest and fastest modeling procedure, necessitating only the wide spectrum and the calculated $IMFP_{eff}$. Here, we present the results of HAXPES-IBA of the Ga 2p – Ga 2s spectra of GaN buried underneath Al_2O_3 overlayers.

Since the GaN layer is taken to be bulk, we use the Start Depth of Ga 2p-2s as representative of the interface location between the Al_2O_3 and GaN layers, as well as the overall thickness of the Al_2O_3 overlayer to be cross-checked with IBA of Al 1s and O 1s. In Figure 68(a) – (e), we see that $K_{Universal}$ enables a perfect fit of the Ga 2p and Ga 2s inelastic backgrounds. Ga depth distribution was able to be analyzed over a wide energy range from 4225 – 3900 eV KE. As the overlayers increase in thickness, however, the IBA solution is increasingly in conflict with the nominal values. It is expected that the fitting uncertainty will increase with the buried depth, as the IBA model is less-sensitive to variations in the Start and End depth parameters when deeply buried [11]. The error between the nominal values versus the IBA model, however, should not increase as a function of the buried depth. The exact

densities of the Al_2O_3 overlayer and GaN buried layer remain unknown. This, in addition to the uncertainty in the TPP-2M calculation, may signal the cause of the underestimation of the Ga Start Depth. This is discussed in Chapter 6. Focusing on Ga $2p_{3/2}$, Table 16 gives the $IMFP_{eff}$ for all samples. The thicker overlayer samples have an $IMFP_{eff}$ of approximately 7 nm, while the $IMFP_{eff}$ needed to reach a Start Depth aligned with the ALD target is around 8 nm. This 12.5% error is within the expected uncertainty of the IMFP determination at high energies [12,13]. In recent studies, it was shown that individual EAL and albedo value calculations are helpful to determine overlayer thicknesses for overlayer and substrate materials with different transport properties. This was especially true for HAXPES (synchrotron excitation energy = 4510 eV) [14–16]. The latest study was published in 2022 and was outside the scope of this work, but individual EAL determinations may be useful to the HAXPES-IBA method.

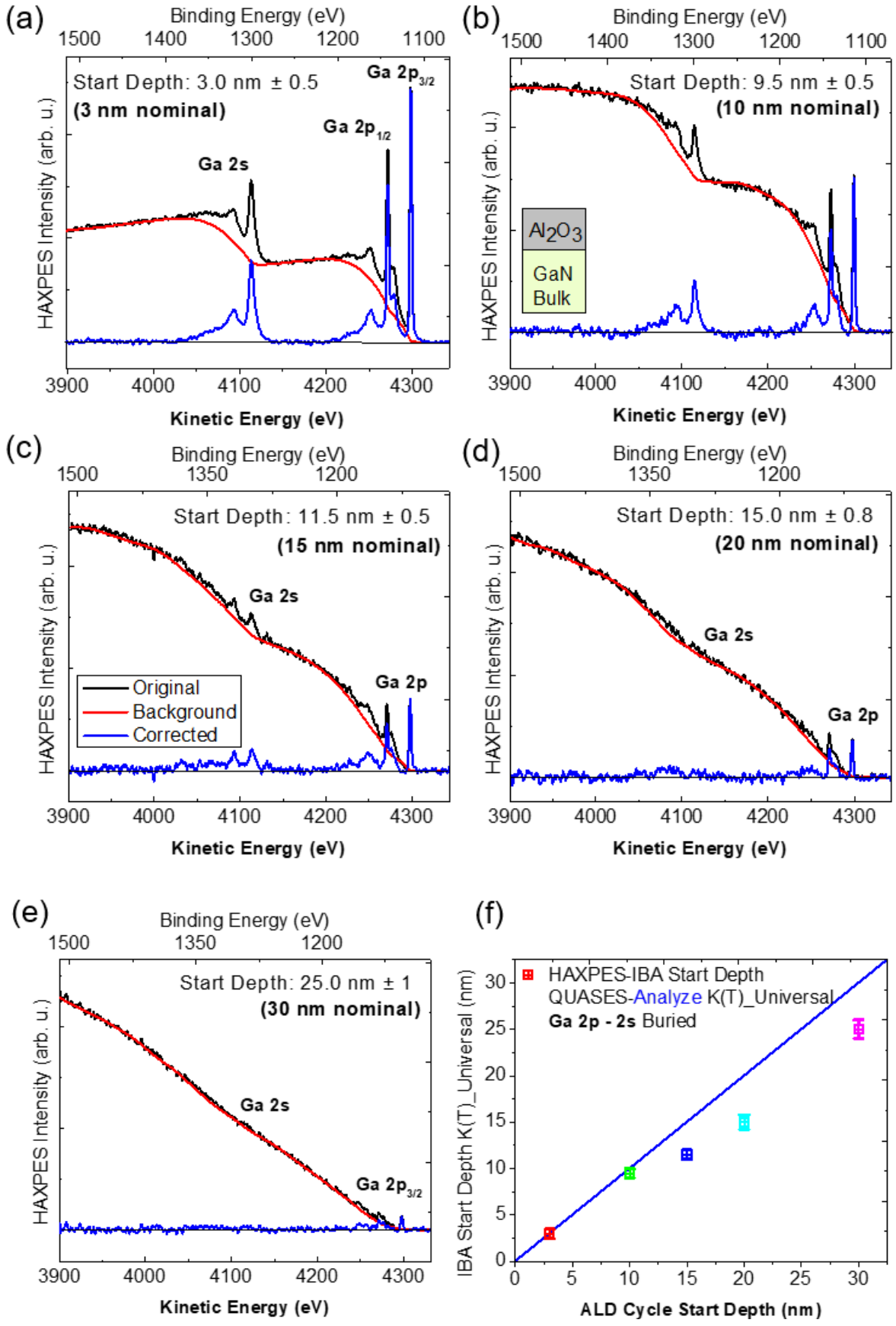

Figure 68. HAXPES-IBA of Ga 2p and 2s. The HAXPES-IBA solution for the Start Depth of the GaN layer does not agree with the nominal Al_2O_3 thickness.

Table 18 lists the Start Depths for each sample in the Al_2O_3/GaN series along with the fitting uncertainty and % error of the IBA solution to the nominal thickness. As discussed earlier, knowledge of the thickness of one monolayer of Al_2O_3 and the number of ALD cycles gives a good estimation of the total thickness. The 20 nm Al_2O_3 overlayer sample had the greatest error at 25% but modeled with the same -5 nm increment as the 30 nm sample. The 15 nm overlayer sample was similarly off by 3 – 4 nm.

Table 18. Ga Start Depth determinations by the number of ALD cycles and the HAXPES-IBA method using the two-parameter Universal inelastic scattering cross section. The Start Depth of Ga in the thick Al_2O_3 samples is consistently underestimated by HAXPES-IBA.

Nominal ALD Start Depth (nm)	HAXPES-IBA Start Depth (nm)	Fitting uncertainty (nm)	% Error to nominal thickness Start Depth
3	3.0	0.5	0.0 %
10	9.5	0.5	5.0 %
15	11.5	0.5	23.0 %
20	15.0	0.8	25.0 %
30	25.0	1.0	17.0 %

While the two-parameter inelastic scattering cross section is well suited to describe the Ga 2s/2p inelastic background, an alternative method using a reference spectrum from bulk GaN is available in the QUASES-Generate software. This circumvents the need for an optimized inelastic scattering cross section, as the inelastic losses and plasmons are modeled in a simulated spectrum.

5.2.1.2 Method using a reference spectrum in QUASES-Generate

Here we use a reference spectrum from bulk GaN to improve the HAXPES-IBA method described in the previous section. The two-parameter Universal inelastic scattering cross section is well suited for most transition metals and their oxides, but a reference spectrum which can accurately model the peak intensities and plasmon signals may improve the analysis. A full description of the modeling procedure in QUASES-Generate is available in section 3.1.3, but as a summary, after the spectrum from a bulk homogenous reference material is loaded in the Generate window, the Start and End Depth values may be modified in order to simulate a J(E) spectrum of a certain depth distribution. The depth distribution in the measured original spectrum may be found by changing the Start and End Depth parameters until a good fit between the peaks and inelastic background is achieved between the simulated and measured spectra.

Figure 69 shows Cr Kα HAXPES spectra of the energy region from Ga $2p_{3/2}$ to Ga 2s for the five Al_2O_3/GaN samples as modeled in QUASES-Generate. The generated model spectrum is shown in red, and the original measured spectrum is the color teal. The peak intensities between the model and measured spectra are well-matched for all five spectra. The modeled Start Depth of Ga increased in all spectra save for the 10 nm-estimated Al_2O_3 overlayer sample, which remained at 9.5 nm ± 0.5. The best inelastic background fit solution for the spectral region following the Ga 2p peaks (4225 – 4135 eV KE) is not the same as the ideal fit solution following the Ga 2s peak (4075 – 3900 eV KE). Therefore, the selected solution takes both regions into account, with a slight bias towards the continuous background at the higher energy loss region since it is the larger range of energy available. Individual IBA on the two regions was attempted, but a lack of sufficient continuous background and instability in the baseline parameter before the Ga 2s peak prevented improvement in the fitting procedure.

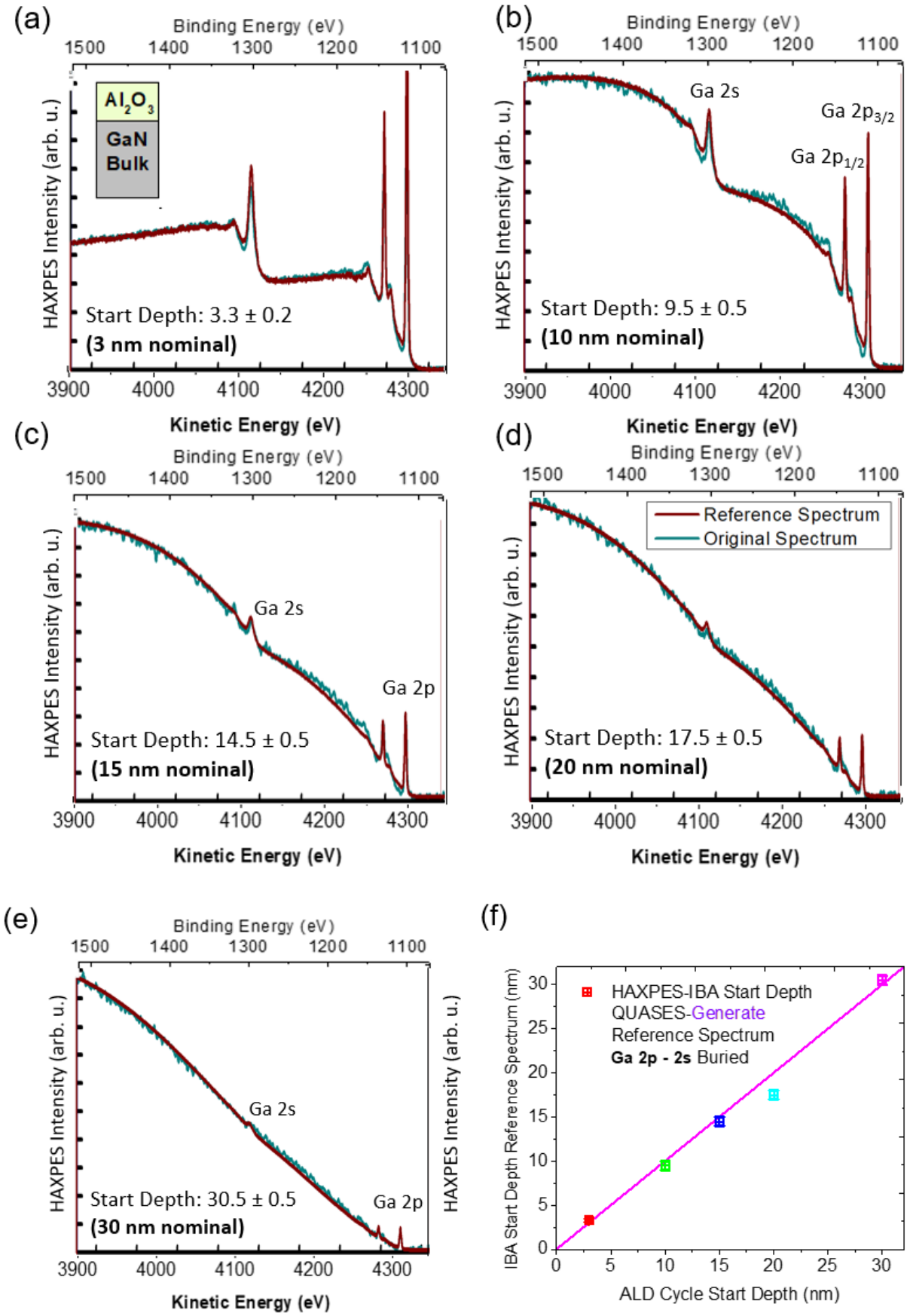

Figure 69. HAXPES-IBA of Ga 2p – 2s using a reference spectrum from bulk GaN to model the elastic and inelastic losses in the spectrum. The resulting Start Depth of Ga agrees with the overlayer nominal thickness.

The Start Depth solutions achieved in QUASES-Generate and calculated error to the nominal thickness of Al_2O_3 are available in Table 19. The samples with thicker Al_2O_3 overlayers have IBA solutions closer to the nominal thickness.

Table 19. Ga Start Depth determinations by the number of ALD cycles and HAXPES-IBA method. A reference spectrum from GaN was applied in the QUASES-Generate software to model the depth distribution of Ga. The Start Depth of Ga in the thick Al_2O_3 samples is consistently underestimated by HAXPES-IBA.

ALD Cycle-Determined Start Depth (nm)	HAXPES-IBA Start Depth (nm)	Fitting uncertainty (nm)	% Error to nominal Start Depth
3	3.3	0.2	10.0 %
10	9.5	0.5	5.0 %
15	14.5	0.5	3.3 %
20	17.5	0.5	12.5 %
30	30.5	0.5	1.7 %

Disparity between the QUASES-Analyze and QUASES-Generate Ga Start Depth solutions requires additional information from the depth distribution of the Al_2O_3 overlayer. Both the Al 1s (3855 eV KE) and O 1s (4884 eV KE) transitions were available for HAXPES-IBA of the Al_2O_3 overlayer. Analysis of the O 1s distribution can also provide information on a potential Ga_xO_y oxide that may form at the interface, as significant overlap in the two distributions would indicate its existence.

5.2.2 HAXPES-IBA of Al 1s in the Al_2O_3 Overlayer

Cr Kα radiation permitted IBA for both elements in the Al_2O_3 overlayer, allowing for a holistic analysis that was self-contained.

5.2.2.1 Baseline setting procedure in IBA of Al 1s

An important parameter in the IBA methodology is the baseline which effectively sets the continuous background to y = 0 at higher KE's from the main peak. This allows analysis of the inelastic background solely from the photoelectron signal of interest. Figure 70 shows hand-set baselines for the Al 1s signal in three of the samples. The baseline is drawn based on the continuous background and its projected direction. In the case of the thinnest Al_2O_3 overlayer sample (black), the Ga photoelectrons are traversing a shorter distance and lose less energy. This allows the continuous background signal to stabilize before the Al 1s peak. We see in the 10 nm Al_2O_3 sample (red) that the inelastic background signal from Ga continues to increase up to the Al 1s peak. Since the background signal is not flat, it is

harder to determine where the continuous background signal should be set for y = 0. This effect is even more pronounced in the 30 nm Al_2O_3 overlayer sample (blue), where the proper baseline may be interpreted with a range of inclinations. This uncertainty in the baseline-setting procedure may add to uncertainty in the IBA solution since different IBA solutions may be possible depending on the spectrum.

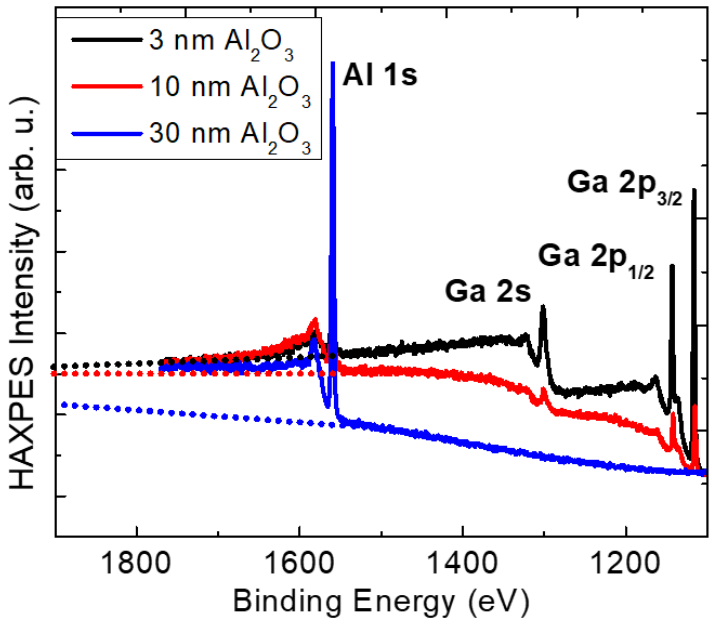

Figure 70. Hand-drawn baselines for IBA of Al 1s (dotted). The continuous background following the Ga signals is increasingly distorted with increasing buried depths of the Ga photoelectron, complicating the baseline-setting procedure.

Several baselines were selected for Al 1s in the 20 and 30 nm overlayer samples and the range of depth distribution solutions were determined. Since the continuous background before the peak in these spectra is still increasing as it approaches the peak, the range over which the baseline is drawn impacts the slope of the baseline. Choosing to respect the slope of the background 20 eV before the peak will favor a more flat slope, while 40 eV slopes the baseline upwards towards the inelastic background being analyzed. Whether this affects the resulting IBA solution is dependent on the spectrum, and varies for each case. In the case of Al 1s in the Al_2O_3 overlayer, changing the slope of the baseline did not affect the accuracy of the IBA solution in comparison to the nominal values. A more complete discussion of the baseline fitting procedure is available in Chapter 6.

5.2.2.2 IBA of Al 1s in QUASES-Analyze: Two-parameter Universal inelastic scattering cross section

In any case, the resulting HAXPES-IBA solutions are increasingly uncertain for the Al 1s transition. The full IBA of Al 1s executed through QUASES-Analyze is shown in Figure 71. The large plasmon following the Al 1s peak necessitated evaluation of the IBA solution beginning 75 eV after the peak. A 100 eV energy range was available for analysis from 3770 – 3670 eV. The models have a Start Depth of 0 nm, indicating that there is little to no contamination at the surface. While the layer thicknesses are aligned

with the nominal values, uncertainty in the fitting procedure increases with the overlayer thickness (see Table 7). The fitting uncertainty is increased in comparison to Ga 2p due to uncertainty in the baseline-setting procedure and insensitivity in the Al 1s IBA model for thicker overlayers.

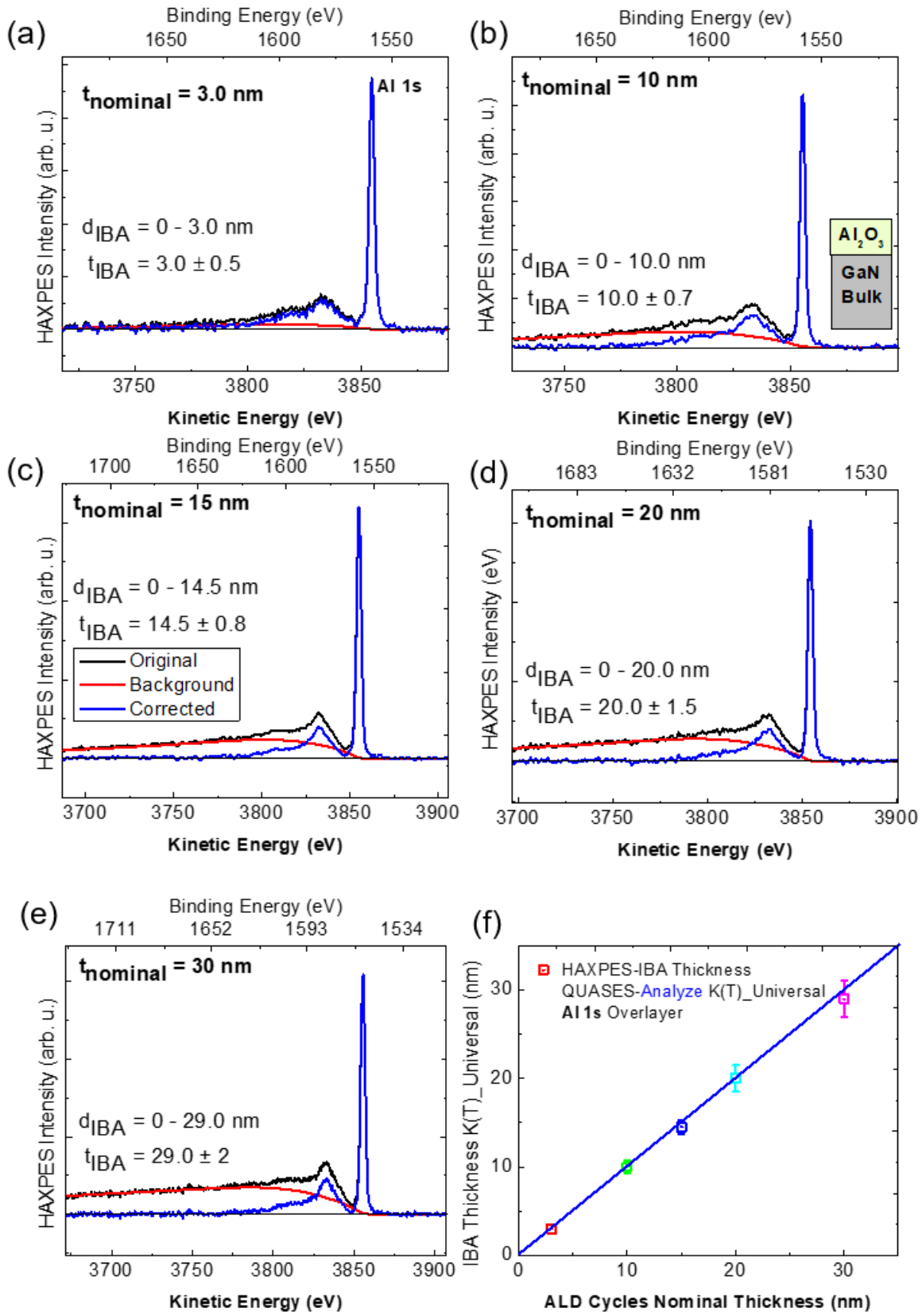

Figure 71. (a-e) HAXPES-IBA of Al 1s in the Al_2O_3 overlayer in the range 3-30 nm. (f) HAXPES-IBA solution agrees with the nominal thickness. The fitting uncertainty is increased in comparison to Ga 2p due to uncertainty in the baseline-setting procedure and insensitivity in the model for thicker overlayers.

The median thickness results achieved in QUASES-Analyze and calculated error to the ALD nominal thickness of Al_2O_3 are available in Table 20. The fitting uncertainty in each case permits 0% error to the nominal thickness in each case.

Table 20. HAXPES-IBA Thicknesses of Al 1s in the Al_2O_3 overlayer modeled in QUASES-Analyze. Al 1s IBA agrees with ALD cycle-determined overlayer thicknesses. Uncertainty in the fitting procedure is due to an uncertain baseline and a lack of sensitivity in the IBA model.

ALD cycle-determined thickness (nm)	HAXPES-IBA thickness (nm)	Fitting uncertainty (nm)	% Error to nominal thickness
3	3.0	0.5	0.0 %
10	10.0	0.7	0.0 %
15	14.5	0.8	3.4 %
20	20.0	1.5	0.0 %
30	29.0	2.0	3.4 %

As in Chapter 4, we find here that the IBA solution using the two parameter cross section is accurate despite the issue mentioned regarding the baseline determination. In the next section we propose a reference spectrum and compare it to the previous results.

5.2.2.3 IBA of Al 1s in QUASES-Generate: the use of a reference spectrum in QUASES-Generate

A 60 nm sample of Al_2O_3 was specially prepared by ALD to serve as a reference material. The reference spectrum was used in QUASES-Generate to model the plasmon and inelastic losses in spectra of different depth distributions. The inelastic background in the model spectrum was not sensitive to changes in the End Depth parameter, so a wider range of thickness solutions were acceptable. It is important to recall that in Chapter 4, using reference spectra in QUASES-Generate increased uncertainty in the Al 1s and O 1s fitting procedure as well. The spectra in QUASES-Generate are shown below in Figure 72. The thickness solutions are in agreement with the nominal thicknesses. As with QUASES-Analyze and $K_{Universal}$ alone, the Al 1s IBA model starts at 0 nm, suggesting no significant surface contamination layers.

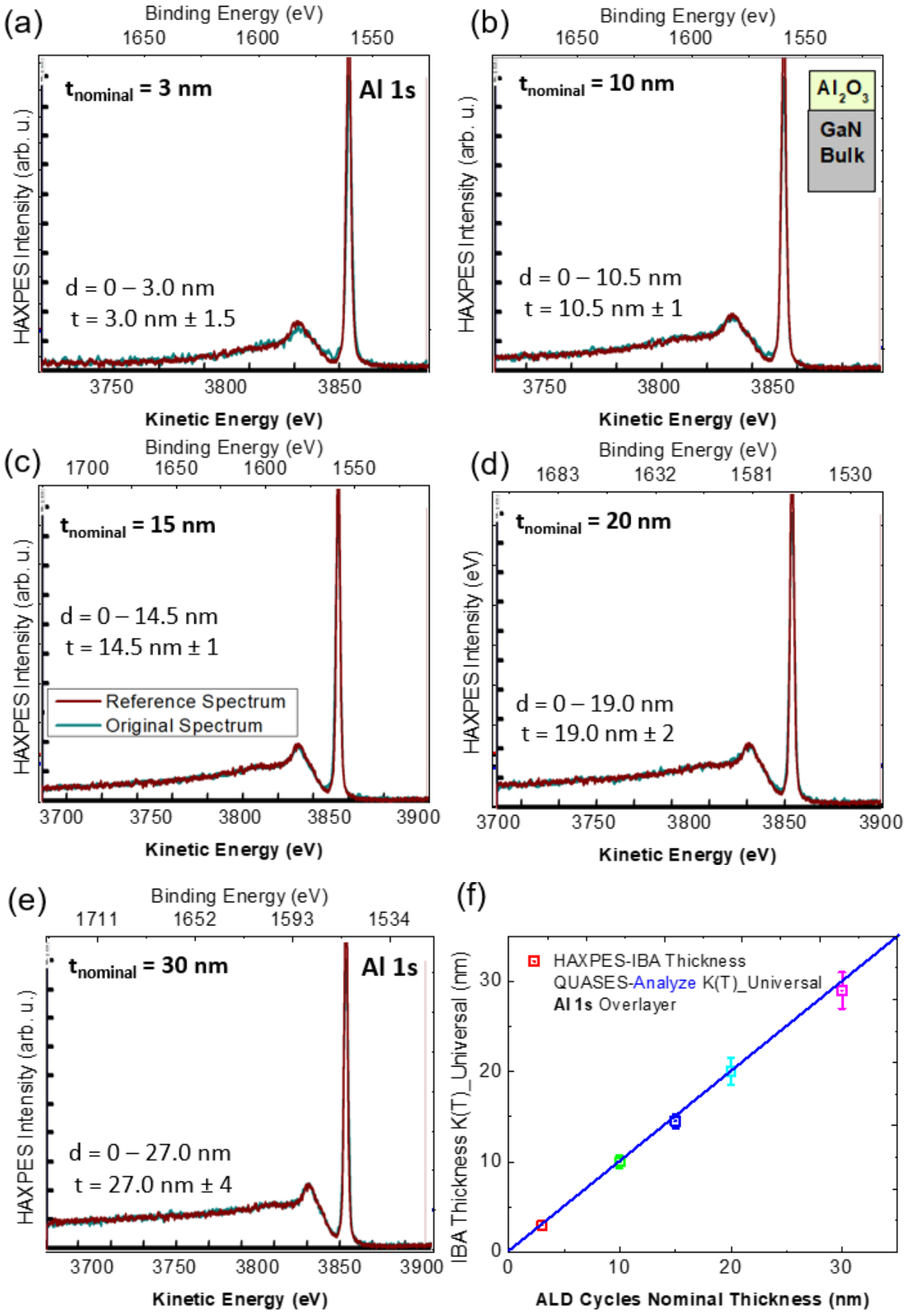

Figure 72. (a-e) HAXPES-IBA of Al 1s in the Al_2O_3 overlayer in the range 3-30 nm. (f)The HAXPES-IBA solution agrees with the thickness. The fitting uncertainty is increased in comparison to Ga 2p due to uncertainty in the baseline-setting procedure

and insensitivity in the model for thicker overlayers. A 60 nm Al_2O_3 reference sample was made in order to model the experimental spectrum without the use of $K_{Universal}$. The reference spectrum is red and the experimental spectrum isin the color teal.

Table 8 shows the results of the Al1s IBA analysis using the reference spectrum in QUASES-Generate. We see very good agreements between the IBA-derived thicknesses and the nominal thickness, with errors of 5-10%. This enables to prove the validity of the determination of the nominal thickness, in absence of any other measured value. Increasing uncertainty in the IBA method is also demonstrated in Table 21. The calculated error is based on the median IBA End Depth solution and is not the best indicator of agreement of the IBA and ALD cycle-determined overlayer thickness. Rather, Figure 72 (f) is the best demonstration of the relationship between the two determinations.

Table 21. Overlayer thicknesses of Al_2O_3 as determined by the number of ALD cycles and the End Depth parameter of the IBA solution for Al 1s.

ALD nominal thickness (nm)	HAXPES-IBA thickness (nm)	Fitting uncertainty (nm)	% Error to nominal thickness
3	3.0	1.5	0.0 %
10	10.5	1.0	5.0 %
15	14.5	1.0	3.3 %
20	19.0	2.0	5.0 %
30	27.0	4.0	10.0 %

For complete IBA of the overlayer, O 1s was also modeled in QUASES-Analyze and Generate.

5.2.2.4 IBA of O 1s in QUASES-Analyze: Two-parameter Universal inelastic scattering cross section

HAXPES-IBA of O 1s in the five Al_2O_3 overlayer samples is shown in Figure 73. The inelastic background modeled using $K_{Universal}$ (red) is well-fitted to the measured inelastic background in the original file (black). The depth distributions have a Start Depth of 0 nm, which agrees with the Al 1s results. The O 1s background intensity is low and complicates the analysis. With less information in the background signal, the IBA method is less precise, as a wider range of End Depths are possible. The signal-to-noise ratio before the peak is also higher and increases uncertainty in the fitting procedure. An oxide at the GaN/Al_2O_3 interface is often present in these structures, so the End Depth parameter in the O 1s model may overlap with the Start Depth of Ga $2p_{3/2}$. Unfortunately, the fitting uncertainty in the visual inspection is too high to definitively identify an oxide. This is especially true in the results from 5.2.1.1 where Ga $2p_{3/2}$ is consistently modeled several nanometers closer to the surface than the target

overlayer thickness would allow. The End Depth of O 1s is consistent with the results from the IBA of Al 1s for all samples in the series.

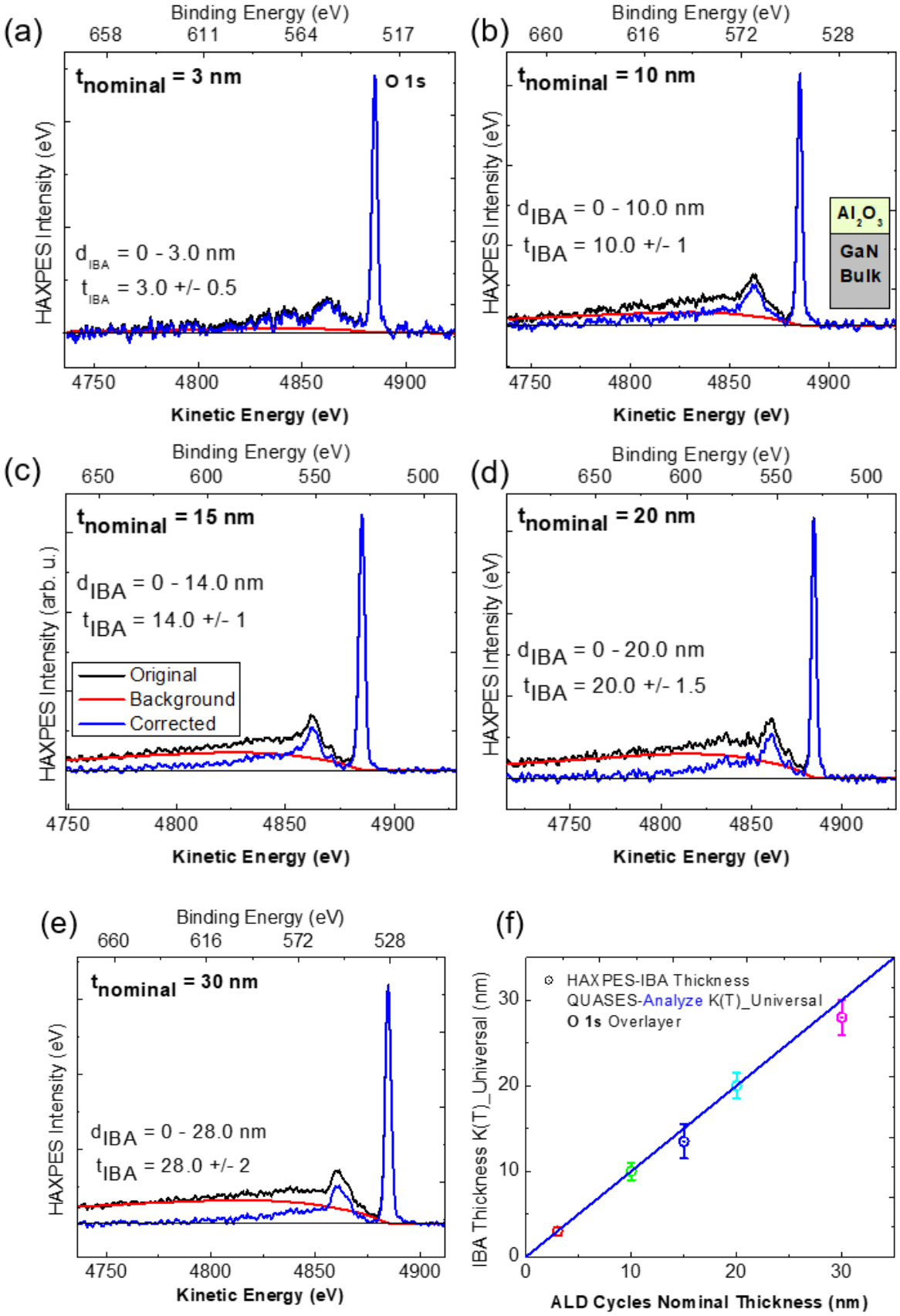

Figure 73. (a-e) HAXPES-IBA of O 1s in QUASES-Analyze using $K_{Universal}$ alone. (f)The HAXPES-IBA solution agrees with the thickness estimated by the ALD process. The calculated inelastic background (red) is well-fitted to the experimental background (black).

As shown in Figure 73 (f), the O 1s IBA thickness is in good agreement with the nominal values of the ALD process, with errors less than 7% and a fitting uncertainty of less than 10%. These results, combined with those from Al 1s, may help us to define a critical procedure for judging the accuracy of the analysis which is as follows:

1) Low-uncertainty IBA in Al 1s validates the nominal thicknesses over the 5 different samples and determines a minimum interface location with buried Ga.
2) Therefore, we may confidently take the nominal thicknesses as « true » values.
3) Accuracy in the O1s analysis may now be determined from the nominal thickness rather than the fitting uncertainty.

A summary of the results is available in Table 22.

Table 22. Overlayer thicknesses of Al_2O_3 as determined by the number of ALD cycles and the End Depth parameter of the IBA solution for O 1s.

ALD nominal thickness (nm)	**HAXPES-IBA thickness (nm)**	**Fitting uncertainty (nm)**	**% Error to nominal thickness**
3	3.0	0.5	0.0 %
10	10.0	1.0	0.0 %
15	14.0	1.0	6.7 %
20	20.0	1.5	0.0 %
30	28.0	2.0	6.7 %

The Al_2O_3 reference sample was again used to record a reference spectrum of O 1s for comparison to the results above using $K_{Universal}$ alone.

5.2.2.5 IBA of O 1s in QUASES-Generate: Reference Spectrum

The O 1s spectra as they appear in QUASES-Generate are shown below in Figure 74. The elastic and inelastic effects in the original spectrum are well accounted for by the model spectrum. The comparison in the background intensities is easier to see than in Figure 73 where the background is modeled by $K_{Universal}$ only. In several of the spectra, the median End Depth of the O 1s distribution when modeled with QUASES-Generate is different from that found in QUASES-Analyze (see previous section). The sample previously modeled as 10 nm is now 11 nm, the 15 nm overlayer is 17 nm, and the 28 nm increased to 35.5 nm. The uncertainty in the fitting procedure is high enough to allow either

thickness, but the use of a reference sample may reveal the oxide anticipated at the Al_2O_3 and GaN interface, thereby providing a more effective analysis.

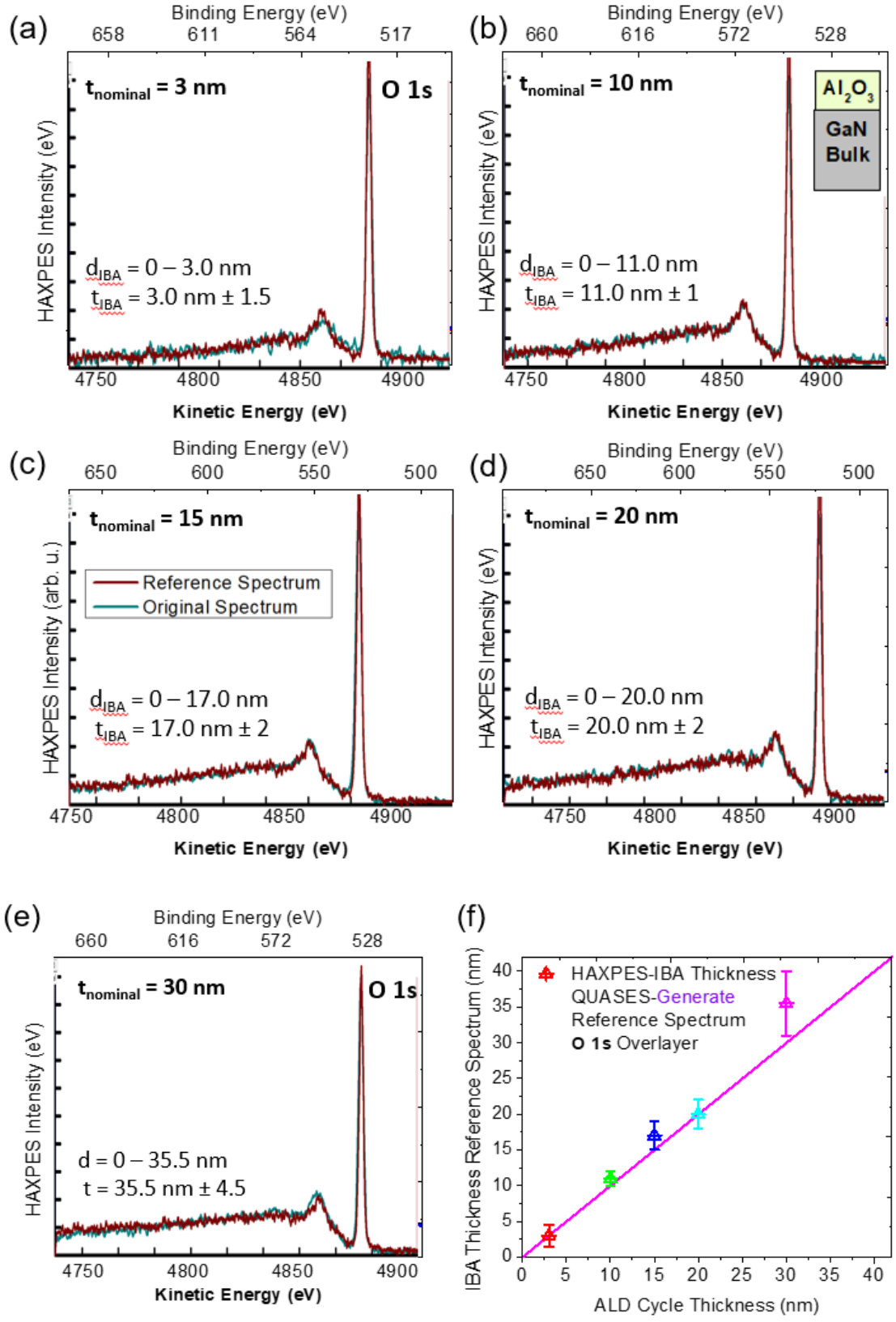

Figure 74. HAXPES-IBA of O 1s in QUASES-Generate. A 60 nm Al_2O_3 reference sample was made in order to model the experimental spectra of varying overlayer thicknesses. The reference spectrum is red, and the experimental spectrum is teal.

A potential oxide may be indicated by overlap in the interface positions of Ga $2p_{3/2}$ Start Depth values and O 1s End Depth values, with a constraint of the minimum Al 1s End Depth to limit the beginning of the oxide layer model. The relationship is shown in Figure 75, where the orange zone is where a Ga_xO_y layer may exist. Δd_i indicates the range of possible Start or End Depth values due to uncertainty in the fitting procedure and therefore a potential interface location between the Al_2O_3 and GaN layers.

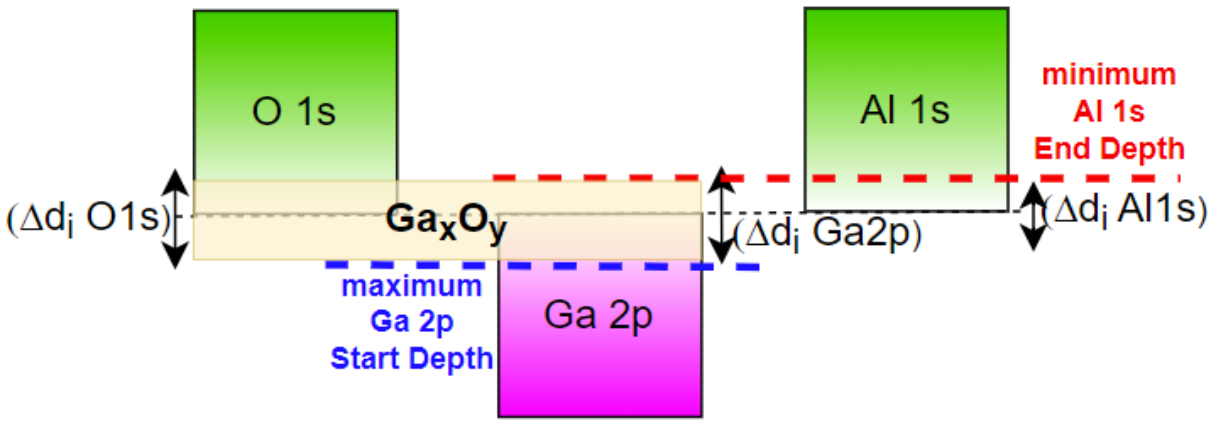

Figure 75. Overlap in d_1 positions as modeled by the O1s End Depth solution, maximum Ga 2p Start Depth, and minimum Al 1s End Depth.

The overlap in the range of Ga $2p_{3/2}$ Start Depth values and O 1s End Depth values are shown in Table 23. An oxide at the interface may exist in all five samples. The possible thickness increases with the overlayer thickness, which is expected based on increasing fitting uncertainty in the IBA solution.

Table 23. HAXPES-IBA of O 1s modeled in QUASES-Generate with a reference spectrum from Al_2O_3. The overlap distance between the O 1s End Depth and Ga $2p_{3/2}$ Start Depth supports the presence of an oxide at the Al_2O_3/GaN interface.

ALD nominal thickness (nm)	HAXPES-IBA thickness (nm)	Fitting uncertainty (nm)	% Error to nominal thickness	Overlap thickness with Ga $2p_{3/2}$ Start Depth (nm)
3	3.0	1.5	0.0 %	1.5
10	11.0	1.0	10.0 %	2.0
15	17.0	2.0	13.3 %	4.0
20	20.0	2.0	0.0 %	4.0
30	35.5	4.5	18.3 %	9.0

Due to uncertainty in the IBA fitting procedure, complimentary analyses are necessary to confirm or deny the existence of a GaN-O oxide. Such an interfacial Ga oxide was evidenced in an indirect way by HAXPES of the Ga2p core-level [4] using a spectrum of a bulk GaOx reference sample to help the peak

fitting procedure. The quantitative determination of the Ga-oxide concentration seems not to be a very sensitive method in this case. In the next section, we present TOF-SIMS depth profiling on the first four samples in the series.

5.2.3 Comparison to TOF-SIMS depth profiling

TOF-SIMS is a locally destructive technique which permits direct qualitative information about the depth distribution of elements in the structure and much more. It is the most sensitive microanalytical technique to dopant distribution variations, and has been integral to semiconductor research since the mid-20th century [17]. The experiment was performed at Cs+ 500 eV, and the full description can be found here [4]. The TOF-SIMS technique is presented in Chapter 2. The study discussed in this section will be included in another thesis (T. Spelta, "Fine chemical nanocharacterization of GaN structures for nano and opto-electric applications," Université Grenoble-Alpes).

The TOF-SIMS profiles for the 3, 10, 15, and 20 nm Al_2O_3 overlayer samples are shown in Figure 76. A stoichiometric oxide at the Al_2O_3/GaN interface would be evidenced by concurrent plateaus in the $^{16}OCs_2^+$ and $^{69}GaCs_2^+$ signals while $^{27}Al^+$ declined. This trend is not seen in any of the depth profiles, rejecting the possibility of a true oxide layer. In the profiles, however, a $^{16}OCs_2^+$ plateau is seen at the same time as $^{69}GaCs_2^+$ (2-5 nm in 3 nm in (a), 10-12 nm in (b), 15 nm in (c), 21 nm in (d). This supports the presence of an ultrathin layer of Ga_xO_y with a nonstoichiometric ratio strongly favoring Ga. This was previously observed by Duan *et al* In Al_2O_3/GaN structures using the same precursors with a HF surface preparation [18].

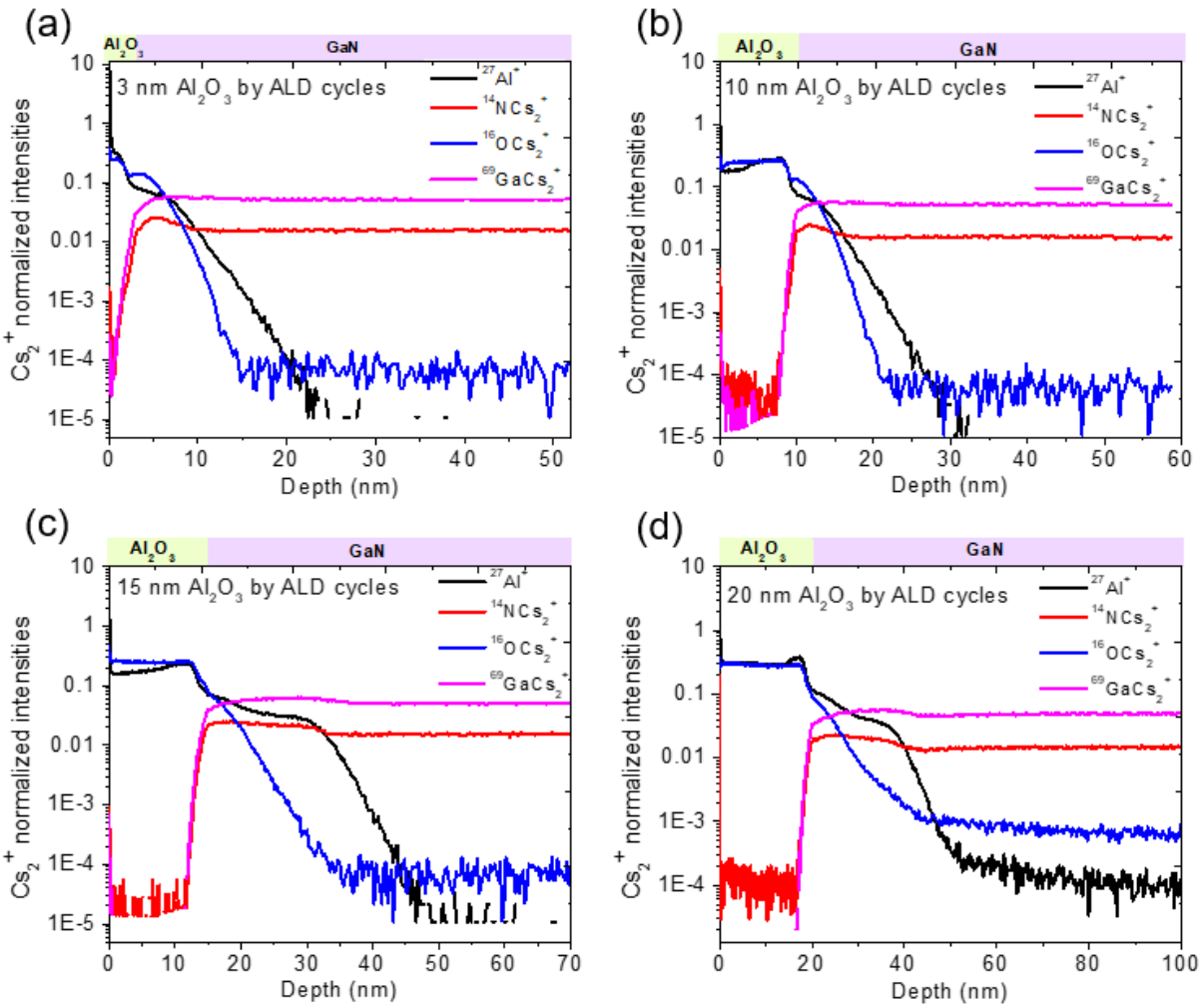

Figure 76. 500 eV Cs+ sputtering depth profiles of the first four Al_2O_3/GaN samples obtained with ToF-SIMS at a 45° incident angle. The sputter time was converted to depth based on the sputter rate.

The depth profiles achieved by TOF-SIMS support the nominal thicknesses of the ALD process. In the HAXPES-IBA analysis of Ga $2p_{3/2}$ using a reference spectrum in QUASES-Generate, the overlayer thicknesses were confirmed for all samples except for the 20 nm Al_2O_3, which fit best to a model with a Start Depth of 17.5 nm ± 0.2. Al 1s had a median End Depth of 19 nm ± 2 when a reference sample was used (Table 21), so the IBA method is not conclusive in this regard. A comparison of the TOF-SIMS sputter times to remove the Al_2O_3 overlayer vs the HAXPES-IBA thickness determinations is shown in Figure 77. A linear relationship was established for the first three samples.

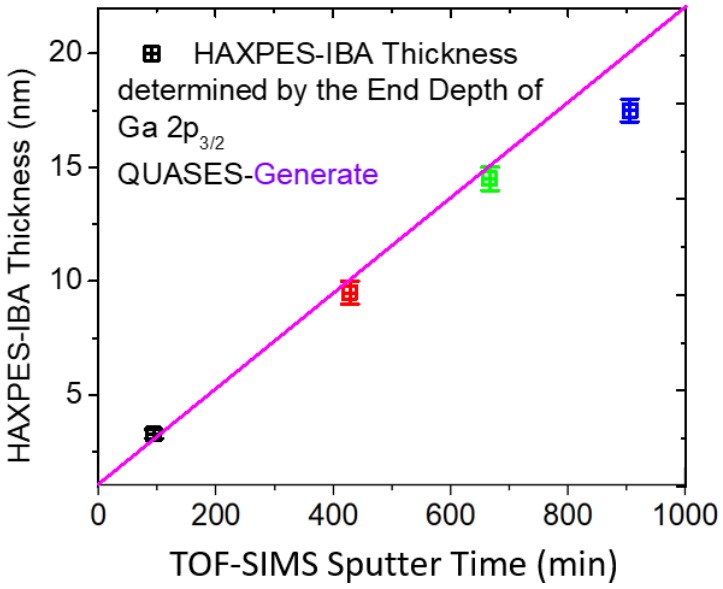

Figure 77. TOF-SIMS sputter times to remove Al_2O_3 overlayer vs HAXPES-IBA Start Depth of Ga $2p_{3/2}$ modeled with a GaN reference spectrum in QUASES-Generate.

Here we have confirmed HAXPES-IBA as an accurate and non-destructive technique capable of matching the results from highly quantitative depth profiling by TOF-SIMS in the analysis of Al_2O_3 and GaN. In support of the results from Chapter 4, we show that a reference spectrum is not necessary in the analysis of Al_2O_3 and may even increase uncertainty in the fitting procedure. In the case of buried GaN, however, the resulting Start Depth value improved by several nanometers in several cases and brought the IBA results closer to the nominal values of the ALD process which were confirmed by TOF-SIMS. The ideal IBA method and resulting error to the nominal and TOF-SIMS values are shown below in Table 24.

Table 24. The ideal IBA method and resulting error to the nominal and TOF-SIMS values.

ALD nominal Start Depth (nm)	Element transition	Best QUASES method	% Error to nominal and TOF-SIMS Start Depth	
3	Ga $2p_{3/2}$	QUASES-Analyze	0.0 %	
10	Ga $2p_{3/2}$	both	5.0 %	
15	Ga $2p_{3/2}$	QUASES-Generate	3.3 %	
20	Ga $2p_{3/2}$	QUASES-Generate	12.5 %	
30	Ga $2p_{3/2}$	QUASES-Generate	1.7 %	
			Al 1s	**O 1s**
3	Al 1s, O 1s	QUASES-Analyze	0.0 %	0.0 %
10	Al 1s, O 1s	QUASES-Analyze	0.0 %	0.0 %
15	Al 1s, O 1s	QUASES-Analyze	3.4 %	6.7 %
20	Al 1s, O 1s	QUASES-Analyze	0.0 %	0.0 %
30	Al 1s, O 1s	QUASES-Analyze	3.4 %	6.7 %

5.3 Results of IBA on TiN/HfO_2 samples

The other high-k material studied in Chapter 4, HfO_2, is studied in this section in a TiN/HfO_2 heterostructure for applications in MOSc-FET technologies. HfO_2 is one of the most preferred gate oxide materials to replace SiO_2, but point vacancies and interface stoichiometry with TiN have a great influence on the effective work function (EWF) in CMOS devices [19,20]. It is important to investigate these effects without disturbing the TiN/HfO_2 interface. XPS is established as an ideal surface analysis technique in CMOS technology, and increasing the probing depth with HAXPES allows for the investigation of even more complex heterostructures and deeply buried, critical interfaces.

The complete TiN/HfO_2 structures studied in this work are shown in Figure 63, but a simplified model is available below in Figure 78. The models in Figure 78 (b) and (c) reflect a TiN(10)/Ti(10) nm overlayer which has undergone Ar^+ sputter treatment. Depth profiling of the layer thicknesses was able to be achieved through maintaining the sputter rate at 0.8 nm/per minute and confirming the resulting thickness with HAXPES-IBA.

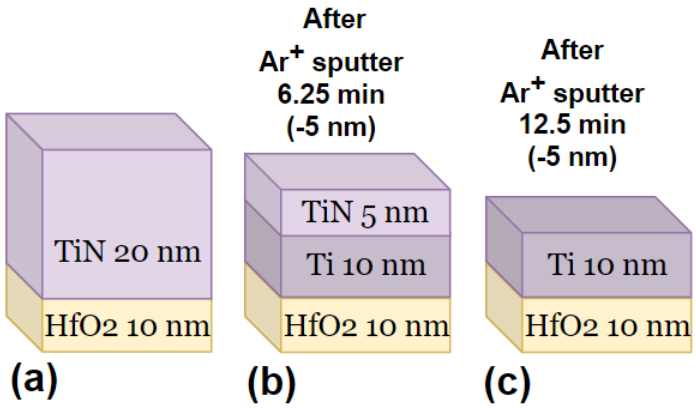

Figure 78. Simplified models of the TiN/Ti/HfO_2 structures. (b) and (c) are from a TiN(10)/Ti(10) overlayer sample which underwent Ar^+ sputter abrasion to remove 5 and 10 nm, respectively. (a) is a substitute sample with an IMFP almost identical to the original complete stack and thus fit for a sputter depth profiling study.

As will be shown in the following results, the IMFP of Ti 1s (1.22 nm) is too short for analysis of the buried Ti layer. The several buried layers profile of Ti 1s was used to replicate the sandwich but was unsuccessful. It's for this reason that our simplified model does not include the 100 nm TiN layer shown in Figure 63.

5.3.1 HfO_2 buried layer depth distribution

As shown in Figure 79, the spectral region containing the Hf $3d_{5/2}$ and Hf $3d_{3/2}$ signals was affected by Ti KLL Auger signals present in the 1400 – 1550 eV BE range. While this would apparently hinder the baseline-setting procedure, IBA was still able to be performed for an accurate Start Depth determination. Interestingly, trying different baselines which accounted for more or less of the continuous background from higher KE relative to the peak did not significantly affect the resulting solution.

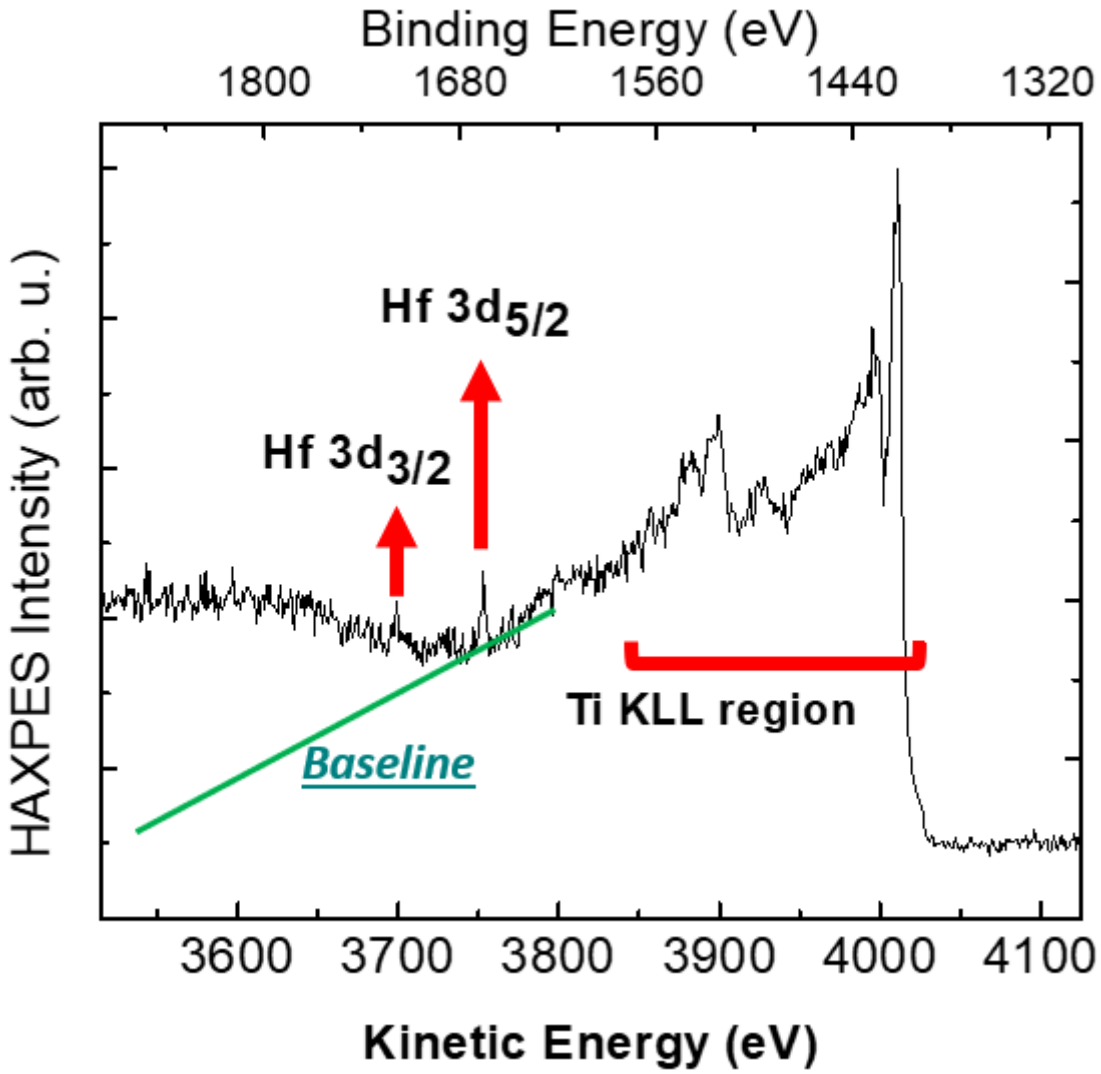

Figure 79. Cr Kα HAXPES spectrum of the Hf $3d_{5/2}$ and Hf $3d_{3/2}$ analysis region. Ti KLL Auger electron signals drastically affect the continuous background before the Hf peaks. The baseline (green) is set only 20 eV into the continuous background before the peak where it begins to stabilize.

The Hf $3d_{5/2}$ inelastic background was modeled in QUASES-Analyze using the two-parameter Universal inelastic scattering cross section (Figure 80). The median target Start Depths were achieved within 1 nm for all three samples with fitting uncertainties that allowed for the expected value. The sputter procedure had a target rate of 0.8 nm per minute: this was confirmed accurate by IBA (Figure 80 (d)). Although the Hf 3d peaks are very small in the 15 and 20 nm overlayer samples (Figure 80 (b), (c)), the background was still well modeled in the 3650 – 3550 eV KE region. Indeed, the background was better fit for the thicker samples than the 10 nm Ti overlayer sample (Figure 80 (a)), where plasmons following the Hf $3d_{3/2}$ peak impede the fit. An infinitely thick HfO_2 layer was the best solution for all three samples. This is unexpected especially for the thinnest sample, since Hf $3d_{5/2}$ has an $IMFP_{eff}$ of 5 nm. This study is concerned, however, with the interface position of the Ti overlayer an buried HfO_2 which is represented by the Start Depth of Hf $3d_{5/2}$.

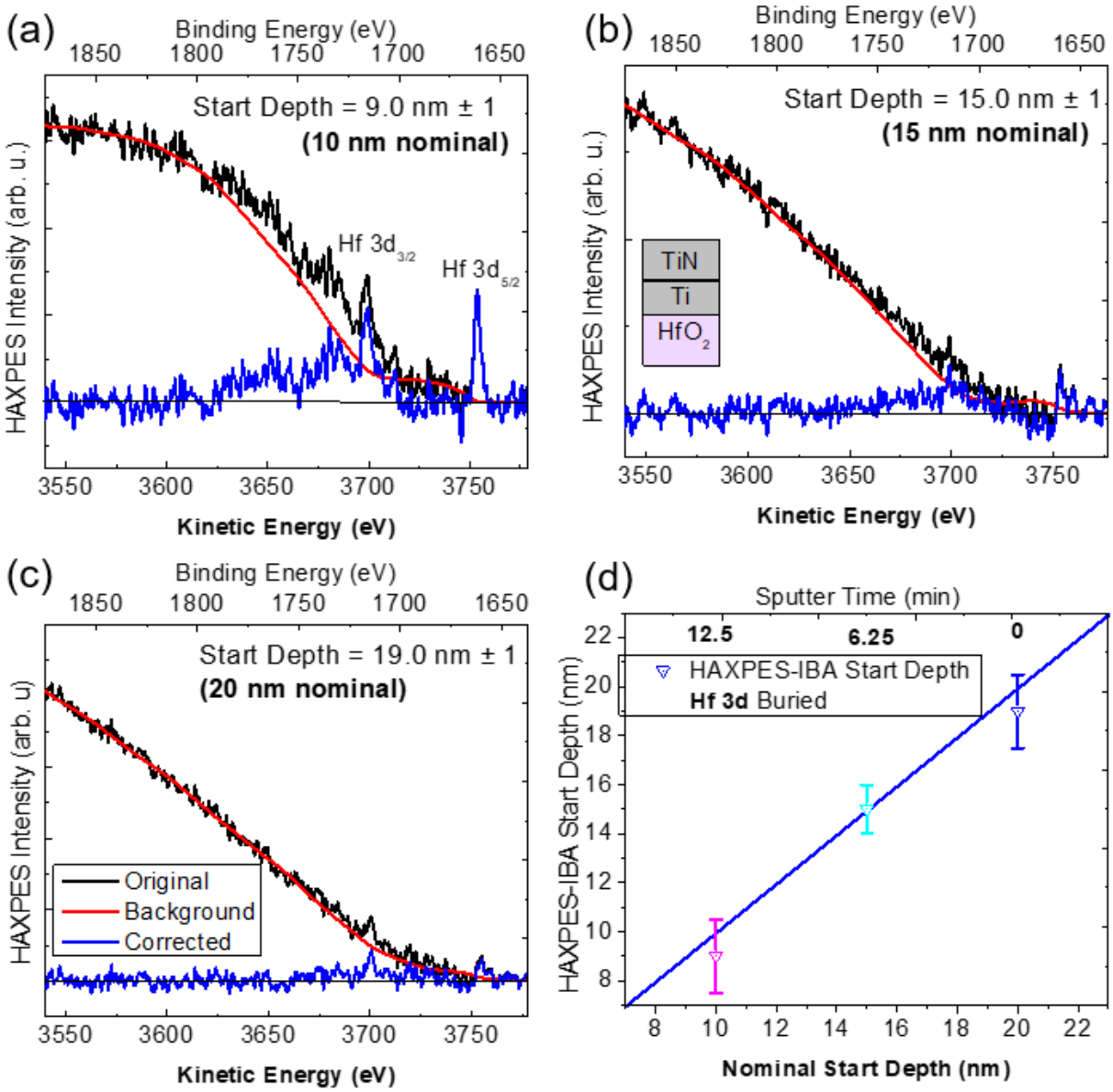

Figure 80. HAXPES-IBA of Hf 3d buried under TiN and TiN/Ti.

The Start Depth of the Hf layer is a good indicator of the total Ti and TiN overlayer thicknesses. The low BE range of the TiN/HfO_2 spectrum contains too many peaks, preventing the analysis of Hf 4p or Hf 4s. Therefore, IBA of these samples is only possible thanks to the 5415 eV Cr Kα radiation. This is especially true for Ti 1s, which lies at 4960 eV BE.

5.3.2 Overlayer depth distribution

The case of the Ti 1s photoelectron signal is particular, as the spectrum contains a strong plasmon signal at 380 eV and a Ti LMM Auger 425 eV KE. The two-parameter Universal inelastic scattering cross section does not account for plasmon contributions. This, along with the Auger and a restricted background region due to the limit of the source energy, results in a fit so poor that it is not possible to calculate the background. A three-parameter Universal inelastic scattering cross section is available

in the software which gives a good fit to narrow experimental cross sections [21]. The three-parameter Universal cross section is defined in section 3.1.3 and the values for the numerical parameters C and D are determined based on a good fit of K(E) and the plasmon [7,9,10]. The region of the spectrum in which Ti 1s is found is not occupied by many other signals, and the sole O KLL at 518 eV is not intense enough to affect the continuous background. This led to an uncomplicated baseline-setting step.

The full IBA of Ti 1s is shown in Figure 81. The model for the 10 nm overlayer sample (12.5 minutes sputtered) (Figure 81 (a)) indicates a median End Depth of 10.5 nm ± 0.5, while the Hf 3d model (Figure 80 (a)) is best modeled at 9.0 nm ± 1. Fitting uncertainty in the Hf 3d model allows for an interface at 10 nm for which both models agree. The 15 and 20 nm-estimated overlayer samples agree with an interface at 15 and 19 nm, respectively.

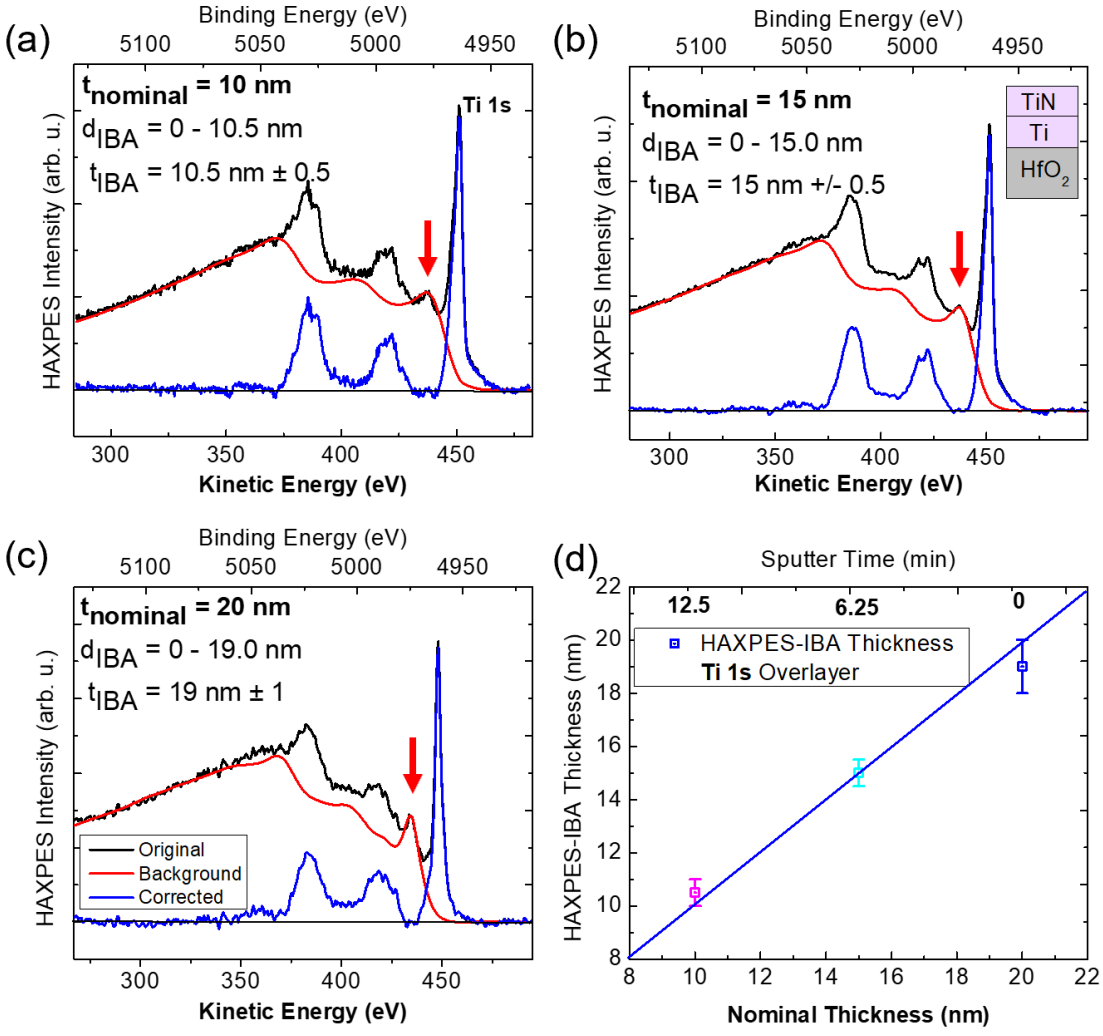

Figure 81. HAXPES-IBA of Ti 1s in the TiN and TiN/Ti overlayers. The plasmon used to determine a good fit with the three parameter universal cross-section is indicated with a red arrow.

An Auger from C KLL at 5450 eV prevented IBA over a long background range. The analysis, however, was not hindered, since the three-parameter cross section accounted for the narrow plasmons at 380 and 425 eV. This allowed the inelastic losses to be accurately calculated along a range of 275 – 370 eV.

This is a particular case in which external thickness measurements were not included in the study. Through HAXPES-IBA and sputter depth profiling, the Ti 1s overlayer thickness and Hf 3d Start Depth were determined with high accuracy. The sputter rate of 0.8 nm/min was confirmed accurate as well. The Ti 1s transition has an IMFP of 1.22 nm with Cr Kα radiation, the ability of the method to model the 20 nm overlayer means that this method exceeded the probing depth to just over twice the anticipated 8×IMFP. This is important since the low BE region where Ti 2p (458 eV BE) is found is usually crowded with other core peaks such as O 1s and Hf 4p. We show that the weak Hf 3d signal was able to be analyzed despite a strong background before the peak. The influence of the continuous background in the higher KE range before the peak is discussed further in Chapter 6.

5.4 Summary and Conclusion

MOSc-FET device structures have come a long way in scaling down since the 1960s, from several µm to sub-10 nm in the gate oxide [19]. GaN-based HEMT technology is innovative in increasing the mobility of charge carriers, but in order to obtain a normally-OFF device necessary for safety reasons, advanced fabrication steps are needed [22]. As these devices complexify, non-destructive characterization of the interface is challenged to overcome thick dielectrics and insulators. Here we present a HAXPES-IBA method capable of interpreting the overlayer thickness and interface position through the analysis of Ga $2p_{3/2}$, Al 1s, O 1s in Al_2O_3/GaN heterostructures, and Ti 1s and Hf $3d_{5/2}$ in TiN/Ti/HfO_2 multilayer stacks. In the case of Al_2O_3 deposited over GaN in a fabrication process representative of a MOSc-HEMT device, the Al_2O_3 overlayer thickness and Al_2O_3/GaN interface position was determined using a HAXPES-IBA technique which combined QUASES-Analyze and QUASES-Generate. In line with the results from Chapter 4, we confirmed that the two-parameter Universal cross section was preferable to a reference spectrum in the analysis of Al_2O_3 for minimizing the fitting uncertainty measure. In the study of Ga $2p_{3/2}$ through Ga 2s, however, we found that a GaN bulk reference spectrum increased the Start Depth parameter by several nm, reducing error to the ALD cycle determined Al_2O_3 overlayer thickness from 25% to 12.5% in the most extreme case. A slight overlap in the O 1s and Ga $2p_{3/2}$ depth distributions indicated an ultrathin oxide at the interface. These results were corroborated by a TOF-SIMS depth profile performed on the first four samples in the series, which confirmed the presence of a nonstoichiometric oxide as well as the nominal overlayer thicknesses. HAXPES-IBA in Ti/TiN/HfO_2 heterostructures delivered overlayer thicknesses and interface

positions consistent with sputter times in a depth profiling which removed 0.8 nm per minute. The Ti 1s and Hf $3d_{5/2}$ depth distributions permitted an interface position of $d_1 = d_2$. The probing depth of the IBA-HAXPES method reached 16×IMFP in the analysis of Ti 1s in the overlayer, supporting recent studies which show that the previously reported 8×IMFP can be exceeded with HAXPES radiation.

These results confirm HAXPES-IBA with lab-based Cr Kα radiation as a fast and effective technique for non-destructive thickness confirmation and interface oxide detection. As more lab-based HAXPES instrumentation is implemented in clean room environments, IBA can provide valuable information on device fabrication processes and experimental parameters, and with only the routine measurements already performed on the sample.

[1] O. Renault, P.-M. Deleuze, J. Courtin, T.R. Bure, N. Gauthier, E. Nolot, C. Robert-Goumet, N. Pauly, E. Martinez, K. Artyushkova, New directions in the analysis of buried interfaces for device technology by hard X-ray photoemission, Faraday Discuss. 236 (2022) 288–310. https://doi.org/10.1039/D1FD00110H.

[2] J. Widiez, M. Vinet, T. Poiroux, P. Holliger, B. Previtali, P. Grosgeorges, S. Deleonibus, M. Mouis, TiN metal gate thickness influence on Fully Depleted SOI MOSFETs physical and electrical properties, in: 2005 IEEE Int. SOI Conf. Proc., IEEE, Honolulu, HI, USA, 2005: pp. 30–31. https://doi.org/10.1109/SOI.2005.1563523.

[3] T. Szyjka, L. Baumgarten, T. Mittmann, Y. Matveyev, C. Schleuter, T. Mikolajick, U. Schroeder, M. Müller, Enhanced Ferroelectric Polarization in TiN/HfO2/TiN Capacitors by Interface Design, ACS Appl. Elect. Mater. 2 (2020) 3152–3159. https://doi.org/10.1021/acsaelm.0c00503.

[4] T. Spelta, M. Veillerot, E. Martinez, N. Chevalier, D. Mariolle, R. Templier, B. Salem, P.F. Paes Pinto Rocha, L. Vauche, S. Boubenia, B. Hyot, Characterization of GaN structures for power electronics by secondary ion mass spectrometry and atomic force microscope approach, J. Vac. Sci. Technol. B. 41 (2023) 034003. https://doi.org/10.1116/6.0002573.

[5] L. Grenouillet, T. Francois, J. Coignus, S. Kerdiles, N. Vaxelaire, C. Carabasse, F. Mehmood, S. Chevalliez, C. Pellissier, F. Triozon, F. Mazen, G. Rodriguez, T. Magis, V. Havel, S. Slesazeck, F. Gaillard, U. Schroeder, T. Mikolajick, E. Nowak, Nanosecond Laser Anneal (NLA) for Si-Implanted HfO2 Ferroelectric Memories Integrated in Back-End of Line (BEOL), in: 2020 IEEE Symp. VLSI Technol., IEEE, Honolulu, HI, USA, 2020: pp. 1–2. https://doi.org/10.1109/VLSITechnology18217.2020.9265061.

[6] M. Kachan, J. Hunter, D. Kouzminov, A. Pivovarov, J. Gu, F. Stevie, D. Griffis, O2+ versus Cs+ for high depth resolution depth profiling of III–V nitride-based semiconductor devices, Appl. Surf. Sci. 231–232 (2004) 684–687. https://doi.org/10.1016/j.apsusc.2004.03.211.

[7] A. Müller, K. Sparnacci, W.E.S. Unger, S. Tougaard, Determining nonuniformities of core-shell nanoparticle coatings by analysis of the inelastic background of X-ray photoelectron spectroscopy survey spectra, Surf. Interface Anal. 52 (2020) 770–777. https://doi.org/10.1002/sia.6865.

[8] S. Tougaard, M. Greiner, Method to correct ambient pressure XPS for the distortion caused by the gas, Appl. Surf. Sci. 530 (2020) 147243. https://doi.org/10.1016/j.apsusc.2020.147243.

[9] S. Tougaard, Guide to the posted videos, (2021). http://www.quases.com/data/documents/Videos/Guide%20to%20the%2014%20posted%20videos.pdf (accessed September 20, 2023).

[10] 10. Using 1 the external cross section facility, 2021. http://www.quases.com/data/documents/Videos/Using_1%20the%20external%20cross%20section%20facility.mp4 (accessed September 20, 2023).
[11] P. Risterucci, Coupling of electron spectroscopies for high resolution elemental depth profiles in complex architectures of functional materials, University of Lyon, 2015.
[12] M. Krawczyk, A. Jablonski, S. Tougaard, J. Toth, D. Varga, G. Gergely, The inelastic mean free path and the inelastic scattering cross-section of electrons in GaAs determined from highly resolved electron energy spectra, Surf. Sci. 402–404 (1998) 491–495. https://doi.org/10.1016/S0039-6028(97)00939-4.
[13] G. Gergely, A. Sulyok, M. Menyhard, J. Toth, D. Varga, A. Jablonski, M. Krawczyk, B. Gruzza, L. Bideux, C. Robert, Experimental determination of the inelastic mean free path of electrons in GaSb and InSb, Appl. Surf. Sci. 144–145 (1999) 173–177. https://doi.org/10.1016/S0169-4332(98)00793-4.
[14] J. Rubio-Zuazo, G.R. Castro, Non-destructive compositional depth profile analysis by hard x-ray photoelectron spectroscopy, J. Phys. Conf. Ser. 100 (2008) 012042. https://doi.org/10.1088/1742-6596/100/1/012042.
[15] A. Jablonski, Evaluation of procedures for overlayer thickness determination from XPS intensities, Surf. Sci. 688 (2019) 14–24. https://doi.org/10.1016/j.susc.2019.05.004.
[16] J. Rubio-Zuazo, G.R. Castro, Experimental effective attenuation length on solids for electron kinetic energies between 1 and 14 KeV: Determination of a simple practical equation, Appl. Surf. Sci. 599 (2022) 153918. https://doi.org/10.1016/j.apsusc.2022.153918.
[17] P. van der Heide, Secondary Ion Mass Spectrometry: An Introduction to Principles and Practices, Wiley, 2014.
[18] T.L. Duan, H.Y. Yu, L. Wu, Z.R. Wang, Y.L. Foo, J.S. Pan, Investigation of HfO_2 high-k dielectrics electronic structure on SiO_2 /Si substrate by x-ray photoelectron spectroscopy, Appl. Phys. Lett. 99 (2011) 012902. https://doi.org/10.1063/1.3609233.
[19] J. Robertson, High dielectric constant gate oxides for metal oxide Si transistors, Rep. Prog. Phys. 69 (2006) 327–396. https://doi.org/10.1088/0034-4885/69/2/R02.
[20] R.K. Pandey, R. Sathiyanarayanan, U. Kwon, V. Narayanan, K.V.R.M. Murali, Role of point defects and HfO2/TiN interface stoichiometry on effective work function modulation in ultra-scaled complementary metal–oxide–semiconductor devices, J. Appl. Phys. 114 (2013) 034505. https://doi.org/10.1063/1.4816090.
[21] S. Tougaard, Universality Classes of Inelastic Electron Scattering Cross-sections, Surf. INTERFACE Anal. 25 (1997) 18.
[22] J. He, W. Cheng, Q. Wang, K. Cheng, H. Yu, Y. Chai, Recent Advances in GaN-Based Power HEMT Devices, Adv. Electron. Mater. 7 (2021) 2001045. https://doi.org/10.1002/aelm.202001045.

6 Critical Review of HAXPES-IBA

Chapter 1 discussed the current state of nanodevice technology, and the apparent need for nondestructive thickness measurements of the deeply buried layers that make up increasingly complex semiconductor components. A key challenge faced in thickness metrology is achieving high throughput for inline processes. Automation in interpretating results allows for increased data processing and reduces the need for specialist intervention. Here we discuss an error calculation for evaluating the fit between the original measured spectrum and the inelastic background calculated by the QUASES-Analyze software.

6.1 Previous work in HAXPES-IBA to implement and error calculation

Extensive work has been done to develop guidelines for the ideal weights when calculating $IMFP_{eff}$ and $K(E)_{eff}$ [1–3]. Theoretical spectra were modeled using QUASES-Generate by applying input parameters reflective of sample stacks with varied thicknesses and buried depths to bulk reference spectra. Materials with different or similar IMFP and K(E) parameters were combined in different stacking orders. Indeed, it was found that the operator must take into account these differences when defining the weighted calculation for the two parameters, and the species used whether polymer or pure metal mattered [2,3]. The backbone of this comprehensive and large-scaled work were the thousands of possible IBA Start Depth and End Depth values that were passed into QUASES-Analyze as possible "solutions." An error calculation was then applied over the calculated inelastic background and experimental background to determine the solution with the best fit. Given the solution was clearly known, one could then find the $K(E)_{eff}$ and $IMFP_{eff}$ input parameter combinations whose error calculation gave the correct solution and thus determine the input parameters.

In the recent theoretical study [2] discussed above, HAXPES spectra from Si 1s at 6099 eV and Al Kα XPS spectra from Au 4d at 1152 eV were modeled in QUASES-Generate as layers buried under Si, Au, Al, Ta, or polymer. Si and Ta inelastic cross sections were calculated from REELS analysis, while the Universal, Al, and polymer cross-sections are included in the QUASES software. These cross sections were selected because they are very different (Figure 82).

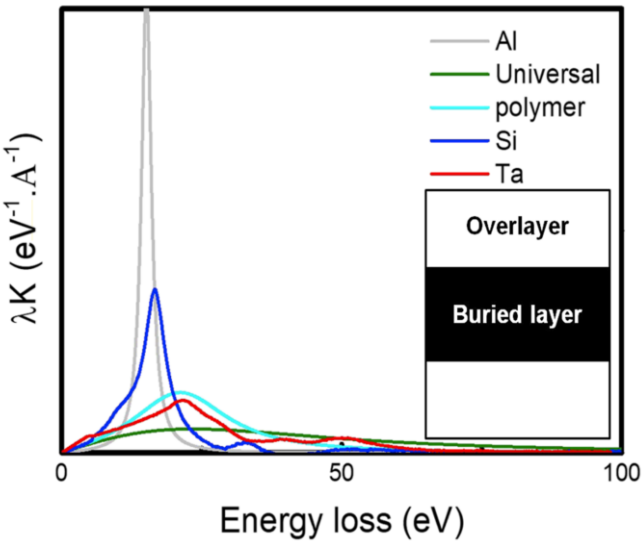

Figure 82. Cross sections used in the virtual stacks with individual Si, Au, Al, Ta or polymer layers. Taken from [2].

The error calculation was a simple area error calculation on a controlled range of the spectrum together with a calculation of the mean deviation. It was determined that a half-contribution from the buried layer as presented in section 3.1.2.2 of Chapter 3 provided the best input parameters for the effective IMFP and K(E) determinations, except in the case of Au or Si buried under a polymer. In this case, the full contribution of the buried layer is best for calculating the IMFP. This is what was used in this work.

Given that the interest of this thesis is to evaluate how lab-based HAXPES-IBA would be of interest for the inline fabrication process, and that one the incentives of current metrology is automation in routine analysis, an error calculation to determine the experimental thickness would advance the method to a great degree.

6.2 Error calculation methods for IBA solution

Various error calculations may be made to evaluate the closeness of the measured values from the original spectrum and the values of the simulated background calculated with the inelastic scattering cross section in the QUASES software. The first thesis on this subject [4] used a regularization procedure by means of two quantities, the residual norm χ and the solution norm α. The residual norm is the standard deviation root mean square χ and is expressed as the formula:

Equation 42

$$\chi = 100 \times \sqrt{\sum_i \frac{\left(y_i^m - y_i^b\right)^2}{n_i}}$$

with y_i^m the measured intensity at energy i, y_i^b the modelled intensity at energy i and n_i the number of points considered. A smaller value of χ indicates a better match between measurement and modeling. The solution norm is a measure of the complexity of the proposed depth profile.

The following thesis [5] applied an area error calculation which accounted for all of the space between the two signals.

In our method, we use the mean squared error (MSE):

Equation 43

$$MSE = \frac{1}{n}\sum_{i=1}^{n}(Y_i - \hat{Y}_i)^2$$

Where n is the number of data points in the range, Y_i are the measured values (Original) and $\hat{Y}_i$ are the calculated values (Background).

All three methods will have increased error for noisy spectra, with the extremes misrepresenting the closeness of the two signals. The smoothing method applied in the QUASES software when preparing the spectrum for analysis reduces noise, but this bias is still present. Noise increases for spectra of more deeply buried elements, as shown in Figure 83. Here, we see a close up of the energy range over which the MSE was performed in analysis of buried Hf $3d_{5/2}$ with overlayers of (a) 9.9 and (b) 24.4 nm Al_2O_3. (b) contains much more noise, and the MSE will account for more extremes between the two signals.

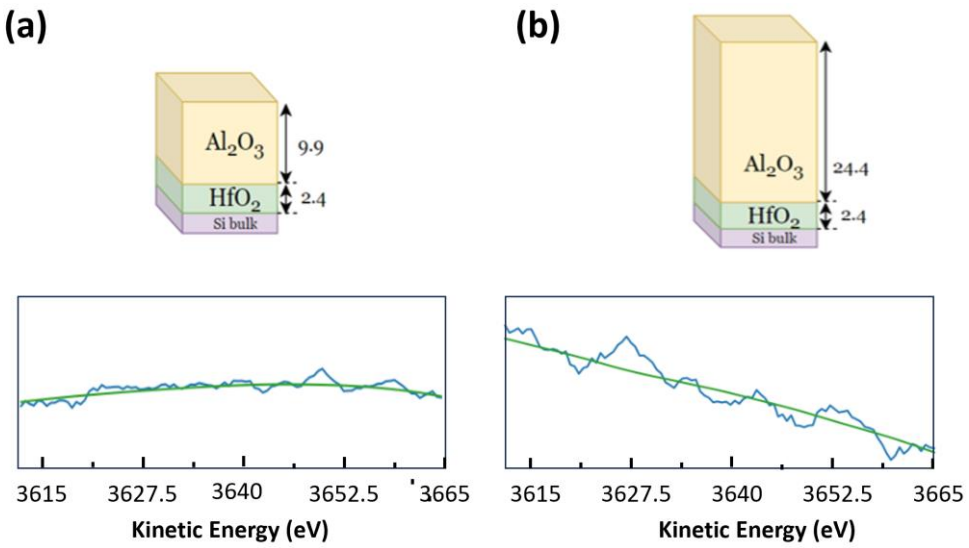

Figure 83. IBA fits in Hf $3d_{5/2}$ spectra over the energy range of error calculation for (a) 9.9 nm Al_2O_3 overlayer sample and (b) 24.4 nm Al_2O_3 overlayer sample.

This uncertainty should be considered, and will be different for spectra from various elements and depth distributions. This dilemma is only one source of uncertainty in an error calculation to evaluate the IBA fit.

6.3 Operator bias in range selection

Unfortunately, while the error calculation is a necessary and useful tool when determining input parameters for the QUASES software, it is not an accurate solution for removing the error implicit in the visual inspection. In the case of using the Universal inelastic scattering cross-section and even when using a specified cross-section, the calculated and measured background do not perfectly overlap. As shown in Figure 1 of Ga $2p_{3/2}$ in bulk GaN buried under (a) 3 nm Al_2O_3 and (b) 15 nm (nominal layer thicknesses predicted by the ALD process), the calculated inelastic background (red) does not overlap perfectly with the measured inelastic background (black). Additionally, the Ga 2s peak and its plasmon "break" the alignment. The calculated background between the Ga 2p and Ga 2s peaks is too high but is well-fitted in the region with increased energy losses.

It is possible that favoring a good fit in the region between the Ga 2p and Ga 2s peaks would have a different minimum error value than that at the higher energy loss region of the spectrum and would thus be associated with a different IBA solution. Instead, the minimum error calculation will be associated with a different IBA solution. And so, the bias implicit in a visual inspection of the background fits remains when selecting the range over which the fit is assessed mathematically. An additional complication over the bias of the region of fit is the standardization of range-setting for

spectra from different layer thicknesses and buried depths. This is shown in Figure 84, where the range of fit is 25 eV larger in the higher energy loss region for (a) than (b). The 70 eV range of fit between the Ga 2p and Ga 2s peaks is shifted by 20 eV. At this stage one may assume that the noise level of the inelastic background signal is one factor that could explain such discrepancies. In the next example we see it is not the case.

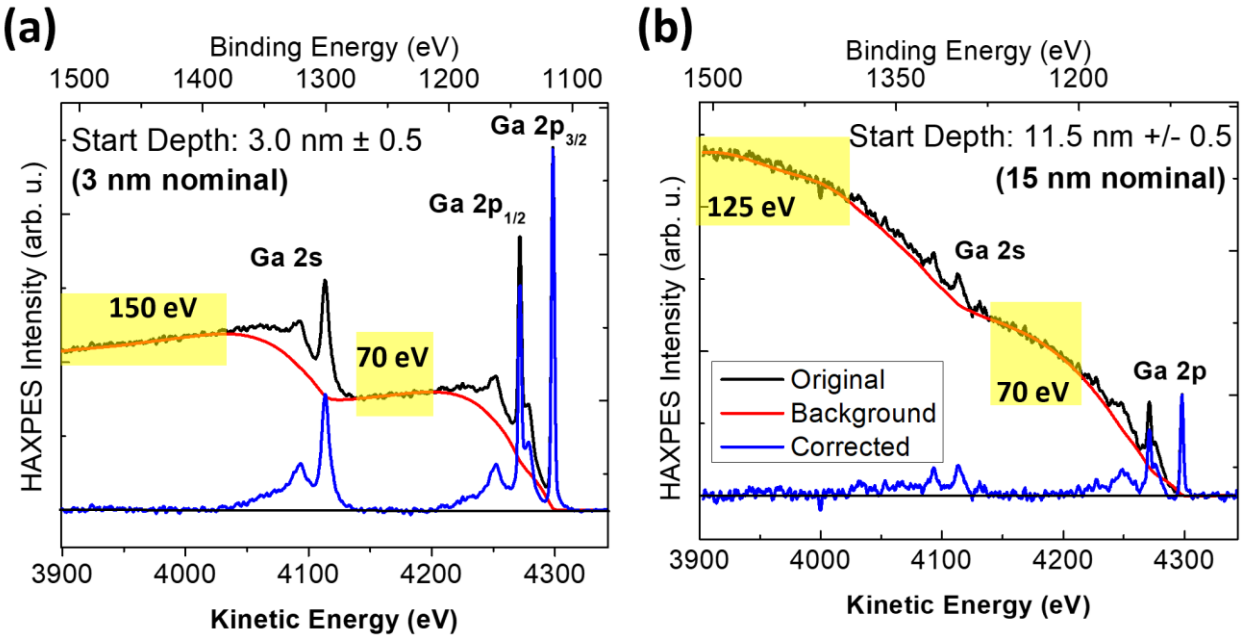

Figure 84. HAXPES-IBA of Ga 2p – 2s in bulk GaN buried under (a) 3 nm and (b) 15 nm Al_2O_3. An error calculation performed over one range (highlighted yellow) of the spectrum over another may change the best fit solution. The size and boundaries of the range over which the fit inspection is different for different buried depths.

The inconsistency in the region of fit analysis is also present when changing the energy of the photon source. Figure 85 shows the HAXPES-IBA of Hf 3d in HfO_2 (2.4 nm confirmed by XRR) buried under Al_2O_3 (9.9 nm confirmed by XRR) (sample A1 from Chapter 4) recorded using (a) Cr Kα and (b) Ga Kα HAXPES. The energy range and location of best fit is once again different, despite similar noise levels of the background signal in both spectra. From this we can see that even the same sample does not have a general recommendation for the range over which to apply an error calculation when using different photon source energies.

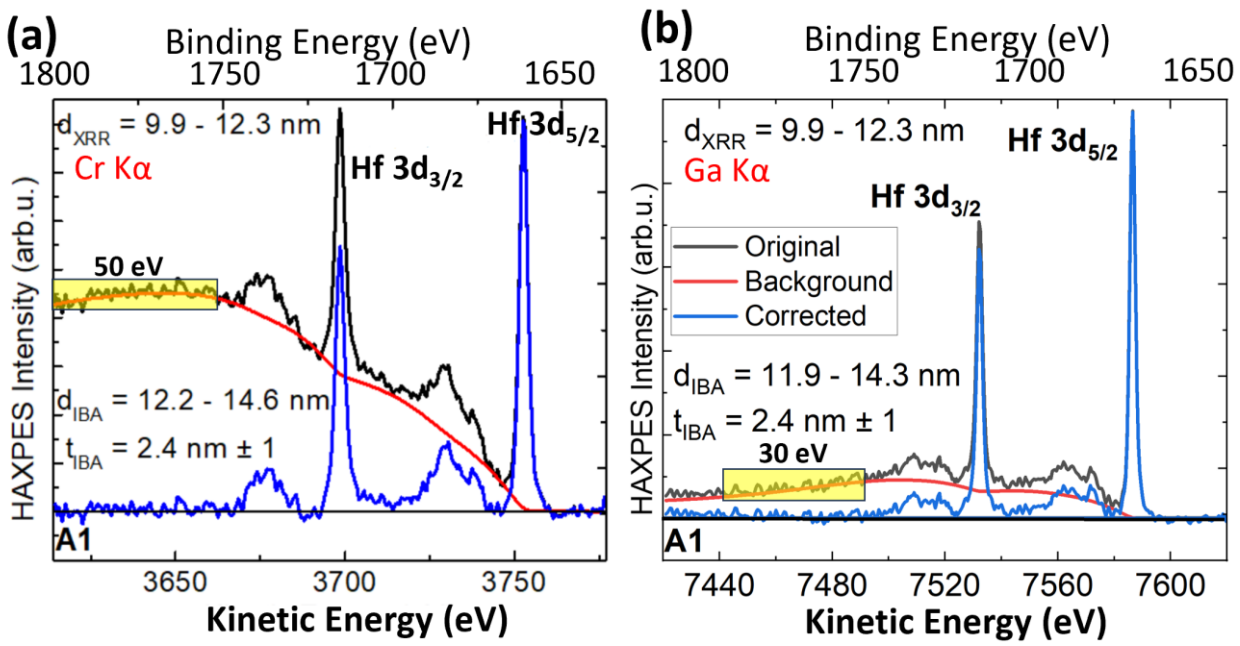

Figure 85. HAXPES-IBA of Hf 3d in HfO_2 (2.4 nm) buried under Al_2O_3 (9.9 nm) (sample A1 from Chapter 4) recorded (a) Cr Kα and (b) Ga Kα sources.

From Figure 85 and Figure 86, we can conclude that a quantitative and automated solution for determining layer thicknesses and depth distributions will require a method more sophisticated than a simple error correction applied over a pre-determined energy range.

6.4 Error calculation vs visual inspection

In our attempt, we chose the MSE (Equation 43) to address the issue of the error calculation.

6.4.1 Buried GaN Start Depth

In the Al_2O_3/GaN samples from Chapter 5, we evaluated 12 possible solutions for the GaN Start Depth (d_1) (Figure 3) in the 3 nm-buried sample with 0.2-nm increments from 0.2 nm to 5.2 nm, and 100 possible solutions for the 10, 15, 20, and 30 nm-buried samples in 0.2-nm increments to ± 10 nm of the nominal value.

Since the fit range between Ga 2p and Ga 2s changed dramatically across varied overlayer thicknesses, we restricted our assessment to the 3900 – 4020 eV KE range (120 eV) at the higher energy loss region of the spectra (highlighted region in Figure 86).

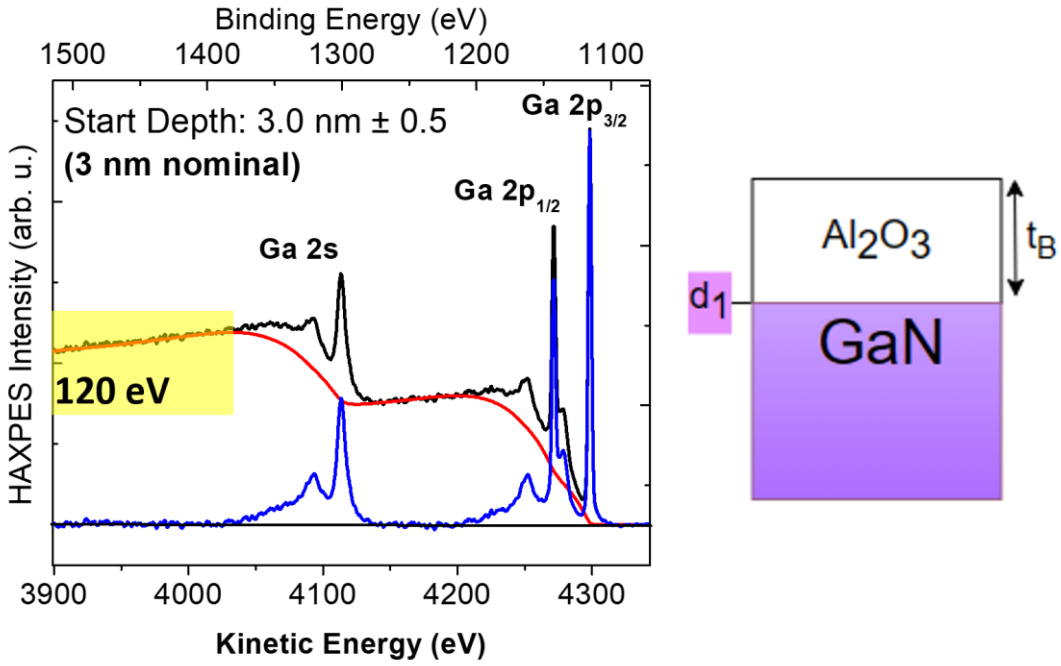

Figure 86. HAXPES-IBA of Ga 2p – Ga 2s in Al_2O_3/GaN series. The 3900 – 4020 region was selected for the error calculation assessment.

The resulting minimum MSE Start Depth solutions are compared with the nominal values and visual inspection solutions in Table 25 below. Recall from Chapter 5 that the HAXPES-IBA Start Depth solutions were systematically underestimated when using the Universal 2 parameter cross-section. This is again reflected in the minimum MSE value solutions (excepting for the thinnest overlayer sample). In fact, the minimum MSE value solution underestimated the Start Depth even more than with a visual inspection. Since the Start Depth solution improved with the use of a reference spectrum, this may indicate bias in the visual inspection as we search for the "desired" value. In any case, we see that **the results from an automated error correction method are in general agreement with the visual inspection** (20 % and lower and as low as 4 %).

Table 25. Minimum GaN MSE Start Depth solutions are compared with the nominal values and visual inspection solutions

Sample	Nominal Al_2O_3 overlayer thickness	Minimum MSE solution **Start Depth**	Visual inspection **Start Depth**	% error nominal vs MSE	% error Visual vs MSE
3AlGaN	3	3.6	3.0	20 %	20 %
10AlGaN	10	9.0	9.5	10 %	5 %
15AlGaN	15	12.0	12.5	20 %	4 %
20AlGaN	20	13.2	15.0	34 %	12 %
30AlGaN	30	20.2	24.0	33 %	16 %

6.4.2 Buried HfO_2 Start Depth

We also applied the MSE calculation to the Start Depth solutions from Cr Kα spectra of buried Hf $3d_{5/2}$ in the Al_2O_3/HfO_2 samples studied in Chapter 4. The Start Depths d_1 (Figure 6) determined by XRR and IBA of Al 1s in the overlayer are as follows: A1 = 9.9 nm, A2 = 14.8 nm, A3 = 24.4 nm. The range over which the MSE was calculated was 3615 to 3665 KE eV (50 eV). 185 possible Start Depth solutions were tested in 0.2-nm increments to ± 2 nm of the nominal Start Depth and End Depth with the layer thickness bound to between 0.2 nm and 24 nm.

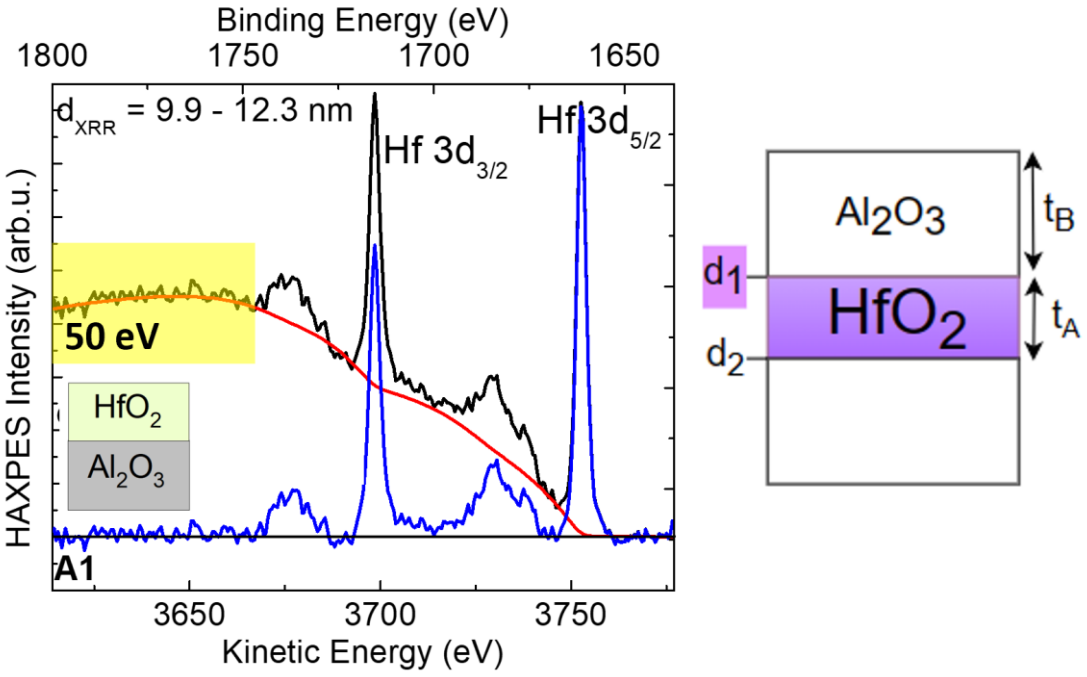

Figure 87. HAXPES-IBA of Hf 3d in the A-series from Chapter 4. The 3615 to 3665 KE eV region was selected for the error calculation assessment.

The resulting minimum MSE Start Depth solutions are compared with the nominal values and visual inspection solutions in Table 26 below. In Chapter 4, we found that HAXPES-IBA of buried Hf $3d_{5/2}$ gave accurate thickness measurements, but with Start Depth parameters ~2 nm deeper into the sample than determined by XRR measurements and IBA of Al 1s in the overlayer. Similar results have been found, where HAXPES-IBA indicated a 2 nm "gap" between the End Depth of Zn 2s in the overlayer and the Start Depth of Si 1s from the substrate in a ZnO/Si system [6].

In the results below, we see that the solution determined from the minimum error value in the MSE assessment performed similarly to the visual inspection (0 % error in A1 and A2). These results show that **in the case of a small sample set and IBA region, an error calculation can give results aligned with the visual inspection traditionally used in IBA.** Unfortunately, only three samples were available in the Al_2O_3/HfO_2 series.

Table 26. Minimum HfO_2 MSE Start Depth solutions are compared with the nominal values and visual inspection solutions.

Sample	XRR & Al 1s **Start Depth**	Min MSE **Start Depth**	Visual inspection **Start Depth**	**% error** XRR vs MSE	**% error** Visual vs MSE
A1	9.9	12.3	12.3	24%	0%
A2	14.8	16.6	16.6	12%	0%
A3	24.2	20.6	22	16%	8%

6.5 Conclusion

With increasing needs for semi-automated solutions in metrology, the fitting procedure would benefit from an error calculation in order to reduce analysis time. Selection of the location and range over which region the error calculation is performed, however, must be decided by the user, and spectra from different layer thicknesses and energy sources must be evaluated before putting an automated procedure into place. This is due to the intensity of plasmons and accompanying peaks impacting the background region where an error calculation would be implemented. We tested an MSE calculation to determine the IBA solution with minimum error between the experimental and simulated backgrounds. We found the MSE method to generally agree with the visual inspection solution. In the case of buried Ga $2p_{3/2}$, we saw a potential bias in the visual inspection towards the nominal overlayer thickness estimated by the ALD process. Strict boundaries of possible Start Depths and thicknesses,

however, were necessary in order to rule out unrealistic solutions. The purview of this work is to reduce free parameters and identify uncertainty in the lab-based HAXPES-IBA method. We conclude that while automating the fitting procedure is an important step in the future of the technique, it will require advanced algorithms in order to reduce uncertainty and time spent on the analysis.

[1] P. Risterucci, O. Renault, C. Zborowski, D. Bertrand, A. Torres, J.-P. Rueff, D. Ceolin, G. Grenet, S. Tougaard, Effective inelastic scattering cross-sections for background analysis in HAXPES of deeply buried layers, Appl. Surf. Sci. 402 (2017) 78–85. https://doi.org/10.1016/j.apsusc.2017.01.046.

[2] C. Zborowski, S. Tougaard, Theoretical study toward rationalizing inelastic background analysis of buried layers in XPS and HAXPES, Surf. Interface Anal. 51 (2019) 857–873. https://doi.org/10.1002/sia.6660.

[3] C. Zborowski, O. Renault, A. Torres, Y. Yamashita, G. Grenet, S. Tougaard, Determination of the input parameters for inelastic background analysis combined with HAXPES using a reference sample, Appl. Surf. Sci. 432 (2018) 60–70. https://doi.org/10.1016/j.apsusc.2017.06.081.

[4] P. Risterucci, Coupling of electron spectroscopies for high resolution elemental depth profiles in complex architectures of functional materials, University of Lyon, 2015.

[5] C. Zborowski, Characterization of deeply buried interfaces by Hard X-ray Photoelectron Spectroscopy, University of Southern Denmark, 2018.

[6] C. Zborowski, A. Vanleenhove, T. Conard, Comparison and complementarity of QUASES-Tougaard and SESSA software, Appl. Surf. Sci. 585 (2022) 152758. https://doi.org/10.1016/j.apsusc.2022.152758.

General Conclusion

The framework of this work is nanodevice technology and the need for nondestructive thickness measurements of the deeply buried layers that make up increasingly complex semiconductor components. We started by presenting in more detail the challenges of characterization and metrology for such layers, making the point that, among the various experimental methods available in the laboratory or in the clean room, X-ray photoelectron spectroscopy is widely used as it allows to obtain the chemical environment of an element nondestructively. The limiting factor of XPS measurement is the probing depth of 3λ which is not beyond 9 nm with soft X-ray laboratory sources. Increasing the probed depth by analysis of the inelastic background allows to retrieve the depth distribution of deeply buried layers many times past that of core peak analysis. Chapter 1 and 2 provided a view regarding the possible contribution of inelastic background analysis in characterization and metrology of buried layers, in the framework of the recent advent of HAXPES spectrometers fitted with hard X-ray laboratory sources. One the singularity of our work is that we explored the implementation of inelastic background analysis, presented in detail in Chapter 3, from two types of novel laboratory spectrometers fitted with Cr Kα (hv = 5.41472 eV) and Ga Kα (hv = 9.25174 eV) photon sources, increasing the IMFP past 10 nm for many core transitions.

Then, our work focused on the results of a method for lab-based HAXPES-IBA of high-k oxides and semiconductor materials used in OxRRAM and MOS-HEMT structures, described in Chapter 4 and 5.

We started in Chapter 4 with the study of model, well-controlled technological samples of minimal surface roughness, in the form of bilayer oxide layers of Hf- and Al-oxide. We began with ultrathin Al_2O_3, from which we established the quantitative capability of non-destructive WDXRF by confirming the linear dependence of the layer thickness determinations to the Al-dose measured with LPD-ICPMS. Then, we showed how pARXPS was uniquely capable of discerning between the Si substrate and native oxide at the interface. This is important when studying the effect of Si surface treatment by HF and tracking the linear growth cycle of the ALD process. Next, with having previously-established the reliability of ALD for producing thin films, the XPS-IBA method was evaluated in determining the layer thicknesses of a thin bilayer system of Al_2O_3 (2 nm) deposited over HfO_2 (1.5 nm) with a native oxide (1 nm). We found that GCIB at low energy/atom effectively removed surface contamination, reducing error in the analysis to 6%. In this sample, crowding in the Al Kα XPS spectrum prevented IBA of Al and Si. Instead, the depth distribution of Hf $4p_{3/2}$ was subtracted from the O 1s total distribution, giving an

estimation of all three layers in the sample. This shows the versatility of the IBA technique. The IBA results were compared with pARXPS and GIXRF for a complimentary nondestructive analysis.

Finally, lab-based HAXPES-IBA was tested on the Al_2O_3 and HfO_2 ALD materials. Six samples of Al_2O_3 and HfO_2 bilayer stacks with increasingly thick overlayers up to 24.4 nm and buried layers of approximately 2.5 nm were measured with Cr Kα and Ga Kα laboratory sources to give maximum O 1s IMFPs of 8.4 and 13.6 nm, respectively. Every element in the sample was studied for a self-contained analysis, and the results were compared with XRR. The IBA technique was originally developed for soft X-ray energy. In this chapter, we aimed to provide a comprehensive study of IBA when applied to lab-based HAXPES. The resulting thicknesses were in complete agreement with XRR thicknesses. For the Cr Kα HAXPES-IBA method we evaluated a weighted inelastic cross-section for Si 1s in the substrate, and the use of a reference spectrum in QUASES-Generate. In the comparison of IBA results using Cr Kα vs Ga Kα excitation we assessed the impact of the source energy on precision in the visual inspection of the QUASES-Analyze solution. We found that IBA with Ga Kα HAXPES radiation increased uncertainty in the QUASES-Analyze solution due to a reduced background signal. This emphasizes the need to select the photon energy based on the thickness of the sample. Part of the results of Chapter 4 were published in Applied Surface Science in January 2023 [1].

In Chapter 5, we applied the method developed in Chapter 4 to more realistic samples based on the same oxide materials with applications in well-defined technologies. In the first study, we present a sample class of Al_2O_3 deposited over GaN by ALD representative of a recessed gate metal oxide semiconductor channel High Electron Mobility Transistor. Quantitative secondary ion mass spectrometry (SIMS) measurements complement the IBA technique by confirming the need for a Ga $2p_{3/2}$ reference spectrum. The second study focused on the analysis of HfO_2 used for oxide resistive random access memory technology. Here, the HAXPES-IBA method is combined with ion sputtering to confirm the Ti/TiN overlayer thickness in a Ti/HfO_2-based structure. The modifiable 3-parameter Universal scattering cross section was used for accurate HAXPES-IBA of Ti 1s, and we demonstrated the robustness of the IBA technique by accurately modeling Hf $3d_{5/2}$ despite intense Ti Auger signals in the lower energy loss region just before the peak.

A final chapter discussing an error correction applied to the IBA solution presented the challenges of a semi-automated method, and highlighted case studies previously presented which compared the error correction to visual inspection of the IBA result. IBA results from buried Hf $3d_{5/2}$ and Ga $2p_{3/2}$ yielded similar solutions for mean squared error (MSE) and visual inspection of the spectra.

[1] Bure, T.R., Renault, O., Nolot, E., Lardin, T., Robert-Goumet, C., Pauly, N., 2023. Assessing advanced methods in XPS and HAXPES for determining the thicknesses of high-k oxide

materials: From ultra-thin layers to deeply buried interfaces. Appl. Surf. Sci. 609, 155317. https://doi.org/10.1016/j.apsusc.2022.155317.

Annex A

These tables were taken from the work of *C. Zborowski* [1].

technique	TEM [106]	APT [107]	SIMS [108]
samples	Conductor	conductors and insulators	all elements
preparation	maximum thickness: 100 nm	tip	electron gun if charge effect
source	electrons (100 -200 keV)	laser impulsion	Cs, O or Ar ions (0.2 - 15 keV)
secondary beam	electrons	ions	emitted ions from material
detector	EDS	PSD (position and ToF)	ToF
invasive			no
destructive	yes	yes	yes
energy resolution	0.1 - 0.8 eV	/	/
in-depth resolution	0.2 nm	0.05 nm	0.5 nm
lateral resolution	0.2 nm	0.2 nm	100 nm
detection limit	$1x10^{19}$ at/cm^3	$1x10^{18}$ at/cm^3	$1x10^{12\text{-}16}$ at/cm^3 100 ppb
probing depth	1-10 nm		0.5 nm
Information	-imaging -crystalline structure -geometry, thickness -composition contrast	-3D mapping -chemical composition -concentration profile -quantitative analysis	-3D distribution mapping -in-depth concentration profile -composition, doping, diffusion

technique	Ellipsometry [109]	FTIR [110]	XRD [111]	XRR
samples	all elements flat surface	all elements transparent substrate Si	all elements except H	all elements except H
preparation	no	no	no	no
source	UV - visible (1-10 eV)	IR	X-rays (1.5 keV)	X-rays (1.5 keV)
secondary beam	UV-visible	IR	X-rays	X-rays
detector	photomultiplicator	thermal MCT	Vantec scintillator	Vantec scintillator
invasive	no	no	no	no
destructive	no	no	no	no
energy resolution	0.01 eV	$1x10^{-4}$ at/cm^3	5 % 75 eV	5 % 75 eV
in-depth resolution	0.5 nm	20 nm	3 nm	3 nm
lateral resolution	30 µm	1.5 µm	10 µm	10 µm
detection limit	$10^{15\text{-}16}$ at/cm^3	$10^{15\text{-}16}$ at/cm^3	1 % at ppm	1 % at ppm
probing depth	nm - µm	µm	3 nm - 10 µm	3 nm - 10 µm
Information	-material optical constants -thin film thickness -interfaces (roughness)	-chemical composition -chemical binding -surface chemistry and contaminations	-composition and structure measurement -Stress, grain size	-roughness, geometry, thickness, thermal expansion coefficient

technique	AES [112]	RBS [113, 114]	XPS [29, 115]
samples	Z<30 not for heavy elements and insulators	5 < Z < 50 heavy atoms sensibility	all elements except H and He
preparation	thickness < 1 cm	/	no
source	electrons (1 -10 keV)	light ions (MeV)	X-rays < 1.5 keV
secondary beam	Auger electrons	retrodiffused ions	photoelectrons
detector	MCD	surface barrier	MCD
invasive	no	localy	no
destructive	yes for depth profile mode	yes	yes for depth profile mode
energy resolution	0.02 - 0.2 % 2 eV	0.2 % 10 keV	0.02 % 0.42 eV
in-depth resolution	0.2 nm	2 - 20 nm	2 - 20 nm
lateral resolution	20 nm	100 µm	15 - 20 µm
detection limit	$1x10^{19}$ at/cm^3 0.1% at	$1x10^{19}$ at/cm^3	$5x10^{18}$ at/cm^3 0.1 % at
probing depth	3 - 5 nm	1 - 10 nm	1 - 10 nm
Information	-Auger mapping -chemical bindings -in-depth profile -quantitative analysis (composition, doping) -diffusion	-elemental analysis -in-depth profile -quantification (reference) -composition, doping, diffusion	-mapping -depth profile -chemical binding

[1] Zborowski, C., 2018. Characterization of deeply buried interfaces by Hard X-ray Photoelectron Spectroscopy. University of Southern Denmark, CEA-Grenoble.

Annex B

Here, we provide a walkthrough of QUASES-Analyze and QUASES-Generate in the HAXPES-IBA method used in this thesis.

The guide proceeds in three parts:

1. Preparing spectra for QUASES analysis
2. QUASES-Analyze
3. QUASES-Generate

Annex B. 1

To begin in either QUASES-Analyze or QUASES-Generate, the user must select the file format to display the proper energy range with:

Setup > file format > select file

In the case of HAXPES, select **synchrotron energy** and enter the source energy.

Next the spectrum is treated with a smoothing method using the Savitsky-Golay Algorithm. This step reduces noise in the spectrum, and can improve uncertainty in the analysis. To do this, go to:

Tools > Smooth and Derivative by Savitsky-Golay Algorithm

Click the file name in the File Manager (

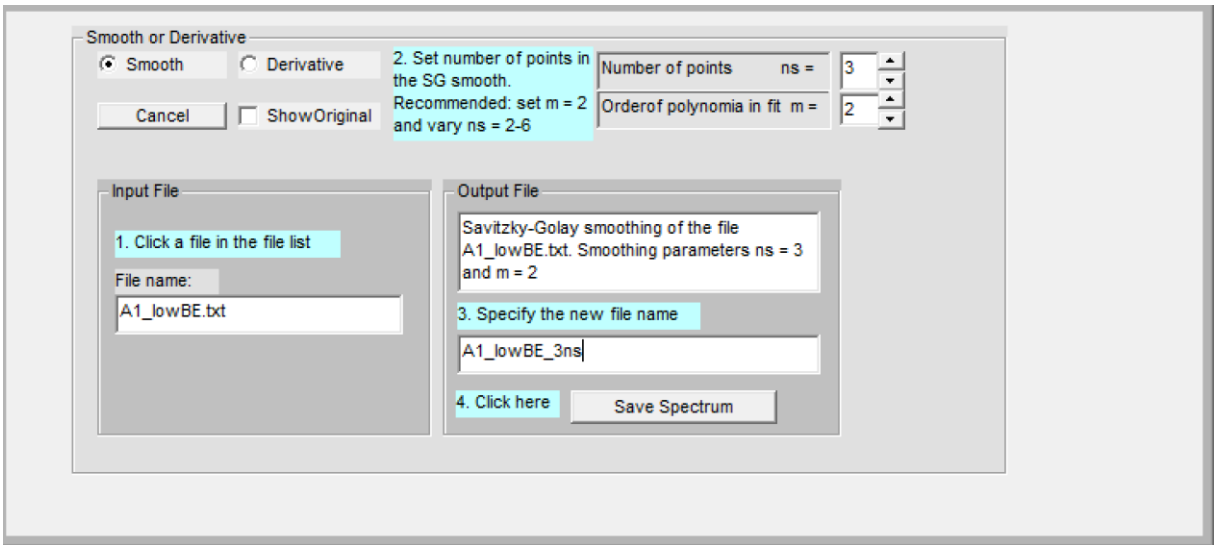

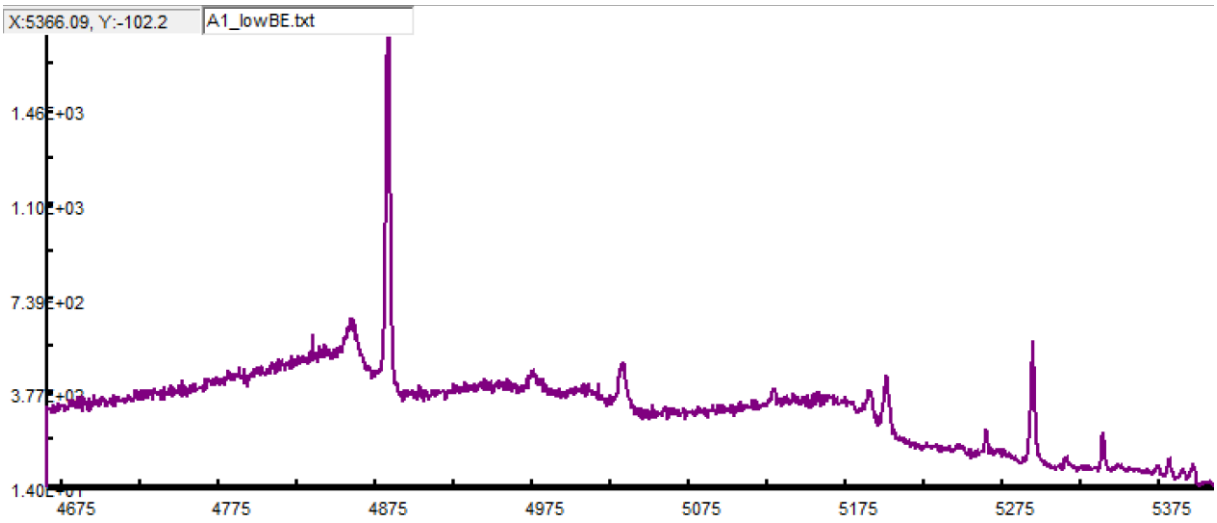

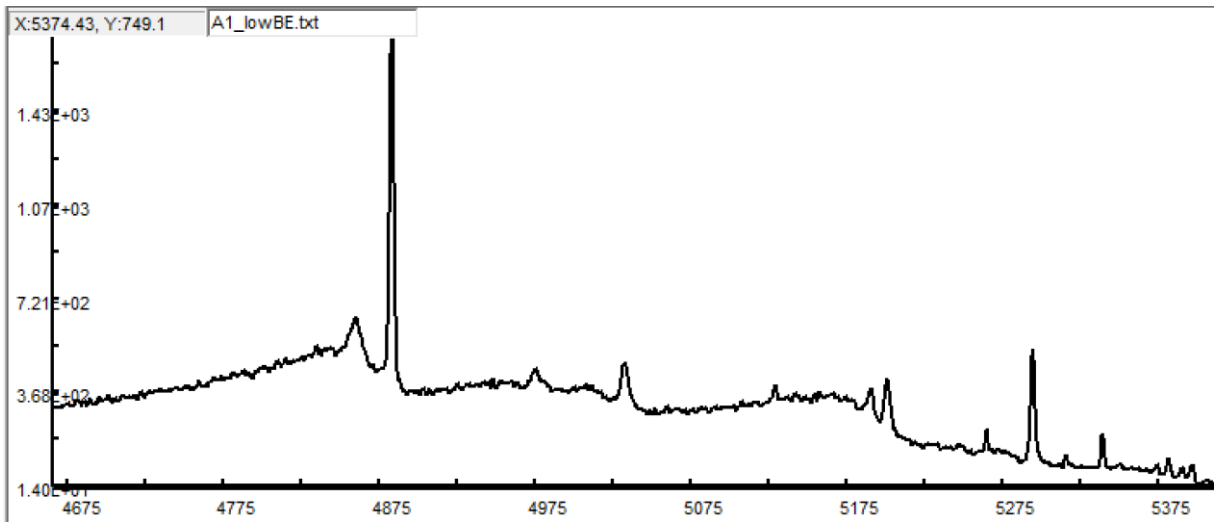

No Ref Spectrum

1. Set file format for source energy

2. Measure survey spectrum. Optional SG smoothing if very noisy-does not affect result

3. Correct spectrum for the analyzer transmission function

4. Isolate Peaks

a. Align with 30 nm to the higher intensity side on right of the peak

b. Note takeoff angle of background in Analyze section

c. Avoid peaks from other species

5. Calculate a weighted IMFP for the photoelectron traveling through the material

6. Correct the x-scale to ,95

7. Choose model

8. Vary values for start and end depth until Jcalc(E,Ω) is equal to the Jmeasured(E,Ω) or F(E,Ω) = 0

Preparing Ref Spectrum

1. Requires a wide scan spectrum from the reference sample

2. Correct for analyzer transmission function

3. Isolate Peaks

4. Set IMFP and angle of emission

5. Use Buried Layer profile

6. Start depth = 0 end depth = 9999

7. X-scale must be between ,87 and 1,02

The reference can be a pure material, reasonably thick thin flim, or alloy of known composition. Use the same spectrometer settings and geometry for the reference and other samples. Resolution does not matter.

Using a Reference Spectrum

1. Choose “Out+Scaled ref” in “Plotted spectra”

2. Change the Eshift to align the peaks

3. Scalefactor = 1

The peak intensity must be the same. The area of the two are compared and the ratio is the ScaleFactor, which should equal 1

The shape should be the same. Differing chemical states might change the shape in the energy range close to the peak. (Hansen et al., 1992)

Baseline Setting

The user must also set the baseline for the isolated peak region of interest. The shape of the inelastic background calculated by the software will more or less correlate to the experimental background for various angles of the baseline. An accurate baseline gives a calculated inelastic background, which lifts

off at the middle of the peak, and runs through the center of the experimental background preceding the peak. The fit can be further assessed for how well the modeled inelastic background superimposes over the experimental background after the peak. A baseline angled too wide from the background results in a modeled background whose lower KE signal is too high, and vice versa.

According to QUASES-Analyze guidelines and tutorial videos available through QUASES.com, the baseline should align with the overall background trend before the peak and delineate the shape of the spectral background if the photoelectron peak was not present. It should begin 30 eV before the peak and continue to the next peak [7]. Contributing literature impresses the importance of an accurate baseline in obtaining reliable depth distribution models.[9] It is further instructed that the baseline may be restricted to less than 30 eV before the peak if it results in a better fit of the simulated background to the experimental background. A “good fit” is indicated by overlap and similar general trajectories: the simulated background should not appear to have a different takeoff angle than the experimental. Restricting the baseline while maintaining the angle does not change the solution. It does allow, however, greater control over setting the angle, since there is less signal before the peak to match up with.